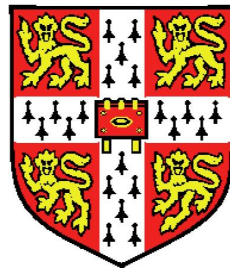


Modelling of Friction Stir Spot Welding



Mr Aidan Reilly MA MEng
Department of Engineering
Sidney Sussex College
University of Cambridge

A thesis submitted for the degree of
Doctor of Philosophy

25 May 2013

Preface

This dissertation sets out my work on friction stir spot welding from 2009 to 2013. Although owing much to many other people, the thesis as set out here is entirely my own work except where specifically noted. In particular, it draws heavily on work published by a wide range of other authors for specific details. These contributions are all noted in the text, with details of sources given in the section titled ‘References’. The first version was submitted for examination on 28 March 2013. Following my viva on 22 May, this revised version was completed on 25 May 2013. This work comprises 56375 words and 120 figures.

A handwritten signature in dark blue ink, reading "Aidan Reilly". The signature is written in a cursive style with a long, sweeping underline that extends to the right.

Acknowledgements

I would like to express my sincere gratitude to everyone who has helped me in my work and without whom it would not have been possible. There are too many to name everyone individually, but in particular I would like to thank my academic supervisor Hugh Shercliff and advisor Graham McShane for their invaluable advice and assistance throughout the project. I would also like to thank my parents Tom and Sue for their support, both during the last four years and before, and I would like to thank my indefatigable proof-reader Tasha for her patience in reading through many early drafts and pointing out my mistakes. My sister Alice has provided me with much encouragement, as has my brother Jonathan, and I hope he is successful with his own thesis; I am also deeply indebted to Hazel for urging me to finish on time, and had it not been for her I would probably still be writing.

I would like to thank Bethany Parker and Patryk Jędrasiak for their contributions, and I would like to acknowledge the assistance of Yingchun Chen and Phil Prangnell from Manchester for their collaboration, and for the many useful discussions.

Finally, I would like to express my gratitude to all my supervisors, tutors and fellow students at Trinity Hall, without whom I would not have started my Ph.D., and to everyone at Sidney Sussex College, without whom the last four years would have been much less fun.

This work was funded by the Engineering and Physical Sciences Research Council.

Contents

Preface	iii
Acknowledgements	v
Summary	xi
Nomenclature	xiii
1 Introduction	1
1.1 Motivation for the project	3
1.2 Friction stir process descriptions	5
1.2.1 Friction stir welding	5
1.2.2 Friction stir spot welding (FSSW)	7
1.2.3 Pinless FSSW	8
1.3 Comparison between FSSW and other processes	10
2 Literature review	13
2.1 Welding process modelling	13
2.2 Background to FSSW	17
2.2.1 Development of pinless joining	17
2.2.2 Failure modes	18
2.2.3 Optimum conditions	22
2.3 Previous modelling approaches	22
2.3.1 Advantages of modelling	22
2.3.2 Introduction to modelling	23
2.3.3 Friction stir spot welding	24
2.3.4 Friction stir welding and related processes	25
2.3.5 Empirical testing and validation	39

2.3.6	Microstructural modelling	41
2.3.7	Modelling of related non-welding processes	42
2.4	Constitutive data	42
2.5	Issues for further study	45
2.5.1	Need for new techniques	46
3	Experimental work	49
3.1	Introduction	49
3.2	Methodology	50
3.3	Welding parameters	55
3.3.1	Welding time	55
3.3.2	Rotation speed	57
3.3.3	Workpiece material	59
3.3.4	Welding time — Al to Fe	62
3.3.5	Rotation speed — Al to Fe	63
3.4	Tool types	65
3.5	Weld quality	67
3.6	Sources of error	70
3.7	Plunge depth and surface finish	72
3.8	Backing plate material	77
3.9	Flow visualisation	78
4	Thermal modelling	79
4.1	Introduction	79
4.2	Timescale of welding	81
4.3	FE model description	82
4.4	Axisymmetric modelling	86
4.5	Thermal contact problems in Abaqus	89
4.6	Mesh effects	91
4.7	Model calibration	92
4.7.1	Material properties	93
4.7.2	Power input	97
4.7.3	Heat losses	106

4.8	Plunge depth effects	112
4.9	Model to experiment comparison	114
4.10	Optimum welding conditions	117
4.10.1	A process window for FSSW	117
4.10.2	Alternative backing plate materials	122
5	Kinematic model	127
5.1	Model development	129
5.2	Tool contact boundary condition	132
5.3	Through-thickness heat flow	136
5.4	Dissimilar joining: aluminium to steel	140
5.4.1	Welding Al to uncoated steel	140
5.4.2	Welding Al to galvanized steel	142
5.5	Deep plunge welds	144
5.6	Comparison with experiments	147
5.7	Variation in $\bar{\omega}$ for experimental welds	152
5.8	Analysis of actual slip conditions during welds	154
5.9	Tool features and hooking	155
5.10	Conclusions	158
6	Sequential small-strain analysis	159
6.1	Introduction	159
6.2	Static plunge modelling	160
6.2.1	Model setup and initial tests	161
6.2.2	Methods of simulating downforce	162
6.2.3	Mesh sensitivity analysis	167
6.2.4	Further investigation of the Boussinesq problem	167
6.2.5	Plasticity	171
6.2.6	Analysis of thin plates	172
6.3	Sequential small-strain analysis	174
6.3.1	Aim	174
6.3.2	The model	175
6.3.3	Proof-of-concept	183

6.3.4	Thin plate welding	187
6.3.5	Adaptive timesteps	189
6.3.6	Case study and validation	189
6.3.7	Optimum welding with a copper backing plate	192
6.4	Conclusions	197
7	Conclusions and further work	199
	References	203

Summary

Friction stir spot welding (FSSW) is a solid-state welding process which is especially useful for joining precipitation-hardened aluminium alloys that undergo adverse property changes during fusion welding. It also has potential as an effective method for solid-state joining of dissimilar alloys. In FSSW, heat generation and plastic flow are strongly linked, and the scale of the process in time and space is such that it is difficult to separate and control the influence of all the relevant input parameters.

The use of modelling is well-established in the field of welding research, and this thesis presents an analysis of the thermal and mechanical aspects of FSSW, principally using the finite element (FE) technique. Firstly, a thermal FE model is shown, which is subsequently validated by reference to experimental temperature data in both aluminium-to-aluminium and aluminium-to-steel welds. Correlations between high-quality welds and temperature fields are established, and predictions are made for peak temperatures reached under novel welding conditions.

Deformation and heating are strongly linked in FSSW, but existing modelling tools are poorly suited to modelling flow processes in the conditions extant in FSSW. This thesis discusses the development and optimisation of two novel techniques to overcome the limitations of current approaches.

The first of these uses greatly simplified constitutive behaviour to convert the problem into one defined purely by kinematics. In doing so, the boundary conditions reduce to a small number of assumptions about the contact conditions between weld material and tool, and the model calculation time is very rapid. This model is used to investigate changes in the slip condition at the tool to workpiece interface without an explicit statement of the friction

law. Marker experiments are presented which use dissimilar composition but similar strength alloys to visualise flow patterns. The layering behaviour and surface patterns observed in the model agree well with observations from these experiments.

The second approach extends the FE method to include deformation behaviour without the need for a fully-coupled approach, guided by the kinematic model. This is achieved using an innovative sequential small-strain analysis method in which thermal and deformation analyses alternate, with each running at a very different timescale. This technique avoids the requirement to either remesh the model domain at high strains or to use an explicit integration scheme, both of which impose penalties in calculation time and model complexity. The method is used to relate the purely thermal analysis developed in the work on thermal modelling to welding parameters such as tool speed. The model enables predictions of the spatial and temporal evolution of heat generation to be made directly from the constitutive behaviour of the alloy and the assumed velocity profile at the tool-workpiece interface. Predictions of the resulting temperature history are matched to experimental data and novel conditions are simulated, and these predictions correlate accurately with experimental results. Hence, the model is used to predict welding outcomes for situations for which no experimental data exists, and process charts are produced to describe optimum welding parameters.

The methods and results presented in this thesis have significant implications for modelling friction stir spot welding, from optimising process conditions, to integration with microstructural models (to predict softening in the heat-affected zone, or the formation of intermetallics at the interface in dissimilar welds). The technique developed for sequential small strain finite element analysis could also be investigated for use in other kinematically constrained solid-state friction joining processes.

Nomenclature used in this work

Symbol	Definition	Units
a	Thermal diffusivity	$\text{m}^2 \text{s}^{-1}$
a	Asymptotic power fraction	-
A, B	Material fitting parameters	Pa
C	Specific heat capacity	$\text{J kg}^{-1} \text{K}^{-1}$
C	Material fitting parameter	-
h	Heat flow per unit area	W m^{-2}
h	Workpiece thickness	m
h_c	Contact conductance	$\text{W m}^{-2} \text{K}^{-1}$
\dot{h}	Rate of change of h	$\text{W m}^{-2} \text{s}^{-1}$
L_P	Pin length	m
K	Bulk modulus	Pa
K_1, K_2	Material fitting parameters	Pa
l, m, n	Material fitting parameters	-
P	Instantaneous power	W
P_0	Initial power	W
q	Area or volumetric heat input	(W m^{-2}) or (W m^{-3})
\dot{q}	Rate of change of q	$\text{W m}^{-2} \text{s}^{-1}$
Q	Heat input	W
Q	Activation energy	J kg^{-1}
Q'	Heat input	W
R	Specific gas constant	$\text{J kg}^{-1} \text{K}^{-1}$
R	Radius	m
R_S	Shoulder radius	m
t	Time	s
T	Temperature	K
T_{melt}	Solidus temperature	K
T_0	Room temperature (293 K)	K

Symbol	Definition	Units
U	Internal energy per unit volume	J m^{-3}
v'	Slip velocity	m s^{-1}
v_H	Characteristic heat flow speed	m s^{-1}
x, y, z	Space dimensions	m
Z	Zener-Hollmon parameter	s^{-1}
α	Material fitting parameter	-
δ	Dimensionless slip rate (see page 34)	-
ε	Strain	-
$\dot{\varepsilon}$	Strain rate	s^{-1}
λ	Thermal conductivity	$\text{W m}^{-1} \text{K}^{-1}$
ν	Poisson's ratio	-
ρ	Density	kg m^{-3}
σ	Normal stress	Pa
σ_y	Normal stress at yield	Pa
σ_0	Base stress for material models	Pa
σ_∞	Limiting stress at large strain	Pa
τ	Shear stress	Pa
τ_y	Shear stress at yield	Pa
ω	Angular speed or velocity	rad s^{-1}
$\bar{\omega}$	Dimensionless angular velocity	-

Chapter 1

Introduction

This project is an investigation into a newly-developed joining technique: friction stir spot welding, an offshoot of the closely-related (and more established) friction stir welding. Friction stir spot welding (FSSW) was first reported in 2000 (Schiling et al., 2000), and it is commonly used to weld aluminium and steel. These two processes are illustrated in Figures 1.1 and 1.2, respectively. Both work in a similar fashion: a hard, rotating tool plunges down into the workpieces to be joined. Energy dissipated by friction and plastic work heats and softens the material, allowing it to deform. As the downforces are in general sufficient to produce at least some sticking friction, the deformation pattern broadly tracks the rotating motion of the tool. They are versatile and efficient processes that can join sheets of circa 1 to 50 mm thickness, though because of the equipment requirements (primarily stiffness) they are currently limited to factory/machine shop use and similar settings.

By comparison with more established welding methods and other join-

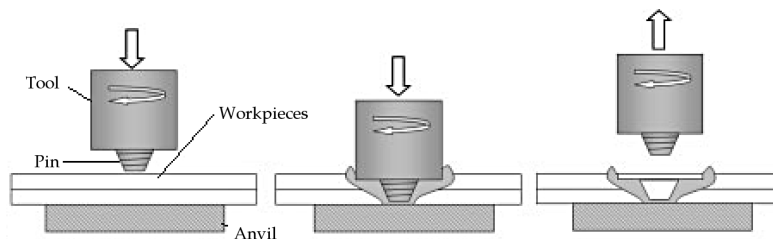


Figure 1.1: The FSSW process (image from Bakavos & Prangnell, 2009)

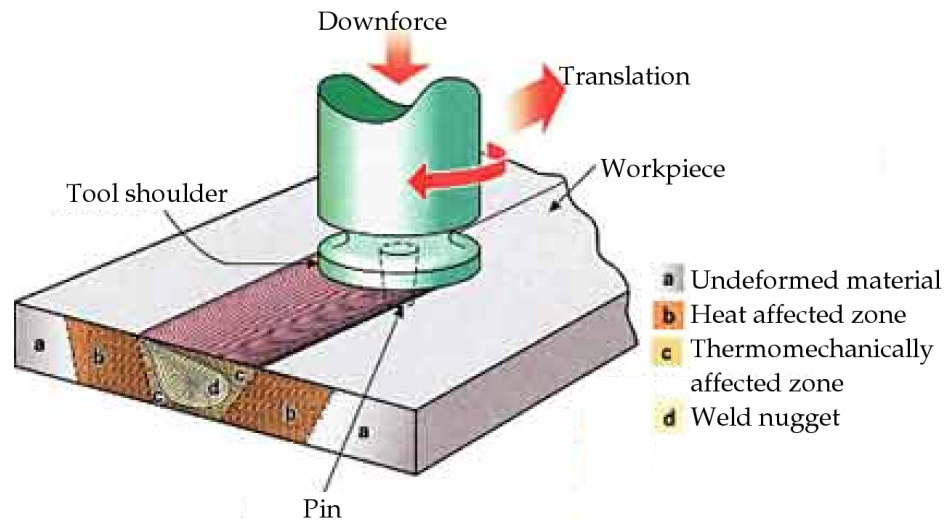


Figure 1.2: The FSW process for seam welding (from Smith et al., 2004)

ing techniques, these are poorly understood processes; they are not well-characterised, and much work remains to be done to develop optimum conditions for many alloys. Owing to the metallurgical advantages conferred by these processes, there has been significant investment in empirical testing, however the same attention has not extended to mathematical modelling. Development of accurate, fast predictive models will enable the optimisation of current techniques and the application of these joining and processing techniques to new materials or combinations of materials. In particular, there are many outstanding issues surrounding joining between dissimilar alloys, including problems caused by different material strengths and thermal properties, interfacial reactions leading to embrittlement, and corrosion resistance. However, an efficient method of joining dissimilar metals will allow greater variation of properties within a product, leading to lower weight, higher strength, and other benefits. The resulting microstructural changes can be exploited purely for their effects on mechanical properties, without being used to create a joint; when used in this way, the technique is termed friction stir processing. A greater understanding of these processes is of relevance to many industrial areas, but in particular to the transport sector, where the ability to use lightweight aluminium alloys, with high strength and stiffness but low density, is especially important.

1.1 Motivation for the project

There have always been incentives to reduce the weight of vehicles, both because of the costs associated with raw materials for production, and because of the cost of energy used in transport. More recently, a growing awareness of the environmental impacts of transport energy use has provided further pressure to reduce vehicle weight. In developed economies, transport accounts for approximately a third of all primary energy use, so there is a clear incentive to reduce the weight of vehicles in order to reduce energy use. Furthermore, vehicle weight has an impact on many issues besides fuel consumption and emissions, such as noise pollution, road damage and the rate of road accident casualties. As the total distance of passenger journeys correlates strongly with gross domestic product, which is expected to increase, and fuel reserves become more scarce, there is reason to believe that these incentives will grow over the short-to-medium term future (Schipper et al., 1992). Additionally, the increased use of alternative propulsion (i.e. alternatives to petrol or diesel, such as hydrogen fuel cells or battery-powered electric motors) could provide an additional push towards lightweight vehicles (Carney, 2008).

Application to the transport sector leads to a focus on particular materials that are either already widely used in transport, or are considered important for the near future. Although specific strength is the overriding performance criterion for structural components, there are other factors which have a strong influence including cost, toughness, toxicity¹ and ease of processing and recycling. Steel dominates the automotive industry due to cost, but aluminium and other light alloys (such as titanium and magnesium) are widely used in sectors such as aerospace where a higher premium is placed on performance.

The light alloys are often considered difficult to join, whether considering welds between the same metal, or to other light alloys or to steels (Polmear, 1995). Joining these metals to steel is of considerable importance

¹For example, beryllium has a low density and high specific strength, but due to its toxicity its use is limited to specialist applications such as spacecraft and X-ray equipment.

within the automotive industry despite the trend towards lighter parts as key components will continue to be made from steel, even in vehicles that are predominantly made from other metals, or composites. Although this discussion focuses predominantly on the transport sector, light alloys are widespread in many other engineering fields, with aluminium being the most widely used metal after iron and steel, and the most abundant metal in the Earth's crust.

Other alloys of commercial importance include titanium, which has a very high specific strength, but also a high cost; consequently its use as a structural material is confined to areas such as high-end aerospace applications and bicycle frames. It also finds many uses in the chemical industry due to its corrosion resistance. The most versatile titanium alloys are β -stabilised² and heat treatable (Hampel, 1961), of which the commonest alloy in industrial use is Ti-6Al-4V. Other common alloying elements include chromium, molybdenum and manganese (Carpenter, 2012).

Magnesium is the lightest structural metal in use. It is usually alloyed with aluminium and zinc, and its alloys are generally easy to cast; alloys containing zirconium are also widely used in more specialist applications. The primary applications of magnesium are in automotive and aerospace components, and die cast parts for consumer electronics. Its wider use is limited by its reactivity and poor performance at elevated temperature, with most alloys only being usable up to 500 K (Magnesium Industry Council, 1962). By comparison, steels typically retain sufficient usable strength up to at least 700 K.

Friction stir spot welding's advantages are explored in depth in the final section of this chapter (Section 1.3); it is an attractive process for the transport industry since its inherently low energy use and favourable joint properties could allow the construction of lighter vehicles with a lower embodied energy. As an example, the energy use of FSSW can be less than 1% of that required for an equivalent resistance spot weld, the current industry standard (Iwashita, 2003).

² β -stabilised alloys contain elements that form a solid solution in the β phase, which stabilise the ductile body centred cubic β phase to lower temperatures.

1.2 Friction stir process descriptions

1.2.1 Friction stir welding

Friction stir welding (FSW) is a novel joining process that was patented by Thomas et. al. in 1992. A diagram of the welding process is shown in Figure 1.2. This shows a butt joint configuration between two workpieces and the rotating tool above. The tool rotates at high speed, typically 30 to 300 rad s^{-1} (300 to 3000 rev/min), and this supplies both the heat and deformation to create a joint. In FSW, the tool translates slowly along the joint line (typically at 0.01 to 1 mm s^{-1}). As it does so, the rotation of the tool forces hot material around it, with most of the metal flowing past on the retreating side (the side where the translational and tangential velocities are in opposite directions; the opposite side is the advancing side). The whole process takes place with the weld material in a solid state, with heat generated by some combination of friction and plastic deformation. The balance between these two heat generation effects is a point of debate in the literature (see e.g. Mishra et al., 2000, Mahoney et al., 2001 and Charit et al., 2002).

Originally, FSW was developed for Al. Compared to traditional fusion welding processes, the temperature is lower and so problems associated with melting do not occur. This is particularly advantageous when working with heat-treatable, precipitation-hardened alloys such as the 2000, 6000 and 7000 series, which have Cu, Mg and Si, and Zn as the primary alloying elements. FSW has now been applied to many other metals, including steels, Ti and Mg. Threadgill et al. (2009) summarised the current state of research into friction stir welding of many metals in their review.

As well as being used for butt welds, the FSW process can also be used for other welding geometries, such as lap welds, and it is currently under research for complicated shapes such as T joints. However, the tooling and parameters required to make high-quality welds in a lap configuration are substantially different to those required for butt joints. In general, the joint must be wider and the range of optimal parameters is narrower for lap welds, owing to the

difficulty of breaking up the oxide layer on the two joining surfaces. Despite these difficulties, FSW is rapidly becoming a standard technique for lap joints as well as butt joints in many applications.

FSW tooling consists of two parts: the shoulder, which may be flat or profiled, and the pin, which projects from the shoulder. Various designs have been used for the pin, from smooth cylinders, through the addition of simple threads or flukes, through to the complexity of tools like the Triflute (see Figure 1.3).

For welds in Al and other light alloys, tools are commonly made from high-alloy steel. However, when welding steel the high wear rate of the tool is a particular problem (Mandal *et al.*, 2006). While tools may last for many welds in Al, a single long weld may have a non-negligible probability of tool failure when welding steel; the much higher strength of steel at elevated temperatures is compounded by the lower ductility of the tool materials. For welds in steel, tools based on tungsten or boron nitride are the most common. Tungsten-rhenium (W-Re) is one of the most durable tool materials, but is exceptionally expensive and difficult to manufacture, as is polycrystalline boron nitride (PCBN). W-Re tools can only be ground, as opposed to conventional machining, and PCBN tools are manufactured under very high temperatures and pressures.

A large fraction of the wear occurs during the plunge, when the tool encounters cold base metal. Tool wear with steel workpieces presents a particular problem, despite the use of special methods to reduce the wear rate. One of the most promising is the use of pre-drilled holes in the material to reduce wear during the plunge, but it remains a significant problem (Thomas, 1999, and Thomas *et al.*, 1999).

The reactivity of Mg and Ti presents further problems; tungsten-based tools are the most common choice for these metals and show promise. Ni-Fe or Ni-Cu based tools with W particles are under development, and these tools are substantially cheaper to produce than W base alloys.

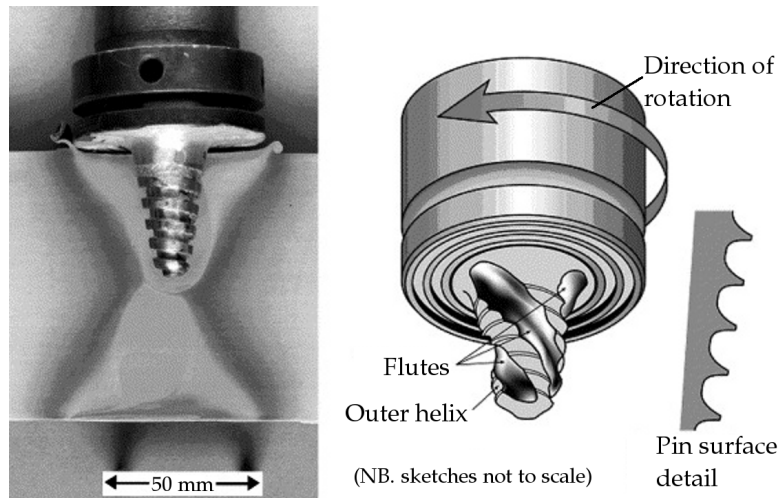


Figure 1.3: MX Triflute tool (from Mishra & Ma, 2005)

1.2.2 Friction stir spot welding

Friction stir spot welding (FSSW) grew out of FSW in an attempt to transfer some of the advantages of FSW to spot welding. While it has been used in production (including for spot welds in automotive bodies: see Bakavos & Prangnell (2009) and Iwashita (2003)), it is still considered an immature process. In its simplest form, it comprises 3 phases: a plunge, dwell, and retraction, with no lateral movement or translation. The process whereby this forms a joint is similar to that for seam FSW: heat created by friction and plastic work softens the workpiece material, and the rotation of the tool causes the workpiece to deform plastically to large strains.

Owing to this development path, initially the same tools and process parameters were used for FSSW as had been found suitable for FSW. This has been found to be suboptimal; the key differences between FSW and FSSW are:

- spot welding is a transient process, while seam welding in many cases takes place in a steady-state environment;

- the demands and loading patterns placed upon a spot weld vary markedly from those on a seam weld;
- the translation present in seam welding has an influence on the weld, despite its low speed compared to the tangential tool speed;
- spot welds are often made in thinner sheet than is typical for seam welds.

Some authors have started to publish studies studying FSSW specifically in more detail, and these are summarised in detail in Chapter 2.

1.2.3 Pinless FSSW

FSSW is FSW without translation, but this introduces a unique set of difficulties. One of the issues is the production of a ‘keyhole’, the hole in the centre of a spot weld left by the tool pin. This is not usually a problem with FSW; the weld can be continued into a blank, which is then machined off, or if not, it is often the case that the hole does not necessarily create a significant loss of strength due to the greater length of the joint. However, it is a more significant problem for FSSW simply because the hole occupies a much larger fraction of the joint area and volume. Consequently, current research is focusing on ways to create a weld without leaving a keyhole at all. The simplest approach, considered in detail by this project, is to form welds using a tool with no pin, relying entirely on the shoulder contact to generate heat and induce deformation in the workpieces. This process is illustrated in Figure 1.4.

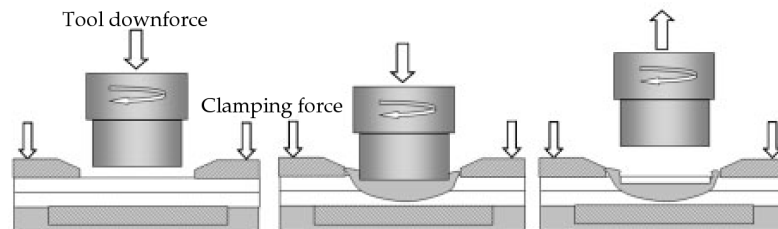


Figure 1.4: The pinless FSSW process (from Bakavos & Prangnell, 2009)

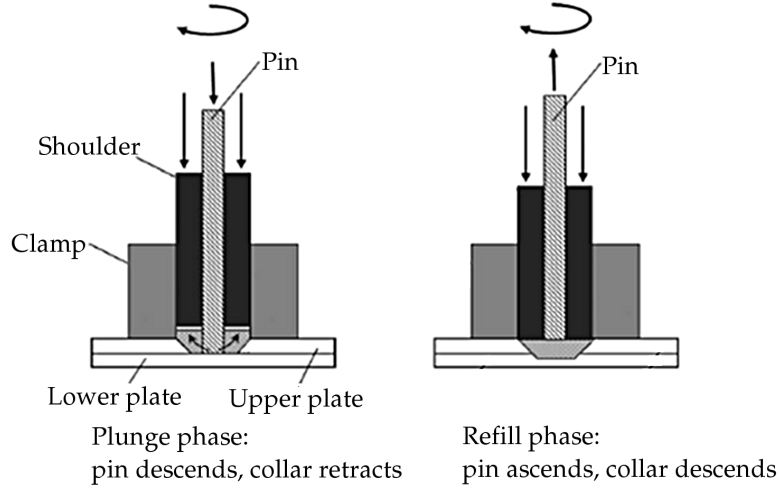


Figure 1.5: The refill FSSW process (from Muci-Kuchler et al., 2010)

Another technique that shows promise is refill FSSW, shown in Figure 1.5. This technique uses an independently movable collar surrounding the main part of the tool; on contact with the surface, this collar retreats, filling up the space with extruded workpiece material. The extruded material is then forced back into the weld zone by the collar as the tool retracts. This approach is very promising, but at the moment is too expensive and time-consuming to have been widely adopted for production use. Circular FSSW uses a conventional tool with a superimposed circular motion to increase the area of the joint. Using this method a keyhole is still formed, but a smaller hole is left for the same joint area. Different shapes besides a circular joint have been investigated, and while no fixed terminology has yet become standard the term swing FSSW is becoming popular for this method (Badarinarayan et al., 2007). However, this method — like refill FSSW — is considered too time-consuming for production use in the automotive industry where cycle time is considered a critical factor.

1.3 Comparison between FSSW and other processes

Many considerations determine which process is chosen for any particular application; for welding processes, key factors are the microstructural change induced by heating during the weld, the bulk property changes thus caused, and the cycle time of the process.

Conventional fusion welding involves substantial melting, usually of both workpieces to be joined. The two parts mix in the molten state, and when the weld nugget cools and solidifies a solid monolithic joint is formed. FSSW takes place entirely or almost entirely within the solid state (Babu, 2009). Melting a metal provokes large changes in microstructure, and the resulting microstructure on resolidifying can be very different from the pre-welded condition, even in a weld between identical alloys. This is especially noticeable with heat-treatable aluminium alloys; Al alloys also tend to exhibit large distortions and residual stresses on cooling after being fusion welded (Barnes & Pashby, 2000).

Heat-treatable Al alloys are those in the 2000, 6000 and 7000 series (with the primary alloying elements being Cu, Mg and Si, and Zn, respectively). These derive a significant proportion of their strength from precipitates — in the case of 6000 series alloys, Mg_2Si particles. Upon reheating, the precipitates entirely dissolve, and the weld will require extensive heat-treatment to return its properties to the pre-weld, parent material state. Such treatment may be impractical for a large component, so FSSW is particularly beneficial for these alloys. (Indeed, 2000 and 7000 series alloys are still referred to as ‘unweldable’, although this is no longer strictly the case as these alloys are quite easily joined with FSSW and FSW (Khalid, 2002).)

Since steel is so widespread many joining techniques were originally developed for steel. As process parameters have to be adapted before transferring a joining technique to a different material, it is difficult to be certain about the potential of a new process without extensive testing and research. However, one parameter that is comparatively easy to assess is the capability of a new process to join various thicknesses of material. The capability of FSW is

limited primarily by the size and stiffness of equipment required to join large thicknesses, and buckling/tearing of the workpiece for thin foils. Figure 1.6 shows the range of section thicknesses that can be routinely joined by a range of metal joining techniques, with selected welding processes highlighted; this gives a useful indication of the types of process that seam FSW competes with. FSSW works well for thin sheet, but has not yet reached the same level of development as FSW for joining thick plates, though no fundamental limit on this is envisaged beyond practical machine limits. The considerations outlined in this section apply to the use of FSSW for what may be considered ‘general factory welding’ conditions; in various more specialised tasks practical considerations may override concerns regarding the optimum process from a metallurgical point of view. This can work both ways: due to the equipment involved, FSSW is unlikely to ever become a technology in use on construction sites, or for field repairs to vehicles, despite current development work on hand-held FSSW devices. On the other hand, it is impossible to join closed-section components with resistance spot welds, but may be possible with FSSW (Zhao et al., 1999).

To be accepted industrially, many demands are made of a joining process besides the quality of the joint it makes; for example, diffusion bonding can produce very high-quality joints, but due to the time involved it is unsuitable for mass-production automotive applications, where joining processes must be kept below 10 s to be seen as competitive. FSSW is potentially competitive in this regard, although welding time probably represents its greatest weakness when compared to resistance spot welding (RSW), the dominant competing technology in the parameter space filled by FSSW.

The comparison with RSW becomes more favourable to FSSW when discussing light alloys specifically. Light alloys in general, particularly Al alloys, are much more conductive than steel; they also have a tendency to degrade electrodes due to their reactivity (Peng et al., 2004). Neither of these problems apply to FSSW.

Low temperatures and a small weld nugget mean that the heat input during FSSW is lower than in many other processes. Laser welding, which can produce high-quality, deep welds with a small heat-affected zone (HAZ)

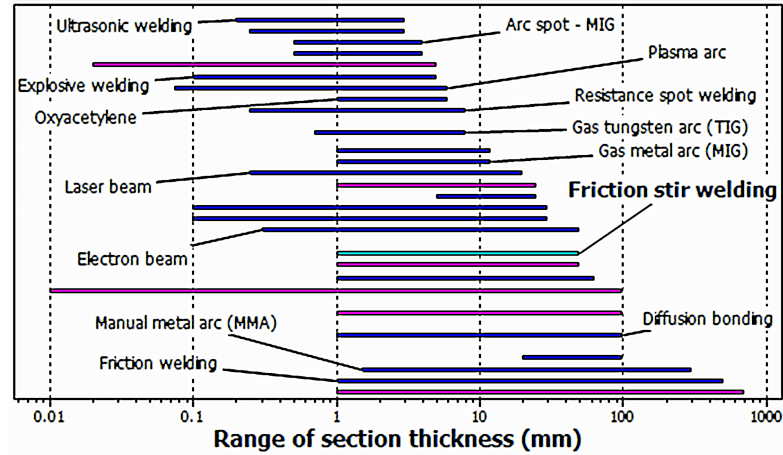


Figure 1.6: Selected joining techniques by section thickness, with welding techniques shown in blue. Data from CES (Granta Design).

and is capable of joining many light alloys, uses 50 times the energy of FSW (Mishra & Mahoney, 2007). Laser welding requires exceptionally high powers to join high-purity Al (1000 series alloys or higher) as they are very reflective (Mackwood & Crafer, 2005). FSSW uses around 10 % of the energy of RSW per weld (as an average — this figure can be as low as 1 % in specific conditions (Iwashita, 2003)), so a dramatic reduction in the energy needed to fabricate components is possible by switching from RSW to FSSW.

Emission of toxic gases during the process and the requirement for shielding gases to prevent oxidation are two common problems with traditional arc welding; they increase the difficulty and cost of using these processes in industrial settings. Arc welding processes convert 0.5 % to 1 % of the consumables used into gas and dust (Yeo & Neo, 1998). Altogether the annual emissions of metal oxides caused by welding within the EEC are around 6×10^6 kg (1998 estimate); a small fraction of total emissions, but still harmful and locally problematic. FSW avoids entirely the emission of these gases, which are associated with MIG and MMA welding, and which are a particular problem when welding Al (and also Cu). Such gases typically include a high proportion of Si, K, F, Ti, Ca, O_3 and oxides of nitrogen. As FSSW neither emits toxic gases nor requires shielding gases it has a lower environmental impact than other welding processes. These reasons also make it an attractive process from a manufacturing point of view, as it is much easier to handle.

Chapter 2

Literature review

This project is about friction stir spot welding, and specifically, it is an investigation into modelling of thin sheet welding using a pinless tool. The development of pinless FSSW took place at Manchester University, and this project is a continuation of that research, in collaboration with the original developers of the process. Key results that have already been published by other researchers in the team are included here; further details of their experimental work, along with experimental work conducted by the author, are given in Chapter 3.

2.1 Welding process modelling

Welding processes have changed substantially over time, with many new processes being invented. Arguably the first form of welding invented was forge welding as practised by blacksmiths for many centuries. However, it was not until the close of the 19th century that arc, oxyacetylene, thermite and resistance welding were invented. During the 20th century, many new welding techniques were invented, and the existing methods were refined and enhanced. Amongst these new developments, laser welding, the various forms of friction welding, and the use of shielding gas stand out prominently. Welding techniques may be usefully categorised in two ways: by grouping together either those processes where significant deformation is induced or

Significant deformation	No significant deformation
FSSW & FSW	Arc welding
Ultrasonic welding	Gas welding
Rotary friction welding	RSW
Linear friction welding	Electron beam welding
Forge welding	Thermite welding
Explosive welding	Laser welding
Magnetic welding	Plasma welding

Table 2.1: Welding types, categorised by degree of deformation

not (Table 2.1), or by grouping together those where the heat input is independently adjustable or not (Table 2.2).

The first grouping is probably the most significant if one wishes to group welding processes by the resultant microstructure; those with no significant deformation all rely on melting, and mixing between the workpieces occurs in the molten state. Those where significant deformation processes are involved often take place in a solid state, and consequently the microstructures formed by the two groups can be very different. From a modelling viewpoint the processes that involve no significant deformation — with the exception of laser and plasma welding — can generally be modelled for most purposes as a purely thermal problem (laser and plasma welding are exceptions as the extreme temperatures reached cause evaporation of workpiece metal). Those processes where deformation takes place require more complicated models.

The grouping shown in Table 2.2 is also directly relevant to modelling, with the processes in the left-hand column being the easiest to model: for these types, the heat input is known a priori, so temperatures and material responses are easy to calculate. For the operations in the right-hand column the heat input depends on the response of the material, often in a complicated feedback loop. For example, during resistance spot welding (RSW) the input voltage and current are known, so the workpiece temperature can be calculated from a purely thermal model; while in laser welding, the power absorbed depends on the microstructural state of the metal and on the shape of the hole formed, which both vary during the course of a weld (Zhao et al., 1999).

Heating controlled independently	Heating primarily via a dependent process
Arc	Laser
Gas	Explosive
RSW	Magnetic
Thermite	Rotary friction
Forge	Linear friction
Electron beam	FSSW & FSW
Plasma	Ultrasonic

Table 2.2: Welding types, categorised by the existence or otherwise of a feedback loop controlling the heat input during welding

The welding processes which fall into the right-hand column of Table 2.1 and the left-hand column of Table 2.2 are, in many respects, easier to model than the others. In these processes, the dominant effect is melting of the workpieces due to a known, controllable power input, and hence these welding operations may be modelled by numerical implementations of Fourier’s Law, or by analytical models of the type described by Rosenthal (1946). Although such models necessarily avoid much of the detail of the process, they are nevertheless accurate and robust enough to produce useful results, for example as the basis for microstructural models. By contrast, with processes like explosive and forge welding it is difficult to estimate the power input, making microstructural modelling very difficult. However, Rosenthal’s work provides a starting point for a thermal analysis of FSW, as carried out by Russell (2000) (described later).

Meanwhile, even a thermal model for the other processes listed can be difficult to implement as the power is an unknown quantity. In this regard, these processes are similar to FSSW in that the heat input is coupled to deformation of the workpiece in some way. As an example, laser welding is one of the most difficult processes to analyse, and so an extensive body of literature is dedicated to coupled models including a range of physical effects. Although some progress has been made, particularly the finding that power absorption is strongly linked to the presence of volatile materials in the surface layer of the workpiece, detailed modelling still involves computationally

intensive fully coupled FE models; these take of the order of many months or even years to simulate a full weld (Katayama, 1996, Bachmann et al., 2012, Gatzen & Chongbunwatana, 2012 and Balasubramanian, 2012).

The models that are most similar to FSSW fall into the same columns in both tables: linear and rotary friction welding, and ultrasonic welding, are likewise based on a friction process so the similarities between these types are the strongest. These processes are shown schematically in Figures 2.1, 2.2 and 2.3.

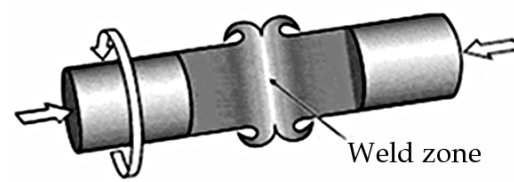


Figure 2.1: Rotary friction welding (image from TWI Ltd.)

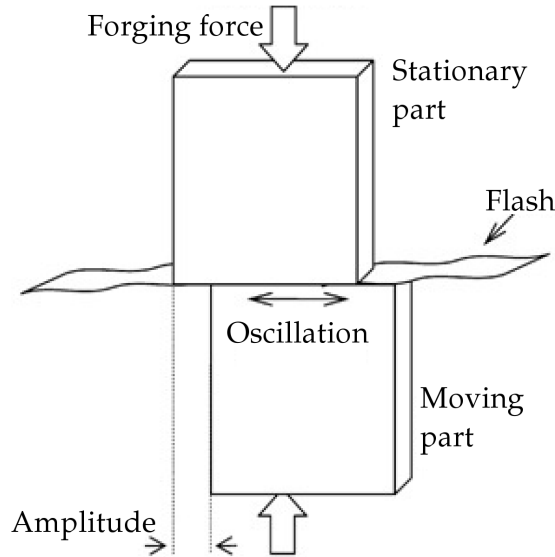


Figure 2.2: Linear friction welding (image from TWI Ltd.)

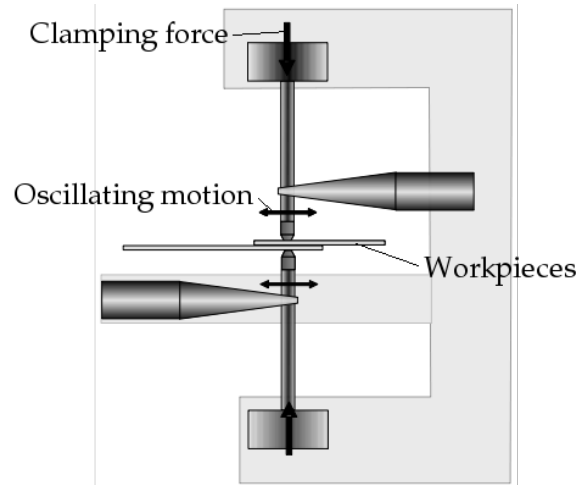


Figure 2.3: Ultrasonic welding (image from Haddadi, 2012)

2.2 Background to FSSW

2.2.1 Development of pinless joining

The concept of pinless FSSW seems simpler than FSSW with a pin; nevertheless, it was almost discovered by chance, as part of a study into the optimum pin length in FSSW by Bakavos & Prangnell, 2009. The reason for the lack of interest or development in the most obvious pinless approach appears traceable to a conference paper (Addison & Robelou, 2004), from which it was generally assumed that the pin had to penetrate into the bottom sheet by at least 25 % of the sheet thickness to form a successful lap joint. Many authors have cited this paper (see e.g. Valant et al. (2005); Fratini et al. (2007) and Buffa et al. (2008)), but the only other study to independently examine the effect of pin length appears to be that by Bakavos and Prangnell. This work examined the effect of pin length on the shear strength of lap joints in AA6111. While other authors have looked at this effect, like Addison & Robelou (2004) they did not control for the plunge depth of the shoulder. Bakavos and Prangnell suggest that the strengthening effect seen by Addison et al. is due to a correlation between shoulder plunge and joint strength, rather than pin length per se. In their study, Bakavos and Prangnell controlled for shoulder plunge by using a selection of different tools, each

with a different pin length. In this way, the shoulder plunge depth could be maintained constant, or nearly so, between welds. This gives a better measure of the effect of increasing the tool pin length independently from other parameters. Their results, for lap welds in 0.9 mm sheet, are shown in Figure 2.4; this figure shows a clear trend towards decreasing joint strength as the pin length is increased.

A number of authors are generally cited as having studied the effect of pin length; however, these studies are more properly described as varying the plunge depth. For example, Mitlin et al. (2006) studied the failure strength of lap joints in AA6111. Although their work is described as varying the pin penetration depth, they used the same geometry tool for all welds. As the shoulder was in contact with the workpiece in each of their welds, the shoulder plunge depth was also being varied.

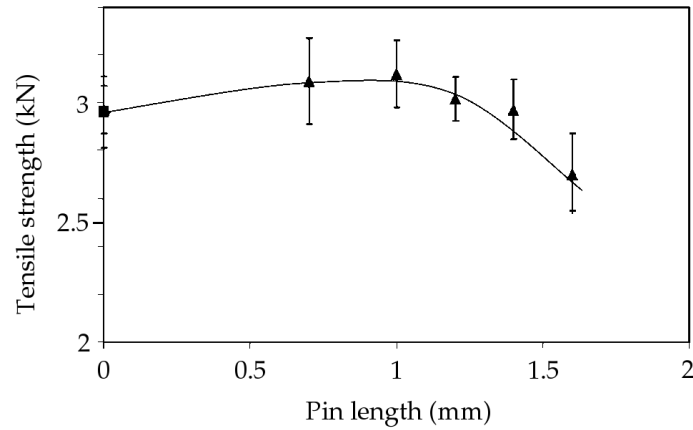


Figure 2.4: Variation of joint strength with tool pin length for lap welds between two 0.9 mm thick sheets (from Bakavos & Prangnell, 2009)

2.2.2 Failure modes

Part of the complexity in indentifying trends in the strength of joints made by FSSW is that there are a number of distinct modes by which a joint can fail. Mitlin et al. found the failure mode of the joint changed from brittle pull-out fracture for small plunges to ductile fracture around the edge of the nugget for large plunges. They found a peak in shear strength for the joint,

increasing then decreasing with increasing plunge depth, and suggest that the joint strength increases because the area of full metallurgical contact increases (see Figures 2.5, 2.6 and 2.7). Bakavos and Prangnell put forward the theory that this is due to the influence of the shoulder rather than pin penetration.

Tozaki et al. (2007*b*) identified three modes of failure of lap joints:

- Shear failure/debonding: in this type of failure, the joint comes apart along the line of the original interface between the two sheets. It is more commonly seen in thicker plate since with thin sheet the off-centre shear loading tends to peel the sheets apart, rather than causing a pure shear load; however, it can occur with very weak welds in thin sheet material.
- Nugget pull-out: in this failure mode, the nugget pulls cleanly out of one sheet, with a ductile failure occurring in a ring around the edge of the nugget. Typically, this will occur in the top surface, though the fracture would presumably form in the lower sheet under the right conditions.
- Combined debonding and pull-out: where failure begins in the manner of a pure shear failure, but then a portion of the nugget is pulled out at a smaller diameter than the tool shoulder. This usually occurs when the pin (if present) has penetrated into the lower sheet.

Of these three failure modes, that which involves a pull-out of the whole nugget usually has the highest performance. Peak failure forces can be similar to that of the combined debonding/pullout failure, but the failure energy is highest in the case where the whole nugget pulls out. Images of the post-failure surface for welds in thin sheet AA6111 are shown in Figure 2.8.

The presence and thickness of the surface oxide layer is thought to play a strong part in determining the quality and strength of the metallurgical joint (Badarinarayan et al., 2009). A requirement of a joining process that relies on forming a chemical bond between metals (such as FSSW) is that it breaks up the surface oxide layer on both surfaces. This is seen in other applications, for example in diffusion bonding where reactive metals like titanium must

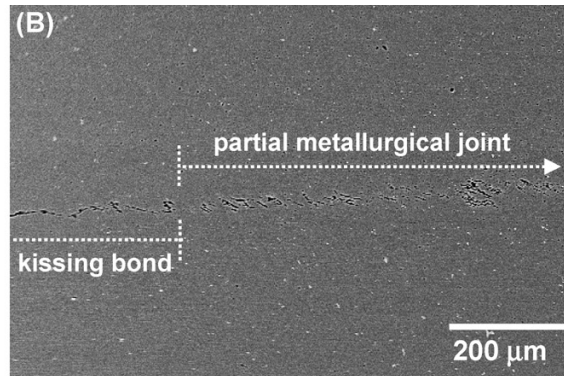


Figure 2.5: Micrograph of a kissing bond and partial metallurgical contact (from Mitlin et al., 2006)

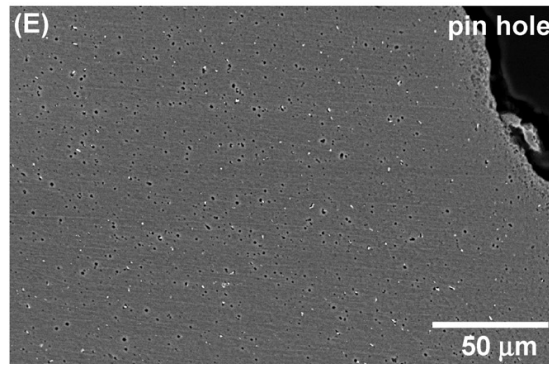


Figure 2.6: Micrograph of full metallurgical contact (from Mitlin et al., 2006)

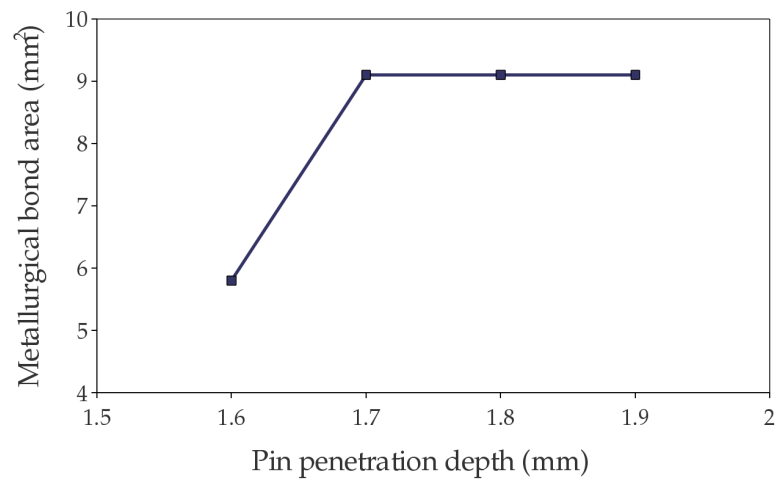


Figure 2.7: Variation of full metallurgical contact area with tool penetration (from Mitlin et al., 2006)



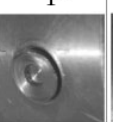
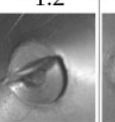
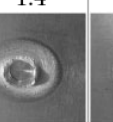

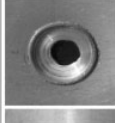
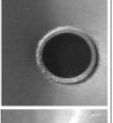
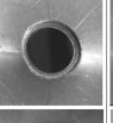
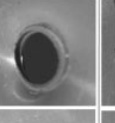
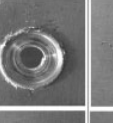
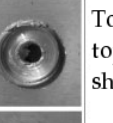
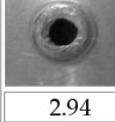
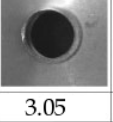

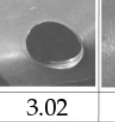
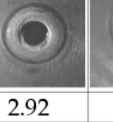
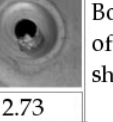
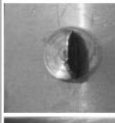


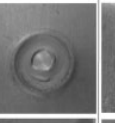

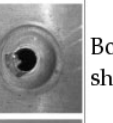
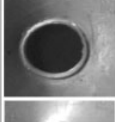
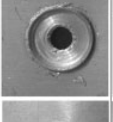
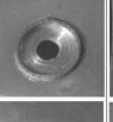
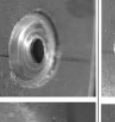

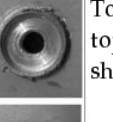
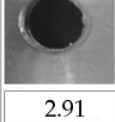
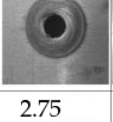
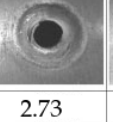
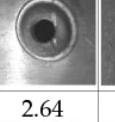
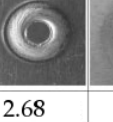
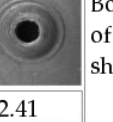
		Pin length (mm)							
		0	0.7	1	1.2	1.4	1.6		
Steel anvil								Bottom sheet	
								Top of top sheet	
								Bottom of top sheet	
Strength (kN)		2.94	3.05	3.15	3.02	2.92	2.73		
Energy (J)		3.9	2.95	4.9	3.95	2.33	2.15		
Ceramic anvil								Bottom sheet	
								Top of top sheet	
								Bottom of top sheet	
Strength (kN)		2.91	2.75	2.73	2.64	2.68	2.41		
Energy (J)		5.1	1.9	2.8	3.12	1.97	1.12		

Figure 2.8: Failure modes in thin sheet AA6111 joints (from Bakavos & Prangnell, 2009)

have their oxide layers removed and be joined in an oxygen-free atmosphere. FSSW relies on tool-induced deformation to break up the oxide layers.

2.2.3 Optimum conditions

There seems to be a requirement for deformation to reach the interface in order for a proper joint to form. However, once this point is reached there is then a balance between longer, hotter and deeper welds, which increase the surface area of the full bond and the joint strength (after Mitlin et al., 2006), and thinning of the workpiece caused by a deeper plunge (after Bakavos & Prangnell, 2009). In general, thinning of the workpiece dominates, so the optimum weld appears to be one where the deformation is just sufficient to reach the interface, but no more. Other considerations also tend to favour using the smallest plunge possible which will produce a weld: larger plunges lead to greater surface imperfections, larger forging forces and a weaker HAZ (Nishihara & Nagasaka, 2003, and Johnson et al., 2001).

2.3 Previous modelling approaches

2.3.1 Advantages of modelling

Empirical experimental investigations are the foundation of many areas of scientific endeavour, and welding research is no different. However, experiments in welding present a unique set of challenges, and modelling efforts are used extensively in all branches of welding research to investigate welds on scales and in ways that are impossible or impractical experimentally (Cerjak & Bhadeshia, 2002). In FSSW, many of these challenges are magnified:

- it is a short duration process: typically a weld takes of the order of 1 s
- it involves high forces, of the order of 10 kN
- the rotational speeds are high, of the order of 200 rad s⁻¹ (2000 rpm)
- complex flow patterns develop during the weld

- steep thermal gradients occur, both in time and space
- the volume of the total weld zone is small

Owing to these characteristics, developing a thorough understanding of the process through experiments alone is fraught with difficulty. For example, simply measuring temperatures accurately is itself an experimental challenge: the smallest thermocouples reasonably available are around 0.5 mm in width, while temperature gradients can be as much as 100 K mm⁻¹; thermocouples are destroyed if placed too close to the weld stir zone; and thermal cameras are somewhat unreliable and in any case can only measure temperatures on exposed surfaces. Flow visualisation is even more difficult, as flow patterns inside solid metal are very difficult to observe. Finally, the process outputs (in terms of temperatures and flow patterns) depend on a complex interplay of many different factors (such as tool downforce, tilt angle, rotation speed, clamping forces and material properties) such that it can be very difficult to produce exact repeat experiments.

For all these reasons, modelling FSSW is vital to develop a greater understanding of the process.

2.3.2 Introduction to modelling

Weld modelling may be divided into two categories: analytical models, involving continuous equations to describe the temperature field, power input and other parameters, and numerical solutions that work with a mesh or similar discrete representation of a weld and calculate a solution at finite time steps. Analytical models provide broad insight into the process, and in general the solution time is much shorter. However, analytical solutions struggle to represent many of the features in real welds, such as finite tool sizes, contact conditions and heat losses to a backing plate, and irregular geometries. By contrast, numerical models cope well with such finite effects. Numerical models, however, require much greater computing resources, and are less suitable for providing broad process windows of the kind that may be desired when introducing a new alloy, for example. Since numerical models

do not provide the same degree of insight into the process, it is often difficult to estimate the influence of any particular parameter on the final solution. This kind of work is particularly important for judging the sensitivity of a model to variations in input data. The time or computing resources required to carry out large numbers of similar calculations means that this important step is often not conducted, leading to less robust and less reliable predictions (Mishra & Mahoney, 2007, Colegrove & Shercliff, 2006).

As all types of FSW, but in particular FSSW, are comparatively new welding techniques most analytical approaches are based on a model of the thermal field alone, since these techniques were developed for analysing fusion welds where the flow pattern is not usually important. Consequently, many models only look at this side of the problem and do not attempt to include flow effects. This is not necessarily a big drawback, depending on the aims of the model: understanding the evolution of the temperature field is a very important outcome, as it strongly affects the behaviour and properties of the workpiece material.

2.3.3 Friction stir spot welding

The only detailed models of FSSW to date are based on numerical approaches; so far, no analytic models have been developed. It is worth noting that FSW and FSSW are both processes in which the flow is kinematically constrained rather heavily, making analytical models more promising. Fully-coupled thermomechanical models have been produced for FSSW, although a lot of the parameters are unknown. For example, Awang et al. (2005) developed a thermomechanical model using Abaqus Explicit. In this model, the heat input is assumed to be generated by Coulomb friction with a temperature-dependant coefficient of friction. A convection coefficient (of $30 \text{ W m}^{-2} \text{ K}^{-1}$) is used for heat losses from the workpiece-air interfaces, but there is little indication that this value is correct. Although this model gives believable results for the flow pattern (which are hard to verify experimentally), the temperatures calculated are far higher than generally accepted peak temperatures for FSSW. They calculate a peak temperature of 1200 K

for FSSW in AA6061, which is far above the melting point. Some experimental results have found structures consistent with local melting (Park et al. and Sato et al., 2002), but there is no possibility that temperatures so far in excess of the solidus can be reached during FSW or FSSW, so such studies must be dismissed.

Temperature regime in which FSSW operates

It is well-established that the peak temperature during FSW is limited at the solidus temperature (T_s), due to a great reduction in material flow stress at T_s . This also applies to FSSW. The majority of published literature supports this, with most authors finding a peak temperature close to the solidus. Gerlich et al. (December 2005) review a number of other authors' work in their paper, including Colegrove and Shercliff's work on AA7075 and Su et al.'s work (2006) on 6061, 7075 and 2024 alloys; these authors report peak temperatures around the solidus. Murr et al. (1998*a*) report a peak temperature of $0.7 T_s$ and Somasekharan & Murr (2004) report a peak temperature of $0.8 T_s$. Gerlich et al. measured peak temperatures during FSSW of 6111 and 2024 Al alloys and AZ91 Mg, and found temperatures within 6% of the solidus temperature ($0.94 T_s$ for Al alloys and $0.99 T_s$ for Mg). It is uncommon to find temperature measurements taken during dissimilar FSSW; Prangnell et al. measured the temperatures during dissimilar FSSW and found temperatures substantially below the solidus, though these measurements were taken away from the tool (so peak weld temperatures would be higher). Park et al. (2004) and Sato et al. (2004) observed microstructures in AA1050/AZ31 welds consistent with melting and mixing, implying higher temperatures were achieved in these welds than in welds of either material to itself. However, no direct temperature measurements were made during these welds.

2.3.4 Friction stir welding and related processes

There is relatively little literature devoted specifically to FSSW and much more to seam FSW. Given the similarities in the two processes, there is much

that can be learnt from a study of this larger body of work. Other modelling techniques may also be relevant, and likely processes can be selected by choosing those that operate in a similar parameter space. Peak temperatures reached in FSSW are generally of similar magnitudes to the solidus temperature of the alloy being welded, due to the negative feedback mechanisms discussed earlier. There is some discussion in the literature regarding the strain rates reached, with authors claiming strain rates for Al welding from 20 s^{-1} (Frigaard et al., 2001) up to 500 s^{-1} (Colegrove & Shercliff, 2006). Rotary friction welding (RFW) operates in similar regimes of temperature and strain rate (with strain rates of up to 1000 s^{-1} being found by Midling & Grong, 1994). Modelling of RFW tends to use similar approaches to those used for FSSW and FSW (with heat and flow models linked in some manner), and consequently has similar difficulties regarding temperature measurements for validation of models and selection of appropriate constitutive laws.

Analytical models

Heat flow during welding is governed by Fourier’s 2nd law (Equation 2.1). Analytical solutions to this problem are known for many different boundary conditions, including various scenarios representative of welding. The seminal work in this area is that by Rosenthal (1946), who presented an analytical model for heat flow through conducting plates from a moving heat source (see also Rosenthal (1941) and Rosenthal and Schmerber (1938); and see Grong (1997), for an extensive rework of Rosenthal’s solutions and broadening of their application). The motivation behind this work was the intention to develop a model for arc welding, however, the models developed by Rosenthal have since been applied to other welding situations, including seam FSW (Gould et al., 1996, Russell et al., 1997, Russell, 2000, and Shercliff & Colegrove, 2002).

$$\rho C \frac{\partial T}{\partial t} = \lambda \left(\frac{\partial^2 T}{\partial x^2} + \frac{\partial^2 T}{\partial y^2} + \frac{\partial^2 T}{\partial z^2} \right) + q \quad (2.1)$$

Rosenthal’s solutions are divided into 3 categories depending on the work-

piece thickness. These are:

- a thick plate solution, which assumes that the workpiece is a semi-infinite solid with a heat source on the surface;
- a thin plate solution, which assumes that all heat flow is within the plane of the plate (i.e. there is no through-thickness variation in temperature);
- a medium thickness solution.

The medium plate solution is the most general (and consequently the most complex). In the case of seam welding at sufficiently high welding speeds the heat source travel time is short compared to the heat diffusion time. In this case, the thick plate solution simplifies to a 2D calculation and the thin plate solution to a 1D case. Grong's process map was considered in relation to FSW by Russell (2000). This work provides a map of the conditions under which each model is accurate based on the dimensionless thickness, power and peak temperature (Figure 2.9).

Grong's work also provides useful insight into the timescales associated with various processes. While steady-state solutions are often considered for seam welding, these generally take 10 s or more to become established under typical conditions, indicating that a transient solution will be necessary for spot welding.

A complicating factor in applying Rosenthal's work to FSSW is that it assumes constant material properties, while the thermal properties of Al vary with temperature. This variation is commonly ignored to reduce the complexity of the calculation. Sometimes room-temperature properties are assumed for the whole calculation, and sometimes average values over the temperature range of interest are used. An additional reason for using room-temperature properties, is the difficulty of measuring the correct properties at elevated temperature: most measurements of properties take place after long hold times. This allows equilibrium microstructures to form, which may not happen during welding. Indeed, Colegrove & Shercliff (2006) found a better match to experimental data using room-temperature values, rather than

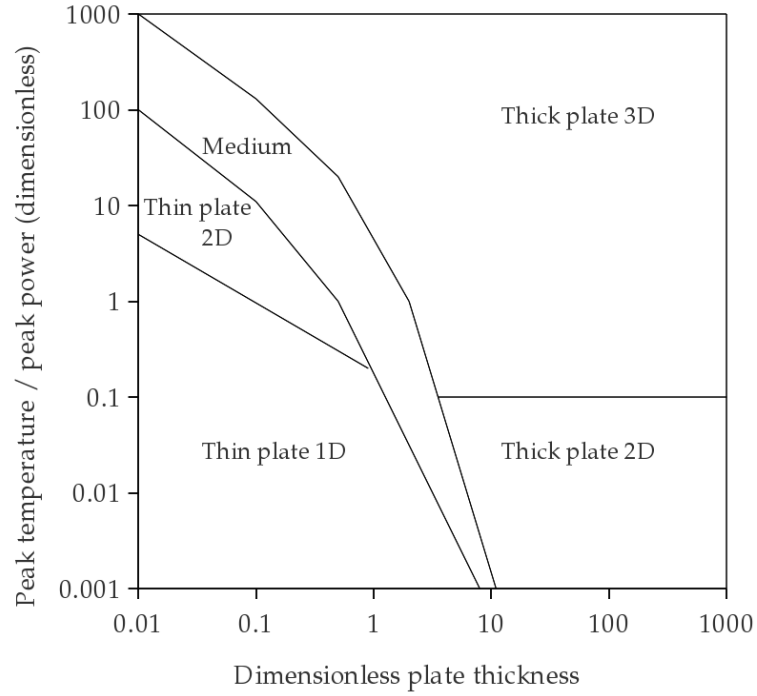


Figure 2.9: Rosenthal solution map (image after Grong, 1997)

values for equilibrium microstructures at the correct temperatures (though this was with a numerical, rather than analytical, model).

Numerical modelling

The most common class of numerical models, by far, consists of those based on a finite grid representation of the deforming material. Grid-based models use either an Eulerian mesh, where the grid is fixed and material flows through the grid (the typical approach for fluid dynamics), or a Lagrangian approach, where the grid deforms with the material (typically used for small-strain, quasi-static problems such as elastic structural analysis). These models can either calculate the coupled behaviour taking into account thermal properties and constitutive behaviour, or examine only one aspect of the problem — typically the thermal problem in isolation. In the latter case, it is common to neglect heat transfer by convection, and solve for a purely conductive problem represented by a fixed grid in a rigid solid, using the

FE method. Fully-coupled models need a representation of the material constitutive behaviour. This may either be derived empirically, or be derived by modelling the microstructural changes. One of the difficulties in modelling the microstructure during the process is that, owing to its transient nature, the material is often very far from equilibrium.

Although finite element models are the most common by a large margin, models based on the finite difference method are also in use (Frigaard et al., 2001).

Thermal modelling

All thermal modelling is, at its heart, an attempt to find solutions to Fourier's 2nd law (Equation 2.1), with appropriate boundary conditions.

Unlike many thermal processing problems (including most other welding processes — see Section 2.1), in FSSW the heat input is not an independent, adjustable parameter, but is intricately bound up with the flow pattern and deformation forces in the stir zone. Nevertheless, many approaches treat the thermal field as a separate problem, and develop a solution based around a volumetric or, more commonly, surface heat input, such as the models described by Colegrove & Shercliff, 2006, Colegrove et al., 2007, Khandkar et al., 2003, Russell & Shercliff, 1999, Lambrakos et al., 2003, Frigaard et al., 1999 and others. One major problem with this approach is the need to fix parameters for the heat input. For example, the common parameters used to control FSW are the downforce or plunge depth, traverse speed and rotation speed, with the latter usually kept constant throughout a weld. Torque or power are not normally measured, at least not unless the weld is being conducted under experimental conditions. This leaves the power, in a purely thermal model, to be fixed by reference to the temperatures that are the outputs of the model. Experimental welds with power measurement have been modelled, but there is still considerable freedom to fit other parameters, as seen for example in Khandkar et al.'s 2003 paper where the power input is fixed, but heat losses (modelled therein as convective backing plate losses) are freely adjustable.

A recent modification to the FSW process is the development of torque control (Longhurst et al., 2010). This is described in the literature as having promising applications for automation; additionally, it could make rapid modelling of welds in a commercial environment easier by depositing a constant, known, power into the weld, removing a free input variable from the model.

Heat losses

Heat loss to the backing plate or anvil is an important factor in FSSW and FSW, and it is vital to incorporate it into a model to make accurate predictions of heat flow. Many different ways of describing heat losses within models are described in the literature, and there is no consensus as to the best approach. These methods are summarised here.

Some models include the backing plate explicitly in the model domain; such models require a gap conductance for the contact between the workpiece and backing plate, and a boundary condition for heat loss from the backing plate to machine bed interface. Some models do not include the backing plate, but instead model heat loss to the backing plate as a boundary condition at the edge of the workpiece. The latter approach is more common in fully coupled models, as there is a greater computation penalty for including the backing plate in the meshed domain. Though it is possible (see, for example, Ulysse, 2002), models including the backing plate tend to be thermal-only models.

For models which include the anvil explicitly, the gap conductance between the workpiece and backing plate is an input parameter to the model. However, it is not usually possible to measure this directly. It can be estimated from the downforce and a knowledge of the contact mechanics at the interface, and interface pressure is widely recognised as a key parameter in the contact conductance between smooth surfaces. Cooper *et al.* (1969) and Mikic (1974) explore the pressure dependency of thermal contact conductance at length. However, this simply shifts the problem back a step, as the required pressure is also locally unknown and will vary strongly during the course of a weld. Owing to the elastic nature of forces in the vertical direction, it is

not possible to calculate such forces from a CFD calculation. An uncoupled elastic analysis is also probably unable to predict the contact forces with sufficient accuracy as plastic deformation is significant. Schmidt et al. (2004) developed an analytical model for the heat flow during a weld based on the contact forces, and the gap conductance typically increases during a weld as the hot weld metal conforms more closely to the backing plate.

Another approach is to estimate the heat flow to the backing plate using experimental measurements of the backing plate temperature. This can be achieved by placing thermocouples in the backing plate — this has been carried out at Cambridge (Dickerson, 2002) and Manchester (Prangnell & Bakavos, 2010, and Chen, 2010). Wang et al. (2013) extend this approach using an artificial neural network, described below.

Despite these difficulties, Soundararajan et al. (2005) used a constant gap conductance in a fully coupled model and report predictions of the thermal field that are within 10 % of measured values. Colegrove et al. (2007) state that better thermal contact is achieved between the backing plate and the workpiece after welding, due to flattening of surface asperities. They incorporate this into their model of seam welding by adjusting the contact conductance, setting it to be high under and behind the tool and low elsewhere. This model is used to predict temperatures at thermocouple points to within about 10 K. However, one effect that is not captured is the non-uniform temperature field (it is not symmetric about the weld line, with an 18 K difference between the advancing and retreating side). They suggest that this is due to deflection of the tool towards the retreating side (thereby making the retreating side thermocouple closer to the actual weld line than thought).

In the work by Wang et al. (2013), experimental temperature measurements were combined with results from numerical models as the inputs to an artificial neural network. Various features of the temperature curves (such as peak temperature, cooling rate, or total integral) were used to estimate contact conductance values in a more systematic way than by trial and error. The contact conductance model used in this work split the metal-to-metal contacts into two zones, a high-conductance and a low-conductance zone,

with temperature-dependent values.

Heat is lost to the surroundings through the backing plate, from the top surface to the surrounding air, to the tool and to the clamps. Heat loss from the model boundary is often modelled by a convective heat flow. Heat loss to the air is a convective solid-fluid heat transfer problem, but for solid-solid contacts this is not a physically realistic model; therefore, it is not possible to measure this parameter directly. The problems with including parameters such as unknown gap conductance and/or convective heat transfer are illustrated by Khandkar et al. (2003). In an attempt to improve confidence in FSW/FSSW models they measured the power input to the workpiece and used this to fix the power input to their model, rather than adjusting the power input based on the recorded temperatures. However, the convective heat loss from the backing plate was still unknown, and had to be adjusted to fit the calculated temperatures to the measured data. Although there may still be confidence in the heat flow profiles so produced, it is very difficult to generalise such a model to accurately predict weld temperatures under other welding conditions or geometries.

Models for contact conditions and heat generation

During FSSW, heat is generated through a combination of surface friction and bulk heating due to deformation. Many welding studies use simplified models where the heat is assumed to be supplied by a point heat source, and the exact details of how the heat is generated are ignored. This provides acceptable results for the temperature field at a large distance from the tool, but the accuracy decreases as the distance from the tool decreases. In FSSW it is often temperatures in the HAZ that are of interest (as this is the region of weakest material in the post-welded state — see e.g. Bakavos & Prangnell, 2009). Models of finite-sized contact patches were used by Colegrove, and other authors have used similar approaches for other types of welding: Ion et al. (1992) analyse a distributed source for modelling laser welding, and Midling & Grong (1994) use this approach with rotary friction welding of bars. This last is of particular relevance for the present work, as rotary

friction welding bears many similarities to FSSW: in both, frictional heating causes a loss of strength and possible asperity melting with bulk material remaining solid, and the dimensions, rotation speeds and forces involved are very similar. Midling & Grong (1994) examine friction welds in AA6082, updating Rykalin’s 1971 solution for an infinite rod to account for finite geometries, and they introduce a steady-state phase where the contact surface is held at a constant temperature. This latter approach accords better with the qualitative opinion of many authors that melting does not take place in FSSW due to a negative feedback loop as the solidus is approached, which occurs since loss of strength in the material leads to a lower heat input. (It should be noted that, in a later study, Midling & Grong (1994) did in fact find evidence of melting, but this was confined to very small regions around asperities.)

Russell & Shercliff (1999), Colegrove et al. (2000), and Upadhyay & Reynolds (2012) have all examined the contact condition at the interface between the tool and the workpiece, as this is critically important for understanding the mechanisms of heat generation. Schmidt et al., 2004 summarised many of the existing approaches. They define a dimensionless slip parameter as:

$$\delta = \frac{v_w}{v_t} \quad (2.2)$$

where v_t is simply the velocity of the tool at that point (i.e. $v_t = \omega \times r$) and v_w is the velocity of workpiece material directly under that point on the tool.

The possible states of the system and the corresponding values of this parameter are given in Table 2.3.

Condition	Matrix velocity	Shear stress	State variable
Sticking	$v_{workpiece} = v_{tool}$	$\tau_{friction} > \tau_{yield}$	$\delta = 1$
Sticking/sliding	$v_{workpiece} < v_{tool}$	$\tau_{friction} \geq \tau_{yield}$	$0 < \delta < 1$
Sliding	$v_{workpiece} = 0$	$\tau_{friction} < \tau_{yield}$	$\delta = 0$

Table 2.3: Definition of contact condition, velocity/shear relationship and state variable (dimensionless slip rate), after Schmidt et al., 2004

Which of these states applies in any particular case depends on the relative values of the contact friction and yield stresses; it seems probable that the tool interface may typically pass through all stages over the course of a single weld, with different parts of the tool interface in different states at any instant. For a thermal model, the heat input is often assumed to be a surface heat flux lying between the two extremes of a fully sticking contact and a fully sliding contact. A sticking contact model generally assumes a constant shear stress over the tool surface; such models are used by Song & Kovacevic (2003*a*), Zhu & Chao (2002), Khandkar et al. (2003) and Bastier et al. (2006):

$$Q = \frac{2\pi}{3}\tau\omega R_s^3 \quad (2.3)$$

where Q is the input power, R_s is the radius of the shoulder, τ is the shear stress and ω is the angular speed.

Though this can be used to predict the heat input from known material parameters under the conditions of temperature and strain rate commonly found in FSW, it requires an estimate of the shear stress. It has been suggested that the best experimental method to measure the desired material properties might be to use the FSW process itself (Schmidt & Hattel, 2005 and Schmidt & Hattel, 2008). The relationship in Equation 2.3 above may also be used to predict the shear stress from a known power input (the power is quite easily measured with a dynamometer). If one assumes yield takes place according to the Tresca criterion with uniform contact pressure and material state (temperature), Equation 2.3 becomes:

$$Q = \frac{\pi}{3}\sigma_y\omega R^3 \quad (2.4)$$

Russell, 2000 uses this approach to estimate the contribution to heating from 3 regions in conventional seam FSW: the pin, the shoulder, and bulk deforming of the workpiece. The contribution from the shoulder is as given in Equation 2.4, that from the pin and the workpiece is shown overleaf (the slip surface for the workpiece region is assumed to be a vertical surface, with radius R_3).

$$Q_P = \frac{\pi}{3} \sigma_y \omega R_P^2 L_P \quad (2.5)$$

$$Q_W = \frac{\pi}{3} \sigma_y \omega R_3^2 L_P \quad (2.6)$$

where Q_P and Q_W are the powers dissipated by slip lines along the pin and within the workpiece, respectively, R_P and L_P are the pin radius and length, and R_3 is the radius of the deforming region of the workpiece.

Using typical values for 2000 series alloy, Russell finds that the contribution from the shoulder is around 90 % in 2 mm plate, 75 % in 4 mm plate and 65 % in 6 mm plate. However, it should be noted that this analysis provides an overestimate of the power required since the proposed mechanism activates redundant slip surfaces — if the shoulder and pin are sliding with $\delta = 0$ there will be no workpiece deformation. In such a case $Q_W = 0$. With partial slip, all the mechanisms will be active to some extent, but the applicable value of ω will be different in each term (and unknown, if the degree of slip is unknown).

Despite the assumptions in previous analyses, the power input will not be evenly spread over the entire tool area; one approach is to model the power input as a linear function of power density with radius, from a known total power (Schmidt & Hattel, 2005 and Schmidt & Hattel, 2008):

$$q(r) = \frac{3Qr}{2\pi R_s^3} \quad (2.7)$$

where q is the power input per unit area as a function of radius and Q is the total power; other variables are as defined previously.

Colegrove & Shercliff (2005 and 2007) used the above relationship, but truncated the power input function at a smaller radius than that of the shoulder. This was justified by them by reference to experimental temperature measurements; based on the accuracy of their predictions, it seems likely that this is a good match for the power input function. This could indicate a boundary between different power dissipation mechanisms — i.e. between stick and slip — occurs at this point. The issue of stick vs. slip, and its impact on heat generation, are therefore central to modelling processes such as FSSW.

Flow modelling

Models have been developed to investigate the flow pattern during FSW. Accurate numerical models that incorporate fully-coupled interactions between temperature and strain must take account of elastic and plastic strains, heat losses, and the response of the material as a function of strain rate and temperature. There are two major issues with running fully-coupled models: firstly, it is rare that the boundary conditions and material constitutive model are known with sufficient accuracy to produce a generally applicable integrated model; and secondly, such a model is very labour-intensive to create and computationally expensive to run. A simplified approach to modelling the flow pattern is to neglect elastic strains and to import a prior calculation of the thermal field into a flow model (e.g. using CFD) to determine the material deformation at each point. This method is demonstrated by Colegrove and Shercliff (2007).

Examples of fully-coupled calculations applied to seam FSW are the arbitrary Lagrangian-Eulerian (ALE) finite element models developed by Schmidt and Hattel (2005). This work looked at the conditions under which a void will form during FSW, modelling in detail the welding of a sample of AA2024 using Abaqus Explicit. By comparison with their earlier, purely Eulerian CFD models, and experimental results, they find that the ALE approach makes more accurate predictions but at a heavy computational price. The greatest error with the CFD models was due to the assumption of incompressibility, which leads to unrealistically low predicted pressures behind the pin. (The assumption of incompressible flow is reasonable for metals in the plastic regime, but it is a poor model for elastic regions, given that Poisson's ratio is around 0.33 for most metals.)

The plunge stage of FSW is essentially identical to the FSSW process, although the goals of modelling each are different. Modelling of the plunge stage of FSW is usually approached with a view to understanding tool wear (because most tool wear occurs during the plunge), with its effect on the workpiece of somewhat secondary importance. Tool wear is fastest during the early part of the weld as the workpiece is strongest when cold. Both

solid mechanics and fluid mechanics approaches have been attempted as methods of modelling the plunge, and each approach has its advantages and disadvantages. One of the main problems with simulating the plunge using solid mechanics approaches is the large deformation during this stage of the process, which causes excessive mesh distortion when attempting traditional FE analysis. However, as the elastic forces are important, computational fluid dynamics (CFD) is also somewhat limited. Nevertheless, Gerlich et al. (2005) presented a CFD approach to the problem. Kakarla et al. (2005) investigated the behaviour during the plunge using an isothermal FE solid mechanics model, in Abaqus Explicit. The behaviour during the plunge is very poorly characterised and this work adds to the available knowledge; however, it is unlikely that an isothermal model can give accurate quantitative predictions of the wear rate as attempted in their paper. As temperature rises from room strength to the solidus, the workpiece yield stress can fall by a factor of 20 or more (Colegrove et al., 2007), and this will strongly influence the wear rate. Attempts have also been made to model the plunge stage of seam FSW using fully-coupled models, such as that by Mandal et al. (2008). This work is applicable to FSSW also, since the tool does not translate during the plunge.

Schmidt et al. (2005) modelled the plunge using an arbitrary Lagrangian-Eulerian mesh to cope with the large strains. The constitutive behaviour assumed for this work includes the Norton-Hoff model for viscoplastic flow at high temperatures, whereas most other models assume Johnson-Cook behaviour; these laws both relate flow stress to temperature and strain rate, however the latter is a poor representation of the measured response for Al alloys. The divergence of the Johnson-Cook model from measured behaviour is greatest near the solidus — precisely the region of interest for FSSW. This is explored further in Section 2.4. The work by Mandal et al. is of particular note as it compares calculated results to experimental measurements (both their own, and previously published work by Feng et al., 2005).

Arbitrary Lagrangian-Eulerian (ALE) models are, as the name suggests, a hybrid between those two methods (i.e., between Lagrangian (‘solid’) meshes and Eulerian (‘fluid’) ones — explained in more depth in Section 2.3.4).

Developed for solving multiphysics problems that could not be reasonably solved using either discretisation technique on its own, they are commonly used for situations with a free surface, or with a moving interface between a solid and a fluid. Guerdoux et al. (2004*a*) have compared similar models using both Lagrangian and ALE methods; in their later work (Guerdoux & Fourment, 2007) they apply this to a full seam weld using the Forge3 code. A Lagrangian mesh is used to model the plunge and a fixed mesh is used to model the steady-state phase. However, the model shows extreme void formation and flash extrusion during the plunge to a degree that is not observed during real welding.

Another class of modelling approach is smoothed particle hydrodynamics. This is a mesh-free numerical method that has seen use in time-dependent fluid mechanics problems, and to a more limited extent in solid mechanics work. Recently, some authors have taken this method and applied it to FSW. Bhojwani (2007) developed a 2D smoothed particle hydrodynamics (SPH) model of the flow problem during FSW and attempted quantitative analyses, but this work is still at a very early stage.

Tartakovsky et al. (2006) published one of the earliest reports of SPH applied to FSW, developing 2D and 3D models of various tool shapes, though in their paper they only report qualitative comparisons with experiment. Das & Cleary (2007) developed a single-phase SPH model of fusion welding, which captures both elastic and plastic behaviour and predicts temperatures and deformation.

The SPH approach holds considerable promise for future modelling, as it has no problems associated with large deformations, but the mathematical underpinnings are not yet as robust as for FE and CFD codes. In other fields where it is used (primarily those dealing with hypersonic flow problems) it is generally considered to be a much faster modelling approach than grid-based solvers, though less accurate.

2.3.5 Empirical testing and validation

The power input is an important parameter for all modelling. With some experimental welds, the power is known, being measured by a dynamometer or other means. For other cases it must be estimated somehow, either from the weld parameters or from measured temperatures. A flow model may be able to predict the heat generation, as shown by Colegrove and Shercliff (2003 & 2006), and Colegrove et al. (2007), whereas for a purely thermal model it is an imposed boundary condition as discussed earlier.

Colegrove et al. (2007) modelled the heat input by assuming contact between the tool and workpiece only up to a certain fraction of the shoulder radius, and found that this improved agreement with experimental results. However, there are no direct measurements of the spatial power distribution available in the literature; most of these assumed profiles come from theoretical considerations, and their validity derives from the ability of the models to predict the final temperatures. A knowledge of how the profile influences the final weld will be useful for designing new tools both to improve the weld properties and to reduce tool wear.

On the other hand, the temporal variation in power input is much more easily measured. A good example of such work is that by Gerlich et al. (2005), who measured the downforce and torque during FSSW, as shown in Figure 2.10. This clearly illustrates the softening of the workpiece as the temperature rises (the drop in axial force and torque from about 3 s onwards, at constant displacement). The two peaks in force are due to the pin and shoulder respectively.

There is a strong tendency within the existing literature to use numerical approaches, particularly thermal FE and fully-coupled FE models, to produce models of particular welding cases without much regard to their experimental accuracy. Substantial numbers of papers can be easily found that present the results of a finite element model without any experimental results for comparison, or by comparing predicted temperature outputs at a point with a single thermocouple measurement, often for one single weld.

The author does not consider single output thermocouple locations, nor

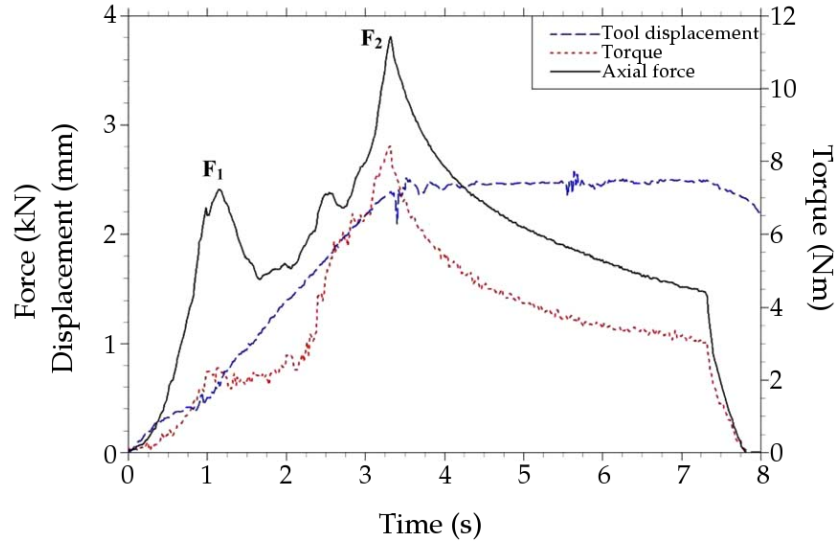


Figure 2.10: Sample downforce and torque measurements from FSSW
(figure from Gerlich et al., 2005)

unvalidated FE calculations, to be sufficiently reliable as to form the basis of further work without much more extensive experimental comparisons. One of the few papers with a more through investigation into the accuracy of modelling approaches is by Su et al. (2006a), wherein an attempt is made to verify model approaches by measuring the total heat input into the workpiece by calorimetry. This is done by using an oil bath to measure the heat content of the workpiece at the end of welding. These calorimetry results are of particular interest, as they found that a low fraction of the input energy is deposited in the workpiece, with the rest of the energy being lost to the tool, backing plate, anvil and other surroundings. 12.6 % of the energy was deposited in the tool with a steel backing plate, and 50 % with a mica backing plate (for AA6111 welds). During plunge testing, around 4 % of the total input energy was used in stir zone formation. Although FSSW is already a low-power and efficient process by comparison with its main competitor RSW, these results raise the possibility that further reductions in energy input may be possible.

In a separate paper (Su et al., 2006b), the same authors report on experimental visualisation of the flow pattern during FSSW using two techniques:

firstly, etching of dissimilar welds between AA5754 and AA6111 (where the different etching characteristics show the final pattern), and secondly by using finely-dispersed particles of alumina in an AA6111 weld.

Given the lack of existing validated approaches within the literature, an important component of this present work will be to examine the robustness of FE models and estimate their reliability.

2.3.6 Microstructural modelling

In practice, it is rarely worth the complexity of using a dynamic microstructural model to determine the constitutive behaviour, and this is measured experimentally and fed into the deformation analysis. Microstructural models are then incorporated as a post-processing step, using the calculated thermal history.

Kamp et al. (2006*a,b*) demonstrated the application of a kinetic reaction model to a FSW thermal cycle by using the Kampmann and Wagner method to model the response of AA7449 to FSW. This method is based on classical nucleation and phase transformation theory, is capable of tracking the precipitate size distribution over the course of a non-isothermal heat treatment. They used both isothermal holds and Jominy end quench tests for calibration. This model has been used extensively to model thermal cycles due to other welding processes (see e.g. Myhr et al. (1997, 1998), who applied it to AA6082).

A simpler model has been developed by Hyoe et al. (2003) that only takes account of the thermal effects, and does not account for the effect of deformation on the reaction kinetics. This model assumes that the precipitate content is at a maximum prior to welding (and is therefore only applicable to certain tempers). Nevertheless, this model predicts hardnesses that are in good agreement with experimental results.

Robson et al. (2007) used a semi-empirical properties model linked to a thermal model developed by Mackwood (2001) to predict hardness profiles in 7449 and 6013 Al alloys, and found agreement with experimental results. Their model can predict the microstructure and properties of age-hardenable

alloys after non-isothermal heat-treatment, based on work by Kampmann & Wagner (1991) who developed a microstructural model to predict the evolution of precipitates in the HAZ. It relies on calibration data derived from isothermal experiments on the same alloys, and can predict the form of hardness profiles with some degree of success. As expected from the general consensus in the literature, hardness in the HAZ is found to depend strongly on the peak temperature, with hold times at lower temperatures having a much smaller effect, due to the reaction rate terms containing a 4th order dependence on temperature.

Deschamps et al. (2005) studied the problem of independently measuring the parameters applicable to non-isothermal kinetic models in substantial depth, using less complex thermal histories than those imposed by FSW to study precipitation. Other models of microstructure evolution in Al welding have been developed by Grong (1997), Bjorneklett et al. (1999), and more recently Babu (2009) and Mathon et al. (2009), but substantial research remains to be done in this area.

2.3.7 Modelling of related non-welding processes

Non-welding processes that involve deformation, heating, and deformation-induced heating of Al include extrusion and forging. Section 2.3.3 discussed the temperature and strain rate regime in which FSSW operates; both extrusion and forging tend to operate at much lower levels — strain rates of 1 s^{-1} are generally considered high for both processes (Ferrasse et al., 1997, Prasad et al., 1984), so models for these processes will have only limited applicability to FSSW.

2.4 Constitutive data

All the modelling approaches described here share one thing in common: they require accurate material models to produce useful, realistic results. For the conditions that prevail during FSSW, it is difficult to obtain accurate material data, and data for many materials is lacking. The range of temperature

(up to the solidus, for Al, around 800 K), strain-rate (from quasi-static up to around 1000 s^{-1}) and strains (many times the strain to first yield) are difficult to reproduce in any environment apart from that of friction welding processes, although hot-working deformation testing machines such as the GleebleTM system may be able to with careful setup, at least for Al. However, even when the desired test conditions are obtained, there are problems with knowing what the correct outcome measures are. Material models used in these ranges include, amongst others, the Zener-Hollomon model and the Johnson-Cook model. Each of these was originally derived for specific metals under specific conditions, and the extrapolation of any of them outside these conditions is problematic. Voce's equation (given in Equation 2.8 from Voce, 1955) incorporates a strain dependent term and has been cited in later work, but is clearly not suitable for present purposes as it does not include a strain-rate dependent term.

$$\sigma = \sigma_{\infty} - (\sigma_{\infty} - \sigma_0)e^{-(\varepsilon/\varepsilon_c)} \quad (2.8)$$

Ludwik's equation is widely used in the literature on casting and forging in an effort to include the effects of creep and strain hardening, which are applicable in different but overlapping temperature regimes. (See, for example, measurements of the Ludwik parameters for 3000, 5000 and 6000 series Al alloys, including AA6111 in Alankar & Wells, 2010). Work hardening is strongest at low temperatures, creep at high temperatures. However, Ramaekers and Veenstra (1970) find that, using reasonable experimental data for steel, Ludwik's original equation (Equation 2.9) leads to a prediction of negative yield stress when large deformation data is included in the dataset. This has led to the adoption of a modified Ludwik equation (Equation 2.10) which is extensively used in casting and forging.

$$\sigma = \sigma_0 + K_1[\bar{\varepsilon}]^l \quad (2.9)$$

$$\sigma = K_2(\varepsilon_p + \varepsilon_{p0})^n(\dot{\varepsilon}_p + \dot{\varepsilon}_{p0})^m \quad (2.10)$$

where K_1 , K_2 , l , m and n are empirically measured material parameters.

The Johnson-Cook model (Equation 2.11, below) is one of the most commonly-used material models in the literature on FSSW and FSW. It is widely used in the ballistic and impact testing community, and because of this, it is also used extensively in FE simulations of slower processes — such as FSW — but its use at lower strain-rates is questionable. Furthermore, the Johnson-Cook model was initially developed for austenitic steel, and this is the only material for which extensive tests of the model exist in the literature. However, it is important to document it here since many authors use it in FSSW modelling (e.g. Schmidt & Hattel, 2005 and Awang & Mucino, 2010, both of which are regarded as key papers in the field).

$$\sigma = (A + B\varepsilon_p^n)(1 + C \ln \frac{\dot{\varepsilon}}{\dot{\varepsilon}_0}) \left(1 - \left[\frac{T - T_0}{T_{melt} - T_0}\right]^m\right) \quad (2.11)$$

where A , B , C , m and n are material parameters and other symbols have their usual meanings.

Like Johnson and Cook's work, the Zener-Hollomon law was also originally developed for steel (Zener & Hollomon, 1944). Many constitutive laws are derived purely from experimental correlations; unlike these, the Zener-Hollomon law is based on an assumption that mechanical flow properties have associated activation energies, and depend on a dimensionless group such that the temperature and strain rates are linked to the flow stress through a single parameter as seen in Equation 2.12. Sellars & Tegart (1972), proposed a relationship between this parameter and the strength of Al which has the form given in Equation 2.13 (as modified by Sheppard & Wright, 1979). This relationship has been successfully used in previous studies of seam FSW (e.g. Colegrove et al., 2007 and Frigaard et al., 2001) and is widely accepted in the literature as a suitable material model for Al under the conditions that prevail during FSSW.

$$Z = \dot{\varepsilon} e^{\frac{Q}{RT}} \quad (2.12)$$

$$Z = A \sinh(\alpha \sigma)^n \quad (2.13)$$

where A , n and α are material constants.

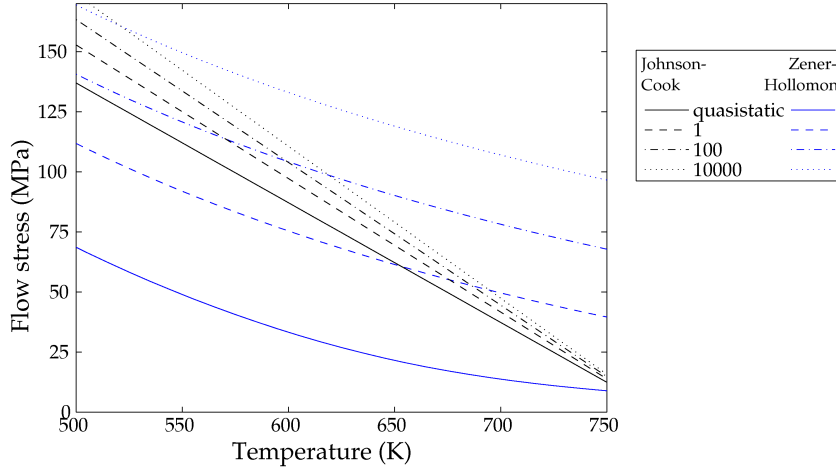


Figure 2.11: Zener-Hollomon and Johnson-Cook models for AA2024

The Zener-Hollomon and Johnson-Cook laws give very different results in the temperature region of interest for FSSW. See Figure 2.11 for a comparison of these two models for AA2024: as temperatures approach the solidus, the models diverge even further. An advantage of the Johnson-Cook model is that it includes strain-dependent behaviour, which the Zener-Hollomon model neglects, though this is not an issue for Al alloys during FSSW.

2.5 Issues for further study

Initial studies, such as those by Bakavos & Prangnell (2009) and Bakavos et al. (2011) described earlier, have investigated the variation of weld strengths and failure energies with sets of welding parameters, and also looked at the flow patterns and microstructures produced. However, there remains a lack of understanding regarding exactly how changes in process variables affect welds, and also regarding the mechanisms by which FSSW forms successful joints. A systematic and structured experimental programme can address these issues to some extent, however, there remain three main areas of study which cannot be understood exclusively by reference to experiments

at present.

The first of these is to develop a detailed understanding of heat flow within the workpiece (and the tool, to a lesser extent). While thermocouple measurements are reliable, practical limitations mean that the details of heat flow in weld nuggets cannot be resolved at present. It is precisely this region under the tool where the temperatures are of most interest, but the spatial resolution of the thermocouples available (0.5 mm at best) and their fragility makes them unsuitable for this purpose. Other measurement techniques are available, notably thermal cameras, but these all have their own particular limitations. Thermal cameras can only measure surface temperatures, and for this purpose they are not as precise as thermocouples, nor as reliable with aluminium. An accurate thermal model can be used in models of microstructure evolution to understand the processes taking place at a microscopic level.

The second aim of modelling efforts must be to understand the flow pattern. Etched images of interrupted welds between AA6111 and 6082 are innovative and very useful in this regard, but again the experiments alone are insufficient to establish an understanding of the flow. In this case, practical limitations on the number of experiments and the difficulty inherent in interrupting a weld at a specific point are the limiting factors. The experiments conducted so far have provided evidence for what structures form, but there is a gap of knowledge regarding how they form and what behaviour gives rise to what weld features.

The final modelling goal is to link the flow behaviour to heat generation, torque and power via the constitutive law of the material (or materials) being welded. This will ‘close the loop’ between models, experiments and production welding, and lay the foundation for both an enhanced understanding of the process at a fundamental level.

2.5.1 Need for new techniques

As described, many different modelling techniques already exist, including those developed specifically for welding (such as Rosenthal and Grong’s work), and those of more general application such as FE and CFD codes.

Unfortunately, none of these are entirely suitable for modelling FSSW, for the reasons discussed above.

Analytical models of heat flow, for example, do not capture sufficient detail to be used for accurate predictions of specific welds, such as are required for microstructural models; analytical flow models are not available. (This is not entirely true, as it could be argued that applying the Navier-Stokes equations with correct boundary conditions would solve the flow problem. While this view is possibly correct, a general solution to the Navier-Stokes equations is not known, and in any case there would remain the problem of finding the correct boundary conditions.)

Numerical models have already been used extensively to model FSW, and these techniques can be applied to FSSW. However, they do not provide a physical understanding of the problem, and are in general very sensitive to the constitutive law chosen for the model. Furthermore, the run times for these modelling techniques, particularly for fully-coupled 3D welding simulations, are very large. While quoted values for runtimes are of only limited utility (since hardware differences, reductions in model complexity due to symmetry, and changes in mesh parameters have enormous influence over the time taken), simulation times of over a month are seen in the literature, and anything less than a week is generally considered reasonably quick. A large parametric study might involve four or five variables, each taking three or four values, which would be impractically long — especially when an experimental program could run as many experiments in a few hours or less.

Consequently, there is a need for two types of model, which do not yet exist so far as can be reasonably ascertained. Firstly, an analytical model of the flow behaviour that can give insights into the trends and patterns associated with the kind of flow that occurs in FSSW. It would be useful if this could include thermal effects, but the primary requirement of this model would be to accurately represent flow features. Secondly, a comparatively fast model, which can be used to examine the trends that occur with changes in welding conditions. This latter model should include as much of the real behaviour as is necessary to produce an accurate model, but no more. Simplified numerical methods, e.g. taking account of the symmetry in the

problem or intelligently handling the kinematic constraints show the most promise in this regard.

Such models may turn out to have wider applicability, since there are a number of other processes, friction and ultrasonic welding foremost amongst them, which exhibit similar combinations of strong kinematic constraints, friction and deformation processes, and intense thermal transients.

Chapter 3

Experimental work

3.1 Introduction

This thesis is part of a joint EPSRC-funded project with Manchester Materials Science Centre. Experimental work was predominantly conducted at Manchester, with additional joint experiments conducted at TWI with the author. While the author carried out some experiments at Manchester, the modelling work drew heavily on experiments conducted by other members of the group, and it is most convenient to summarise all of the experimental work together. The primary collaborators were Yingchun Chen and Dimitrios Bakavos (University of Manchester) and Nathan Horrex (TWI Ltd.) for the instrumented weld experiments, and Bethany Parker (University of Cambridge) for the hardness tests and weld profile measurements. For the welding experiments, the author was involved in all of the experiments that took place at TWI (see Table 3.3), and the experiments at Manchester using the flat tool. The remainder were carried out by the collaborators named above. The author set up the Talysurf machine for the weld profile tests and performed the first two experiments, the rest of the profiles were measured by Parker. Except as noted in relevant figure captions, data extraction and plotting was carried out by the author, and the interpretation of the work is the author's own.

This chapter draws together a range of experiments with different goals: some of the experiments presented here were conducted with the express goal of understanding the behaviour of aluminium and steel when subjected to the

FSSW process, and with a view to supporting the modelling work presented in later chapters. Some of the experiments were conducted for related but different purposes, such as optimising tool settings, producing high-quality welds in different materials or finding a viable parameter space for alternative tool types, but are nevertheless useful from a modelling perspective and so are presented here alongside the other work. The primary aim of this chapter is to collate these experiments and organise them to develop a coherent picture of FSSW at a fundamental level.

3.2 Methodology

Friction stir spot welds were performed on two machines for this series of experiments; the machines in question were a CS Powerstir machine at Manchester, and a custom-built machine at TWI. The CS Powerstir machine is shown in Figure 3.1, and it is capable of producing a maximum power output of 25 kW and a maximum downforce of 100 kN, with tool speeds ranging from 0 to 2000 rev/min. The experiments at TWI used the Artemis instrumented tool connector between the tool and the machine; identical tools were used on both machines.

The workpieces were machined into 100 mm x 25 mm coupons for lap welding. For the double lap/butt flow visualisation experiments (described later), 25 mm x 30 mm Al coupons were used. The sheets were all nominally 0.91 mm thick; a sample of sheets were measured to 0.01 mm precision and found to be accurate to their nominal dimension. The arrangement of the tool, workpieces and clamps for a lap weld is shown in Figure 3.2; that for a butt weld was identical except for the horizontal position of the workpieces.

Thermocouples were used to measure temperatures in the welds; these were K-type (NiCr–NiAl bimetallic) thermocouples of 0.5 mm diameter. Grooves were cut into the backing plate and holes were drilled into the workpieces to allow the thermocouples to be located at the appropriate positions, shown schematically in Figure 3.3.

The materials used were AA6111-T4 and AA6082 Al alloys, and DC04 mild steel. The nominal compositions of these materials are given in Table



Figure 3.1: CS Powerstir machine

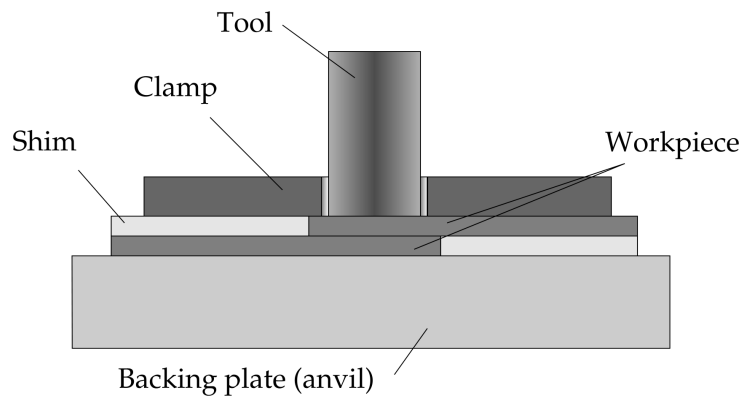


Figure 3.2: Welding setup

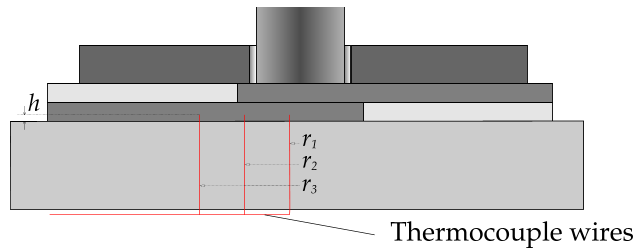


Figure 3.3: Thermocouple locations; typical parameters were $r_1 = 0$, $r_2 = 4$, $r_3 = 8$ and $h = 0.1$ (dimensions in mm), with specific values for each weld given in Table 3.3.

3.1, and their standard properties are given in Table 3.2. All coupons were machined from the same batch to minimise variation between samples. Experimental welds covered a range of rotation speeds, material combinations, plunge depths, dwell times and tool types. A summary of the welds made at Manchester and TWI is given in Table 3.3.

Various tool types were used for welding. The most extensive series of experiments were conducted with a flat tool; a tool with wide grooves ('flutes') extending over approximately 80 % of the tool radius was also used for a large number of welds. This tool was termed the 'wiper' tool and was found to produce stronger joints in Al to Fe welds than the flat tool. A number of other shoulder surface profiles were tested, and these are shown in Figure 3.4; a fuller discussion of their characteristics is given in Section 3.4.

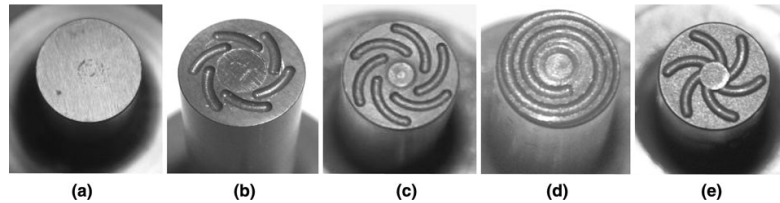


Figure 3.4: The different pinless tool designs compared in this work, from Bakavos & Prangnell (2009): (a) the featureless flat tool, (b) the short flute wiper tool, (c) the long flute wiper tool, (d) the fluted scroll tool, and (e) the proud wiper tool

Alloy	Cu	Si	Zn	Fe	Mg	Mn	Cr	Ti	Al
6082	<1	7–13	<2	<5	6–12	4–10	<2.5	<1	balance
6111	5–9	6–11	<1.5	<4	5–10	1–4.5	<1	<1	balance
	C	Mn	P	S	Fe				
DC04	<0.8	<4	<0.3	<0.3	balance				

Table 3.1: Nominal material composition of the alloys used in this study, in % by weight; composition data from the Aluminium Association and SSAB Tunnplat.

Alloy	Density kg m ⁻³	Thermal conductivity W m ⁻¹ K ⁻¹	Specific heat capacity J kg ⁻³ K ⁻¹	0.2 % proof stress* MPa
6111	2700	143	800	149
6082	2690	172	870	149
DC04	7850	47	419	310

Table 3.2: Material properties of the materials used in this study, at room temperature. High-temperature properties were used in some models, and are given in the relevant chapters. Data from Mills (2001), the Aluminium Association and SSAB Tunnplat.

*The AA6082 used for these experiments was artificially aged to give the same room-temperature hardness as AA6111-T4.

Top sheet material	Bottom sheet material	Tool type	Tool speed rev min ⁻¹	Dwell time s	Plunge depth mm	Backing plate material mm	Thermocouple distances from centreline mm	Thermocouple depths from top surface mm	Institution
AA6111	AA6111	Flat	2000	2.5, 5, 30	0.2	steel	0	1.8	Manchester
6111	6111	Flat	2000	2.5, 5, 30	0.2	Macor	0	1.8	Manchester
6111/6082	6111	Flat	2000	2.5	0.2	steel	2.5, 5, 10	1.7	Manchester
6111/6082	6111	Short flute wiper (CW & ACW)*	2000	2.5	0.2	steel	2.5, 5, 10	1.7	Manchester
6111/6082	6111	Scroll	2000	2.5	0.2	steel	2.5, 5, 10	1.7	Manchester
6111/6082	6111	Proud wiper	2000	2.5	0.2	steel	2.5, 5, 10	1.7	Manchester
6111/6082	6111	Long flute wiper	2000	0.5, 1, 2.5	0.2	steel	2.5, 5, 10	1.7	Manchester
6111	DC04	Flat	1600	1	0.1, 0.3, 0.5, 0.7	steel	-	-	Manchester
6111	DC04	Flat & wiper	2000	1	0.5	steel	0, 2.5	1	Manchester
6111	DX54Z	Flat & wiper	2000	1	0.5	steel	0, 2.5	1	Manchester
6111	DC04	Flat	800, 1200, 1600, 2000 400, 800,	1	0.5	steel	in tool	in tool	Manchester
6111	6111	Flat	1200, 1600, 2000, 3000	1	0.2	steel	2, 6, 10	1.8	TWI
6111	6111	Flat	800	2	0.2	steel	2, 6, 10	1.8	TWI
6111	6111	Flat	2000	1, 2, 4, 6	0.2	steel	2, 6, 10	1.8	TWI
6111	6111	Wiper	800, 2000	2	0.2	steel	2, 6, 10	1.8	TWI
6111	6082	Flat	800	2	0.2	steel	2, 6, 10	1.8	TWI
6111	6082	Wiper	800	2	0.2	steel	2, 6, 10	1.8	TWI
6111	DC04	Flat	800	2	0.2	steel	2, 6, 10	1.8	TWI
6111	DC04	Wiper	800, 2000	2	0.2	steel	2, 6, 10	1.8	TWI
6111/6082	DC04	Flat	800, 1600	0.5, 1, 2, 4	0.2	steel	2, 6, 10	1.8	TWI
6111/6082	DC04	Wiper	800	2	0.2	steel	2, 6, 10	1.8	TWI

Table 3.3: Summary of experimental welds

*Clockwise and anti-clockwise

3.3 Welding parameters

A parametric investigation was undertaken to examine the influence of selected independent welding variables. These experiments were all conducted with the same geometry as specified in Section 3.2, with 2 sheets of AA6111 in a lap configuration as the default case. The standard weld was a 1 s weld at a rotation speed¹ of 2000 rev/min, with a 0.2 mm nominal plunge depth using a flat H13 steel tool. The welding parameters were all kept constant except for the one variable at a time being tested. The variables studied were workpiece material, dwell time and rotation speed.

3.3.1 Welding time

The effect of dwell time on peak temperature, and on the form of the temperature rise, was examined. The variation of temperature with dwell time was examined for the standard case, with dwell times of 1, 2, 4 and 6 s; these results are shown in Figure 3.5. Temperatures at the 2 mm thermocouple (the hottest out of the locations measured) increased slightly between 1 s and 2 s, but then remained constant within the bounds of experimental error.

The conclusions that can be drawn from Figure 3.5 are that the solidus is reached at the interface within a short time (probably less than 1 s), and that the temperature field remains fairly static after about 2 s. This indicates that steady-state conditions are reached by this time. This ties in well with post-weld strength tests conducted by Bakavos and Chen, where optimum strengths were found at 1 s. It appears likely that the joint is entirely formed by this time, with longer dwells simply causing a loss of strength in surrounding HAZ material via processes such as coarsening of precipitates.

Full thermocouple histories for these welds are shown in Figure 3.6. These

¹Although the SI unit is radians per second, many experimental papers still use revolutions per minute, therefore the older unit is used here where appropriate to conform to stylistic conventions in the field. (The conversion factor is $1 \text{ rev/min} \simeq 0.10472 \text{ s}^{-1}$, $\therefore (800 \text{ to } 2000) \text{ rev/min} \simeq (84 \text{ to } 210) \text{ s}^{-1}$.)

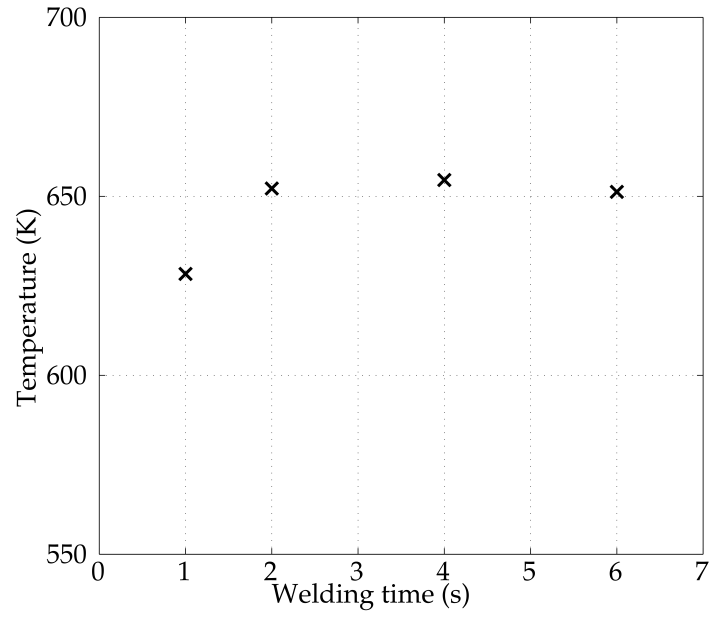


Figure 3.5: Variation in peak temperature with dwell time for the standard welding case

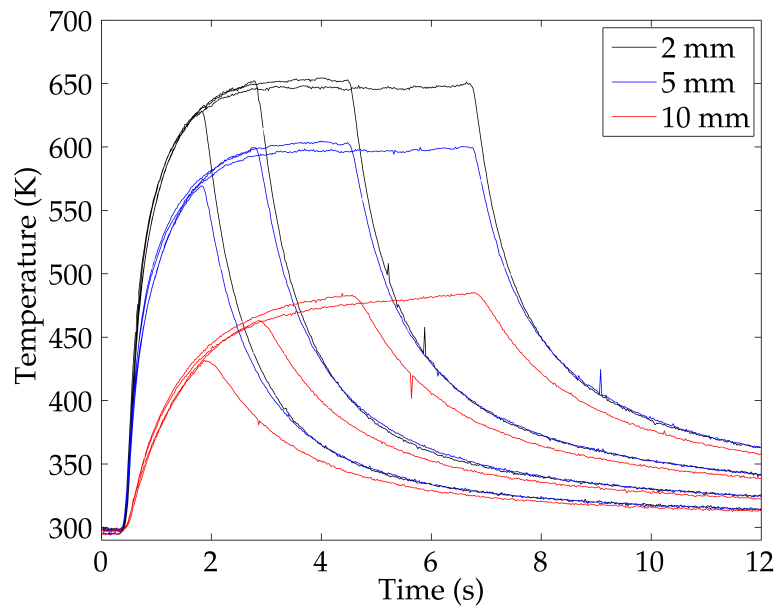


Figure 3.6: Thermocouple histories at 3 thermocouple locations for dwell times of 1, 2, 4 and 6 s

results confirm the previous conclusions — at least in terms of the temperature field, it is apparent that steady-state conditions have been established certainly by the 4 s point for the thermocouples nearest the weld. The 10 mm thermocouple continues to experience a slight temperature rise even at 6 s; as discussed, at this distance the characteristic heat flow time is more similar to the welding time, so it is expected that steady-state conditions will take longer to become established at this distance. This thermocouple is also closer to the edge of the workpiece, and it is possible that edge effects are becoming significant.

Bakavos and Chen have extended this series of welds up to 30 s; steady-state temperatures are definitely reached after 10 s, and the temperature after 1 s is within 5 % of this value.

3.3.2 Rotation speed

The next parameter to be varied was the angular speed of the tool. Speeds tested covered the range from 400 to 3000 rev/min (42 to 315 s⁻¹). All these tool speeds produced a weld, although of varying quality, with the exception of the 400 rev/min (42 rad/s) case. This failed to produce a weld at all, and the two workpieces fell apart post-weld. On inspection of the surface, it appeared that the tool had achieved only a negligible plunge into the top surface, and the interface between the two workpieces underneath the tool showed no sign of deformation. It seems that at this low rotation speed either the heat produced is not sufficient to soften the workpiece and allow the tool to grip, or simply that the forces are insufficient to produce deformation, or both. It is highly likely that a different mechanism is involved in dissipating the power at this speed (i.e. pure surface friction, with no associated plastic work).

The corresponding peak temperatures measured are shown in Figure 3.7. These are the peak temperatures measured by a thermocouple 2 mm from the weld centreline. The temperature would be expected to be higher at higher welding speeds, and this is seen in the results. However, the quantitative form of the relationship between tool speed and temperature is not obvious,

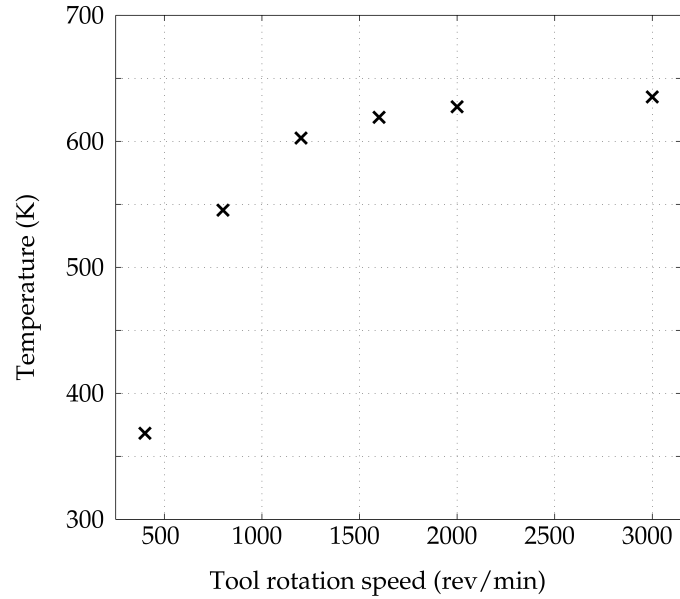


Figure 3.7: Variation in peak temperature with tool speed

due to the interaction between heat input and softening. If the torque was the same in each weld, then the heat input would be proportional to the speed; it clearly is not, indicating that the softening effect is important (as expected).

Fitting functions were plotted on these results, and R^2 values for linear, logarithmic and quadratic fitting functions are 0.59, 0.85, and 0.77. If the 400 rev/min case is ignored the correlation coefficient for the logarithmic case can be improved to 0.99. There is reason to think this is valid, since at 400 rev/min no weld was formed, as described above.

The fact that the torque is not constant, indicates that very simple models that assume heat generation entirely by friction not only ignore the physics of the problem, but that they are not even good approximate empirical models of the overall heat input. Even where models have accounted for additional effects over and above simple Coulomb friction, there is no simple dry friction law which would give rise to a logarithmic variation in power with surface velocity. This is discussed in more detail in the chapters on modelling.

It is surprising that the logarithmic function is such a good fit. This indicates that the torque drops off very steeply as the tool speed increases,

as otherwise the increase in power and peak temperature with speed would be greater than that observed; this tends to support the assumption in much of the literature that peak temperatures at the interface are very close to the solidus over a wide range of welding conditions. If the interface temperatures were substantially below the solidus at low speeds, then an increase in tool speed should more than compensate for the drop in torque caused by softening, and the total power (and hence peak temperature) should increase; if the lower speed is sufficient to bring a layer of material up to the solidus, then an increase in speed will result in a drop in torque such that the total power is largely unaltered.

3.3.3 Workpiece material

The workpiece material has perhaps the largest influence over the behaviour of a weld out of all the variables studied. Chapter 2 describes other studies where the FSSW process is implemented in a wide range of materials; for the purposes of this study, three materials were experimentally tested: AA6082 and AA6111 aluminium alloys, and DC04 steel. Their compositions are given in Table 3.1.

Some of the welds were arranged in a double lap/butt configuration. The weld material in these cases comprised two sheets of Al above a sheet of either Al or steel. The two sheets of Al were made from the alloys AA6082 and AA6111, aged to give the same room-temperature hardness in each.

The primary purpose in using AA6082 alongside AA6111 was to determine the flow pattern: the use of the different alloys makes it possible to section them post-weld and examine the final distribution of the initial sheets. As the strengths are the same, the expectation is that this will produce a weld that is very similar to a single lap weld of Al over Fe.

AA6082 and AA6111

The two Al alloys used were treated to have the same room-strength hardness; despite this, other differences between the two alloys could cause different behaviour under otherwise identical welding conditions. Because of the possible

differences in their high-temperature properties, it was necessary to evaluate welds made in these two alloys to see if they did in fact behave similarly, in order to use them in later Al to Fe experiments.

Temperature histories for these welds are shown in Figure 3.8. These welds have identical parameters, except for the workpiece material. Both welds used AA6111 for the top sheet, while the bottom sheet was either another sheet of 6111, or 6082. These two welds produced thermocouple temperature histories that were identical within the bounds of experimental variation identified in Section 3.6; therefore it is concluded that there is no significant difference between these two alloys under these welding conditions.

Aluminium and steel

The combination of Al and Fe is of particular importance in the automotive industry. An important part of this experimental programme is to study FSSW as a joining method for these two materials, especially AA6111 (as a typical medium-strength, heat-treatable alloy) and DC04 as a representative mild steel.

The standard case for these welds was a 2 s weld at 800 rev/min. (This is different to the Al to Al case, since good-quality welds were desired for the reference cases with each material, and these conditions were required to produce good-quality welds due to the lower conductivity of Fe compared to Al). Under otherwise identical conditions, the peak temperatures recorded at the 2 mm thermocouple were approximately 30 K lower in the weld with an Fe lower workpiece than an Al one (see Figure 3.9). The same difference was observed at the second thermocouple, however, the 10 mm thermocouple measurements were essentially identical.

Clearly, the lower conductivity of Fe as compared to Al has an influence; as the thermocouples are located in the steel sheet, the peak temperatures would be expected to be lower. Correspondingly, the peak temperatures in the upper (Al) workpiece are probably higher (since heat is being conducted away more slowly). Importantly, this will also raise the temperature at the tool–workpiece interface. Since the Al sheet will be hotter in the case of a

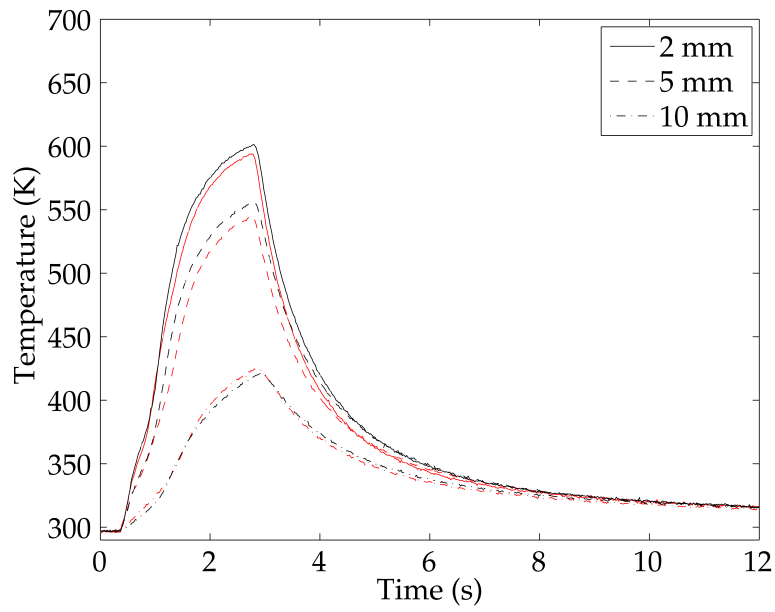


Figure 3.8: Thermocouple histories for 2 s welds at 800 rev/min, between AA6111 and itself (black curves) and 6082 and 6111 (red curves)

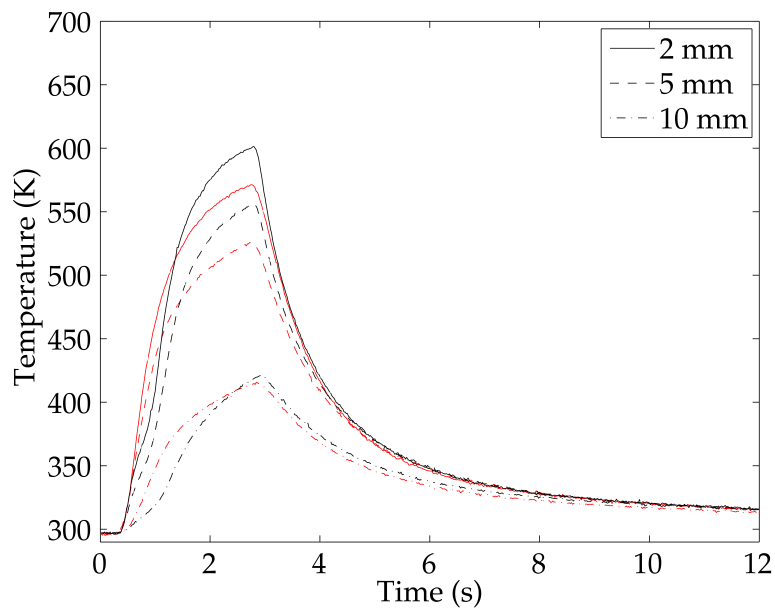


Figure 3.9: Thermocouple histories for 2 s welds at 800 rev/min, between AA6111 and itself (black curves) and 6111 and DC04 (red curves)

dissimilar weld, the deformation pattern could be significantly affected (since most of the deformation occurs in the Al sheet — see Chapters 5 and 6). What is unknown from the experimental data alone, is if the total heat input remains the same as in the Al to Al case, or if it falls due to greater softening of the Al, or if it rises due to some deformation taking place in the lower sheet (which is much stronger in the dissimilar case). As the power input is not known the temperatures in the Al workpiece are not necessarily hotter — it is possible that the power input is lower in the dissimilar case. The fact that the peak temperature recorded at 10 mm from the tool is very similar in the two cases might suggest that the heat input is the same; however, the volumetric heat capacity of the steel workpiece is higher (by approximately 50 %) than that of the Al one, the diffusivities are different, and the contact conductances likely vary too, so this cannot be resolved without thermal modelling. This is explored in Chapter 4.

3.3.4 Welding time — Al to Fe

In Section 4.2, the relationship between welding time and the characteristic heat flow time is discussed. In the context of a steel lower sheet, Equations 4.1 to 4.4 indicate that the two thermocouples nearest the weld centre can be considered to be a short distance from the heat source. The corollary of the argument presented in Section 4.2 is that long dwell time thermal histories appear to be extensions of shorter ones. To check this assumption, thermocouple histories were measured for Al to Fe welds at 0, 1, 2 and 4 s. (NB: all these times are the dwell times after completion of the plunge, when tool vertical motion is nominally zero — hence the weld time in each case is approximately $\frac{1}{2}$ s longer than the quoted time; this cannot be quoted exactly for each weld as the contact time between the tool and the workpiece also depends on the time taken to retract the tool, which in turn depends on the plunge actually achieved — see Section 3.7 and Chapter 5.)

These temperature histories are plotted in Figure 3.10. From this figure, it is possible to see that the assumption that the thermocouples are close to the heat source is valid. Indeed, the temperature histories for the two closest

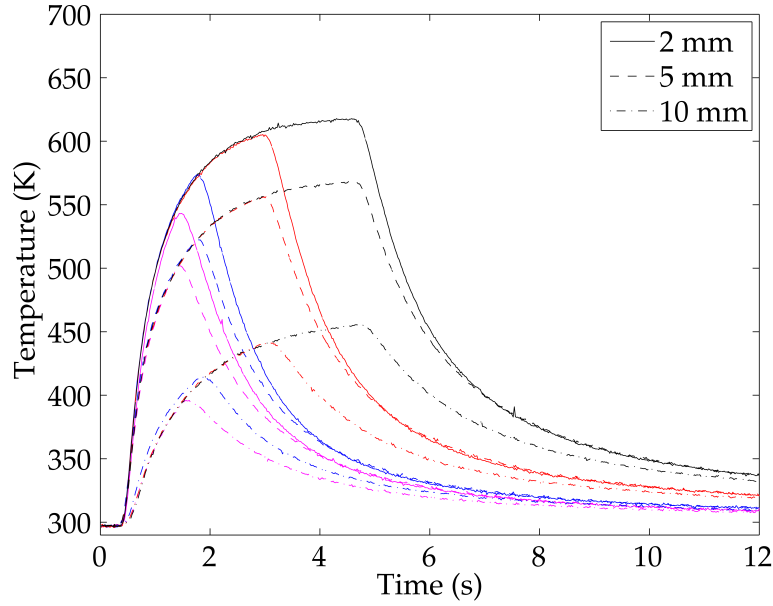


Figure 3.10: Thermocouple histories for welds between Al and Fe at 1600 rev/min, at 0, 1, 2 and 4 s dwell time

thermocouple points lie almost on top of one another, and those at the 10 mm location are also very close. In addition to confirming the validity of the analysis in Section 4.2, this makes the modelling task easier as short-duration welds can be treated simply as truncated versions of long-duration welds.

3.3.5 Rotation speed — Al to Fe

The previous analysis for welds made at different speeds was repeated with dissimilar materials. Due to the clamping arrangements and the smaller parameter space available for producing actual welds between Al and Fe (as compared to Al to itself), the range of speeds covered was smaller than in the study of Al to Al welds, covering only 800 to 1600 rev/min (84 to 168 rad/s).

A similar trend was found as for the previous study: the peak temperature reached increased with welding speed at the bottom end of the viable speed range, reaching a plateau. Temperature histories are shown in Figure 3.11 for the same locations as previously; there is no significant difference between the measured histories for the 126 and 168 rad/s cases. While the number

of data points is not sufficient to establish a quantitative trend, the previous assumed logarithmic fit is at least consistent with these new results. Again, this supports assumptions in the literature that peak temperatures in FSSW are usually at or very close to the solidus.

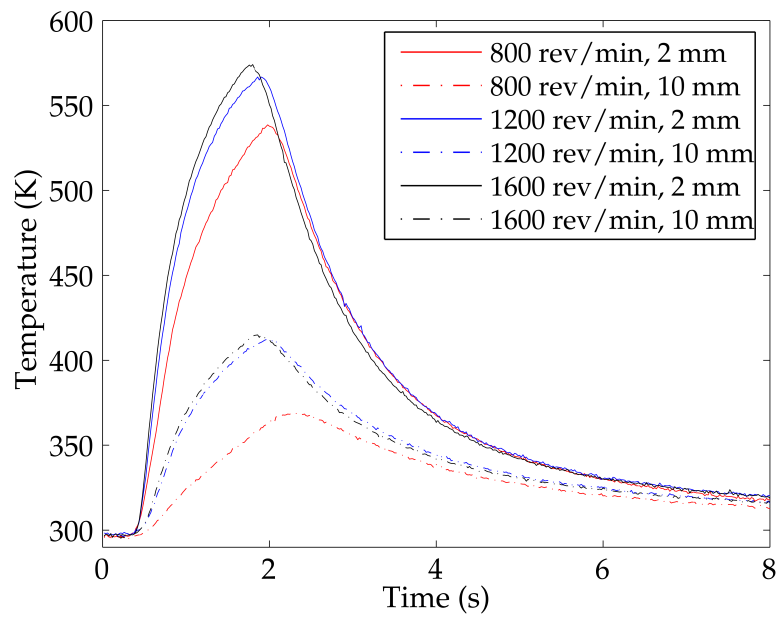


Figure 3.11: Thermocouple histories for 1 s welds between Al and Fe

3.4 Tool types

Welding tools for FSSW and FSW come in a range of sizes and geometries, with patterns on the shoulder and pin and changes in the pin length, quite apart from radically different tool types such as self-reacting bobbin tools (only used for seam welding) and refill FSSW tools. Pin features can include round pins, threaded pins, and more complex helical patterns, while shoulders can have a variety of patterns inscribed on the surface. This study used five different tool types, which are all shown in Figure 3.4. The 2 recessed wiper (long and short) tools have wide grooves cut into the surface, and the scroll tool has longer but narrower grooves. The proud wiper tool has ridges raised out of the surface of the shoulder, with a similar width. These tool designs produce distinct thermal fields in the weldzone, shown in Figure 3.12. The short wiper tool was used twice (once clockwise, once anticlockwise, looking down on the tool). The results for the long wiper are not presented as they were very similar to the results from the short wiper, but the strength of joints made with the short wiper was significantly higher. The welds produced by the proud wiper were not considered to be of acceptable quality; only a very limited range of conditions resulted in a joint at all, and the welds that did form were of very low strength. The tool was described by one investigator as ‘in hindsight, more like a milling tool than a welding tool’. The results from the scroll tool were also found to be rather poor, so further work concentrated entirely on the flat tool and the clockwise wiper tool.

The data presented in Figure 3.12 are only based on one weld run for each case, so there is some uncertainty in each curve. Nevertheless, the maximum temperatures measured in welds with different tools differ by around 50 K; this is greater than the weld-to-weld variability as observed in Figures 3.14 and 3.15 (discussed later).

The difference in tool design could affect the temperature field in various ways. Features on the tool could influence the flow pattern, thus changing the distribution of heat as it flows with the material, or they could change the heat input distribution (and total power input) by altering the contact conditions at the tool–workpiece interface. Both of these effects probably occur.

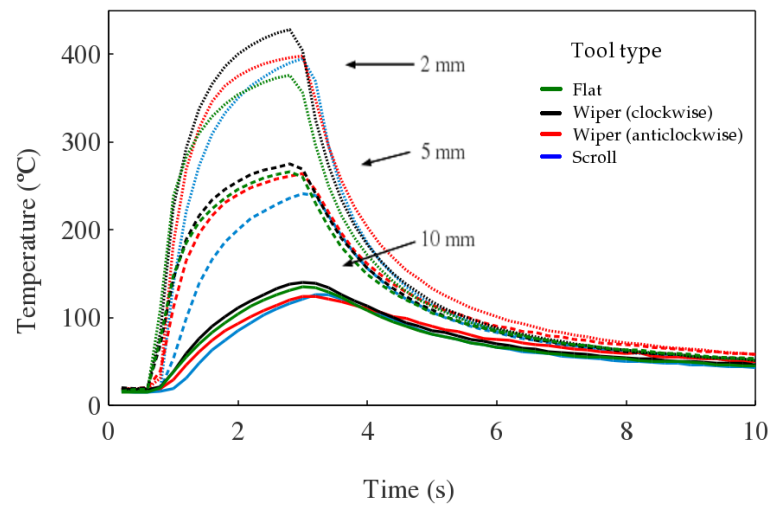


Figure 3.12: Temperature histories measured in the backing plate for various tool types

3.5 Weld quality

Experimental work, primarily carried out by Bakavos and Chen, identified the conditions under which ‘good-quality’ welds could be formed. Good-quality welds were those that were free of obvious defects such as cracks and voids. Once the parameters required to form good-quality welds had been determined, tensile tests were conducted with a number of sample welds. These initial tests were straight pull tests, with shims placed in the machine clamps in an attempt to produce as close to pure shear conditions as possible across the weld interface. The highest strengths were associated — as expected — with nugget pull-out; hybrid failures gave rise to lower failure loads and fracture energies while shear failures across the line of the original interface between the two workpieces resulted in very low strengths. Tool rotation speeds from 800 to 2000 rev/min were found to produce good-quality welds in AA6111 workpieces of 2 mm thickness. Force–displacement curves are shown for these tests in Figure 3.13a; these are used as opposed to stress–strain curves as (in order to assess the quality of a joint) the total force carried by a spot weld is often of more interest than the peak stress. A second measure of weld quality is the fracture energy, which is the area under the force–displacement curve.

The variation of peak load with rotation speed over this range is shown in Figure 3.13b for a constant weld time of 2.5 s. From this figure it can be seen that welds giving rise to the highest failure loads were produced at 750 rev/min, i.e., the lowest rotational speed used that gave rise to a good weld. (Welding was also attempted at 400 rev/min, but at this speed no weld was formed and the parts remained unjoined.) These welds also showed the highest strain to failure.

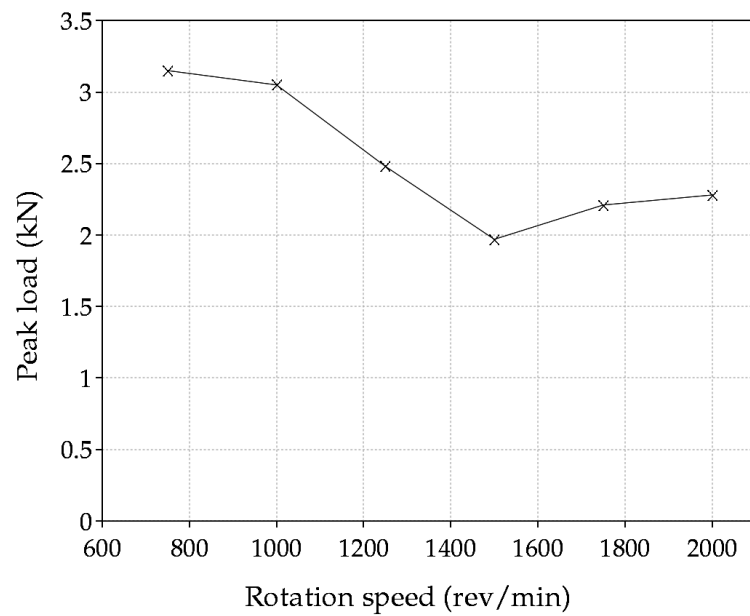
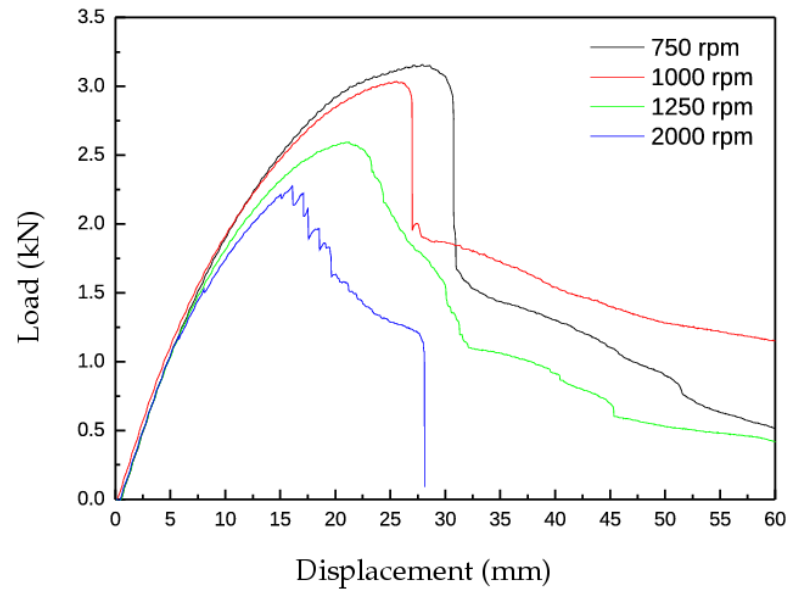


Figure 3.13: Load testing results for selected FSSW joints.

- a. (upper): Load-displacement (figure provided by collaborators at Manchester)
- b. (lower): Peak force (data collected by collaborators at Manchester)

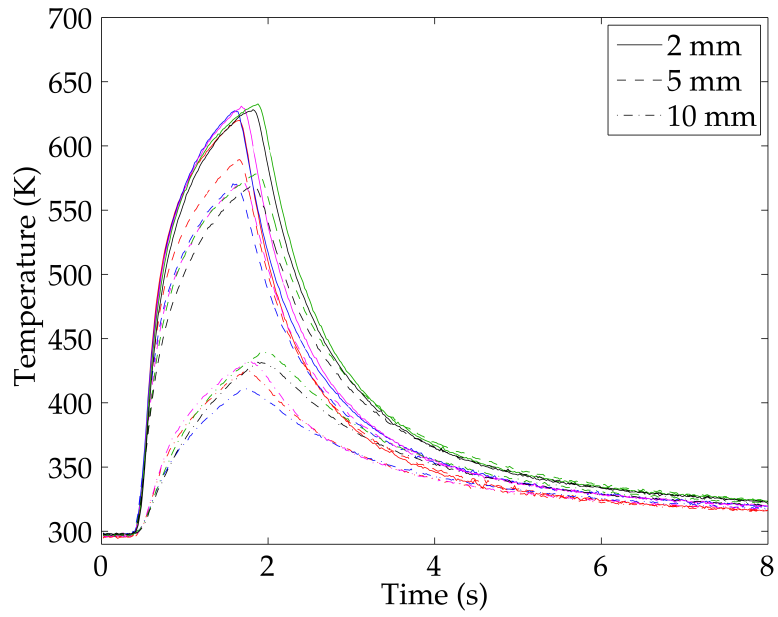


Figure 3.14: Measured temperatures at 2, 5 and 10 mm from the weld centre for nominally identical welds (AA6111, 2000 rev/min)

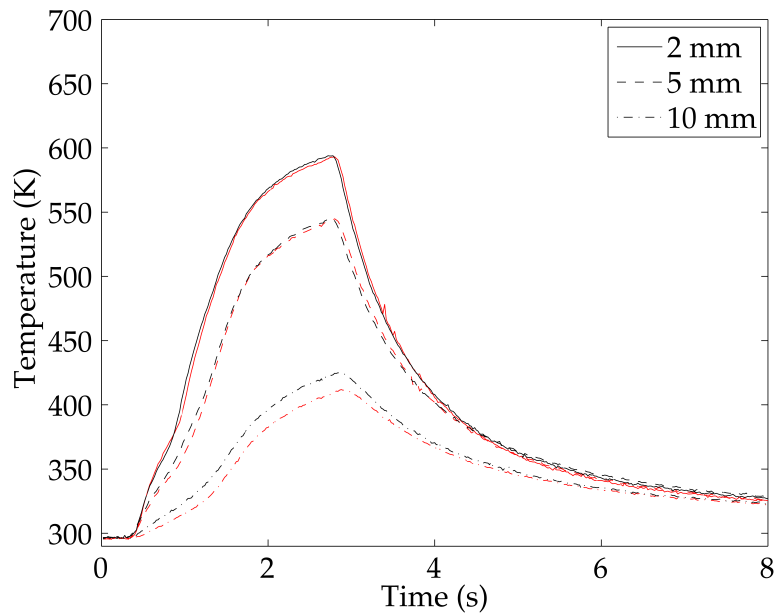


Figure 3.15: Measured temperatures at 2, 5 and 10 mm from the weld centre for nominally identical welds (AA6111 over 6082, 800 rev/min)

3.6 Sources of error

In order to compare experimental and model results, it was necessary to understand and quantify the various sources of error in the experimental measurements (modelling errors are discussed in the relevant chapters). The potential sources of error and an a priori estimate of the importance of each is shown in Table 3.4. Quantitative estimates were made of the total contribution of all errors by looking at the variance in results: a number of repeat welds were produced at TWI for nominally identical conditions and the measurements compared.

Many of the welds made were repeated twice as a check; two welding conditions were repeated more extensively. These were 2000 rev/min (210 rad s^{-1}) with AA6111 and 800 rev/min (84 rad s^{-1}) with AA6082 over 6111 (with 8 and 4 repeats, respectively). Plots of the temperatures recorded at three locations in each weld are shown in Figures 3.14 and 3.15. Temperature measurements were chosen as the appropriate comparison for a number of reasons, both experimental and practical: temperature histories are of great importance for weld modelling, as reaction rates and the rate of growth of intermetallic compounds (IMCs) depend strongly on temperature, while thermocouple data can pick up variations in a wide range of other parameters that may not be measured. It is unlikely that any other parameters of interest could vary independently without affecting the temperature.

Figures 3.14 and 3.15 show substantial variation in peak temperature, and also in the time taken for the weld. The variation in peak temperature near the centre of the weld (the hottest thermocouples) is around 15 K; the variation at the 10 mm location is much larger, about 30 K. Fortunately the hotter temperatures are of most interest, and these seem to experience less variation than the other locations (these temperatures are more important, since at the lower temperatures further from the centre — typically around 430 K at 10 mm — there will be very little reaction between the workpieces, when considered on welding timescales²). Taking into account all relevant factors and looking at the possible sources of error in Table 3.4, it seems that

²Precipitates in Al alloys only start to dissolve above about 450 K.

Source of errors	Mitigation attempts and qualitative estimate of magnitude
Workpiece thickness variation	A selection of samples were measured with callipers; all tested samples were 0.91 mm to 0.01 mm accuracy. The flow pattern could be very sensitive to thickness, so even this variation could be significant.
Workpiece in-plane dimensional tolerance	Not measured, but FE thermal modelling indicates that a variation of up to 1mm (which would be detected by eye when aligning sheets) is not significant.
Variation of workpiece properties (especially temper/aging time)	Potentially significant; all samples were taken from the same batch, so in practice the variation is likely to be small.
Clamping force	Workpieces were held in place by hand-tightened bolts; torque was not measured, and so considerable variability was likely. Its influence is unknown at present.
Machine compliance	Significant, between machines, and likely to form a major contribution. For this reason, caution should be exercised when comparing results from two different machines (this is noted in the text wherever relevant).
Thermocouple errors	The K type thermocouples used are generally considered reliable and accurate to within 1 K. Occasional errors caused by non-functioning thermocouples or thermocouples damaged or destroyed during welding were usually obvious in the data.
Thermocouple location	Estimated to be accurate to within 0.5 mm; owing to the steep thermal gradients, this could be a significant (and possibly the dominant) source of error.
Ambient temperature	Not significant considering the temperatures reached in welding; recorded prior to each weld.

Table 3.4: Sources of experimental errors

errors in the thermocouple location could be responsible for most of the variation seen between different welds. Weld modelling (see Chapter 4) indicates a comparatively flat temperature gradient for the central half diameter or so of the weld, with the steepest gradients occurring at about 5 mm from the weld centre. Slight errors in alignment of the tool with the expected central point on the workpiece could cause similar effects to those seen; however, the larger error at the 10 mm location does not correspond well to this (since the temperature gradient here is fairly shallow).

Clamping force affects the temperature by altering the contact conductance to the backing plate, and variations in clamping force would affect temperatures far from the weld centre more strongly since the tool itself provides a large downforce at the centre. The effect of altering this is explored in more detail in Chapter 4; together these two effects can account for the majority of the variation seen in temperature measurements.

The welds between AA6082 and 6111 (Figure 3.15) show less variation than those between two sheets of AA6111. The former series were carried out at a lower rotation speed; it is likely that the higher speed magnifies small inconsistencies in e.g. thermocouple placement or sample thickness, leading to greater variation in these welds.

3.7 Plunge depth and surface finish

The plunge depth has a large influence over most of the processes taking place in a weld. The forging force is a crucial component in spot welding, and this force varies strongly with plunge depth. While the forging force has been commented on with respect to seam FSW, since seam welding usually reaches a steady state *variations* in plunge depth have not received much attention. It is likely that variations in downforce and/or plunge depth affect the flow pattern directly; these variations will also affect the temperature field, particularly temperatures at the interface (since any heat generated at the interface between tool and workpiece is closer to the weld centre, with a deeper plunge weld). However, due to the finite stiffness of the machine, the clamping arrangements, and the tool itself, as well as the time-dependant

softening of the workpiece, the plunge actually achieved is not always the same as the nominal plunge. All these effects are magnified with thin-sheet welding: the overall distance from the tool to the weld interface is shorter, so a given change will be a greater proportion of this distance, and the workpiece material is more strongly constrained than with a thick workpiece, so its apparent stiffness will be higher.

To begin the investigation into the effect of plunge depth, and the relationship between target plunge depth, forging force, and temperature, final plunge depths were measured for a number of samples after welding. These samples included welds made with a variety of conditions, but all had a nominal plunge of 0.2 mm. The surface profiles of the tool contact patches were measured on a Taylor-Hobson Talysurf. From this data both average plunge depths and surface roughness values could be calculated. Figure 3.16 shows a typical surface profile, in this case from a weld that appeared to be of good quality (the surface finish was comparatively smooth, the flash was not excessive, and there was no visible distortion or slip between the workpieces — such characteristics are indicative of a strong weld). Points of interest on this figure are the average plunge (the distance between the far workpiece surface, represented by the dashed red line, and the surface represented by the solid black line), and the two deeper areas at the edges of the contact patch. These deeper areas are part of a ring in plan section extending round the edge of the contact patch, and have been termed *overplunge*, although their significance is unknown at present and has not been discussed by other authors.

Not all the samples exhibited such a smooth surface finish as that in Figure 3.16, some were much rougher; in addition, few of the samples had a final plunge close to 200 μm . The mean depth was 100 μm and the standard deviation was 89 μm . These differences appear to be systematic: welds made with identical conditions produced similar plunge depth measurements, with the maximum difference in depths for identical welding conditions being 40 μm .

Various correlations between the average final plunge and the welding parameters were studied; the strongest was between plunge depth and tool

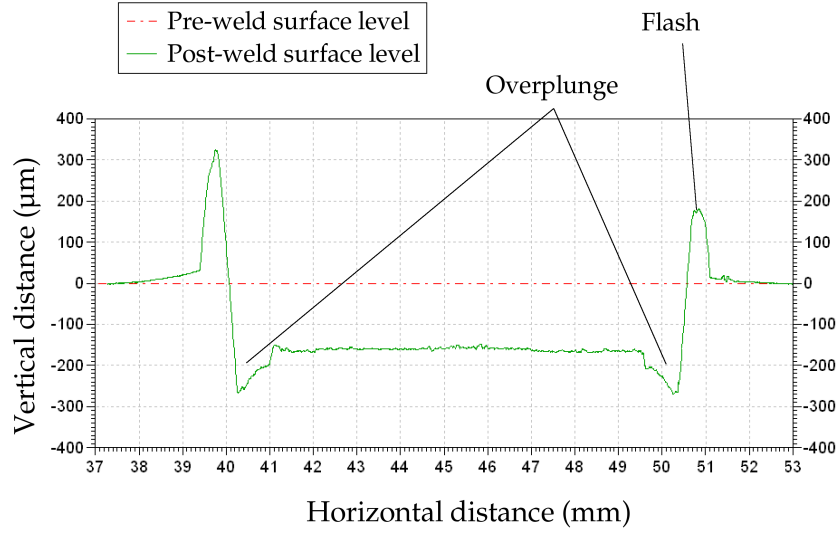


Figure 3.16: Sample weld profile (from Parker, 2011)

rotation speed. This correlation improved further if the correlation was calculated separately for different values of the other parameters (workpiece material and welding time), and a plot of this is shown in Figure 3.17.

These correlations all suggest that there could be a link between temperature and plunge depth. This is plotted in Figure 3.18, where the blue data points show results for Al to Al welds and the red points show results for Al to steel welds. These are plotted as separate series, since the temperature measurements are not directly comparable between the two cases (the thermocouples were placed at the base of the bottom sheet, hence temperatures nearer the nugget and the weld interface will be higher with an Fe lower workpiece, for the same temperature measured at the thermocouples).

From this figure, there is a clear link between the temperature and the measured plunge depth. This makes sense: due to the finite stiffness of the tool and machine, the finite forging force available, and the response time of the machine feedback systems, the increased softening of the workpiece at higher temperatures results in plunges closer to the nominal plunge: the tool can embed further into softer material. Given that the interface temperatures depend strongly on the distance from the tool to the weld interface, modelling should take account of the fact that the plunge is usually less than the

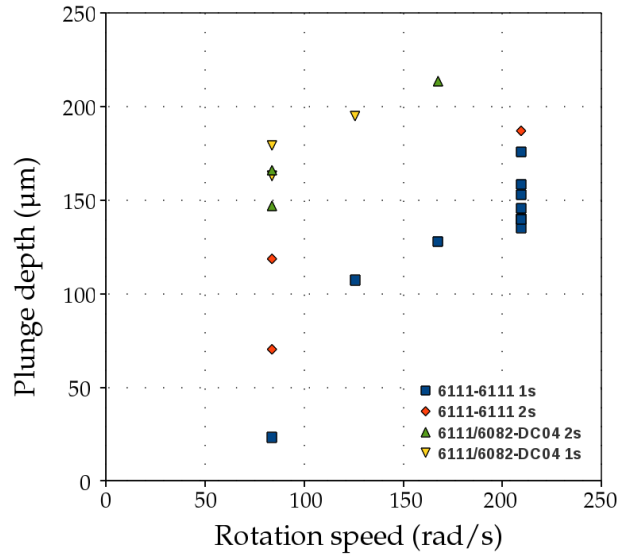


Figure 3.17: Variation in plunge depth with tool rotation speed for a nominal plunge of 0.2 mm

nominal value (in particular, assuming that the plunge is constant and equal to the target plunge is unlikely to be correct).

The previous discussion concerned plunge depth data for welds made with flat tools only. When the same analysis was conducted with the wiper tool, a different phenomenon was observed: the welds made with the wiper tool all had a negative plunge depth, i.e., the final surface of the nugget was above that of the surrounding parent material. The height reached was up to 120 μm , of the same order as the target depth. As the tool cannot have welded the material at this height, some pulling-up effect must have occurred. The most likely explanation is that workpiece material stuck to the tool as it was withdrawn. As the back of the lower workpiece remains level after welding, by conservation of material the wiper tool must form voids in the weld. This was confirmed by imaging the samples in a 3D X-ray machine. In most cases this void took the form of an approximate crescent shape under one half of the shoulder contact area. A particularly large void was formed at 2000 rev/min, and a slice showing a section through such a weld is shown in Figure 3.19.

This is surprising, even more so given that the wiper tool generally

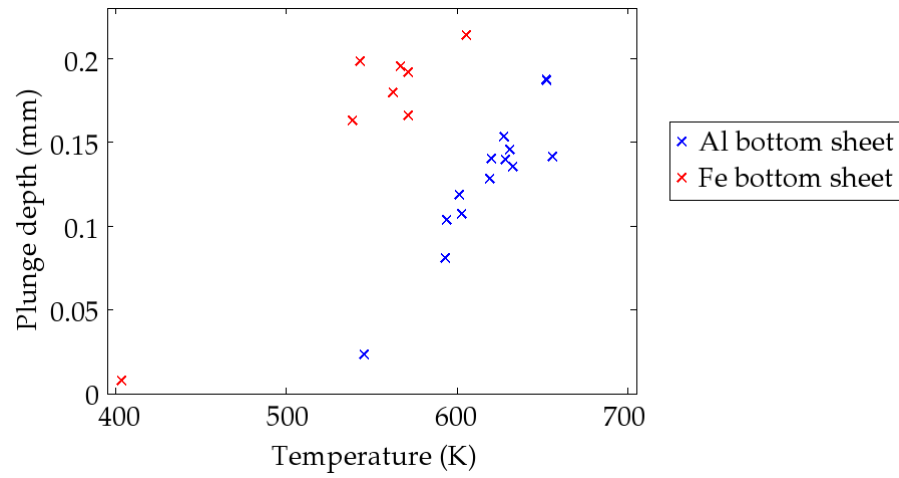


Figure 3.18: Variation in plunge depth with temperature.

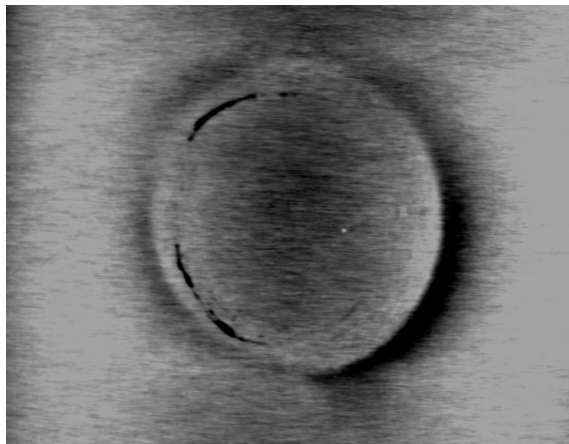


Figure 3.19: X-ray slice showing voiding in a weld produced by the wiper tool (the slice shown is from 0.39 mm below the joint interface; the image is approximately 20 mm across)

produces strong welds, yet voids are usually assumed to indicate poor quality, very weak welds.

Roughness measurements were made of the tool contact areas on all of these welds. The surface roughness of the samples using the wiper tool was slightly more than twice that of those made using the flat tool. This is consistent with sticking between the workpiece and the tool as the tool withdraws and the workpiece cools. However, at present there is no further explanation as to why the wiper tool grabs material on withdrawal in this manner.

3.8 Backing plate material

Bakavos & Prangnell (2009) conducted a study into the effect on welding of two different anvil materials. They conducted two identical sets of experiments: one with a conventional steel backing plate, and one with the same backing plate but coated with 4 mm of Macor ceramic. This has a low thermal conductivity, of $1.46 \text{ W m}^{-1} \text{ K}^{-1}$. The ceramic anvil produced consistently lower-strength welds for all except the pinless case, for which the strengths were almost identical; the results of the strength tests are shown in Figure 3.20. The thermal diffusivity of the backing plate strongly affects the thermal cycle experienced by the workpiece, but experimental data alone is not sufficient to explain the strength difference. This is studied in more detail in Chapters 4 and 6.

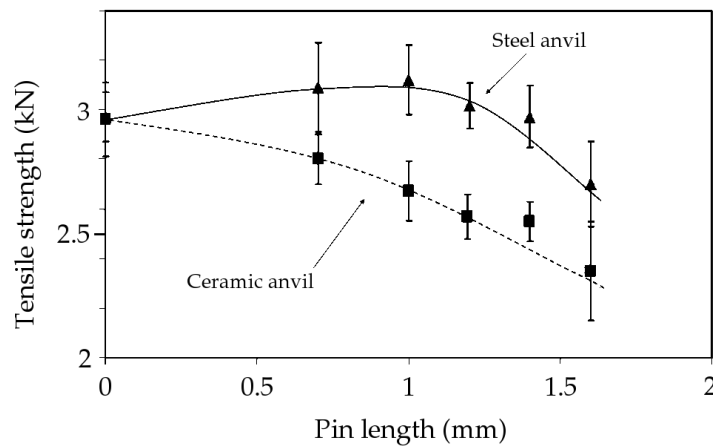


Figure 3.20: Comparison of failure strengths for steel and ceramic backing plates

3.9 Flow visualisation

Flow visualisation has been accomplished on experimental welds made between AA6082 and 6111. The different copper content of these two alloys gives them different appearances when etched. These images are very useful, in combination with flow models, for understanding what deformation takes place. In turn, this provides useful insight into conditions during welding and how the joining process works. Sample images are shown in Figures 3.21; this method is discussed in more detail in Chapter 5.

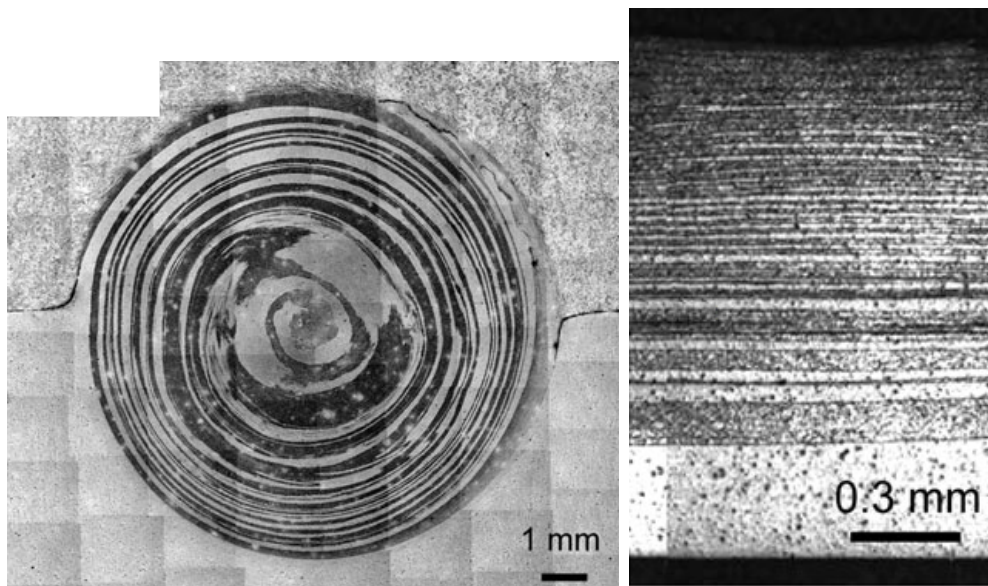


Figure 3.21: Left: Top surface view of the contact patch, post-weld, showing a typical onion-ring pattern, and right: Section view through a weld, showing layering between AA6082 and 6111

Chapter 4

Thermal modelling

4.1 Introduction

As discussed in Chapter 2, there are two broad classes of model: analytical and numerical. The advantages and disadvantages of each type are discussed at more length in the relevant sections of Chapter 2. Analytical models are quick to calculate and provide insight into the mechanics of the process, but they struggle to represent features, such as finite geometries, that can be important in real welds. Within the class of numerical models, finite element (FE) modelling is a mature, well-developed field, and is the dominant modelling technique used by other authors (see for example Colegrove & Shercliff, 2006, Awang et al., 2005 and Schmidt & Hattel, 2008). Consequently, an FE model was selected for this problem, supplemented by analytical models of specific features as appropriate. An analytical model is presented first to examine the influence of welding time.

Existing FE models for seam welding usually concentrate on the steady-state phase of welding, as the majority of time making long seam welds is indeed spent in — or almost in — steady-state conditions. Where a dwell phase with pre-steady-state conditions is considered, this is usually only used to estimate the time needed for steady-state conditions to form. An FE model is presented here that can accurately predict temperatures in a spot weld; this model is then used to examine possible variations in welding conditions

and to understand how these changes can affect the temperatures reached in the weld.

Two further objectives are to produce a model of sufficient accuracy: (a) to combine with a new sequentially coupled thermal and mechanical analysis (described in Chapter 6); (b) to predict thermal histories in the heat-affected zone, particularly at the weld interface, as inputs to microstructural models being developed by the project partners at Manchester University.

One drawback of FEA is the calculation time involved, with some models taking many hours to model a single weld of a few seconds' duration. This is especially important for parametric studies like those in Section 4.10, where numerous calculations must be performed for various load cases, material combinations, and interface conditions. Although hardware capabilities and software performance can vary substantially, there is a common factor across all platforms: a reduction in model complexity can speed up calculation times, often dramatically. Computing resource requirements are strongly linked to mesh characteristics such as the number of elements and the size of the smallest element (which affects the timestep size required for stability). Dimensional reduction, such as the switch from 3D to 2D, can considerably reduce the number of elements required and the running time of the model. The FSSW process is an axisymmetric one, therefore an axisymmetric model is the logical choice (even though the geometry of the workpieces is not axisymmetric). Before an axisymmetric model can be relied upon, it must be tested to ensure the simplification is accurate. This can be assessed by comparing outputs, primarily temperature, from 3D and axisymmetric models. There are a number of features in the experimental welds described in Chapter 3 that are not in fact axisymmetric: comparing 2D and 3D models will show if these features significantly affect the weld and the temperatures reached. This does not, of course, say anything about whether either model is an accurate model of *experiments*, but that is a separate question, which is addressed in Section 4.9.

4.2 Timescale of welding

When considering the effect of dwell time on temperature, there are two possible extreme cases. The first is to assume that the heat source is close to the thermocouples; the second is to assume that it is at a large distance.

If the heat source is very close to the measurement point, and the welding time is much longer than a characteristic heat diffusion time over the distance between the two, then the temperature at the measurement point will be approximately proportional to the temperature at the heat source at all times. In such a case, a 1 s weld will look exactly like the first 1 s of a 2 s weld, and similarly for any longer time.

If, on the other hand, the measurement point is a long way from the heat source, then this will not be the case. ‘Long’, in this context, means that the characteristic heat diffusion time (given by Equation 4.4) between the two points is much longer than the welding time. If the weld geometry and welding time fall into this parameter space, then the heat input can be approximated by a delta function. In this case, the heat equation (Equation 4.1) has the solution in Equation 4.3, and a doubling of the welding time is seen at the measurement point as a doubling of the total heat input, but the temporal variation of the power is unimportant. Put another way, at a location far from the heat source, an increase in the welding time results in an increase in the temperature, but not in the shape of the temperature rise experienced at that point.

Unfortunately for this analysis, the typical thermocouple locations are at neither a short nor long distance from the heat source. An order-of-magnitude estimate of the characteristic heat flow time can be made from Equation 4.4, which, for a thermocouple 10 mm from the weld centre in AA6111, gives a time of about 1.5 s. This is not short enough to treat the heat input as a delta function. However, for short welds, or for thermocouples closer to the centre than 10 mm (which is true for most of the measurements made in this project — 10 mm was the greatest distance used) it may be reasonable to approximate longer welds as extensions of shorter welds. Using Equation 4.4 in reverse, gives a distance of about 8 mm for a 1 s weld in AA6111. This

suggests that the nearest thermocouples may, in fact, be considered to be a short distance from the heat source for welds of 1 s or longer. As AA6111 is the highest diffusivity material used, this will also be valid for Fe workpieces.

$$\frac{\partial T}{\partial t} = a \frac{\partial^2 T}{\partial x^2} \quad (4.1)$$

$$T = \frac{Q}{2\pi} \int_{-\infty}^{\infty} e^{-a\epsilon^2 t} e^{i\epsilon x} d\epsilon \quad (4.2)$$

$$\therefore T = \frac{Q}{2\sqrt{\pi at}} e^{-\left(\frac{x^2}{4at}\right)} \quad (4.3)$$

$$t = \frac{x^2}{a} \quad (4.4)$$

Q is the total heat input in this case, and all other symbols have their usual meanings.

4.3 FE model description

The finite element modelling software chosen was Abaqus, in ‘standard’ (i.e. implicit) mode. The energy balance equation is given in Equation 4.5. The implicit solver uses the backward Euler method (Equation 4.6) to calculate the solution incrementally. The use of the backward Euler method ensures that the calculation is stable. Differentiating 4.5 and substituting 4.6 into the result gives Equation 4.7; this is discretised and an approximate solution is found at each timestep.

$$\int_V U dv = \int_S h ds + \int_V q dv \quad (4.5)$$

U is the internal energy ($U = \rho u$), h is the heat flow per unit area due to the temperature gradient and q is the external heat input per unit volume.

$$\left. \frac{dU}{dt} \right|_{t+\Delta t} = \frac{U_{t+\Delta t} - U_t}{\Delta t} \quad (4.6)$$

$$\frac{1}{\Delta t} \int_V U_{t+\Delta t} - U_t \, dV = \int_S \dot{h} \, ds + \int_V \dot{q} \, dv \quad (4.7)$$

The elements used were linear heat-transfer elements, of Abaqus type DC2D4 for the 2D model, and DC3D6 and DC3D8 for the 3D model. Automatic time stepping was used for all calculations. Using automatic time stepping, the time increment for each step is calculated automatically and may vary within each calculation. When using this method, a value is chosen for the temperature change per increment. If the change in temperature at any node exceeds this value during a single analysis step, the step is halted, and attempted again with a new (smaller) timestep. If the maximum temperature change is smaller than the allowable value, the timestep is increased slightly for the subsequent step. For all calculations in this work other than those described in Section 4.5 the maximum allowable change was set at 1 K per step.

Descriptions of the materials used and the experimental setup are given in Section 3.2; the simulations described in this chapter were based on this arrangement. Models were built in 2D and 3D; a section view through the 3D model showing the parts is given in Figure 4.1. The 2D model can be seen in Figure 4.2, showing the parts, interfaces and a typical mesh¹. Dimensions are shown in Figure 4.3.

Figure 4.2 shows a model with zero plunge. This was used for early work which compared the 2D and 3D models, and for the examination of mesh size effects. Calibration to experimental data used models with a plunge equal to the nominal plunge during welding (i.e. these later models assumed that the tool arrived instantly at the final plunge depth at the start of the weld).

The material properties that are relevant to thermal modelling are summarised in Table 4.1, and these constant property values were used for all models except where noted in the text. The use of constant versus temperature-dependent property values is discussed further in Section 4.7.1.

¹The mesh illustrated is described as a coarse mesh in Section 4.6 — see that section for details of the influence of element size.

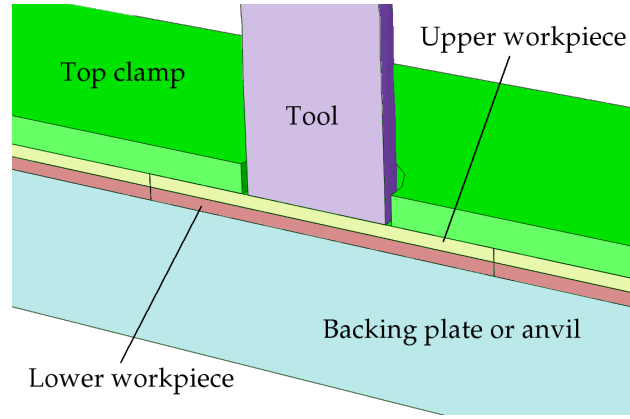


Figure 4.1: Example thermal model in 3D showing the parts and interfaces

Material	Density kg m^{-3}	Thermal conductivity $\text{W m}^{-1} \text{K}^{-1}$	Specific heat capacity $\text{J kg}^{-1} \text{K}^{-1}$	Diffusivity (calculated) $\text{m}^2 \text{s}^{-1} \times 10^6$
AA 6111	2700	143	800	66.2
AA 6082	2690	172	870	73.5
ES EN DC04	7850	47	419	14.3
SAE 4340	7850	44.5	475	11.9
SAE H13	7860	29	495	7.46
Alumina 95% dense	3900	27	900	7.7
Pure copper	8700	400	385	119

Table 4.1: Thermal properties of the materials used, at room temperature. Data from Mills (2001), Hector et al. (2004) and Ashby & Cebon (2009).

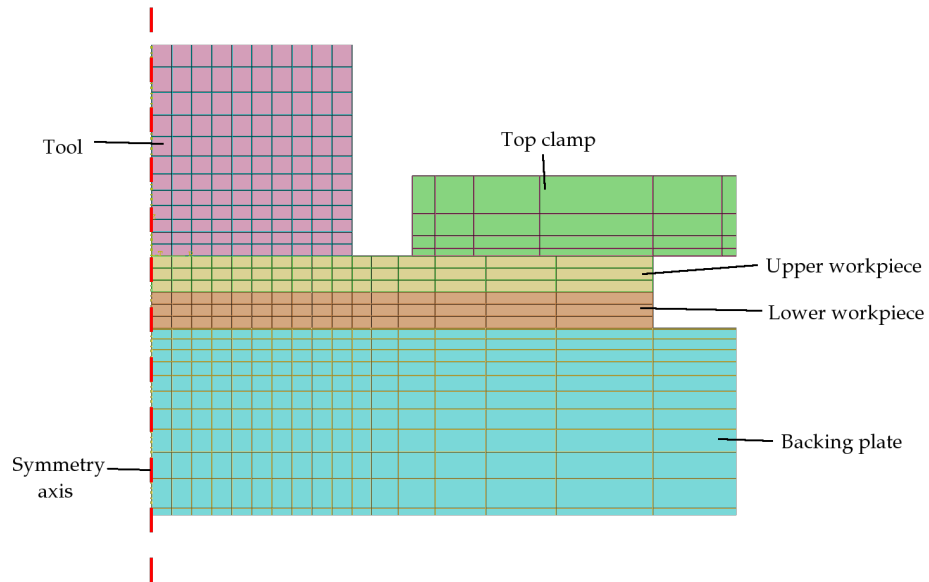


Figure 4.2: Example thermal model in 2D, showing the parts, interfaces and an example mesh

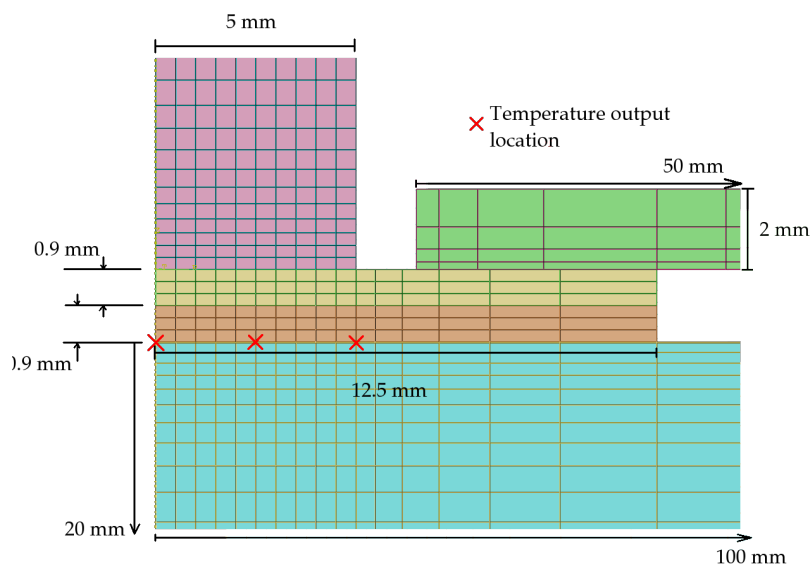


Figure 4.3: Model dimensions and temperature output locations

4.4 Axisymmetric modelling

FE models of the weld were built in 2 and 3 dimensions. Components not essential to the core of the thermal model (i.e. the tool, backing plate and top clamps) were added to the model sequentially. In this model, the workpieces both had the properties of AA6111 Al alloy, the tool was H13 steel and the backing plate and clamps were 4340 steel. A constant (in time) and uniform (in area) heat input was applied to the whole of the tool-to-workpiece contact patch. In the 2D model, the workpieces were represented as discs of 12.5 mm radius (so the diameter is equal to the width of the workpieces in the experimental setup); in the 3D model they were the full size of the experimental coupons (100 mm \times 25 mm). In both models the thickness was 0.9 mm, the same as the experimental sheets. The workpieces were initially thermally tied: the temperatures at the nodes on either side of the interface were constrained to be the same, representing perfect heat transfer between the two parts. As new parts were added in, they were initially tied to the existing parts at the interfaces; a more detailed discussion of metal-to-metal contact is given in Section 4.7.3.

Virtual thermocouple outputs were taken at the base of the lower workpiece at 0, 2.5 and 5 mm from the centre of the weld. Using $t = x^2/a$ gives a time of about 2.4 s as a characteristic heat flow time between the centreline and the edge. Consequently, it was expected that there would be some difference between the temperatures reached in the two models for long welds, and during the cooling phase, but for welds of much less than 2 s the results should be very similar.

Temperatures at the points of the virtual thermocouples are plotted for the 2D and 3D models in Figure 4.4 for a 1 s weld with a 1 kW power input. As the workpieces are insulated from the surroundings in this model, the final temperature rise can be calculated by dividing the energy input by the heat capacity of the workpieces — these values are plotted as asymptotes in the figure. The 2D and 3D models match closely for the initial slope of the temperature rise, although there is a difference of 50 to 100 K in the predicted peak temperature; the temperatures diverge significantly after the

end of the heating phase, which is as expected as the long-term asymptote for the 3D case is much lower (as the volume of material included in the model domain is much greater). Clearly, if this had been a representation of a real weld then the 2D model would not be accurate enough for temperature predictions.

The next stage of the comparison was to add extra features into each model, and again examine the differences between the two. Figure 4.5 shows temperature outputs for the same locations as before: this time, the model includes the backing plate as well (with perfect thermal contact everywhere between the workpiece and backing plate).

This case shows much closer agreement between the two models than the previous one, presumably as the backing plate provides a large heat sink in both cases, thus limiting the overall average temperature rise. The overall energy input is sufficient to raise the temperature of the entire domain by only 3.3 K in the 2D case and 1.3 K in the 3D case — although the temperature rise in the 2D model is still over twice that of the 3D case, the absolute difference is small. It is of interest to note that the greatest difference in temperature profiles under these conditions is found at the 0 and 2.5 mm locations, while the temperature 5 mm from the weld centreline is almost identical in the two models.

A further calculation was performed with each model with the addition of the top clamp to the model domain. The results for this case appeared very similar to those for the previous case with the backing plate; since little heat flows into the top clamp, it makes only a minor difference to the solution.

These results show that the assumption of axisymmetry produces results that are in close agreement with a 3D model, and a 2D model may be used with confidence for short welds. However, owing to the divergence between the two cases at longer times — caused by 'heat reflection' from the boundaries, which are nearer in the axisymmetric case than in reality — the 3D model will be used for modelling longer welds (experimental welds included dwell times of up to 6 s).

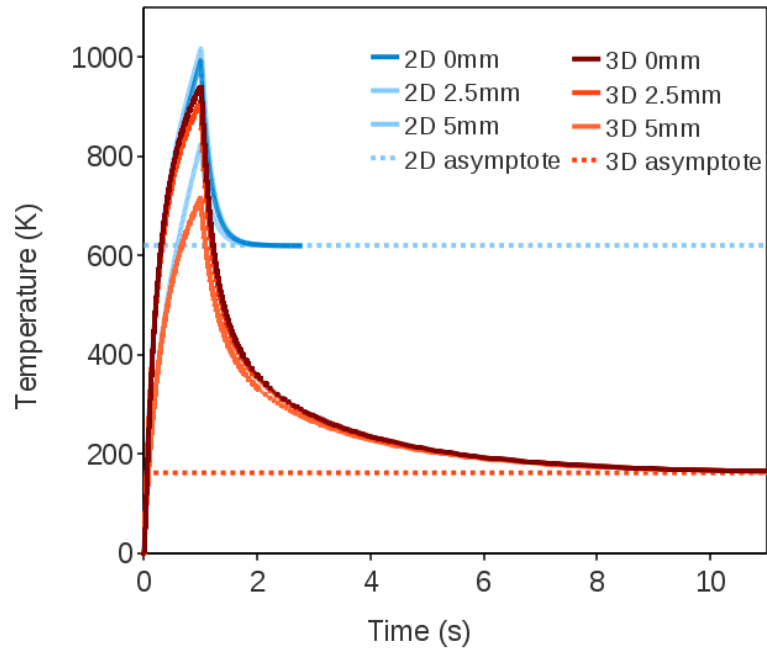


Figure 4.4: Comparison between 2D and 3D models: workpieces only

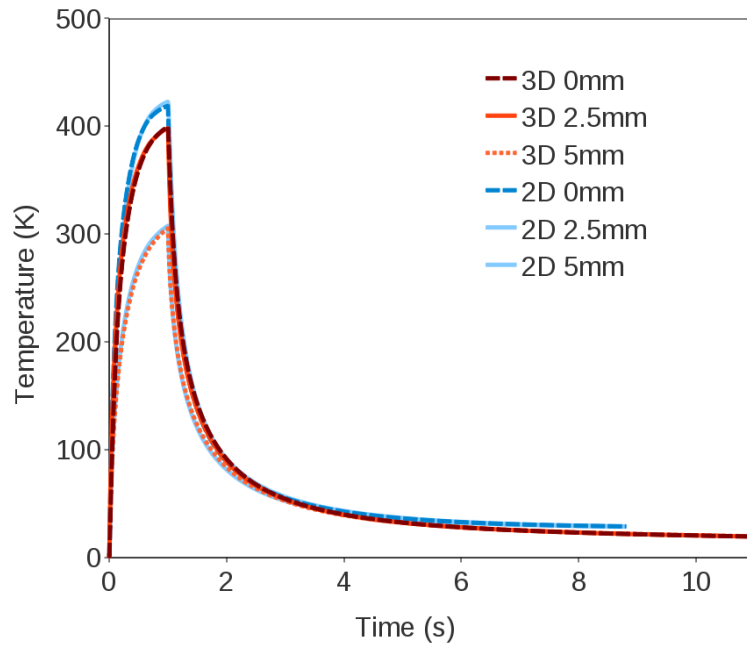


Figure 4.5: Comparison between 2D and 3D models: with backing plate

4.5 Thermal contact problems in Abaqus

The model was built up in stages so that additions could be checked for problems more easily. The first stage included just a single workpiece, then two workpieces tied together, then two workpieces with imperfect thermal contact, then a tool was added into the model. Without the tool present, the input power had to be reduced by a factor to allow for heat loss to the tool; with the tool present, this heat flow could be calculated directly in the model (and in this case the factor could vary throughout the course of a weld). When the tool was incorporated into the model, it was initially included with its surface temperatures tied to the temperature of the workpiece at that point, simulating perfect thermal contact between the two parts.

A more realistic way to model all the metal-to-metal interfaces is to use a thermal contact conductance, which is defined by Equation 4.8. Since contact between the tool and workpiece in the real process is lost at the end of the dwell time, the initial model imposed a step change in contact condition at this interface from thermal conductance to insulated. This coincided with the step change in power input to zero.

$$h_c = \frac{q}{\Delta T} \quad (4.8)$$

Switching instantaneously from an imperfect contact to no contact demonstrated a problem in the way Abaqus handles step changes in thermal boundary conditions. Figure 4.6 shows the problem, which is that the predicted temperature of the workpiece falls below its initial (ambient) value.

Clearly, this is wrong, as the temperature of the workpiece cannot fall below that of the surroundings in the cooling phase. In this model, no heat loss to the surroundings is considered – all boundaries are specified as being perfectly insulated. This leaves only three possibilities (or, perhaps, a mixture of the three):

- the outer boundaries are not behaving as insulators, as specified;
- the boundary between the tool and the workpiece is not being treated correctly, and the heat is flowing into the tool against the thermal gradient;

- energy in the system is not being conserved (i.e. the temperature of some nodes is falling without the heat flowing out or being accounted for).

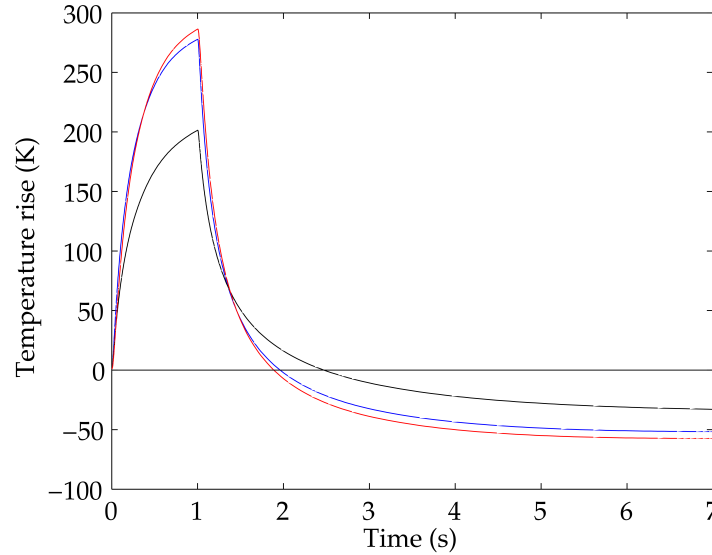


Figure 4.6: Non-physical cooling effects in Abaqus

Further investigation shows that the problem is related to the step change imposed in the load and interface conductance. Figure 4.7 shows the heat flux vectors calculated by Abaqus for one increment in the cooling phase of the weld. The nominal interface condition at this point is one of perfect insulation between the tool and the upper workpiece, however, this is not being respected: there should be no heat flow across the boundaries, yet the heat flux vectors in the region of the (removed) tool clearly show heat flow out of the model domain. This situation is not peculiar to an isolated increment, and heat continues to flow out of the model throughout the cooling phase.

It appears that heat continues to flow into the tool, from the workpiece, even after the tool has been removed from the model (which is done using `*MODEL CHANGE,REMOVE` in the input file). Although the cause of this is unclear, it may be avoided by adding an extra step to the analysis, between the heating and cooling phases. During this phase, the conductance and power inputs are ramped down smoothly throughout the step, rather

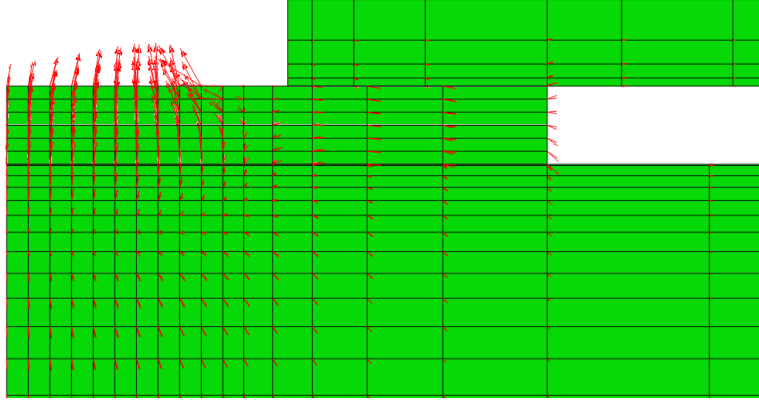


Figure 4.7: Heat flow in Abaqus after an instantaneous change in boundary conditions

than being turned off as a step change; the tool is then removed at the start of the third step (or it may be left in the analysis as a disconnected region, if tool temperatures during the cooling phase are desired). This second step can be made very short: 0.05 seconds is sufficient to eliminate the problem.

4.6 Mesh effects

The precision of an FE model depends strongly on the nodal density. A dense mesh produces more accurate solutions, but takes more computing power, or more time to run. The causes are twofold: firstly, with more nodes, the matrices are larger and more operations are required for each increment. Secondly, the stable time increment is smaller with smaller elements.

In order to check that the mesh density was not adversely affecting the accuracy of the output, a model was run for a 1 s weld with three different mesh densities, with a factor of approximately 5 increase in the number of nodes between each density. Temperature outputs for the centre of the weld at the interface are shown in Figure 4.8. This location was chosen as a critical point of interest in the weld. The mesh density check was performed prior to the analysis and calibration of the model, hence the power input (and temperatures reached) are not realistic. The difference in peak

temperature between the medium and fine meshes corresponds to 0.04%, which was deemed sufficiently small that the medium-density mesh could be used for the rest of the analysis.

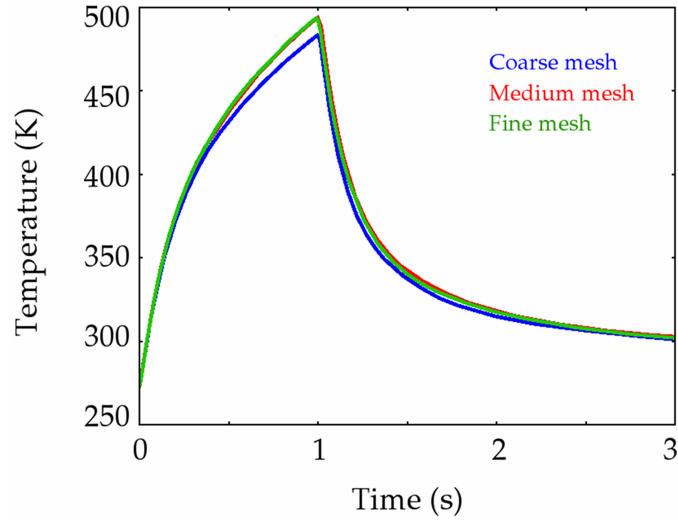


Figure 4.8: Mesh sensitivity analysis

4.7 Model calibration

The FSSW process has numerous input parameters, only some of which are independently adjustable. Many of these parameters, such as interface conductance values, are difficult to measure. Others (such as the total power input) are superficially simple to measure, however the accuracy of these measurements is low. In the case of the total power input, this was measured experimentally but factors such as the machine idling torque and the low sampling rate rendered the data of limited use.

Fortunately, temperature measurements contain a wealth of information about the weld properties: temperature measurements across interfaces can feed into models of contact conductance, the ratio of thermocouple measurements at various radii depends most strongly on the shape of the power distribution, the shape of temperature histories with time is influenced by the variation in the power input, and the total power strongly influences the

peak temperature reached. All these factors are related, but an iterative process can find values of each parameter that lead to a self-consistent model capable of predicting temperatures with accuracy.

4.7.1 Material properties

The thermal properties of Al are widely known to depend on temperature. Both the conductivity and the specific heat capacity vary with temperature, increasing over the range from room temperature to the solidus. While for pure Al both properties increase monotonically with temperature, the presence of alloying elements produces multiple local maxima in both. The underlying reasons depend on an interaction between the precipitate distribution, dissolved solutes and phase changes; the exact effects depend on the alloy composition. Temperature-dependent values of specific heat capacity and thermal conductivity for AA6111 measured after 1 hour hold times are shown in Figures 4.9 and 4.10. Since they both increase with temperature, the overall variation in diffusivity (Figure 4.11) is smaller than that in either the conductivity or heat capacity alone. This data is representative of that available in the literature — measurements of the thermal properties exist for all common alloys, but currently extant data is generally measured at long hold times, typically one hour or more, to allow time for the material to approach equilibrium at temperature before measurements are taken.

Owing to the rapid thermal cycle in FSSW, the use of data measured after 1 hour hold times is not necessarily appropriate for modelling purposes; some authors use room temperature data, and this subject remains a matter of debate. Which of these values is most accurate, or whether an intermediate or different value should be used, depends on the reaction kinetics.

The rate of change of properties will also vary with temperature. The rate of change will be highest in the nugget (as the peak temperatures are highest), and lower in the surrounding HAZ; the nugget is characterised by dissolution and recrystallisation, while precipitates in the HAZ exhibit coarsening; these will affect the materials' properties in different ways.

Colegrove & Shercliff (2006) performed FE calculations using both room-temperature data and values for Al in equilibrium at high temperatures. They found that the former provided a better match for the conditions prevailing during seam FSW, based on a comparison of predicted temperatures with experiments. This would seem to indicate that room-temperature data is also appropriate for FSSW. Since the heat input as a function of time is calibrated in the model, it may be argued that some of the uncertainty arising from the use of constant thermal properties is absorbed within this calibration. There is little justification for the additional complexity of notionally greater precision in the thermal properties, when the heat input is adjusted empirically in this way.

Definitive property values can only be found by measuring the heat capacity and conductivity during a very rapid temperature rise, but this is not practical at present. Differential scanning calorimetry can be used to pinpoint the phase transitions and measure the heat capacity by reference to a known sample, but the rate of heating in such experiments remains orders of magnitude below that applied during welding. A non-equilibrium test on an alloy of interest was conducted by Dutta & Allen (1991), who measured the heat capacity of ice-quenched AA6061 during a continuous temperature rise at a rate of 0.167 K s^{-1} ; this is shown in Figure 4.12 as a difference between that and the values for equilibrium (overaged) samples. This shows a small discrepancy over most of the range (the maximum difference is approximately 10 %, which occurs at circa 575 K). Despite the comparatively high heating rate in this experiment, it was still only 10^{-3} times that during FSSW. It may be that the best approach possible at present is to use FE models of the FSSW process, or other rapid heating processes, and compare the outputs for different material laws against experimental temperature measurements.

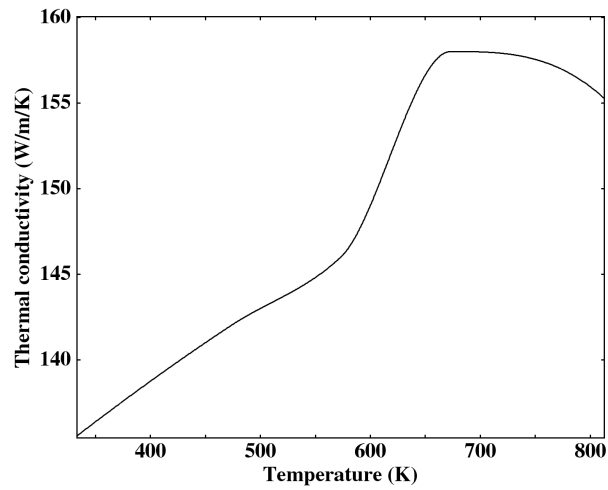


Figure 4.9: Thermal conductivity of AA6111 as a function of temperature (data from Khanna et al., 2005)

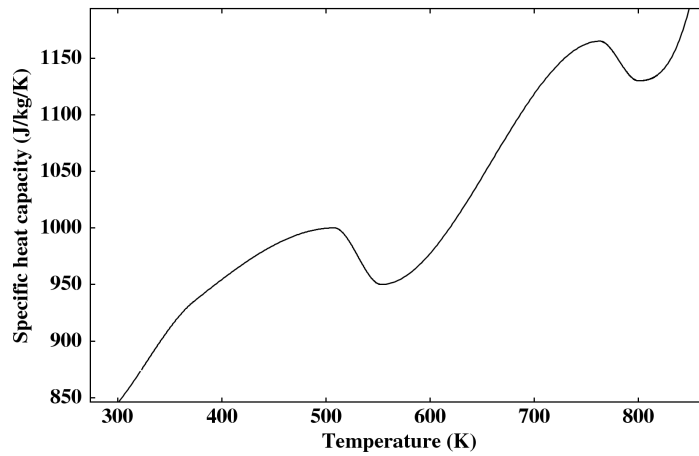


Figure 4.10: Specific heat capacity of AA6111 as a function of temperature (data from Khanna et al., 2005)

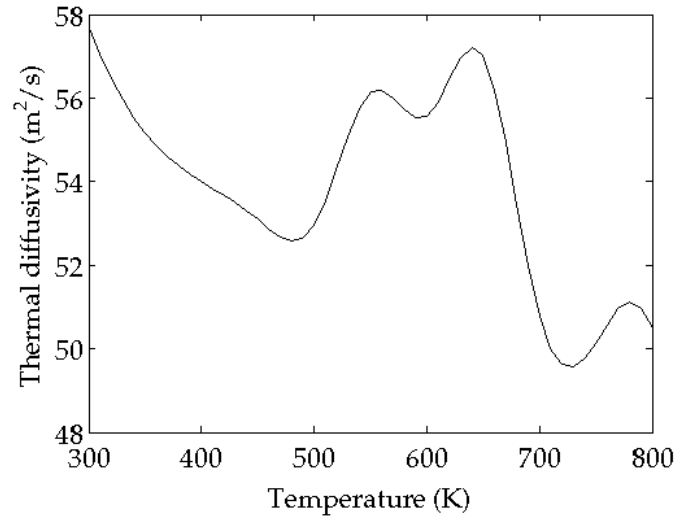


Figure 4.11: Thermal diffusivity of AA6111 as a function of temperature (derived from Khanna et al., 2005)

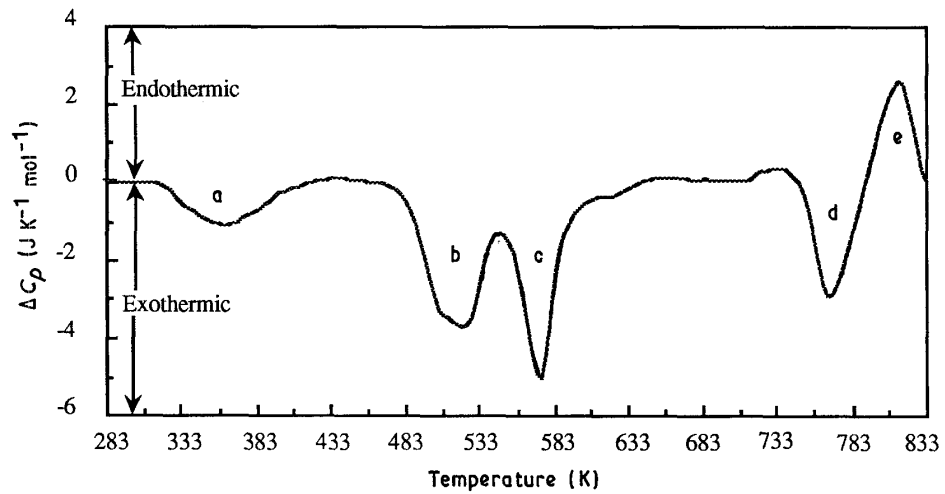


Figure 4.12: Differential scanning calorimetry thermogram of AA6061, showing four precipitate formation peaks, a to d, and one dissolution peak, e. (Image from Dutta & Allen, 1991)

4.7.2 Power input

The power input to the weld can vary in both time and space.² As described in the literature review, other authors have discussed to some extent the spatial variation of the power input function, mostly in the context of seam FSW, but as many studies use steady-state models, variation in time has not received the same study.

Spatial variation

The most common assumptions are to assume that the power input is either uniform over the contact patch between the tool and workpiece, or that it scales with the local tool velocity (so that it varies linearly with radius, as used by Schmidt & Hattel, 2008). This has the form given in Equation 2.7 (reproduced below in Equation 4.9).

$$q = \frac{3Qr}{2\pi R_S^3} \quad (4.9)$$

where q is the power input per unit area, Q is the total power, r is radial position and R_S is the shoulder radius.

Colegrove & Shercliff (2006) used a similar model, but by calibrating the total power to experimental temperature measurements found the best match was obtained by truncating the power input function at a fraction of the shoulder radius. This gives the new power input as shown in Equation 4.10.

$$q = \begin{cases} \frac{2Q'r}{3\pi R_S^3} & , \quad r \leq R_{S'} \\ 0 & , \quad r > R_{S'} \end{cases} \quad (4.10)$$

$$\text{where } Q' \text{ satisfies } \int_0^{R_S} q \, dr = Q \quad (4.11)$$

²For the sake of brevity, ‘power distribution’ is used in this work to refer to the spatial distribution of power input, and ‘power profile’ to refer to the shape of the power vs. time curve.

Models of other friction-based processes usually assume a uniform input power; for example, thermal models of rotary friction welding still use Rykalin’s solution for the heat flow in a bar (Rykalin, 1951). While this solution to Fourier’s Law (shown in Equation 4.12) is accurate for the assumed boundary conditions, the assumption of uniform heat input is likely to be wrong.

$$\Delta T = \frac{-Q}{2A\rho c\sqrt{\pi a}} \int_0^t \left(\frac{1}{\sqrt{t}} e^{\left(\frac{-x^2}{4\pi at}\right)} \right) dt \quad (4.12)$$

(Equation 4.12 concisely demonstrates why lateral heat flow and a time-varying power are important for FSSW. Putting in material data for AA6111 with a 5 mm radius bar and a 1 kW heat source — typical of FSSW — gives temperature rises at the surface of the workpiece shown in Table 4.2. These temperature rises, certainly for longer times, are much higher than those measured experimentally.)

Given the number of competing suggestions for the power distribution in the literature on seam FSW, and the transient nature of spot as opposed to seam welding, additional investigation was warranted to examine which (if any) of these would be most appropriate for FSSW. This was carried out using the basic Abaqus model (described previously), with the backing plate and clamping arrangements included and perfect thermal contact between all parts. Four power distributions were modelled, and virtual thermocouple outputs compared. The power was adjusted in each case to keep the total energy input constant. The four power distributions that were used are described

Welding time (s)	Temperature rise (K)
1	338
2	478
4	677

Table 4.2: Temperature rises in an Al bar with a uniform 1 kW heat source (as given by Equation 4.12)

in Equations 4.13 to 4.16 and illustrated graphically in Figure 4.13. The uniform and ‘top hat’ (truncated uniform) distributions are not considered to be realistic models, as they are not physically representative of the underlying physics. Since they are used by many authors, they are nevertheless included here for comparative purposes.

$$\text{Distribution 1:} \quad q = \frac{Q}{\pi R_S^2} \quad (4.13)$$

$$\text{Distribution 2:} \quad q(r) = \begin{cases} \frac{16Q}{9\pi R_S^2} & , \quad r \leq \frac{3}{4}R_S \\ 0 & , \quad r > \frac{3}{4}R_S \end{cases} \quad (4.14)$$

$$\text{Distribution 3:} \quad q(r) = \frac{3Qr}{2\pi R_S^3} \quad (4.15)$$

$$\text{Distribution 4:} \quad q(r) = \begin{cases} \frac{32Qr}{9\pi R_S^3} & , \quad r \leq \frac{3}{4}R_S \\ 0 & , \quad r > \frac{3}{4}R_S \end{cases} \quad (4.16)$$

The factor of $\frac{3}{4}$ was chosen based on kinematic modelling work (Chapter 5) and an extensive study of the location that gave the best prediction of experimental temperatures; this latter work is given in more detail in Jędrasiak et al. (2012).

Temperature measurements at the same three locations were used to compare the results from these 4 power distributions; these are shown in Figure 4.14. As can be seen in the figure, all these cases give very similar results for the 10 mm location. This is as expected, since a simple analysis (given in Chapter 3, based on an $x = \sqrt{at}$ calculation) shows that at

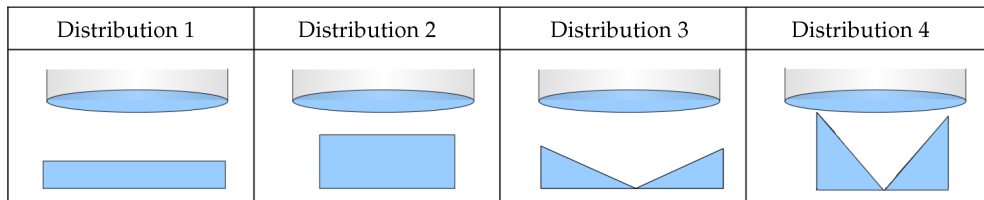


Figure 4.13: Power distributions

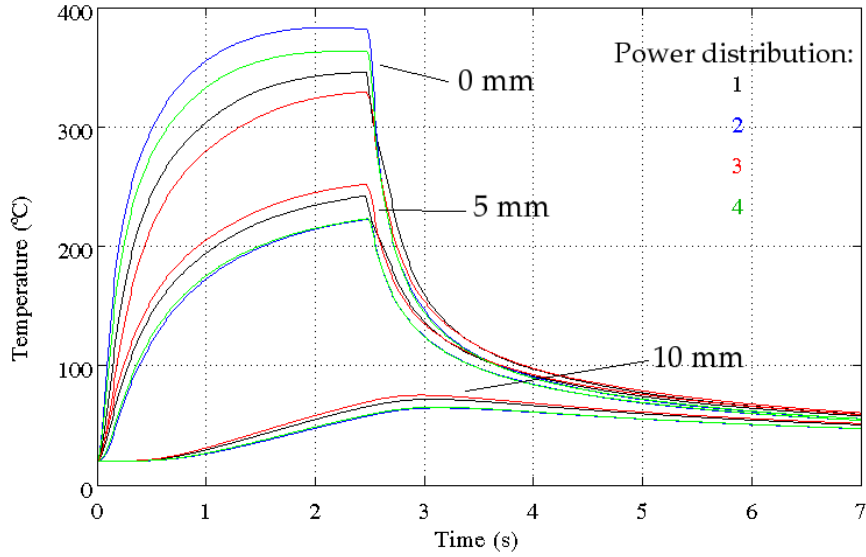


Figure 4.14: Predicted temperature outputs for 4 input power distributions at 0, 5 and 10 mm locations

this distance treating the heat input as a point source is a reasonable first approximation. Comparing the ratio of the temperatures at the two closer thermocouples gives a metric that can be used to quantify the effect of each power distribution on the temperature distribution. Values of this metric for each case are given in Table 4.3. These can be compared to values for the same metric calculated from experimental data, shown in Table 4.4.

If the top hat distributions are discounted (as they are unrealistic, discussed previously) and the variation of power per unit area with radius is taken to be linear, this analysis allows selection of the peak in heat input to

Power distribution	0 mm temperature K	5 mm temperature K	Ratio
1	619	513	1.21
2	656	494	1.33
3	603	525	1.15
4	637	595	1.29

Table 4.3: Power distribution metrics — calculated data

Tool type	Average ratio
Flat	1.23
Short wiper	1.27
Long wiper	1.29
Scroll	1.33
Proud wiper	1.06

Table 4.4: Power distribution metrics — experimental data

match the distribution generated by each tool. This has been done for the flat and wiper tools, the wiper tool generating a peak at a smaller radius than the flat tool. (The anomalous result for the proud wiper tool is not considered important; it has very poor joining ability, discussed in Section 3.4, and produces very different results to the other tools.)

Variation with time

Generally speaking, FSSW takes place at constant rotation speed. As the workpiece heats up, the flow stress falls, leading to a fall in torque and power input. Unfortunately, although the torque was measured in experiments at Manchester, the power losses in the machine were so high, and the sampling rate so low, as to render this data unusable. Torque data was also measured during the experiments at TWI, but owing to software limitations data was only available at intervals of 1 s. However, thermocouples placed in the workpiece respond very quickly to changes in total power input, so it is possible to extract meaningful information about the power input by looking at the temperature histories, in combination with an accurate model. Torque data is also available from other published work, such as that carried out by Gerlich et al. (2005) which is presented in Chapter 2. Figure 2.10 shows a typical torque history, exhibiting an exponential shape once complete shoulder contact is made (after point F_2 in the figure, at around 3 s).

To investigate the effects of fluctuations in the total power input, three different power profiles were tested. Other parameters were kept constant, using those of the standard case for the thermal model (a lap weld between

two AA6111 coupons of the standard geometry, with perfect thermal contact to a 4340 steel backing plate; the spatial power distribution had a linear variation with radial position, as described earlier). The three power profiles used were a constant power, an exponential decrease, and an impulse. An ideal impulse cannot be represented easily in a numerical calculation, so instead a finite-duration impulse was used of 0.1 s. The exponential profile lies between the two extremes, and is probably the most realistic, as discussed later. The three profiles were adjusted so that the total input energy was the same in each case. The exponential power profile has the form $P = P_0 e^{(-t/t_c)}$ where t is time and t_c is the time constant. For the case presented here, $P_0 = 1.5$ kW and $t_c = 5$ s.

The temperature outputs are shown in Figure 4.15; it is clear from this figure that variation in the power profile has a great effect on the peak temperatures produced in the workpiece, even for equal total energy inputs. Compared to an exponential profile, a constant power input delivers a larger proportion of energy towards the end of the weld, resulting in higher peaks near the tool and lower peaks further from the tool, whereas with the exponential input the bulk of the energy is delivered earlier, so it has spread

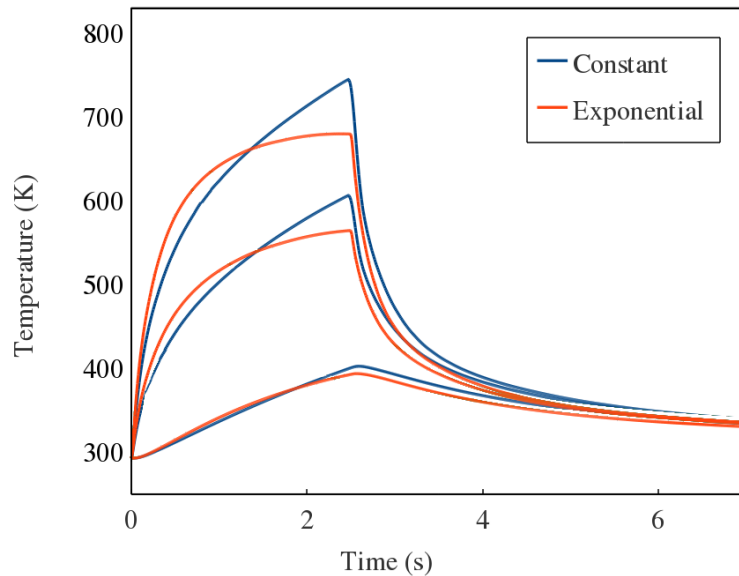


Figure 4.15: Temperature outputs at 0, 5 and 10 mm

further through the workpiece by the end of the dwell time. The case of an impulsive heat input is not physically realistic, and the peak temperatures calculated are far too high.

An exponentially-decreasing power input ties in with current literature about how the process works: as the weld heats up, the flow stress decreases, and hence the heat generation for a constant deformation pattern will decrease, and the process is to a large extent self-limiting. The plasticity analysis in Chapter 6 also confirms that there is a strong physical basis for this profile. Refinement of the power input and study of experimental welds showed that a pure exponential function could not match the observed temperature measurements for welds at longer dwell times. A revised form was chosen, with $P = P_0(a e^{(-t/t_c)} + (1 - a))$.

Total input power

From the two preceding sections, the overall form of the power input can be determined. The form that best matches experimental temperature measurements is a linear power distribution with a cutoff, as given by Equation 4.16, that varies in time as an exponential function with an asymptote. This still leaves a number of variables to be determined by reference to experiments, but has markedly reduced the overall complexity of the problem. The power input can now be completely described by four variables: the initial power; the asymptotic power; the time constant; and the radial cutoff (assumed to be $\frac{3}{4}R_S$ in Equation 4.16).

Assuming that a 1 s weld is the same as the 1st 1 s of a 2 s weld, etc., the most useful approach is to use welds with the longest dwell time available for the initial calibration — this will allow the most accurate estimation of the time-varying parameters. Shorter welds can be used to assess the accuracy of the calibration.

A summary of all experimental welding conditions is given in Chapter 3. Dwell times up to 6 s were modelled in AA6111 to AA6111, with a shallow plunge (of 0.2 mm) and welding speeds of 800 or 2000 rev/min. The metal-to-metal contacts under the tool were treated as perfectly conducting as

the tool downforce applies a high pressure to this contact, and the metal rapidly softens in this region; for the contact between the workpiece and backing plate over the rest of the surface, a value of $100 \text{ W m}^{-2} \text{ K}^{-1}$ was used, after Colegrove & Shercliff (2006). Calculations were run for the standard welding cases, keeping the radial cutoff at $\frac{3}{4}R_S$, and adjusting the other three parameters describing the power input (initial and asymptotic powers, and the time constant) to best match the peak temperatures. Temperature outputs were taken from locations at 1, 6 and 10 mm from the centre of the weld, to correspond with thermocouple measurements made in experimental welds. The three parameters describing the input power were adjusted in an iterative process to provide the best match between the FE predictions and measured temperatures. The power input parameters found to give the best match between model and experiment were a peak power of 1200 W, an asymptotic power fraction of 0.45, and a time constant of 2.3 s. The power profile matching these parameters is shown in Figure 4.16.

After optimising these parameters, the temperature outputs in Figure 4.17 were obtained. These outputs are shown alongside thermocouple data from experiments. This figure shows a very close match for the two thermocouples closest to the weld. The calculated temperature at 10 mm from the weld is lower than that measured, however. This occurs due to the unrealistic contact conductance used in the model; this is explored further, and more accurate values for the conductance are estimated, in Section 4.7.3.

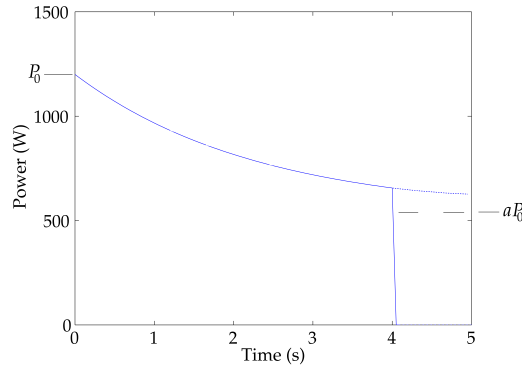


Figure 4.16: Power profile showing the best-match parameters with $P_0 = 1200 \text{ W}$, $a = 0.45$ and $t_c = 2.3 \text{ s}$ for a 4 s weld

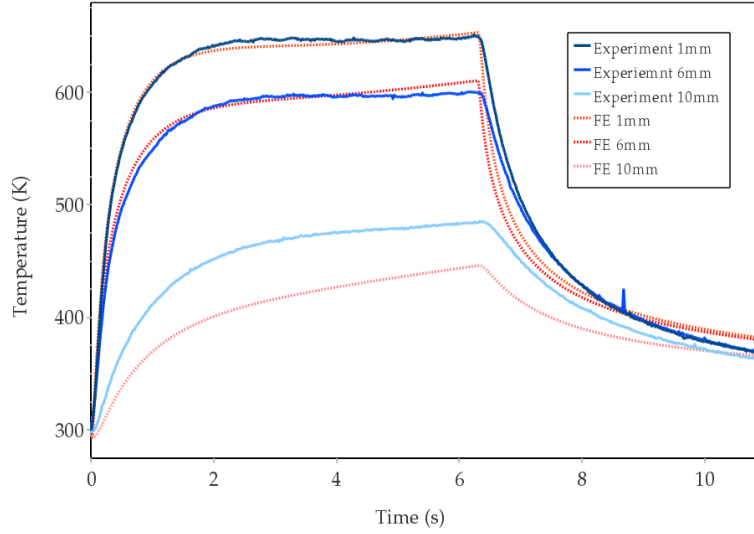


Figure 4.17: Comparison of temperature histories for model and experiment, using the best-match power input profile; weld with a 6 s dwell time

To test to see if the adjusted power input fitted data from other welds, predictions of the temperature histories at the same points were calculated for other welding times. The only parameter that was adjusted for these welds was the welding time, all other parameters were kept constant. A comparison between these predictions and experimental measurements for a 1 s dwell weld is shown in Figure 4.18; this shows a good match for both the heating rate and the peak temperatures within the nugget. Temperatures further out are, again, lower in the model than in experiments, and the cooling rate is higher than that measured. Further validation was performed against separate welds, and the results of this analysis are shown in Section 4.9.

The higher cooling rate in the model is interesting — this is a feature of many thermal models; for example, temperatures calculated by Colegrove et al. (2007) showed very good agreement with experiments for the heating rate and peak temperature, but diverged slightly during cooling.

As the reaction kinetics have a very strong dependence on temperature, the cooling rate has less influence on the microstructure than the peak temperature. The cooling rate is also not needed for a deformation model.

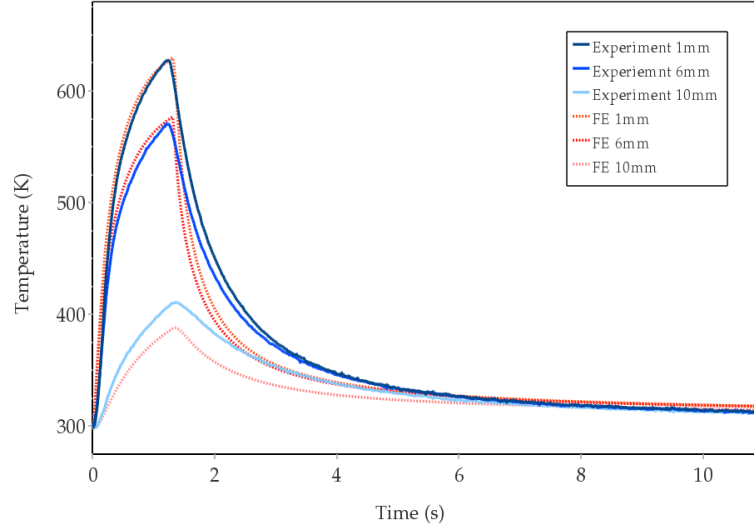


Figure 4.18: Comparison of predicted temperature histories with experimental measurements for a 1 s weld

Therefore, the divergence of temperatures during cooling is not considered to be a critical flaw in the model.

4.7.3 Heat losses

During FSSW, heat is lost from the workpiece by conduction and radiation. Convection in the surrounding atmosphere will also play a role by altering the temperature gradient in the air in contact with the metal parts. To build an accurate and fast model, it is important to take account of the most important sources of heat loss, and to discount those effects that are insignificant. Heat is lost to two main sources during FSSW: the tool and the backing plate. Minor heat losses also occur to the other clamping metal in contact with the workpiece, and through the surfaces of the workpiece that are exposed to air. The model presented so far has only taken account of conduction effects.

Radiation and convection

Radiation and convection both play only a minor role in FSSW. The emissivity of Al is very low: even when heavily oxidised its emissivity is rarely above 0.3. Taking the area to be twice that of the shoulder (to represent heat loss from both sides of an exposed workpiece) and the temperature to be 820 K, $P = \sigma AT^4$ gives $P \simeq 1.2\text{W}$. Consequently, radiation may be neglected in the analysis of FSSW.

Various treatments of thermal losses to the atmosphere from welding are found in the literature. Most of these studies involve FSW, as during FSSW the clamping arrangements are more extensive, and these usually minimise the area of exposed workpiece. The most common approach is to define a convection coefficient and ambient temperature for losses to the surrounding air, with values of the convection coefficient during FSSW typically ranging from 30 to 300 W m⁻² K⁻¹. This coefficient is usually chosen by matching temperature measurements to those observed experimentally. Some models (see e.g. Awang et al., 2005) additionally use a convection coefficient to model heat losses to the backing plate; this is done for reasons of speed, but in the present case the backing plate is explicitly included in the model domain.

With the weld geometry being studied in the present case, very little of the workpiece is exposed to the atmosphere (only the gap between the tool and the top clamping plate is directly exposed). The temperature at the top edge of the top clamp is sufficiently low that heat loss from here to the surrounding air will be negligible. The only surface where the temperature is high enough for heat losses to air to possibly be important are the edges of the tool, and the gap between the tool and the top clamping plate. This latter gap is filled by flash during the weld, hence calling for a more complicated treatment than just consideration of the heat loss.

A rough estimate of the heat lost from the tool to the atmosphere can be made by making an assumption about the thickness of the thermal boundary layer. Assuming that this is at least 1 mm makes the thermal gradient less than $5 \times 10^4 \text{ K m}^{-1}$; taking the thermal conductivity of air to be 0.024 W m⁻¹ K⁻¹ then over the heated, exposed area of the tool the steady-

state heat loss would be around 0.4 W. This is so much lower than the power input that heat losses here, like the radiative losses, can reasonably be neglected.

Contact conductance at metal-to-metal interfaces

As mentioned, in most of the models considered in this chapter the backing plate is included in the meshed domain. The heat loss across the interface between backing plate and workpiece is calculated as a function of the temperature gradient and contact conductance. Accurate values for the contact conductance are crucial, for the interface between bottom workpiece and anvil, and also values for contacts between the two workpieces, and between the tool and the top workpiece. These interfaces are illustrated in Figure 4.19. These interfaces are important because they strongly affect the temperature in the workpiece: realistic contact conductances, based on values found in the literature, can alter the peak temperature reached at the interface by 250 K. However, it is a difficult aspect to model accurately, as can be seen from the range of values quoted in previous studies.

While contact conductances have received extensive study, it is difficult to make any predictions about the conductance due to the number of variables involved. The value of the conductance at any given interface is a function of the conductivity, surface finish, flatness and hardness of both materials in contact and their oxide layers, and of the contact pressure, temperature, and heat flux, as well as the properties of trapped fluid (air) between the

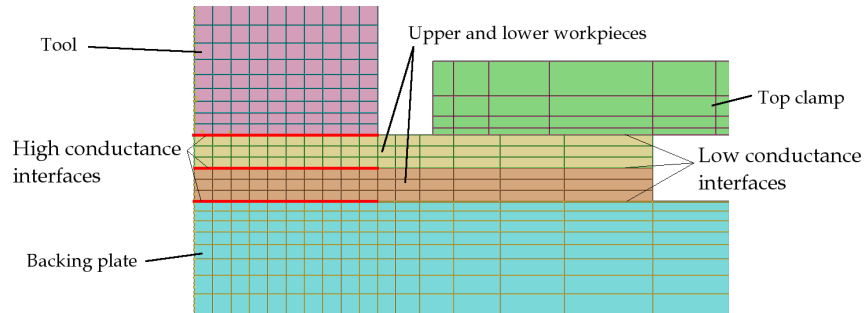


Figure 4.19: Model setup, with interfaces highlighted

surfaces in contact (Rohsenow & Hartnett, 1998). Increasing downforce and temperature make the workpiece conform better to the profile of the backing plate on a small scale, increasing heat transfer, and both downforce and temperature change substantially during welding. Rohsenow & Hartnett (1998) quote values of contact conductance for contacts between Al sheets that vary by a factor of 4 depending on surface roughness, for the same alloys and with all other conditions held constant. Given the variation in contact pressure and surface properties during the course of a single weld, it is not thought possible to make an a priori estimate of the contact conductances during FSSW. However, it is possible to estimate the mean conductances from instrumented welds, by comparing FE models using a range of values for the contact conductance to experimental measurements.

A study was conducted to examine the influence of contact conductance. Conductance values were varied at each interface in turn, and temperature histories at selected points were examined. The power profile and distribution used were those found in Section 4.7.2. As might be expected, this study found that the temperatures away from the tool were more sensitive to the conductance to the backing plate, while those nearer the tool were more sensitive to the heat input. Calculations were performed varying each interface by a factor of 10 from 10 to $10^{10} \text{ W m}^{-2} \text{ K}^{-1}$; the extreme values are essentially indistinguishable from no heat transfer and perfect contact respectively. Time-varying conductance was an additional complication that was not considered.

The optimum values were those that gave the closest match between predictions and measured data. These were found to be 10^6 for the conductance under the tool and 10^3 elsewhere. The calculations are shown in Figures 4.20 and 4.21, along with the experimental results. As more energy was lost to the surrounding clamping arrangements with higher conductance values, the total energy had to be increased to keep the peak temperature predictions for the central node in line with experimental values. The total power had to be increased by 6% when using the best-match conductances, as compared to $100 \text{ W m}^{-2} \text{ K}^{-1}$. Fortunately, the value of conductance required under the tool is so high as to approximate perfect conductance. This is useful, since

it makes the temperature outputs much less dependent on the details of the contact than was first thought. However, temperatures remain sensitive to conductance values outside the direct contact patch.

These calculations were done in 3D so as to properly account for edge effects; a similar study was carried out by Parker (2011) using a 2D model, for the same welds presented here. This study found that the contact conductances that best matched the experimental data were $10^5 \text{ W m}^{-2} \text{ K}^{-1}$ under the tool and $10^3 \text{ W m}^{-2} \text{ K}^{-1}$ elsewhere. For the high conductance patch under the tool, even though the values used differ substantially between the 2D and 3D cases (by a factor of 10), they are both sufficiently high as to be almost perfectly conductive, and it is difficult to differentiate accurately between such high values.

These values, even the low values for poor contact, are substantially higher than those used in most of the literature on seam FSW. Seam FSW tends not to use such high clamping forces near the tool as were used in these experiments (seam welds are usually done without any top clamp arrangement at all), and contact conductance is strongly dependant on pressure, so this is the likely source of this difference.

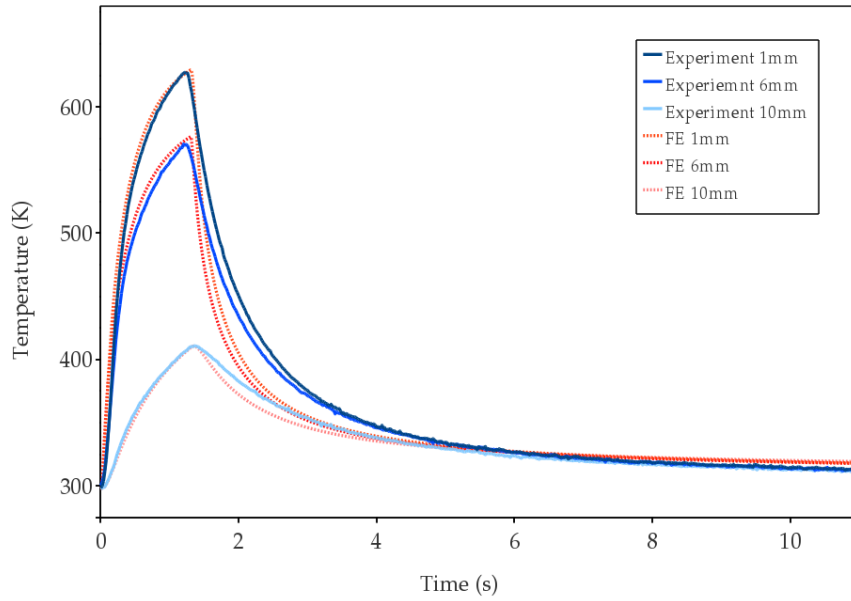


Figure 4.20: Comparison of predicted temperature histories with experimental measurements for a 1 s weld, with adjusted contact conductance values

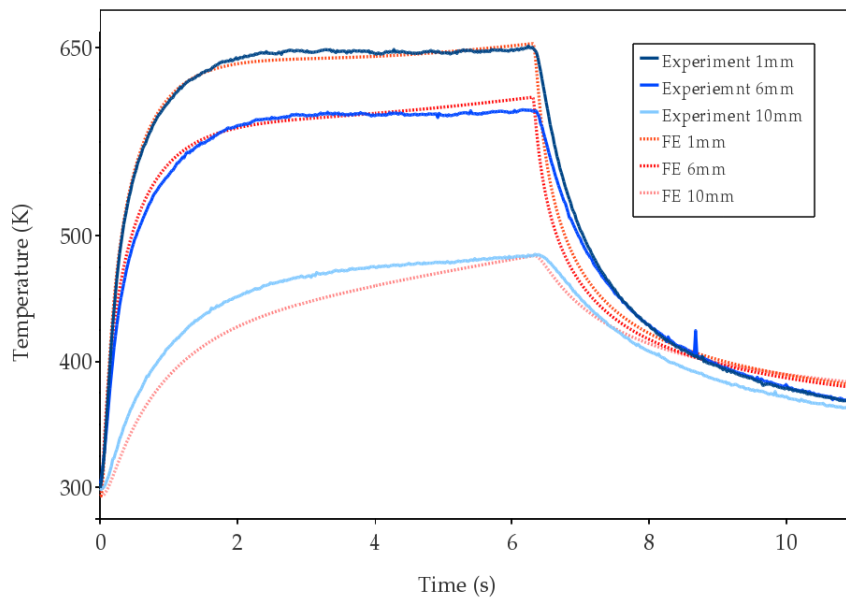


Figure 4.21: Comparison of temperature histories for model and experiment for a 6 s weld, with adjusted contact conductance values

4.8 Plunge depth effects

The typical weld profile for these spot welds is a relatively fast plunge and then a comparatively long dwell, and early thermal modelling work assumed that the tool arrived quickly at the target plunge and remained there for the dwell time; this was modelled by placing the tool at the final plunge depth for the whole duration of the weld. However, the work in Section 3.7 shows that this is not the case, as the actual plunge depth is often less than the target. It is likely that the plunge depth continues to increase during the whole weld, i.e. the tool continues to descend. In addition to this, some of the experimental work was conducted at a much deeper plunge in order to bring the tool closer to the weld interface (this was required in some cases to produce a strong joint, such as short-duration welds between aluminium and steel). As a consequence, further modelling was carried out (in Abaqus) to examine the influence of the plunge depth. Although the actual plunge depth cannot be controlled or predicted accurately, it can at least be measured with reasonable confidence during welding. In order to reduce complexity the tool does not move in the thermal model; tool locations that broadly corresponded to a small, medium and large overall plunge were chosen to provide upper and lower limit estimates of the peak temperature profile.

Three Abaqus models with plunge depths of 200, 400 and 600 μm were chosen, with otherwise identical parameters of heat input, weld duration (0.5 s) and thermal contact conditions between each part. The change in geometry required changes to the mesh. The mesh for the case of a 600 μm plunge is shown in Figure 4.22. Flash height was adjusted to conserve the volume of material in the workpiece. While some of the flash is expelled from the weld zone, this is a comparatively small quantity. In any case, this is hot material which is being expelled at some stage during the weld, so it is more realistic to keep such material in the model than to ignore it entirely.

Figure 4.23 shows predicted temperatures at the joint interface, for a radial line extending from 0 to 5 mm from the weld centre. The temperature histories at the 5 mm location are very similar. However, the difference at the 2.5 mm thermocouple position, of around 70 K, is significant and would correspond to a large change in the reaction rate and intermetallic layer thickness.

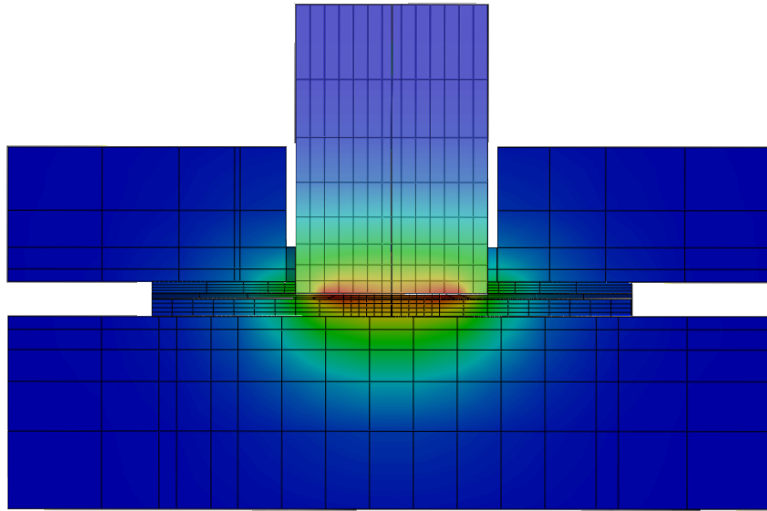


Figure 4.22: Image of a deep plunge weld model; the colours correspond to the peak temperature reached

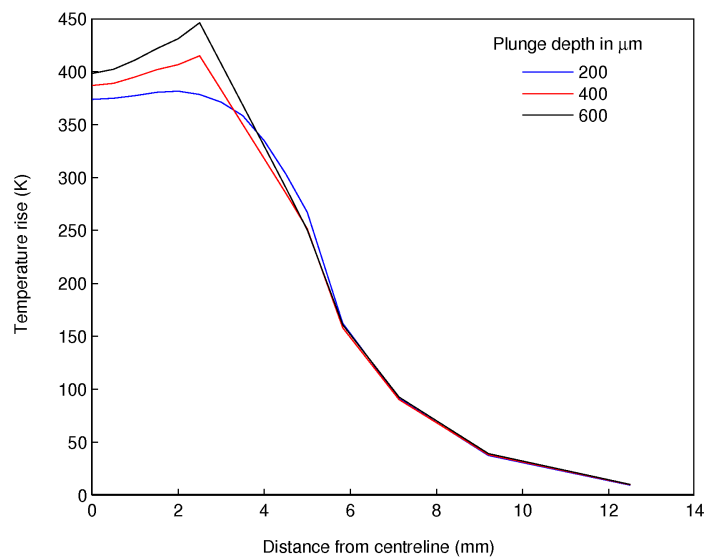


Figure 4.23: Peak temperatures reached at the interface, for various plunge depths

4.9 Model to experiment comparison

Experimental validation was conducted using a separate series of experiments to those used for model calibration. These models used the values found previously: a peak in the power distribution at $0.7R_S$, total power input parameters of 1200 W, 0.45 and 2.3 s, and the contact conductances found in Section 4.7.3. This validation was performed on a number of different welds. Firstly, it was performed on a 2 s weld made in the lab at Manchester. This weld used the same machine as the earlier 1 s and 6 s calibrations, the same speed (2000 rev/min) and the same nominal plunge (0.2 mm). An important difference with this weld is the location of the thermocouples, which were at 2, 5 and 10 mm from the weld centre at the top of the backing plate (as opposed to 1, 6 and 10 mm from the centre with the thermocouples in contact with the bottom of the workpiece, which were the locations used in the previous comparison). The calculation is presented alongside experimental thermocouple data in Figure 4.24. This figure shows a very good correspondence between the calculation and the measured data for most of the weld, with only a slight divergence visible during the cooling phase. That the model can predict these temperatures with such a high degree of accuracy, indicates that the values found earlier for the adjustable parameters are sufficiently accurate.

Following this, a series of experiments were carried out at TWI for the same nominal conditions. The machine used here is much larger and potentially stiffer, so it is possible that some factors — particularly the actual plunge — differ somewhat from the welds made at Manchester. However, a good test of the model is to see if it can accurately model welds with a range of different parameters. These experiments were all instrumented at 0, 4 and 8 mm from the weld centre. Figures 4.25 and 4.26 show comparisons between FE simulations and the TWI experiments for a range of welding times. More extensive comparisons covering a range of welding parameters are presented in Jędrasiak et al. (2012) and Jędrasiak (2012). As well as variations in welding speed and plunge, these two papers also cover Al to Fe welds. The model as presented here has been shown to predict temperatures in experimental welds with good accuracy.

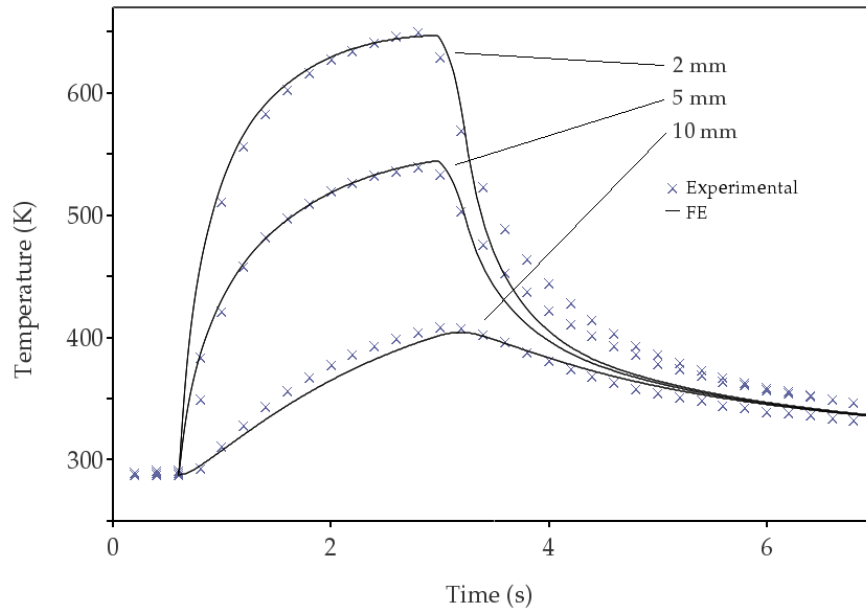


Figure 4.24: Comparison between model and experimental temperature histories for a 2 s weld, with thermocouples at 2, 5 and 10 mm from the weld centre

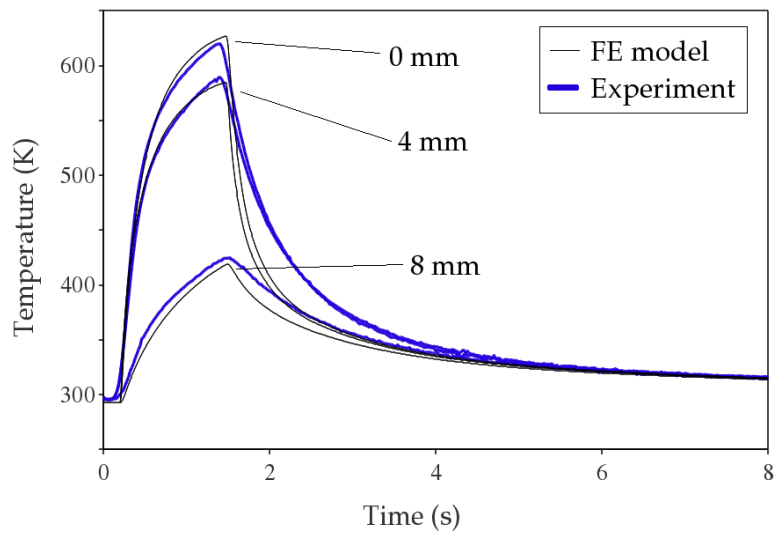
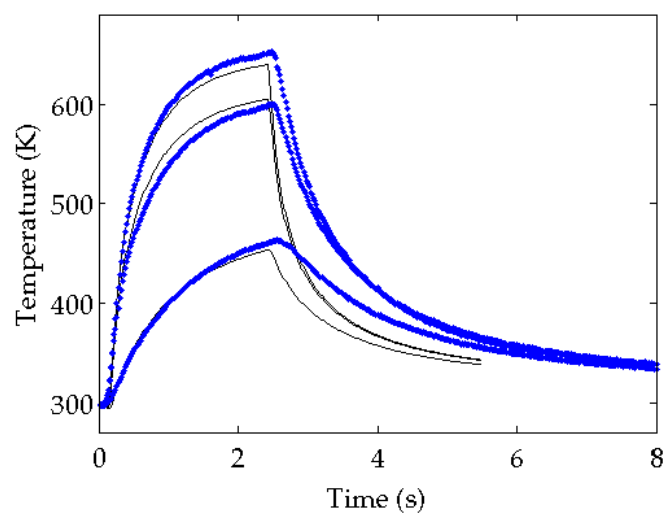
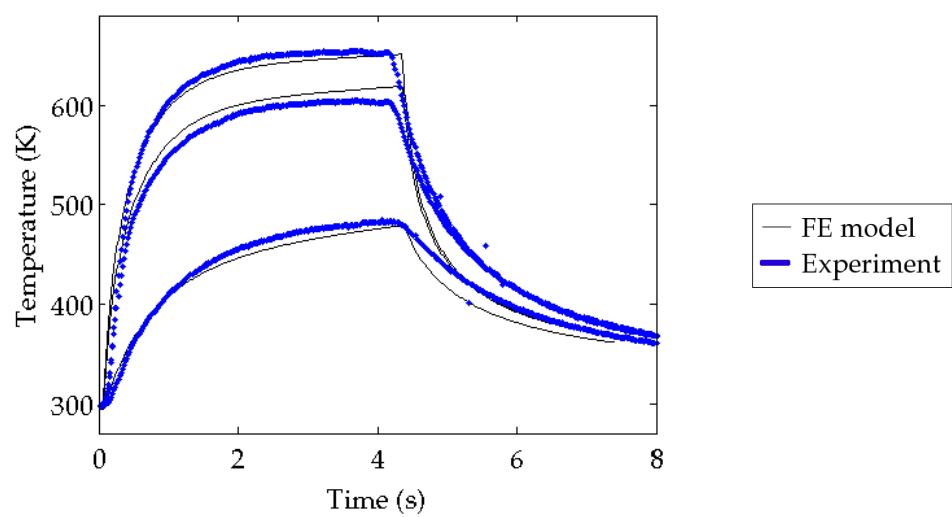


Figure 4.25: Temperature histories for model and experiment, in a 1 s weld made at TWI (thermocouple locations as indicated)

2 s dwell



4 s dwell



6 s dwell

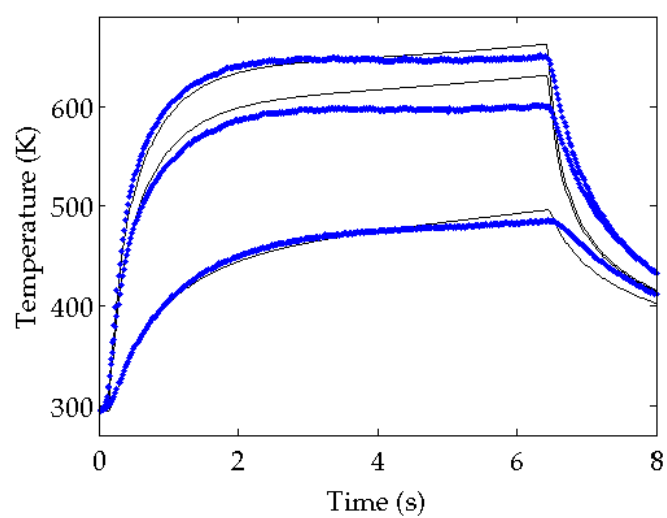


Figure 4.26: Comparisons between FE calculations and experimental results, for thermocouples at the base of the backing plate at 0, 4 and 8 mm.

4.10 Optimum welding conditions

An area where modelling can be of great use is in a parametric study to examine the influence of varying welding parameters. Although a programme of experimental work could be devised to cover a range of values for each parameter, it is expensive to conduct experimental trials without any sense of the likely impact on the outcome of each possible combination of parameters.

4.10.1 A process window for FSSW

A process window can be defined for all welding parameters in terms of their effects on the peak interface temperature. This can describe how one parameter can be varied in order to compensate for a change in another – for example, how the speed could be altered to compensate for a reduction in welding time, in order to maintain the same joint strength. From a purely thermal perspective, the variables of importance are input power and dwell time. The variation of input power with rotation speed and downforce is examined in depth in Chapter 6; for the present discussion, all welding parameters apart from dwell time will be lumped together and represented by altering the power.

The assumption made here, examined in detail in Chapters 5 and 6, is that a certain minimum temperature must be reached at the weld interface. This minimum temperature must allow the metal to soften sufficiently so that deformation can break up the oxide layers at the interface.

As discussed in Chapter 2, the HAZ is usually the weakest point of the weld. Bjorneklett et al. (1999) summarised the loss of strength in the HAZ in precipitate-hardened Al: ‘Particle dissolution is the main factor contributing to strength loss during welding. At the same time, growth of the remaining particles occurs during cooling, leading to solute depletion within the aluminium matrix. This, in turn, reduces the precipitation potential and contributes to the development of a permanent soft zone within the partly reverted region after prolonged room-temperature aging’. This loss of strength is particularly severe in 6XXX-T6 alloys due to reversion of the β'' precipitates.

Both the size of the HAZ and the loss of strength within it can be minimised by minimising the energy input to the weld. However, a certain minimum temperature must be reached in order for a joint to form at all. Peak temperature greatly influences microstructural changes, and as discussed in Chapter 2 has more of an effect than variation in the hold time at temperature. Consequently, the production of optimum-strength welds relies on reaching a certain minimum temperature in the nugget, while keeping temperatures in the HAZ below a maximum. This description is supported by strength-testing results presented in Chapter 3, where it was shown that maxima exist for the variation of joint failure load with welding time, or rotation speed.

Peak temperatures at the weld interface can be predicted from the calibrated model. (It is very difficult to measure peak temperatures at the interface as thermocouples placed here are usually destroyed by the welding process.) Peak temperatures are shown in Figure 4.27 for five different cases. Considering only the Al to Al welds in this figure, hotter (i.e. longer) welds are associated with lower failure loads.

Thermal conditions in the nugget and HAZ were characterised by the temperatures T_1 and T_2 respectively. These were the peak temperatures at two locations: the centre of the weld (T_1), and 5 mm from the centre (T_2), located 0.9 mm above the backing plate (i.e. at the joint interface). Comparing temperatures at these locations with strength data for the same welds suggests that the temperatures that give rise to a high-strength joint are $T_1 > 670$ K and $T_2 < 605$ K. This allows weld modelling to take place to examine the combinations of power input and dwell time that could give rise to optimum welds.

Simulations were run covering a range of welding times, and the peak power was adjusted in each case by a trial and error process until $T_1 = 670$ K. For this series of calculations, the workpieces both had the properties of AA6111 and the plunge was kept constant at 0.2 mm. The power profiles and distributions were otherwise kept constant. The resulting combinations of peak power and dwell time that give rise to a peak temperature of 670 K at the weld centre are shown in Figure 4.28. This indicates the minimum

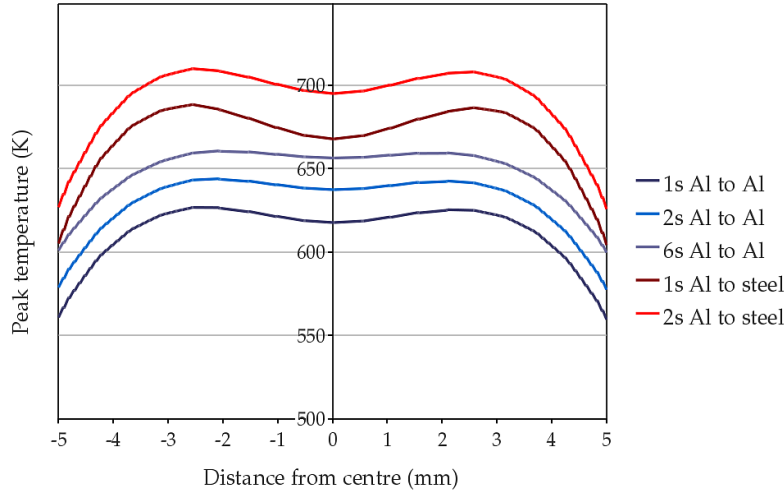


Figure 4.27: Peak temperatures at the interface, selected welding conditions

power required at each dwell time to produce sufficient softening at the weld centre.

The same process was carried out looking at the 5 mm location instead of the weld centre, and combination of dwell time and peak power such that $T_2 = 605$ K are shown in Figure 4.29. This gives the maximum power possible at each dwell time without causing overheating.

These boundaries can be used to define the edge of a process window for optimum welds: the combination of power and dwell time must be such that peak temperatures satisfy $T_1 > 670$ K and $T_2 < 605$ K. These limits are plotted in Figure 4.30. From this figure, the optimum power required for a certain dwell time can be found. Not only does the power required increase as dwell time decreases, but the process window becomes larger — i.e. the range of power that will produce a joint without causing overheating in the HAZ increases. The converse is also true, to the extent that beyond approximately 2.4 s optimum welds are no longer possible: a sufficient energy input to soften the deformation zone will cause excessive overheating in the HAZ.

These results match well with experimental data, in which dwell times need to be at least 1 s to form welds, and at longer times the weld strength falls. There is a very sharp increase in the required power for welds of less

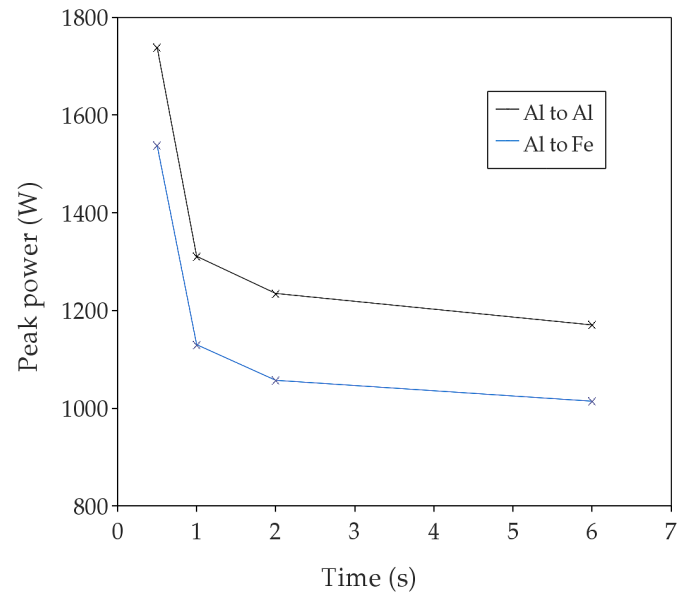


Figure 4.28: Combinations of peak power and dwell time for equivalent temperatures at the weld centre

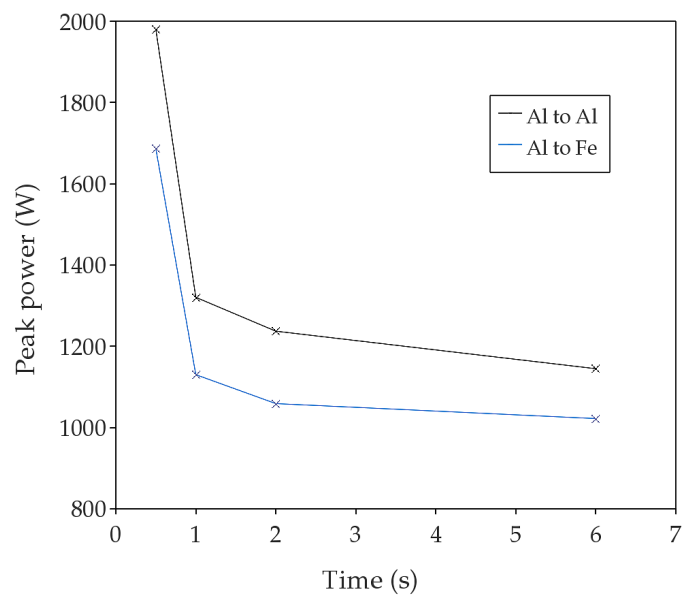


Figure 4.29: Combinations of peak power and dwell time for equivalent temperatures 5 mm from the weld centre

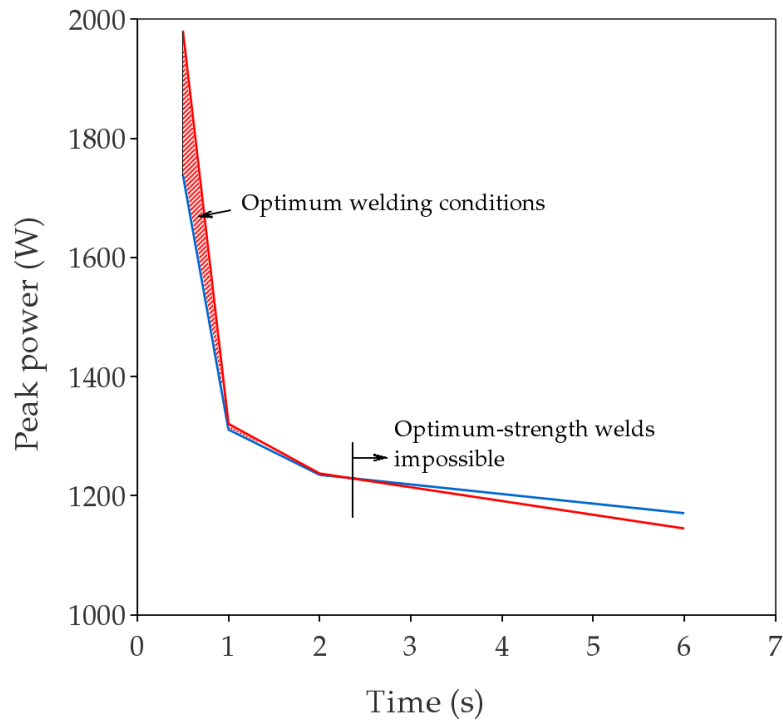


Figure 4.30: Processing window for optimum strength welds (Al to Al).
The blue line indicates the minimum power required to satisfy $T_1 > 670$ K, and the red line indicates the maximum power permissible to satisfy $T_2 < 605$ K.

than 1 s duration, a power that cannot be applied even at very high rotation speeds (see Figure 3.7), or at least, it is impractical to generate such a power using currently-available equipment. At times longer than 2 s, there is very little change in the peak power required — the weld has almost reached a steady-state, and the bulk of any additional energy supplied is lost to the anvil and surroundings.

This analysis suggests that the strength of Al to steel welds could also be improved by reducing the energy input. However, the process window in dissimilar welds is much narrower, owing to the lower conductivity of steel. Further study could refine the exact values of T_1 and T_2 needed to produce optimum welds in various materials. This would not need to be done through FSSW: with extensions to the deformation models in Chapters 5 and 6, it may be possible to define these temperatures based purely on the softening and aging characteristics of the particular alloys being welded, with reference to kinetic models of their microstructures. However, that is beyond the scope of this present study, for which it is sufficient to define T_1 and T_2 by reference to experimental FSSW data.

4.10.2 Alternative backing plate materials

Various backing plate materials have been used in experiments in the literature, but the approach seems to have been scattered, with no systematic studies reported. Complicated setups involving heated plates, or plates with cooling pipes, have been used, and their effects on weld strength and quality reported, but no attempt to understand the mechanisms involved is discussed.

A study is presented here which modelled an otherwise identical weld with four different backing plates. These were made from steel, alumina, copper, and a theoretical material with zero conductivity. Except in the last case, the contact conductivity was not altered, and the previous values found by Parker (2011) and Jędrasiak (2012) for contact conductance were used. The perfect insulator was modelled by removing the backing plate from the model. The top clamp and tool were kept the same in each case, with the properties of steel, as given previously. (The thermal properties of all materials are given in Table 4.1.)

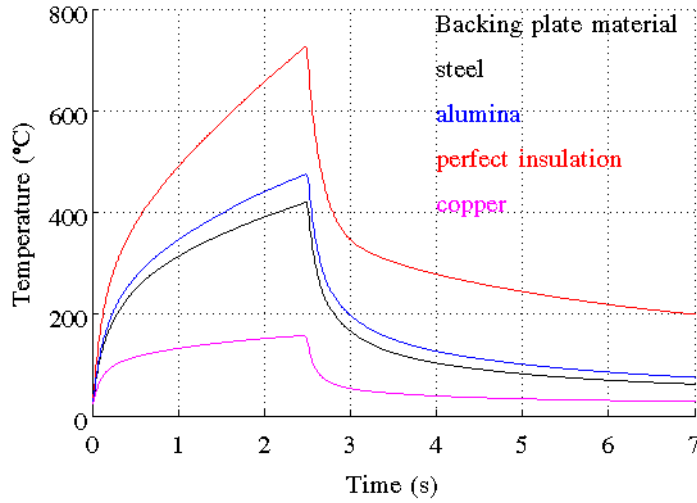


Figure 4.31: Temperatures histories at the weld interface, for 4 different backing plate materials

Temperature histories for each of these cases are shown in Figure 4.31. The difference between the peak temperatures reached in the steel and alumina cases is smaller than may be expected from looking just at their relative conductivities; this is because, as noted, FSSW is a highly transient process and so heat flow is dominated by the diffusivity rather than the conductivity. The perfect insulator creates a higher temperature rise, but perhaps of more note is the copper case: the peak temperature reached in this model is only 429 K, barely enough to produce softening in the workpieces. These results are more extreme than could be achieved experimentally, as the model does not take into account the feedback loop — in experiments, the power would drop off in the case of an insulator as the temperature approached the solidus, and in the copper case the power would be much higher (assuming the tool could grip the workpiece and force it to deform in the same manner).

Strength tests on welds made with a homogeneous steel and a Macor-coated steel backing plate were presented in Chapter 3. In these results, the use of the ceramic coating produced lower-strength welds in most cases.

High-diffusivity backing plates reduce T_2 compared to T_1 , all other parameters being equal; consequently, this increases the parameter space (in

terms of power input and dwell time) that can give rise to optimum welds. To test this in quantitative terms, analysis from Section 4.10.1 was repeated, with $T_1 = 670$ K and $T_2 = 605$ K, but with a copper instead of steel anvil.

Based on the same assumptions as in Section 4.10.1, the range of optimum welding conditions using a copper backing plate is shown in Figure 4.32. This shows that the viable processing window is much larger than with a steel anvil. A drawback of using a backing plate with higher diffusivity is that doing so reduces the proportion of energy retained in the weld. Hence, the input power and the total energy input increase dramatically. This has a number of drawbacks, but it appears to be an unavoidable trade-off.

A surprising result is noticeable in Figure 4.32: not only is the range of power that gives rise to optimum welds increased, but it continues to increase as the welding time is increased. This is in contrast to using a steel backing plate, when there is a time (estimated as about 2.4 s) beyond which optimum welds are impossible with any power input. This situation arises due to the significantly greater thermal diffusivity of Cu as compared to Al: it is possible, with a Cu anvil, to set up steady-state conditions with the weld centre at 670 K and the temperature at the 5 mm location below 605 K. ('Possible' meaning, in this context, there is a solution to the equations of heat transfer that makes the above statements true, not that it can necessarily be achieved with actual welding equipment.)

This is useful; although it may not be precise enough to make exact predictions of the optimum parameters, it indicates where experiments should be focussed within the overall parameter space. One possible drawback was noted above: with a copper backing plate, the power required increases. Furthermore, as shown in Figure 4.33, although the process window covers a wider range of powers at longer times, longer welds also increase the total energy required. Figure 4.33 shows contours of constant weld energy. This places a limit on dwell times that will be practical, in addition to production considerations. Nevertheless, high-diffusivity backing plates could be a subject for productive future research.

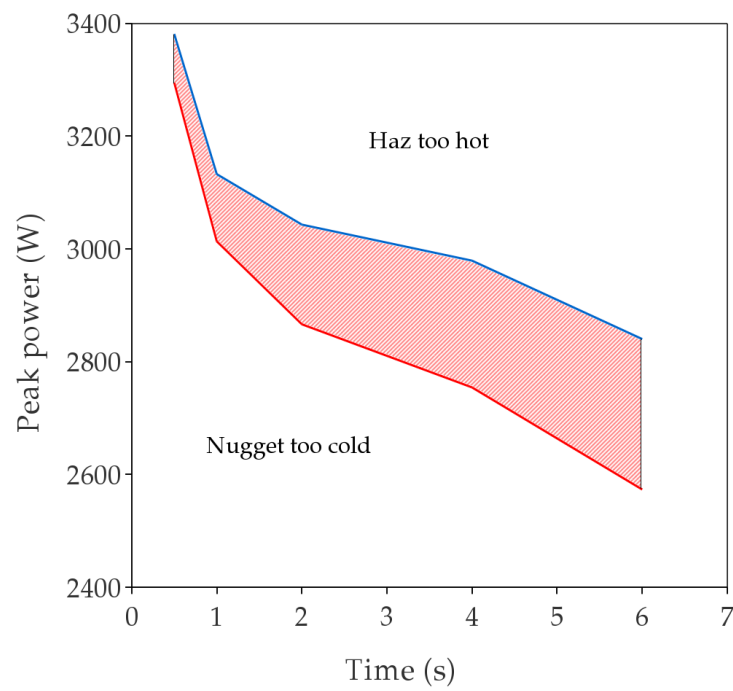


Figure 4.32: Process window for optimum welding, with a copper backing plate

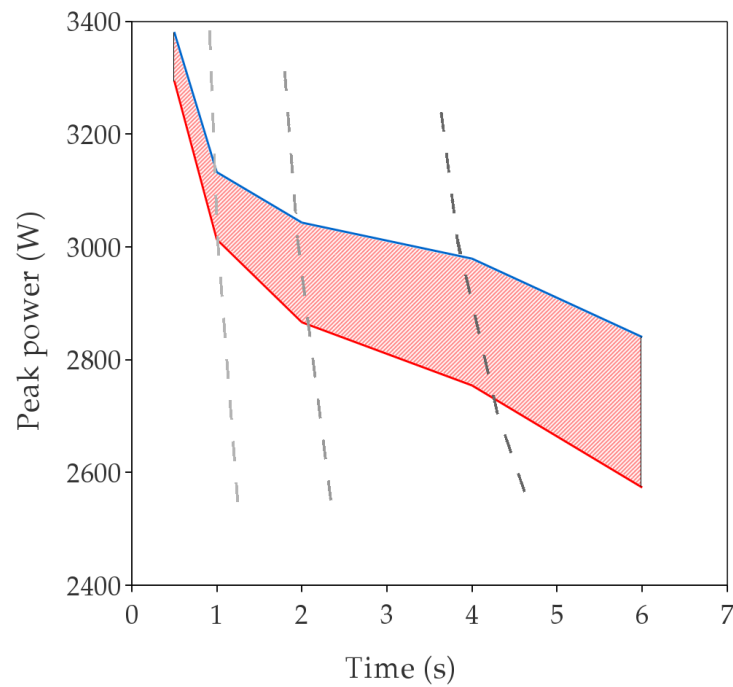


Figure 4.33: Process window for welding with a copper backing plate, showing contours of constant weld energy at 3, 6 and 12 kJ.

Chapter 5

Kinematic model

Friction stir spot welding is a flow process involving heating and deformation. This chapter is primarily concerned with the flow aspect, which has few similarities with flow in other processes. Kinematically, FSSW is a highly constrained process, especially when used with thin sheet workpieces. Although there is intense deformation in the nugget, there is solid, undeforming material only a short distance outside the tool shoulder radius, and the tool and backing plate remain solid and elastic (and therefore essentially undeformed, by comparison with the plastic strains involved). These kinematic constraints mean that the flow, despite its complexity, can be adequately described by a relatively small number of parameters. As a consequence of the boundary constraints, the flow is predominantly cylindrical, i.e. tangential to the tool radius at any point. However, patterns evident in the deformation zone after welding are not simply uniform layers as might be naïvely expected under these flow conditions. Imaging studies, such as those carried out by Bakavos et al. (2011) using dissimilar alloys show features referred to as hooking and dishing that are commonly taken to be a result of vertical and radial flow during welding. This present work shows that tangential flow alone can give rise to many of these features, and they cannot necessarily be taken as signs of more complex flow patterns.

Even with the presence of asymmetric tool features (seen, for example, in the MX Triflute tool) the flow constraints are comparatively simple, and

a great deal of the complexity in the process arises from the constitutive behaviour of the material. Earlier flow models have relied on computationally intensive CFD or FE simulations; however, by making some simplifying assumptions about the material properties a simple deformation model can be developed based on the kinematic constraints imposed on the flow. In particular, by constraining the material to only flow tangentially at any point, a kinematic model can still reproduce many of the post-weld features previously thought to be indicative of more complex flow behaviour.

This approach allows investigation of the contact conditions at the tool-to-workpiece interface, and the influence this has throughout the weld. The degree of slip is closely linked to the flow pattern and heat generation; these parameters are used as an input into many thermal models, however at present such models rely on fitting parameters, such as a correlation between the torque and the heat input determined from reference welds (see, for instance, Khandkar et al., 2003, who summarise a number of similar approaches). Obviously, this approach has substantial limitations, not least of which is the fact that so many parameters may be adjusted in opposition to each other. For example, in Chapter 4 increasing both contact conductance and power input had similar effects on weld temperatures, requiring multiple thermocouple measurements from a number of welds to identify accurate values for both parameters. In general, fully-coupled FE models are also unable to model the slip, as the friction coefficient depends strongly on many factors that are not usually incorporated into such models, and which can be impossible to measure during welding, such as surface finish and roughness. The simplified approach presented in this chapter is a novel approach to weld modelling, and provides many insights into the behaviour of FSSW.

5.1 Model development

As FSSW is so highly constrained, there is a fairly narrow range of possible flow patterns that satisfy continuity. As the process takes place in thin sheet material, the steel tool and backing plate constrain the bulk of the flow to be predominantly in-plane. The shoulder diameter to sheet thickness ratio is typically of order 5, so radial flow is constrained by friction against the tool and backing plate. The tool and backing plate are made of much harder and stiffer material than the workpiece and the stresses within these components remain elastic, so these boundaries may be treated as entirely non-deforming for large-strain analyses. Additionally, there is non-deforming parent material only a short distance outside the shoulder radius, which strongly influences the flow pattern. The process is axisymmetric (at least for the case of a flat shoulder). The angular velocity at any point on the interface can be conveniently described by the degree of slip at that point (this applies to both the tool–workpiece interface, and the workpiece–backing plate interface). For the top interface, a convenient measure of slip is the speed of the workpiece surface as a fraction of the tool speed at the same radius; for the bottom interface, the speed itself is the appropriate measure of slip (as the backing plate is static). In the case of full sticking at the tool–workpiece interface, $v = \omega \times r$ at any point; however, at some radius R_s (close in value to the tool shoulder radius) the velocity must fall to zero. Hence, there must be a transition region between a sticking region and the periphery, giving a region of slip, where the tool moves faster than the workpiece it is in contact with. A kinematic model was developed in Matlab to visualise the flow based on these constraints using greatly simplified constitutive behaviour.

Firstly, by assuming uniform strength in the material, a torque applied to a cylinder gives rise to uniform twist and shear strain along its length. Consequently, the position of any point after a certain twist is applied to the top surface is a function purely of its initial position and the twist angle. The model presented here takes the kinematic equations of motion for each point in an initial point cloud, and tracks the position of each point throughout the course of a weld. If, for example, the point cloud specifies points that

initially lie in a single plane, the position of these points at a later time shows where that plane has moved to. The relationship between the whole weld, the nugget, and the tracked plane is shown graphically in Figure 5.1 for a butt weld configuration. In a butt weld, the two colours in this figure represent the two different workpieces, and each coloured plane in later figures represents the advancing front of that workpiece. In a lap weld, the same flow pattern occurs, though it is not seen in experimental weld sections as there is no physical joint to see in the vertical plane.

The output from the model is a graphical representation of the final positions of the points being modelled. In the first and simplest case, a uniform angular velocity is imposed on the top surface of the stir zone. The bottom sheet is stuck to the backing plate, and the outer boundary of the nugget is allowed to slip freely. The series of images shown in Figure 5.2 represents two alloys being joined in a butt weld configuration. Each image shows the position of the interface between the two alloys as welding time increases. In these views, each colour represents the advancing front of one workpiece, i.e., the region behind the red surface and in front of the blue is filled by the red workpiece.

The model need not be restricted to modelling points in a plane, but may also model points filling the whole stir zone (or any arbitrary region desired). If a ‘solid’ point cloud (i.e. a cloud of points evenly distributed throughout the stir zone) is used, then the resulting graphical output may be sliced either horizontally or vertically to produce top-down or section views. Examples of these views, for the same velocity profile, are shown in Figures 5.3 and 5.4.

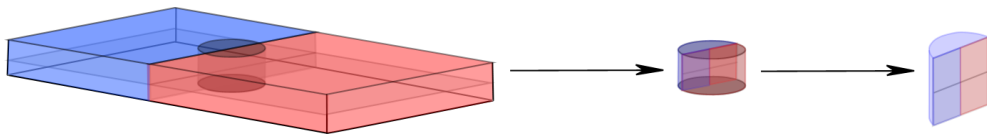


Figure 5.1: Expanded 3D view of the kinematic model, showing a schematic of the whole workpiece, the weld stir zone, and a cut-away view of the stir zone

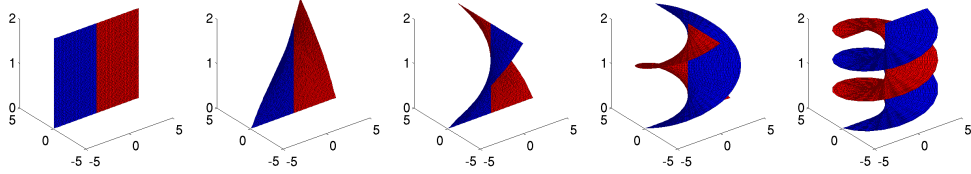


Figure 5.2: Open corkscrew series, isometric view for $0, \frac{1}{6}, \frac{1}{4}, \frac{3}{4}$ and 1.5 rotations (dimensions in mm)

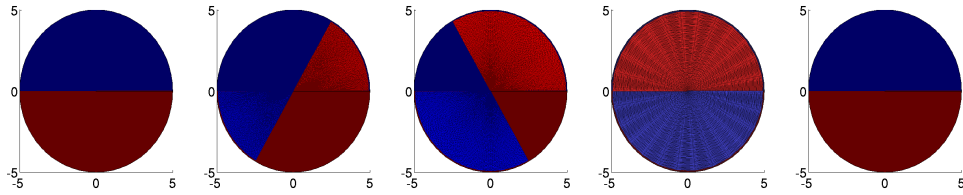


Figure 5.3: Open corkscrew series, top-down view, for $0, \frac{1}{6}, \frac{1}{4}, 2.5$ and 10 rotations; the top down view is indistinguishable from rigid-body rotation for this case, and is shown here only for completeness (dimensions in mm)

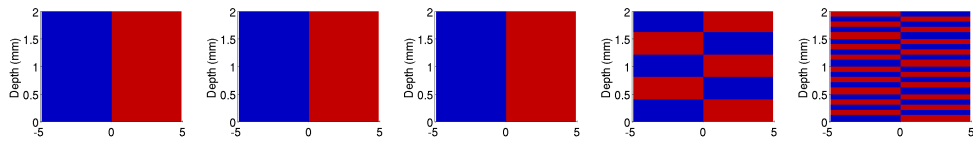


Figure 5.4: Open corkscrew series, section view, showing layering (for $0, \frac{1}{6}, \frac{1}{4}, 2.5$ and 10 rotations)

5.2 Tool contact boundary condition

The model presented in the preceding section serves to outline the concept of the model, but it is not an accurate representation of reality. In particular, it does not satisfy continuity. The boundary conditions that must be satisfied, for all welding conditions, are:

- a fixed boundary at some radius (this is R_S at the surface, but the fixed boundary need not be vertical);
- a boundary at the interface between the workpiece and tool that may be fully stuck, fully slipping, or partially slipping at any point, as a function of radius;
- a boundary condition between the workpiece and backing plate similar to that between the workpiece and tool.

The previous model imposed a velocity of $v = \omega \times r$ across the whole surface of the stir zone, out to $r = R_S$. In conjunction with the condition $v = 0$ at $r > R_S$ this gives rise to a discontinuity at $r = R_S$. A step change in strain within a solid body is a crack; as cracks are not generally observed at this position in real welds, the assumed boundary conditions cannot be correct.

To remedy this, the top surface boundary condition was altered to reduce to zero velocity at the edge of the tool shoulder (R_S). Three new profiles for the top surface velocity were modelled, shown in Figure 5.5. These all satisfy continuity, and so are more realistic than the open corkscrew case. The first of these profiles has $v = \omega \times r$ for $\frac{r}{R_S} < 0.9$, with v then falling back linearly to zero at $r = R_S$. This is not thought of as a particularly realistic profile, but is a sort of ‘minimum required’ case, in that it is probably the simplest case that satisfies the continuity requirements (other than the trivial $v = 0$ everywhere case). The point outside which the workpiece is no longer in sticking contact with the tool is labelled r_1 .

The second and third profiles were created based on FE modelling work described in Chapters 4 and 6. The reasoning set out here describes why they were chosen for investigation. It is not intended to show that these

slip profiles are necessarily realistic — this justification comes later, via the accurate predictions they produce. Extensive empirical calibration work carried out by Jędrasiak et al. (2012) looked at the detailed effect of varying the heat input location on the peak temperatures reached at various virtual thermocouple points. This work was all carried out as a finite element study (in the same manner as described in Chapter 4); in particular, it looked at the influence of surface and volumetric heating. Previous work by Russell (2000) made some simple slip surface estimates of the relative proportions of power contributed due to deformation around the pin and shoulder in seam FSW. Jędrasiak et al. found that a heat input with a peak at $r = 0.7R_S$ was able to provide the most accurate prediction of temperature data across a range of welding conditions. Based on this work, and previous work by Colegrove & Shercliff (2006) and Colegrove et al. (2007), two other velocity profiles were developed: the first simply sets the point of inflection, or point of maximum velocity, r_2 , in the velocity profile to be 0.7 (this is profile 2); the second relies on a knowledge of the stress under the tool (developed with the aid of an FE deformation model described in Chapter 6) to estimate the slip condition required to give rise to the thermal profile found by Jędrasiak *et al.* This third profile introduces a change in gradient, i.e. a change in the rate of slip increase with radius. This point is labelled r_1 , and is set to $0.5 R_S$.

All three top surface boundary conditions can all be described by a single piecewise equation shown in Table 5.1. The innermost zone is a region of no slip, and in the middle and outermost zones the slip velocity varies linearly with radius.

Because of the flow pattern produced by these profiles, the isometric view is not such a useful output (see Figure 5.6: the interface has a vertical component which hides the inner zone of greatest interest). The top-down

Region	Slip velocity (relative velocity between tool and workpiece)
$r < r_1$	$v' = 0$
$r_1 < r < r_2$	$v' \propto (r - r_1)$
$r > r_2$	$v' \propto (r - r_1) + \left(\frac{r - r_2}{R_S - r_2} \right)$

Table 5.1: Top surface slip velocity

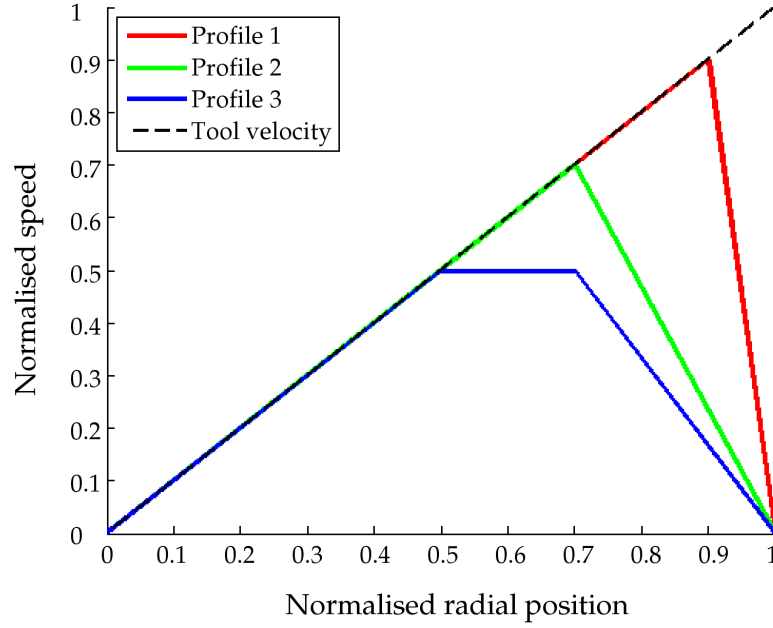


Figure 5.5: Velocity profiles applied to the top surface of the stir zone

and section views are much more informative, and so these are the only views that will be presented further; these views have the additional advantage that they can be easily compared with experimental metallographic sections.

A series of top-down and section views showing the differences between the velocity profiles in Figure 5.5 is shown in Figures 5.7 and 5.8. From the top-down views the effect of decreasing r_2 can be clearly seen: this profile leads to a weld with wider spirals and a smaller central region (the region of no slip). Decreasing r_1 below the value of r_2 leads to a still smaller region of no slip, and a slight change in the shape of the spirals.

The differences are more apparent in the section views. While all of the profiles give rise to broadly similar forms — interlocking layers of the two alloys — increasing the size of the slip zone produces more rounded, bowl-shaped layer boundaries, rather than the hard-cornered layers seen with velocity profile 1. In terms of the local shear strain experienced by the material, profile 1 leads to a much more concentrated shear zone, with very intense deformation in the region where $r > r_2$.

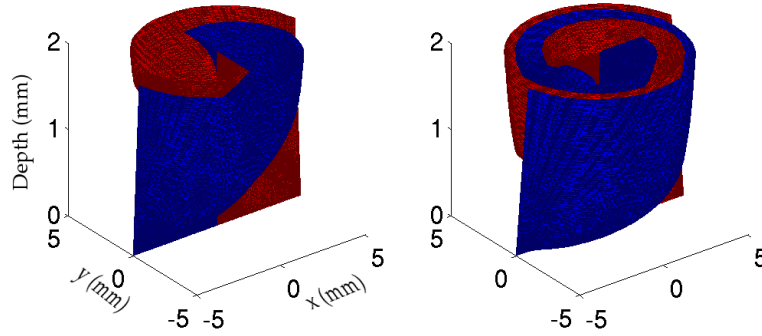


Figure 5.6: Isometric view for 0.75 and 1.5 rotations, with top surface velocity profile 1; compare with the figures in 5.2 and note that now most of the weld is hidden by the outer ring.

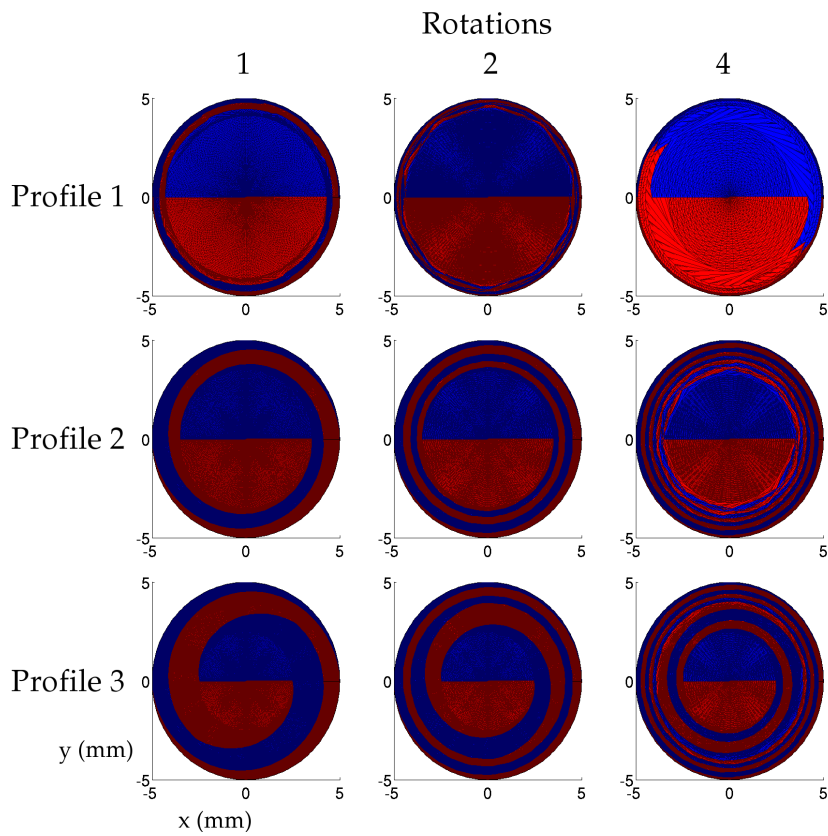


Figure 5.7: Velocity profiles 1 to 3 at 1, 2 and 4 rotations — top-down view

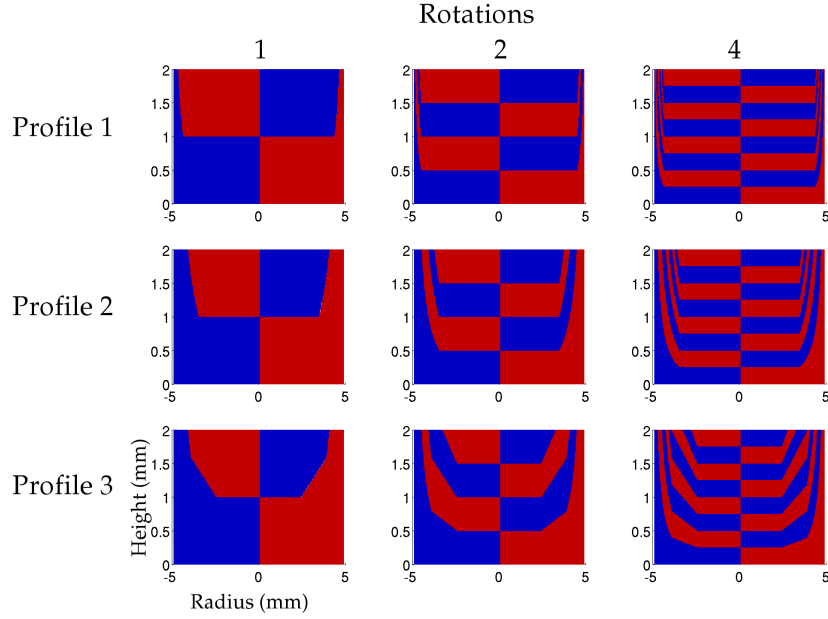


Figure 5.8: Velocity profiles 1 to 3 at 1, 2 and 4 rotations — section view

5.3 Through-thickness heat flow

Initially, the model represents an autogenous weld with uniform material flow properties that are independent of time and position. The physical interpretation of this is that there is no allowance for temperature dependent properties, or alternatively, that the material is all at a uniform temperature for the whole duration of the weld. These two statements are equivalent, and the result of assuming either is that temperature effects do not affect the flow of material. The feedback loop between temperature and deformation is a critical mechanism in FSSW and an understanding of this interaction is a major goal of modelling. Hence, a model that does not capture these effects can only capture a limited part of the behaviour of interest.

A refinement of the model is presented here that can account, in a reduced fashion, for through-thickness heat flow. Radial heat flow is not modelled here (see Section 2.3.4 for an explanation of why this is valid, and the conditions under which it is appropriate; in summary, the parameter space in which FSSW mostly operates is one of 1D heat flow in the nugget).

The feedback loop is incorporated into the present model by changing the constitutive behaviour and making a simplifying assumption about the heat flow. The constitutive law adopted is a simple rigid–perfectly plastic model where the rigid–plastic transition is purely dependant on temperature. The heat flow is assumed to be 1D in the through-thickness direction, from the tool to the backing plate. This is similar to the conditions applicable to the bottom right of Grong’s condition map (Figure 2.9), i.e. a thin workpiece made from high strength, high conductivity material. (Note that the condition map shown in that figure does not correspond exactly to the FSSW process, as there is no translation in FSSW. The heat flow is dominated by flow downwards from the top surface, where the workpiece is in contact with the tool.) The effect of introducing this constitutive behaviour and vertical heat flow, is that at time $t = 0$ all deformation is restricted to a thin layer at the top of the workpiece; the rest of the weld material remains rigid. As welding progresses, the deforming zone spreads through the thickness, capturing the effect of material softening as heat diffuses through the workpiece. This is modelled by assuming a linear increase in deformation depth with time.

Although the number of layers does not alter when this material behaviour is assumed, the relative thickness of each layer depends on the relationship between heat flow and rotation speed. This is characterised by a dimensionless group labelled here as $\bar{\omega}$: alternatively interpreted, this is the time taken for sufficient heat to reach the bottom of the workpiece to allow it to deform, compared to the time taken for one rotation of the tool. The rate of heat flow is governed by the weld material’s thermal properties, specifically, the diffusivity; the rotation speed is a welding parameter. The ‘speed of propagation of heat’, v_h , is found from the rise time of the temperature at a distance x from a heat source, as a solution to the error function. An order-of-magnitude estimate of this rise time is given by $t = \frac{x^2}{a}$. This allows the welding parameters to be linked to the material properties through the use of $\bar{\omega}$ and v_H , as in Equation 5.3. The parameter $\bar{\omega}$ is then the ratio of the maximum linear tool speed (i.e. the speed at the edge of the shoulder) to the mean speed of propagation of heat through the workpiece (v_H). This

propagation speed is assumed to be constant, so the onset of deformation progresses linearly through the workpiece until the influence of the tool reaches the bottom of the workpiece and the whole stir zone starts deforming. Although a non-linear function could easily be introduced into the model, there is at present no information about how it may evolve with time, so a linear function is assumed as the simplest case.

In the model, v_h is a kinematic parameter that is specified directly, but the use of $\bar{\omega}$ allows it to be linked to real welding conditions. A more accurate estimate of v_H could be obtained from, for example, an FE model of the heat flow, which could be used to improve the accuracy of the kinematic model, and in such a case it may become appropriate to consider a time-varying v_H .

$$\bar{\omega} = \frac{\omega h}{v_H} \quad (\text{by definition}) \quad (5.1)$$

$$v_H \sim \frac{a}{h} \quad (\text{from } x = \sqrt{at}) \quad (5.2)$$

$$\therefore \bar{\omega} \sim \frac{\omega h^2}{a} \quad (5.3)$$

(In this equation, h is the workpiece thickness, a is the thermal diffusivity and v_H is a characteristic heat propagation speed, or thermal diffusion velocity, defined as $v_H = \frac{h}{t_1}$ where t_1 is the time between the onset of heating and the temperature rise at the far surface of the workpiece.)

A series of section views showing the effect of varying the $\bar{\omega}$ parameter is shown in Figure 5.9. The figure shows a series of stills at increasing times (corresponding to increasing numbers of tool rotations) from left-to-right and at increasing values of $\bar{\omega}$ from top-to-bottom. These are all shown for velocity profile 3 (Figure 5.5), as this is the best experimental match to the flow pattern (see Section 5.6). The top row is the result of models run with $\bar{\omega} = 0$; this is the same as seen in Figure 5.8. As $\bar{\omega}$ is increased, the layers become increasingly concentrated, and also thinner. While those of $\bar{\omega} = 0$ and $\bar{\omega} = 30$ appear very similar for times after $t = 0.5$ s, in the bottom row (where $\bar{\omega} = 300$) deformation has not reached the bottom of the sheet even after 20 rotations. Qualitatively, the effects are clear: increasing the heat flow time, analogous to modelling a material with a lower thermal diffusivity,

compresses the layers into the upper region of the workpiece. Importantly, the number of layers remains the same — this is a characteristic of each weld that is independent of a .

The calculation of $\bar{\omega}$ for a dissimilar workpiece combination is slightly more complicated due to the non-linear variation in mean heat propagation speed with h . For two layers, let h_1 , h_2 , t_1 and t_2 be the thicknesses and characteristic heat flow times of each layer. In that case, v_h is given by Equation 5.5 and $\bar{\omega}$ for the whole weld is given by Equation 5.6.

$$v_h = \frac{h_1 + h_2}{t_1 + t_2} \quad (5.4)$$

$$\therefore v_h \sim \frac{h_1 + h_2}{\frac{h_1^2}{a_1} + \frac{h_2^2}{a_2} + \frac{2h_1h_2}{a_2}} \quad (5.5)$$

$$\therefore \bar{\omega} \sim \omega \times \left(\frac{h_1^2}{a_1} + \frac{h_2^2}{a_2} + \frac{2h_1h_2}{a_2} \right) \quad (5.6)$$

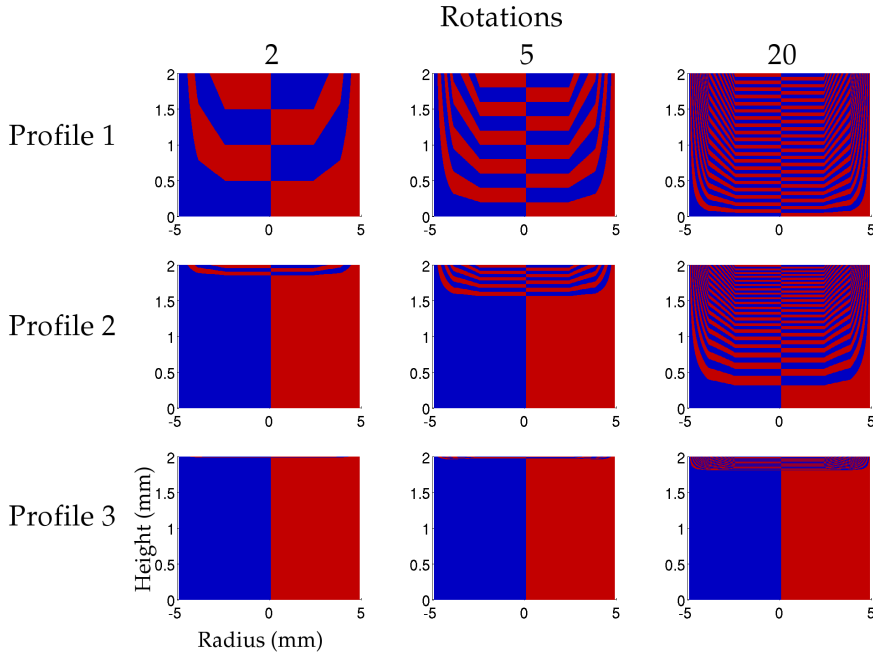


Figure 5.9: Section views showing the changes in layering caused by varying $\bar{\omega}$ ($\bar{\omega}$ values of 0, 30 and 300 for 2, 5 and 20 rotations)

5.4 Dissimilar joining: aluminium to steel

All the analysis so far has been conducted for butt welds between identical workpieces, or alloys with very similar strengths (as in the case of AA6111 and 6082). There is no change in the flow pattern between a butt weld and a lap weld between two Al sheets — the layering pattern continues through both the top and bottom sheets, showing that sticking friction conditions exist at the interface between the two sheets almost immediately, and continue throughout the weld. This has been shown experimentally with ‘dual-lap’ or ‘semi-lap/semi-butt’ welds, i.e. with three sheets forming a butt joint over the top of a lap joint (or with four workpieces forming a ‘double-butt’ joint as in Figure 5.10).

However, as discussed in Chapter 1, one of the key benefits of FSSW over other welding processes is its ability to easily join dissimilar metal combinations, therefore extending the model to handle these cases is important. A case of particular interest is joining Al and Fe. In a lap weld configuration, this combination can be welded either ‘classically’, i.e. with the Al sheet on top, or inverted, with the Fe on top. Only classical welds will be considered in this section. Owing to the strength difference between Al alloys and steels — which becomes more pronounced at elevated temperatures — most deformation during dissimilar welding takes place in the Al workpiece (see e.g. Chen & Lin, 2010). In section views of these welds the layering pattern ceases at the Al to Fe interface. As a first approximation, therefore, the previous kinematic model can be run assuming that all the deformation takes place in the top sheet.

In the present work, welds with AA6111 to both uncoated and galvanised low-carbon steel sheets are considered. The presence of the zinc layer has a significant effect on the flow pattern.

5.4.1 Welding Al to uncoated steel

In the case of a weld between Al and Fe, the strength difference at temperature is so marked that the Fe does not deform plastically, at least in bulk. Micrographs indicate that the oxide layer is broken up, and the intermetallic

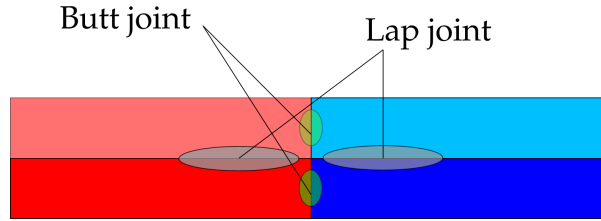


Figure 5.10: Illustrative figure of a ‘double-butt’ weld

layer between the two workpieces shows that the temperature rise is sufficient to cause significant reaction and diffusion. However, for the purpose of modelling the bulk material, these welds can be modelled by assuming that all the deformation takes place in the Al layer. In the case of a plain DC04 steel sheet for the lower workpiece, the hypothesis is that friction at the interworkpiece interface is sufficient to prevent movement of the base of the upper layer. In this case, the section views look the same as for Al to Al welds, except the deformation is confined to the top sheet, and hence the layers are one half as thick — in Figure 5.11, compare the bottom row of images to the top row. Apart from the interface and the fact that the bottom sheet is non-deforming, the boundary conditions are the same in the two cases.

Figure 5.11 is for $\bar{\omega} = 0$. However, the earlier discussion concerning $\bar{\omega}$ still applies. Essentially, the Fe sheet plays no part in the deformation, and the flow is confined to the upper (Al) sheet. The flow patterns look similar to Al to Al cases, but squashed. This is as expected: the materials and forces involved in the contact between the Al and Fe sheets are the same as for a contact between an Al sheet and the backing plate, so the friction and slip velocity will also be similar. The only differences are due to the hotter interface in the case of a steel workpiece (since the distance from the tool is less), the surface finish, and differences due to a difference in alloy between the workpiece and the backing plate (both are mild steel in the experiments conducted in this project; greater differences may be expected with high alloy steels). This similarity was even more apparent when conducting deliberately over-hot welds; in a few experimental cases joining Al to Al the workpieces were inadvertently welded to the backing plate.

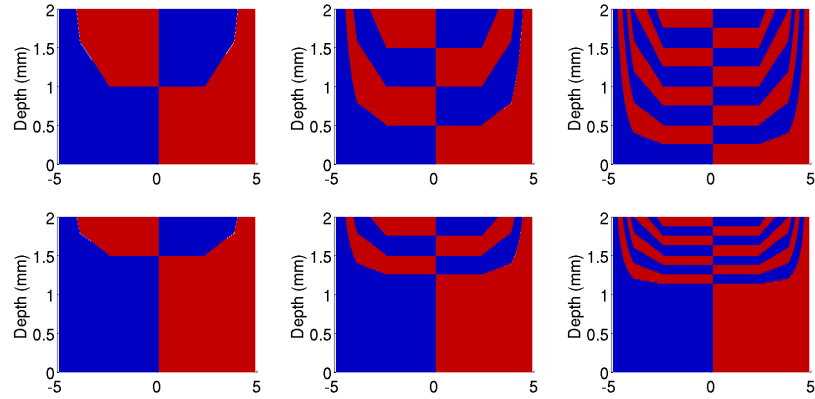


Figure 5.11: Section views showing a model of a 4-sheet double-butt weld, in AA6111 aluminium to itself (upper series) and on top of DC04 steel (lower series) for 1, 2 and 4 rotations

5.4.2 Welding Al to galvanized steel

Galvanized steel is widely used for its corrosion resistance, which makes it an obvious choice in combination with Al for parts in corrosive environments. Welding experiments have been tried using both hot-dip galvanized and zinc electrocoated steels as the bottom workpiece; these two processes both produce a zinc coating with an Fe/Zn intermetallic layer between the parent material and the bulk of the Zn, although the hot dip process produces a much thicker zinc layer. These welds are qualitatively different from those with ungalvanized steel, since the zinc softens and melts, forming a lubricating layer at the joint surface. This is an exception to the general rule that FSSW is a solid state process, and the situation arises because the melting point of Zn is lower than that of the Al. Because of this, further heat generation can take place in the top sheet even after the zinc layer has reached its solidus and experienced the loss of strength that this entails.

A modification to the kinematic model extends it and makes it suitable for modelling these welds. This is studied by reference to Al and Zn welding, but is also applicable for other situations where a layer (or the bottom sheet) has a lower solidus temperature than the upper sheet; the same situation can arise, for example, when welding Al to Fe in the ‘inverted’ case, i.e. with Fe as the upper worksheet (Chen, 2010 and Chen & Lin, 2010).

As a limiting case, a molten layer can be modelled by relaxing the constraint at the bottom of the upper (Al) sheet entirely. This gives rise to the section views shown in Figure 5.12. In this case, the only restraint to motion is the contact between the nugget and the surrounding material in the top workpiece, and the joint line deforms but remains vertical, as seen in the figure. This is representative of an entirely lubricated layer between the two workpieces throughout welding. However, a galvanised workpiece will provide some restraint — the Zn will provide a measurable friction contact between the two sheets until it reaches its solidus. This can be modelled more realistically by allowing a sticking frictional contact between the two layers until some time, then releasing the contact after that to simulate melting of the interface.

This is done in the Figure 5.13, which shows images from simulated welds at a speed of 84 rad s^{-1} . The two section views in this figure are taken after 20 rotations of the model. The image on the left shows the result of full sticking at the interface, simulating plain steel on the lower sheet; as discussed in the previous section, this looks very similar to the case of a weld between two Al sheets, but with the layers confined to the top sheet. Again, for this weld $\bar{\omega} = 0$.

The image on the right of Figure 5.13 shows the effect of a zinc layer between the upper and lower sheets; the layer provides sticking friction until it reaches its solidus, then no resistance to sliding. For this simulation, the zinc melting time was set (somewhat arbitrarily) to 0.4 s after the start of the weld. The change in contact condition at this interface creates a discontinuity

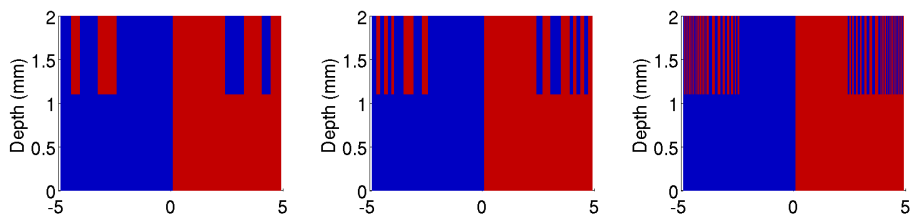


Figure 5.12: Section views showing a lubricating layer between the two sheets (2, 5 and 20 rotations)

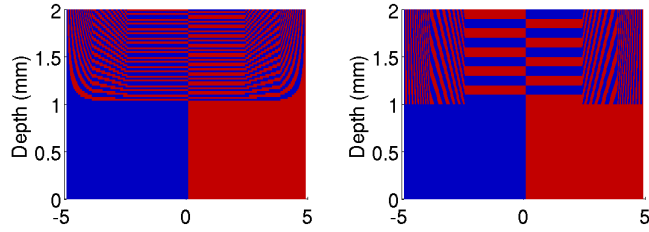


Figure 5.13: Section views after 20 rotations for a zinc layer that melts after 0.4 s (at 84 rad s^{-1})

in the layering pattern when viewed in section. In Figure 5.13, it can be seen that the effect of the melting is to reduce the number of layers in the central portion of the nugget and increase the angle of the outer portion of the layers from horizontal. The horizontal layers form while the interface is a sticking contact, then once the zinc layer has melted the outer 50% of the stir zone experiences horizontal shearing, forming vertical bands, but superimposed on the pre-existing horizontally-layered structure. The central portion of the nugget undergoes a rigid body rotation once the base has melted.

5.5 Deep plunge welds

The previous analysis focussed on spot welds where the plunge is sufficiently shallow by comparison with the overall depth of the combined workpieces that the change in geometry can be ignored. While this is often true for aluminium welds, the search for stronger welds between Al and Fe has led to the production of welds with much deeper plunges. In a weld, this has two advantages: firstly, it increases the temperature at the joint, as the tool is brought closer to the interface. Secondly, it increases the shear strain gradient at the interface, which helps break up the oxide layer and encourage mixing. These two effects have to be balanced against the loss of strength that can be caused by joint thinning and overheating. Bringing the tool closer to the joint interface will clearly increase the local strain rate (although this is not mentioned in published literature); this is supported by the kinematic model, which shows higher strain rates at the base of the upper layer as the plunge depth increases.

From a modelling point of view, a number of simplifying assumptions can be made which allow the kinematic model to be adapted to model deep plunge welds. An unconstrained homogeneous cylinder under pure axial compression will deform outwards. The radial expansion Δr will be independent of z , since the stress state is purely a function of radius, and will depend only on the overall change in height. For a weld, the deforming zone is constrained by surrounding parent material. The only way the tool can plunge into the workpiece is by expelling material and forming flash on the top surface. The material most easily expelled is that near the surface, as lower material is more heavily constrained, much like a punch indentation problem. At the bottom interface, the workpiece is stuck to the backing plate and surrounded by cooler, stronger material, so a reasonable first approximation is to assume that the radial velocity scales linearly with height above the bottom surface. The volume of material expelled is found by volume conservation (as Poisson's ratio $\nu = 0.5$ for plastic deformation).

These boundary conditions will lead to the upper layers of the cylinder deforming outwards more than the lower. As a first approximation, this variation can be assumed to be linear, i.e. $\Delta r \propto z$, as in the series of graphics in Figure 5.14. In practice, the cold outer material prevents bulk radial expansion of the weld nugget, and instead the material expelled from this volume is forced upwards, forming flash. The ultimate effect of this is that the final weld nugget, in the post-weld state, is formed from material that originally occupied the shaded volume in Figure 5.15.

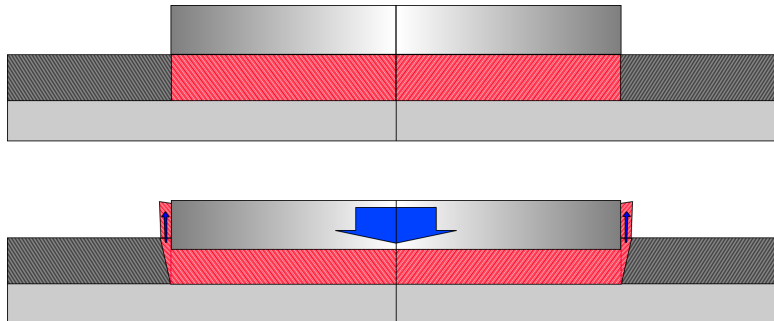


Figure 5.14: Assumed flash extrusion profile

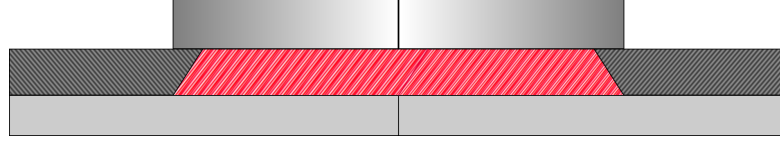


Figure 5.15: Weld nugget volume before a deep plunge weld: the shaded region represents the material that will make up the final volume of the nugget

Together with the original axisymmetric flow pattern, the assumption that the radial expansion is proportional to z is sufficient to specify the radial and vertical motion entirely: as the process is axisymmetric and the flow pattern is incompressible, then for any given plunge rate the radial velocity can only take one value to satisfy continuity. This value is given by Equation 5.7, which comes from equating the volume of the initial cylindrical volume under the tool and the final truncated cone that this material would occupy if the surrounding material did not force it upwards to form flash.

$$\frac{dr}{dt} = \left(\frac{r^2 (h_1 - h_2)}{h_2^3/3 + r_1 h_2^2} \right) \frac{dz}{dt} \quad (5.7)$$

Deep plunges can be incorporated into the kinematic model by imposing a radial and vertical velocity at each point. This is shown in Figure 5.16 for an Al to ungalvanized Fe weld. Within the final nugget volume, to a first approximation the deeper plunge has no effect beyond stretching the layers already formed; importantly, the number of layers will be the same regardless of the plunge depth. This is illustrated in Figure 5.16. At least with a flat tool, the essential flow features of a weld as observed in section are not significantly altered by increases in the plunge depth.

This proposed mechanism of flash formation could be tested empirically by measuring the volume of flash produced and comparing that to the volume ‘excavated’ by the tool during the plunge. However, practical limitations have so far prevented this. Comparison with the model provides a way to check: if the number and form of layers in a weld section agrees with the model output, then the flow pattern assumed in the model is very likely to be correct.

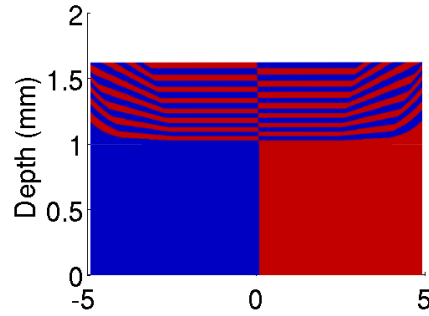


Figure 5.16: Section view through a deep plunge weld

5.6 Comparison with experiments

A number of weld coupons were used in flow visualisation experiments; these were etched according to the description given in Chapter 3. The configuration for these welds was that of a double lap joint, using AA6111 and AA6082 aluminium alloys in a butt weld configuration, over a sheet of DC04 steel. These two Al alloys have different appearances when etched, which allows the flow pattern to be observed both with through-thickness sections and intact views of the top surface of the finished weld. The tempers of the aluminium alloys were chosen to give the same room-temperature hardness value for each, ensuring that as far as possible their behaviour during the weld is similar. As a result the weld is essentially the same as a single lap weld with Al over Fe. The kinematic model treats both materials as identical.

A sample image from one of these welds (from Chen, 2010) is shown in Figure 5.17a. AA6111 contains a higher proportion of copper (typically 0.75% by weight compared to <0.1% for AA6082) and is a lighter colour when etched. The two alloys form distinct regions in the post-weld state, and the top-down view shows a clear spiral pattern. The alloys are not thoroughly mixed but form interlocking regions that are substantially one alloy or the other. (Diffusion between the two alloys can of course occur, but this is insignificant on this time and length scale.)

Figure 5.17b shows a model top view, from a simulation using velocity profile 3 (i.e. $r_1 = 0.5 R_S$ and $r_2 = 0.7 R_S$). By comparison with Figure 5.17a

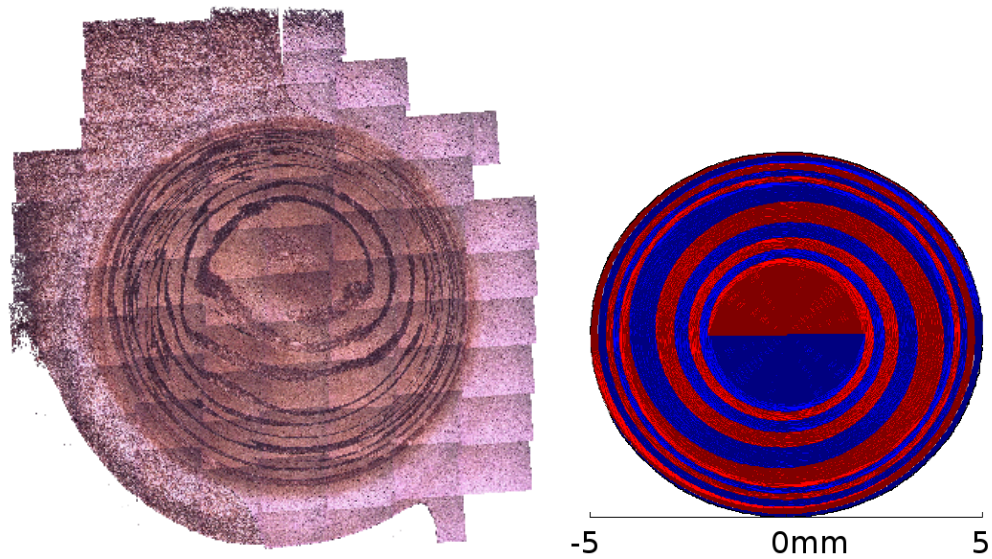


Figure 5.17: a (left): Top-down view of an experimental weld between AA6111 and 6082 over DC04, showing the top surface in the post-weld condition, and b (right): Top-down view of the kinematic model, run with velocity profile 3 for 10 rotations

it can be seen that the kinematic model produces results that are broadly in agreement, at least qualitatively, with experiment. Moreover, it is possible to use this model, in combination with weld metallography, to infer what contact condition must have existed between the tool and top workpiece during the weld.

Figure 5.18 shows the same top-down view of the experimental weld as Figure 5.17a, but with the central portion highlighted. The edge of the highlight indicates the boundary between a heavily-strained outer region and a much less deformed inner zone. The central region shows very little mixing; this is in accordance with the model (the fact that the centre of this region appears slightly offset from the centre of the contact patch could be due to a number of factors, most likely a slight difference in thickness between the two alloys forming the upper sheet). The diameter of this region is approximately 2.5 mm. The model predicts a region of comparatively little deformation out to a radius of r_1 — in this case, 2.5 mm. Consequently, it is possible to infer with a high degree of confidence that sticking conditions existed during the

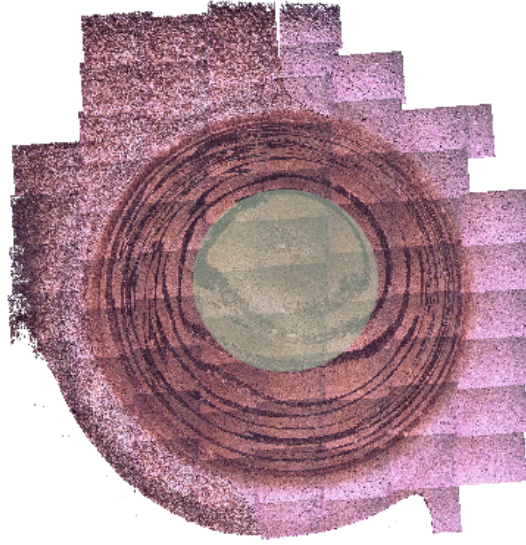


Figure 5.18: Top-down view of the experimental weld (as in Figure 5.17a) with the sticking region highlighted

experimental weld between the tool and the workpiece surface out to 2.5 mm.

The velocity profiles in Figure 5.5 were initially generated based on an analysis of the heat flow, and an assumption that the spatial distribution of heat input could relate to the slip condition. The consistency between the patterns in Figure 5.17 suggests that the velocity profile that applies is indeed close to profile 3. This is the first known work to provide a direct method of estimating the surface slip, and it is independent of any estimate (or measurement) of the local pressure or temperature. Furthermore, this lends support to the original assumption that the heat distribution correlates well with the surface strain-rate.

The effect of r_2 is harder to measure from these views, and no detailed conclusions can be drawn about the form of the slip profile outside 2.5 mm, beyond the recognition that the distance between each layer boundary on the surface reduces towards the outer radius. This suggests a surface velocity profile similar to profile 3 is correct, but the precision of this method is not adequate at this stage to say whether the slope beyond r_1 is linear or if it takes some other form.

In addition to the top-down views, similar welds with the same materials

and configuration were cut vertically to show a section view, etched in a similar manner to the top views. A sectioned view of an experimental weld interrupted after approximately 10 revolutions is shown in Figure 5.19. This image shows alternating layers of the two alloys in a very similar fashion to that predicted by the model. Again using surface velocity profile 3, a sectional view of the model after 10 tool revolutions is shown in Figure 5.20. In this image the model output figure is not stretched on a vertical axis as previous ones have been, but is displayed on an equal axis to facilitate comparison with the experimental figure.

There are lots of similarities between these two figures. The first key point to note is that the number of layers is either identical or almost identical in both cases; the second is that the shape of the layers matches reasonably closely. The kinematic model specifies tangential flow at all points; there is no radial or vertical flow in the model. The fact that these constraints can give rise to such similar features as those seen in experimental welds strongly suggests that the dominant flow in experimental welds is tangential. If there is any radial or vertical flow, this is not required to produce the features seen in real welds.

This comparison between model and experiment definitively fixes the surface slip condition. In the model, layers are produced by tool rotation, and the number of horizontal layers near the centre of the weld cannot be greater than twice the number of rotations plus one (it may be less, in the case of slipping at the base, and the total number of layers may be greater, in the case of melting of an interface coating, depending on the path along which layers are counted). The number of tool rotations in the experimental welds is known, and the number of layers is at or very close to the limit predicted by the model. This shows that a sticking contact exists almost



Figure 5.19: Section view through a weld between AA6111 and AA6082, showing layering

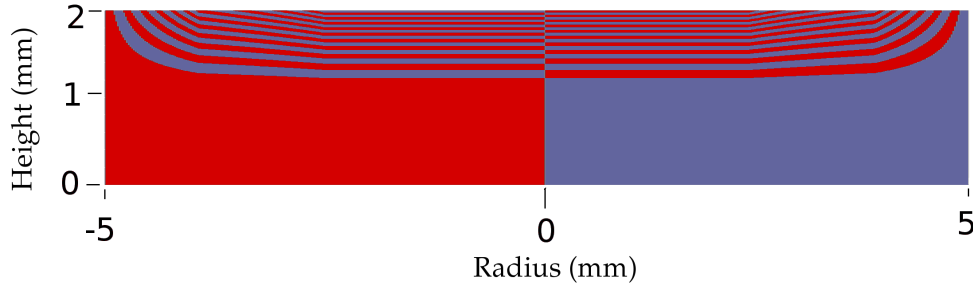


Figure 5.20: Expanded section view through the kinematic model showing bowl-shaped layers

immediately, and this is common regardless of the tool type or downforce. There is essentially no ‘pre-dwell’ phase where the workpiece is being heated purely by friction, but instead the tool grabs the surface as soon as contact is made (or at least, within less than one revolution). The progressive increase in the number of layers, and the thinning of existing layers as new layers are added, is also seen experimentally. Figure 5.21 shows section views for shallow-plunge welds after 0, 0.5 and 1 s of post-plunge dwell time (with a plunge of around 0.3 s). Although the resolution of these images is lower than of Figure 5.19, distinct layers can be seen in the lower portion of each weld. The number of layers within the dashed boxes increases from 0.5 to 1 s. The interface between the upper and lower sheets remains essentially horizontal.

This is an intriguing result, and one that would not necessarily be expected. Owing to compliance in the tool, machine and clamping arrangements, there is some vertical slack in the system, and the tool is approaching comparatively slowly (at 1.55 mm s^{-1} in the weld in Figure 5.19). Due to these factors, the downforce does not undergo a step change, but ramps up slowly as the tool continues to plunge (see Figure 2.10 and Section 3.7 for a fuller discussion of this effect). This suggests that even when cold, a Coulomb friction model would provide a poor match for the conditions prevailing at the tool–workpiece interface.

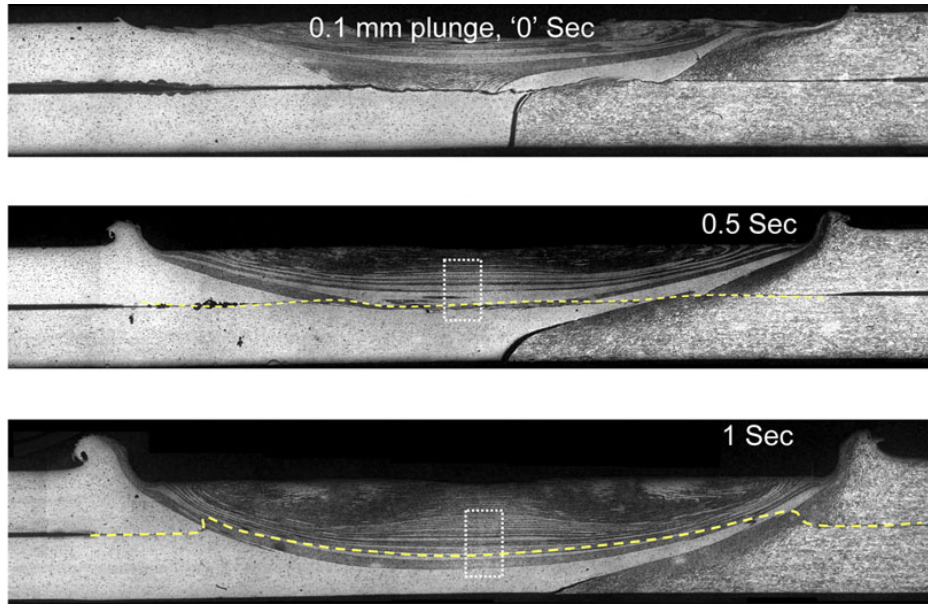


Figure 5.21: Section view showing the increase in the number of layers as determined experimentally (from Bakavos & Prangnell, 2009)

5.7 Variation in $\bar{\omega}$ for experimental welds

The value of $\bar{\omega}$ depends on a combination of welding parameters and material properties. Values of $\bar{\omega}$ for various welding conditions are shown in Table 5.2 (with $\bar{\omega}$ calculated according to Equation 5.3). The corresponding welds were either conducted as part of this project or reported by other authors, as noted.

From this table, it can be seen that, for practical welds, $\bar{\omega}$ generally lies between 30 and 50. This is an intriguing result, and indicates that there is a fundamental balance that must be found to produce good-quality welds. Work carried out for this project found that 84 rad/s was about the lower limit at which good-quality welds could be formed in 0.9 mm thick AA6111; below this speed, no joint formed at all, presumably because the rate of heat diffusion at this lower power was sufficient to cool the contact patch enough to prevent softening. Attempted welding at speeds below this produced fretting on the top surface, but the two sheets fell apart after the process was complete. At the highest rotation speeds attempted (up to 315

Workpiece material and welding conditions	$\bar{\omega}$	Data source
AA6111, 210 rad/s, 2 no. 1 mm thick workpieces, 5 mm radius tool	32	Present work
AZ31 (1.6 mm) to low-carbon steel (0.8 mm), 25 rad/s, 15 mm radius tool	43	Chen & Nakata (2009)
AA6061, 2 mm workpieces, 210 rad/s, 15 mm diameter tool	49	Awang et al. (2005)
1 no. 1 mm Al sheet on top of 1 no. 1 mm Mg sheet, 9.5 mm tool diameter, 108 rad/s	38	Choi et al. (2011)
1.3 mm thick PM2000 ODS steel, 63 rad/s, 12 mm diameter tool	34	Mathon et al. (2009)
6.3 mm thick AA6061, 210 rad/s, 4 mm diameter tool	40	Su et al. (2006 <i>a</i>)
Lower limit on rotation speed for forming welds (limiting criterion: sufficient heating) in AA6111 with 2 no. 0.9 mm thick workpieces and a 5 mm radius tool	13	Present work
Upper limit on rotation speed (criterion: avoid cracking), conditions as above	40	Present work

Table 5.2: Values of $\bar{\omega}$ for various reported welding conditions

rad/s) final welds were observed to be of poor quality, with excessive flash formation and visible defects on the weld surface. This model provides some insight into the reasons for this — it seems to indicate that the reason that higher speeds fail, is that at these speeds heat does not have time to diffuse down into the bulk of the material. As a result, deformation is concentrated in the upper portion of the workpiece, while the lower portion is comparatively undeformed.

5.8 Analysis of actual slip conditions during welds

As mentioned, the degree of slip between the workpiece and tool is of critical importance for the behaviour of FSSW. Analysis of the slip condition that exists during FSSW is a topic of debate in the literature, but there have been as yet no attempts to measure it directly (due in no small part to the difficulty inherent in doing so). Where an estimate is required, e.g. for a numerical calculation, friction is assumed to follow a law such as Coulomb friction, that is very well established for certain regimes, but for which the appropriate parameters are often not known (in particular, the pressure as a function of time and radius is not known with any accuracy, and is often assumed to be constant — this is an especially poor model, as discussed in Chapter 6). The kinematic model is especially useful in this regard, as the amount of slip may be inferred by comparing outputs from the model with experimental weld sections. This is something that is not possible with more complicated flow models such as numerical FE or CFD codes. (In FE models, the slip may be calculated rather than specified directly as an input, but in order to do this assumptions are still required regarding the friction law and values of parameters, e.g. the pressure, which are often not known with accuracy, under the conditions of strain rate and temperature applicable during FSSW.) As discussed in the preceding section, an estimate of the radius outside which slip occurs is comparatively easy with this model. An accurate measure of the slip outside r_1 is more difficult, but could in

principle be possible with appropriate image analysis techniques to measure the average thickness of each ring in the top-down view.

The other parameter that appears to be of great importance is the dimensionless group expressed here as $\bar{\omega}$. This relates the mean speed of heat propagation through the thickness of the weld to the maximum tangential velocity of the tool, and has been shown to take only a small range of values for all good-quality welds — the range of $\bar{\omega}$ is far smaller than the range in any of tool speed, tool diameter, material diffusivity or workpiece thickness.

An experimental definition of $\bar{\omega}$ would be the time taken for the base of the workpiece to soften sufficiently to deform, under the torque being applied by the tool at that velocity. An estimate of this experimental definition of $\bar{\omega}$ could be made from weld sections, from figures such as Figure 5.19). The kinematic model predicts a layer thickness which alters with time, and the rate of change of this thickness depends on $\bar{\omega}$. If the layer thickness can be measured accurately from image analysis, then the experimental value of $\bar{\omega}$ can be compared with that calculated in Equation 5.3, and the accuracy of the dimensionless group as a predictor of the value actually occurring can be calculated.

A more detailed study with higher-resolution experimental images could analyse the other tunable parameters in the model (e.g. to get a much more accurate assessment of r_1 and r_2 than is possible when estimating them by eye, and the variation of $\frac{\partial r}{\partial t}$ with z during the plunge) to estimate their values in a range of welding environments.

5.9 Tool features and hooking

If other tool types do produce vertical flow, then by conservation, they must also produce radial flow. It is likely that the causality of this is reversed — looking at the surface of the ‘wiper’ tool (in Figure 5.22), for example, it has features which can be easily imagined to produce some degree of radial flow, even if this is at a substantially lower speed than the tangential/circumferential flow. This radial flow would then produce vertical flow by the requirements of continuity (since the workpiece is essentially

incompressible). This is supported by images of welds showing hooking behaviour — this occurs more readily for tools with patterned shoulders than for flat tools. Figure 5.23 shows the existence of hooks in 3 welds made with profiled tools, while no hook is produced with a flat tool under identical conditions, showing that pins are not required to produce vertical flow. Unfortunately, radial and vertical flow does not have such simple kinematic constraints as purely circumferential flow, and this tool type requires a more complicated analysis. Analysis of these tool types is undertaken with a finite element model, described in Chapter 6.

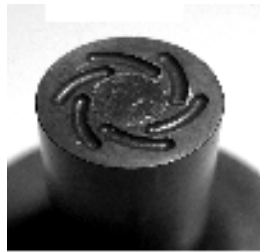


Figure 5.22: Surface view of the ‘wiper’ tool

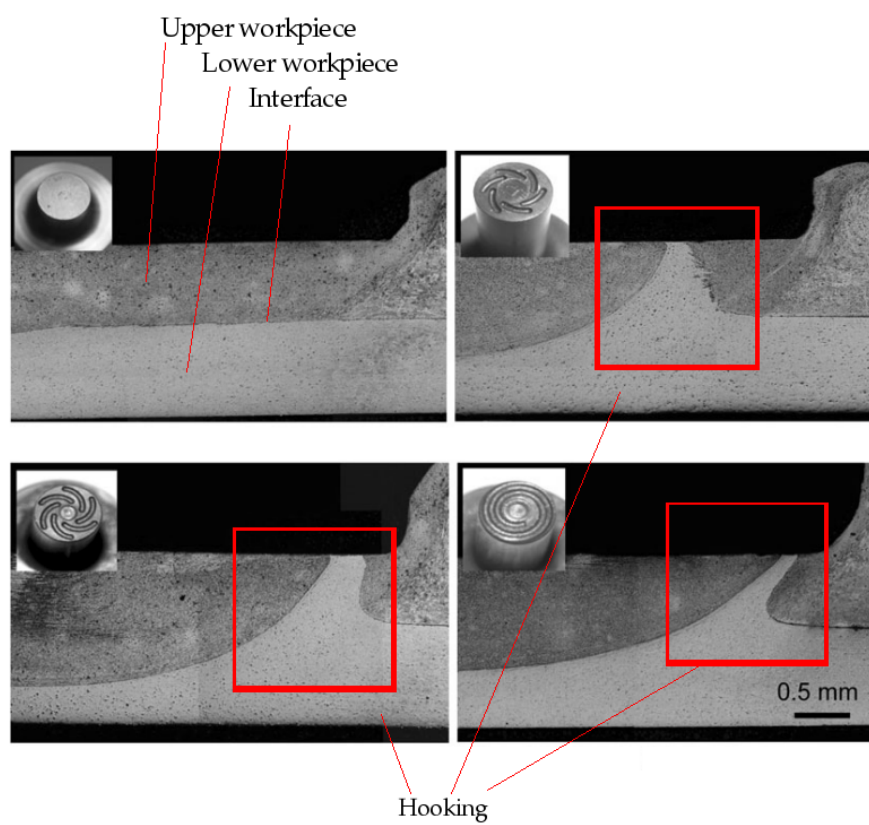


Figure 5.23: Hooking behaviour for 4 tool types under identical welding conditions

5.10 Conclusions

This model comprehensively proves that features seen in experimental welds, like the bowl-shaped layers in Figure 5.19, can be produced entirely by tangential flow at every point in the weld. No radial or vertical flow is required. The general assumption by authors in the field is that vertical flow is promoted by pin features, and that this enhances weld quality by producing patterns that add to the strength of a joint. As vertical flow is not required to produce the observed patterns, it is quite likely that tool features that promote vertical mixing do not strengthen joints in this manner at all. If true, this would explain the somewhat counter-intuitive observation that pinless tools (which, by their nature, can promote only very limited vertical flow) produce unexpectedly strong joints. It may be the case that tool features actually promote enhanced mixing by increasing the circumferential velocity deeper within the body of the weld, increasing the strain rate near the actual joint line.

Chapter 6

Sequential small-strain analysis

6.1 Introduction

The preceding chapters have presented models for the behaviour of metal during FSSW based on thermal and kinematic analyses. This leaves out one key aspect that is important to the process: those aspects of deformation and flow that depend on the material properties, rather than being governed exclusively by the kinematics. As summarised in Chapter 2, other authors have approached this problem by using fully-coupled FE models, but these are computationally intensive and sensitive to the boundary conditions chosen. The goal of the present work is to capture sufficient detail of the plastic flow to predict the heat generation and flow pattern, making the model as simple as possible while retaining accuracy.

To this end, a novel snapshot FE method has been developed, which takes account of the material model while affording a dramatic reduction in run-time as compared to fully-coupled models. The operation of this model is presented, along with more detailed predictions about the copper backing plate welds modelled in Chapter 4. Additionally, a conventional FE model of the plunge is presented; this latter is presented first, as the conclusions are useful when considering the snapshot model.

6.2 Static plunge modelling

In Section 3.7 the results of actual, measured final plunge depths were presented. Accurate plunge depths are most important with pinless tools and thin sheet, as the plunge depth can be a significant fraction of the sheet thickness (typically at least 10%, often as high as 50%). The highest values are typically used in an attempt to create defect-free joints between Al and Fe, in an attempt to heat and deform the interface while minimising overheating in the HAZ.

In addition to identifying the factors that govern the plunge depth, it is important to understand the interaction between plunge forces and in-plane deformation during FSSW. Unlike seam welding, FSSW cannot be considered as a steady-state process, and the stress state of the weld metal is strongly influenced by the downforce. An effort was made to understand the plunge further by modelling it using the finite element method, using the commercially available software package Abaqus.

The plunge modelling study covered the following work: firstly, it examined ways of representing the tool, and how this affects the model (for example, is the tool best modelled as a fixed displacement applied to the top surface of the weld, as a fixed pressure, or is it necessary to include a realistic tool, including its own deformation behaviour?). Secondly, it looked at the effect of a near boundary in the z direction (i.e. the influence of a backing plate, and workpiece thickness).

An initial FE model was developed to model the plunge as a forging process, with no rotation from the tool. As the deforming domain has an axis of symmetry, it is possible to use a 2D model; however, the elements must also be capable of deforming in the tangential direction (to allow for later calculations using the same model). The model consists of a 2D axisymmetric model, built in Abaqus using 2D elements capable of twist distortion (i.e. deformation about the central axis of symmetry). For the first calculations, the twist is constrained to be zero, so the model can only move radially and vertically.

Initially, the physical boundary conditions of the model were a symmetry boundary at the axis (i.e. no movement in the radial nor out-of-plane directions) and an encastre base and far-field boundary (set at twice the tool radius). The upper surface was entirely free to deform. For this stage of the model, the workpiece was represented by a single block of homogeneous material, with boundary conditions representing the backing plate and tool (the backing plate was modelled as a rigid boundary; various boundary conditions were used to represent the tool, which are discussed in following sections). The model geometry and restraints are shown in Figure 6.1, though the tool and backing plate were not included in all stages of the model.

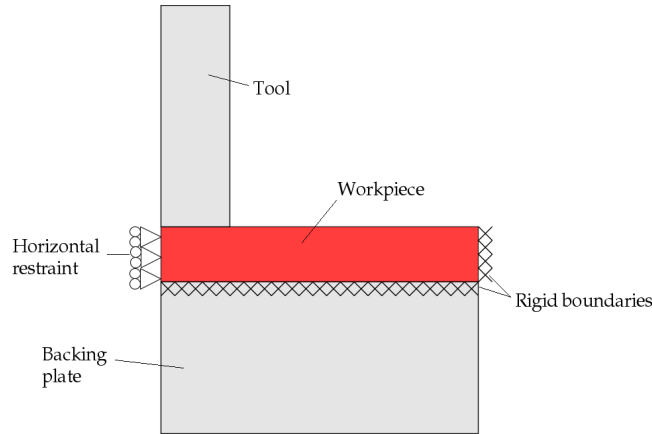


Figure 6.1: Constraints applied to the plunge model (tool and anvil not included initially, shown for reference to their position only)

6.2.1 Model setup and initial tests

A load was applied to a contact patch on the upper surface; this load was set to be sufficient to produce a displacement of around 0.1 mm as the mean vertical displacement of the contact patch (this being a typical value of the plunge during actual welding). The initial material properties specified were those of ‘elastic Al’: a density of 2700 kg m^{-3} and Young’s modulus of 70 GPa, with no yield point.

Two calculations were carried out for results that could be computed by hand as a ‘sanity check’ on the FE output. The first calculation was for a

uniform pressure load. A load of 7 GPa was applied to the top surface over the inner 5 mm of the radius (the unrealistically high value for the pressure load is required to produce high values of deformation in this non-yielding material). The downforce should then be 549.76 kN (from $F = pA$); the downforce calculated by Abaqus with a moderate density mesh was 549.78 kN. Running the model again with a mesh 5 times denser in each linear dimension (i.e. 25 times the number of nodes) produced an identical result. This indicates that the error is not due to a discretisation problem but is instead something more fundamental to Abaqus. However, the error is small enough (34.6×10^{-6}) that other outputs from the model can be regarded with high confidence.

The next case modelled was an imposed uniform displacement over the surface of the shoulder. Imposing a uniform vertical displacement of 0.1 mm produced a net reaction force of 754 kN. However, forcing a flat displacement everywhere under the shoulder caused much higher stresses at the corner, and it also created a ripple effect related to the mesh size. Close inspection of the vertical displacement in the first case, of a uniform pressure, revealed that it was not level under the tool, but varies from about 0.08 mm at the centre to 0.09 mm, then ramped up at the edge of the shoulder to meet the unloaded material.

The actual case in practice must lie somewhere between the two extremes of a uniform displacement (corresponding to an infinitely stiff tool) and a uniform pressure (corresponding to a zero-stiffness tool), as the tool has a finite stiffness. In the case of a steel tool and an Al workpiece, the tool is approximately 3 times stiffer than the workpiece. As the goal is to develop an elastic-plastic model below the tool, these initial trials suggest that it is necessary to take a closer look at the stress state under the tool, before rotation is imposed.

6.2.2 Methods of simulating downforce

Four different methods of modelling the tool loading on the workpiece were simulated. In the order in which they are presented, these are: a uniform

pressure over the contact patch; a uniform displacement over the contact patch; a distributed pressure load corresponding to a modified solution of the Boussinesq problem; and a finite stiffness tool with a uniform pressure applied to its top (i.e. the tool is explicitly included in the FE model). These loading cases are shown graphically in Figure 6.2. These four loads were applied in turn to a large, homogeneous block of AA6111 and the stress fields produced in this block compared. The total load was kept constant in all cases at 7.85 kN, a typical downforce for FSSW. The boundary conditions were kept the same as in Figure 6.1, i.e. an encastre base and far-field r boundary, a symmetry axis with no vertical restraint, and a free top surface outside the contact patch.

The calculation was performed as a 3D static analysis in Abaqus using an implicit formulation. The tool loading was applied to a patch of 5 mm radius (the same area as the tool shoulder in experiments). The contact between workpiece and tool, where this was explicitly included, was set as frictionless. The elements were 4-node linear stress elements, and the model initially comprised 270 elements with a bias distribution in both axes to enhance the resolution of the solution near the tool contact patch.

The uniform pressure and uniform displacement load cases are self-explanatory; case 3 requires more explanation. The load applied in case 3 is a modification of the pressure produced by a uniform displacement. The pressure distribution used is based on Sneddon's solution of the Boussinesq problem for a cylindrical punch. This result (from Sneddon, 1965) gives the pressure under a cylindrical punch into an elastic half-space as:

$$\sigma_{zz}(r) = \frac{-2Kd}{\pi(1-\nu)} \times (R_S^2 - r^2)^{-1/2} \quad (6.1)$$

with σ_{zz} as vertical stress or pressure, r radial position, R_S tool radius, ν Poisson's ratio, K bulk modulus and d as plunge depth of the punch.

The problem with this distribution is that it leads to infinite stresses under the corner of the tool (or under the edge of a displacement boundary condition). To circumvent this issue, the distribution above is modified by taking $r_{(\max)} = 0.95 R$ to ensure the distribution as used has a finite maximum

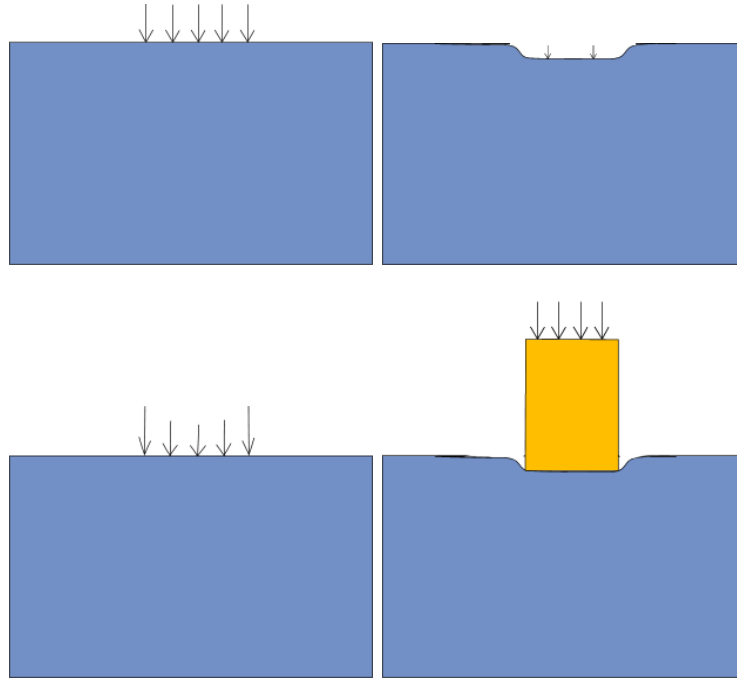


Figure 6.2: Loading cases for the static plunge model

Top left: uniform pressure; Top right: uniform displacement; Bottom left: modified Boussinesq problem; Bottom right: explicit inclusion of the tool

(adjusted by a constant to keep the integral — the total force — the same as in the other cases). This pressure distribution is shown in Figure 6.3 alongside Sneddon's solution.

Each load case was applied to the model in turn, to find the steady-state stress and strain fields. Vertical deflection and Mises stress fields for each of the load cases are shown in Figure 6.4.

These results show a surprising difference in both the displacement and stress produced in the four cases. The far-field, beyond about a tool diameter from the centre of the contact, is the same in all cases, but there is a substantial difference between all the cases in the region closer to the centre. The near-field, or nugget and TMAZ, is the location of interest.

The analytical solution to the uniform displacement case (case 2) gives rise to infinite stresses at the edge of the tool, as in Sneddon's solution. The FE solution, as expected, gives rise to very large stresses at the edge of the

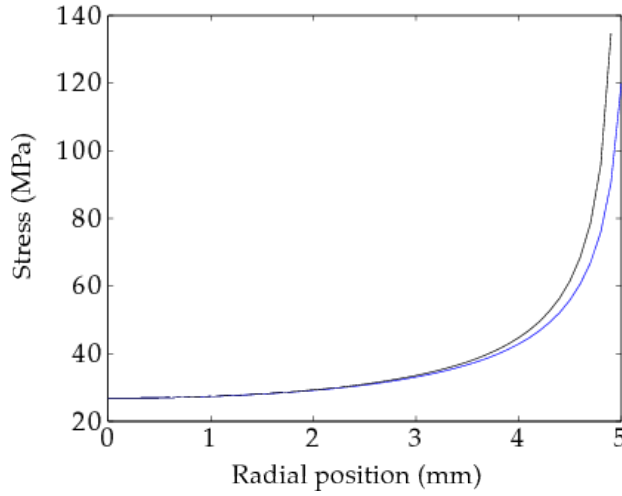


Figure 6.3: Solutions to the Boussinesq problem for the pressure under a flat cylindrical punch in an elastic aluminium half-space at a displacement of 0.0018 mm. The black line gives Sneddon's solution, the blue line gives the distribution used in the present work to avoid infinite stresses under the tool edge.

contact patch. The values produced for the stress here are not reliable and depend on the mesh size chosen (the values increase without limit as the mesh size is decreased), so this load case is not suitable for further analysis of the problem.

Case 1, which models the workpiece as subject to a uniform pressure, closely matches the Hertz distribution of stresses under a spherical contact between hard surfaces (which gives the maximum stress at a distance of $\frac{r}{2}$ below the centre of the contact). However, it is clear that a uniform pressure does not agree well with the other results; neither the stresses nor the displacements produced agree closely, and so this case must be discounted for modelling welds where the tool is significantly stiffer than the workpiece.

The modified Sneddon distribution produces results that are surprisingly different from those produced by a uniform displacement, as is evident in both the displacement and Mises stress fields. This indicates that the very high stresses around the rim of the contact are making a significant contribution to the overall load, despite the small area over which they act.

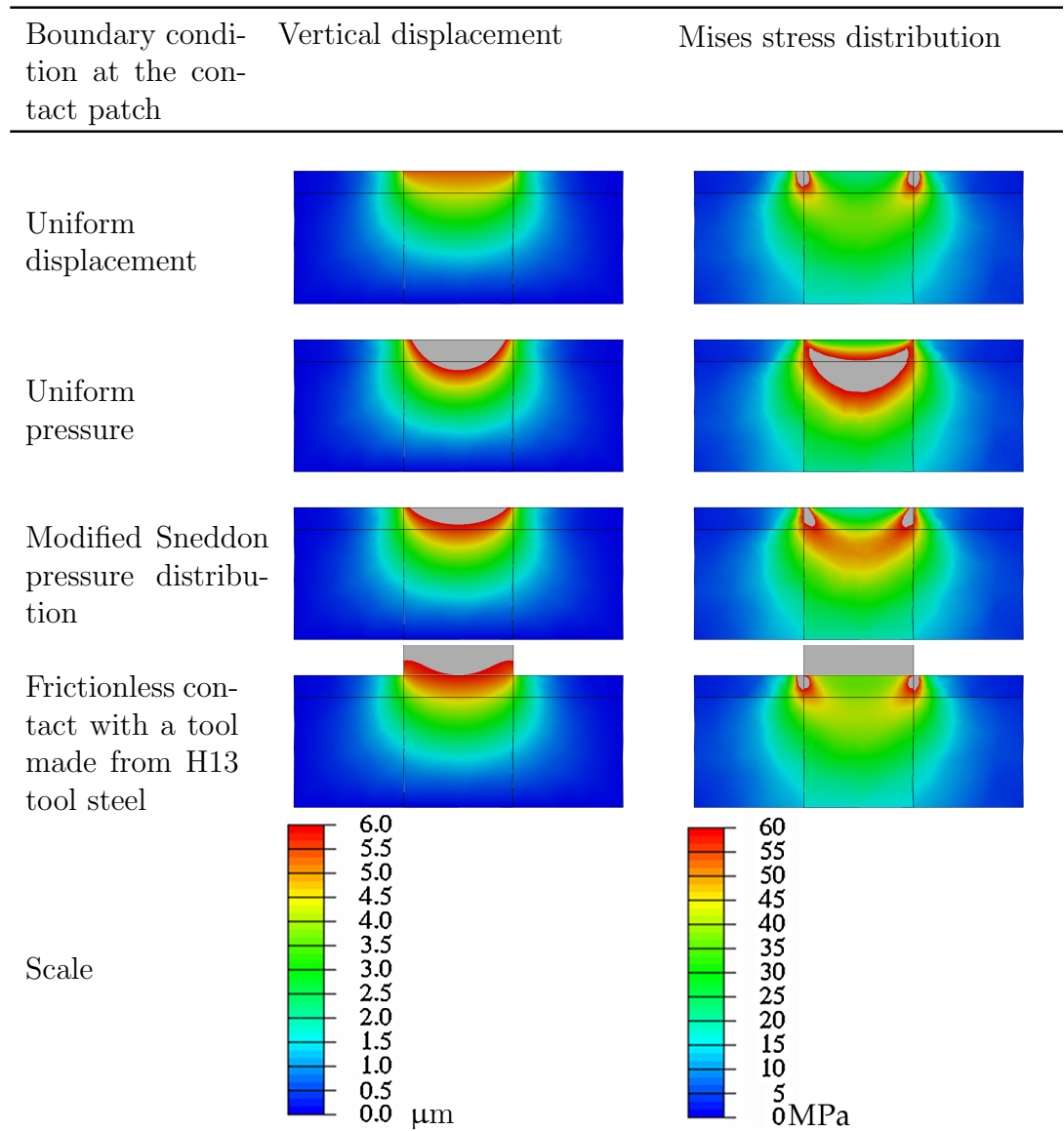


Figure 6.4: Vertical displacement and Mises stress for 4 load cases, normalised by downforce

The final case considered is that of a finite stiffness tool. As can be seen from the figure, this appears on a cursory inspection to lie somewhere between the cases for a finite displacement boundary and the modified Sneddon pressure.

To obtain realistic results for this simulation, the tool must be modelled in a more realistic fashion than either the uniform displacement or uniform pressure loads allow. The tool must either be included explicitly, or the modified Sneddon solution with a value of $R_{(\max)}$ greater than 0.95 could provide a good match.

6.2.3 Mesh sensitivity analysis

A mesh sensitivity calculation was performed for the model with the tool explicitly included (with a tied contact). The mesh for the weld nugget was seeded with both double and half the linear dimensions of the standard case, giving an approximate factor of 8 either way in the number of elements (with 825, 5565 and 40470 elements in each case, respectively). Plots of the Mises stress field for each density are shown in Figure 6.5. From this figure, the maximum stress predicted by the model with the coarsest density mesh is about 217 MPa. Although the intermediate mesh stress field looks broadly similar, the peak stress is 270 MPa, significantly different. Going to a finer mesh decreases this stress slightly to 265 MPa. This is close enough to the value for the intermediate mesh to give confidence that the dependence on mesh density at these values is low; more importantly, it shows that the predicted stress has reached a maximum and will not continue to increase monotonically without limit as the mesh density is reduced. The initial, intermediate-density mesh was used for further calculations as a compromise between speed and accuracy.

6.2.4 Further investigation of the Boussinesq problem

The differences between the stresses produced by the uniform displacement, modified Sneddon pressure, and explicit tool model load cases were much greater than anticipated, and warranted further investigation. Using the

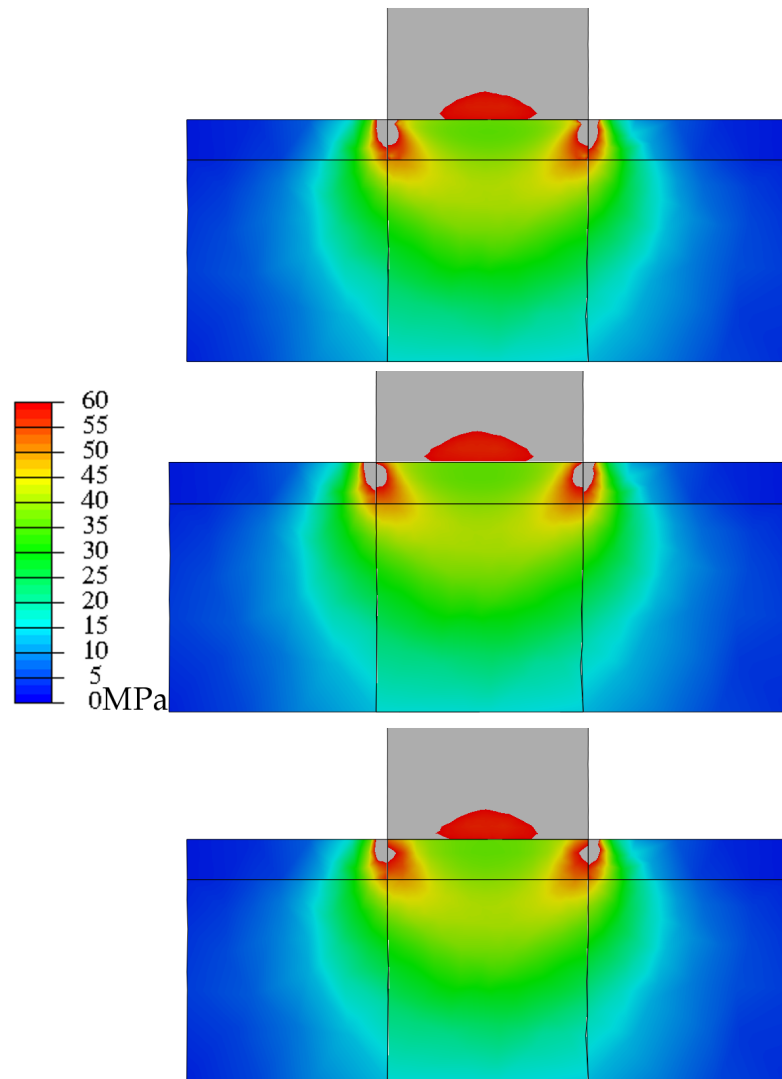


Figure 6.5: Mesh sensitivity analysis for case 4 (Mises stress)
 Top: coarse mesh; middle: intermediate mesh; bottom: fine mesh

mid-sized mesh (found to be adequate for all except the fixed-displacement case) the peak pressures were analysed to see how closely Abaqus conformed to the analytical solution. Two versions of the modified Sneddon solution were used, with $r_{(\max)} = 0.95 R_s$ and $r_{(\max)} = 0.99 R_s$. These cases are shown in Figure 6.6.

The peak pressure (σ_z) in each case is:

- Sneddon solution with $r_{(\max)} = 0.95 R_s$: 158 MPa;
- Sneddon solution with $r_{(\max)} = 0.99 R_s$: 178 MPa;
- explicit inclusion of a finite-stiffness tool: 288 MPa.

There is a surprisingly large difference between the stresses in the 95 % and 99 % cases, and between those and the explicit case. This shows that the very high stresses at the edge influence the behaviour far more strongly than was anticipated, even when keeping the total force the same. This shows that the pressure at the edge of the tool contact is very sensitive to the exact tool geometry and stiffness, and it will be necessary to include the tool explicitly in the FE model to produce accurate results. Fortunately this is possible without adding a great deal of complexity to the model since the tool remains elastic and does not require a very dense mesh over its volume. Furthermore, despite the sensitivity of the displacement boundary condition to the mesh size, it is possible to create a sufficiently fine mesh (as in Figure 6.5) to capture a finite-stiffness tool accurately without excessively complicating the model.

One difficulty that remains and that cannot be easily eliminated from modelling is the sensitivity of the peak stresses at the edge of the contact to the exact tool geometry. All the results presented so far have been for a square corner. In practice, most tools will have a somewhat rounded edge, which could evolve over time as the tool wears. To accurately model this would require a knowledge of the exact profile of the particular tool used. Fortunately however, this problem is expected to become much less important when yielding behaviour is introduced to the workpiece, since a small region of yield is likely with any tool, limiting the peak stress.

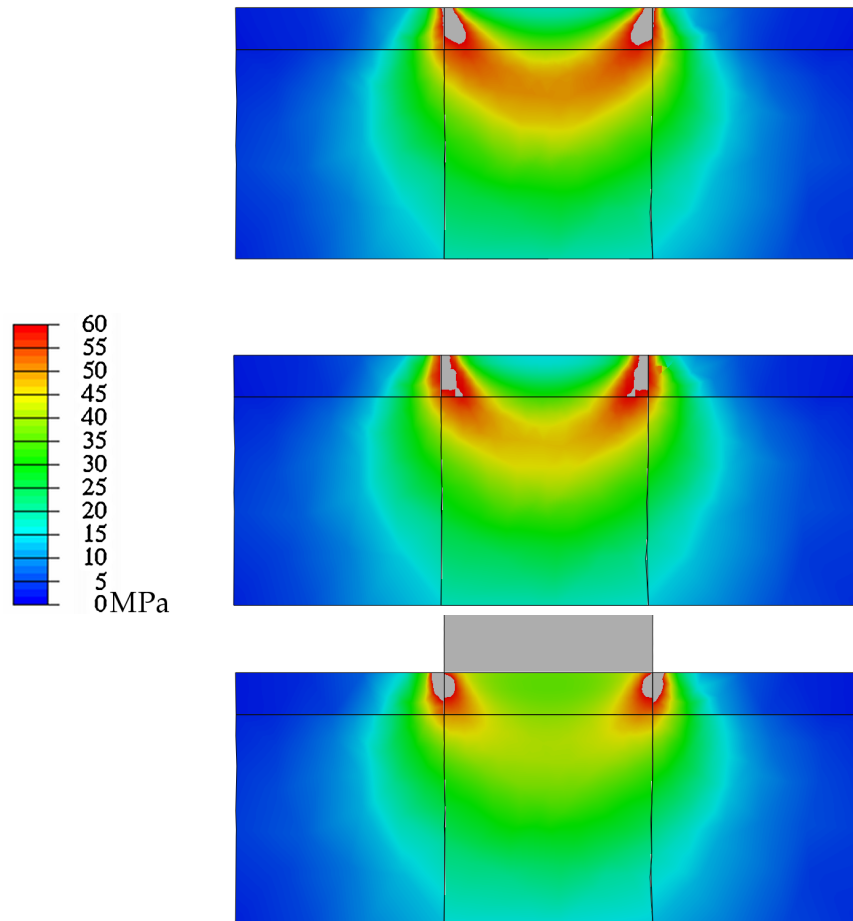


Figure 6.6: Comparison of the Mises stress produced under an explicit tool model, and 2 modified Sneddon solutions
 Top: 95 % Sneddon solution;
 Middle: 99 % Sneddon solution
 Bottom: explicit tool model.

6.2.5 Plasticity

In order to produce more realistic results, the yield behaviour of the material must be included. The material was modified to behave according to an elastic-plastic stress-strain curve with no failure, with a yield stress of 60 MPa. A small amount of work-hardening was added (equal to 0.6 MPa for a plastic strain of 1) to avoid numerical instabilities and localisation effects, as previous work had shown that without work-hardening the deformation could entirely localise into a thin deforming layer one element thick, with the rest of the workpiece remaining elastic. This is lower than the room-temperature yield strength of the alloys of interest but is more representative of their strength at higher temperatures. More detailed models with realistic constitutive behaviour are presented later.

The contact between the tool and workpiece was modelled as both a frictionless contact and a tied contact. In the frictionless case the workpiece was unconstrained radially; including friction at this interface is more realistic, but the frictionless case is better for comparison with other loading patterns. Once this comparison had been established (as in Figure 6.4) a new calculation was performed with a tied contact at this interface. This represents sticking friction (although still in the case of a non-rotating tool). A slipping contact will lie somewhere between these two extremes. The stress fields caused by these two cases differ significantly, as shown in Figure 6.7. Consequently, an analysis of the flow pattern must include some allowance for the radial constraint, as is done in the kinematic model for deep plunge welds.

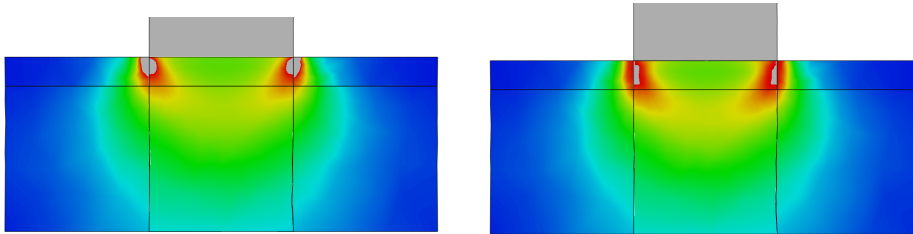


Figure 6.7: Mises stress fields under (left) a frictionless contact and (right) a tied contact with a steel tool

6.2.6 Analysis of thin plates

Following on from the previous section, a study was conducted to assess the effects of a near-field z boundary, as the stresses in a thin sheet can be very different to those in a thick plate when subject to the same loading. The same load cases as in the previous section were applied to a 2 mm thick Al workpiece, with a rigid boundary at the base representing a stiff backing plate. In this case, it was observed that the precise details of the loading condition actually had very little influence over the stresses and strains produced, unlike the model with the thicker plate. The four cases produced almost identical displacement fields, and the stress fields were also very similar. The only significantly different result was for the uniform imposed displacement case, where again the peak stress was a function of mesh size. Nevertheless, even for this case the overall stress field looked broadly similar, except for a narrow ring near the edge of the contact patch. Results for a uniform imposed displacement and pressure (the two extreme load cases) are shown in Figure 6.8 and Figure 6.9.

As including the tool explicitly remains the best model, this ought to be done if possible. However, in cases where model complexity and speed is of great importance, in simulations of thin plate welding the tool can be replaced with an optimised Sneddon-solution pressure without any significant loss of accuracy. In a simulation of thicker plate it may still be necessary to include the tool, depending on the goals and desired accuracy of modelling.

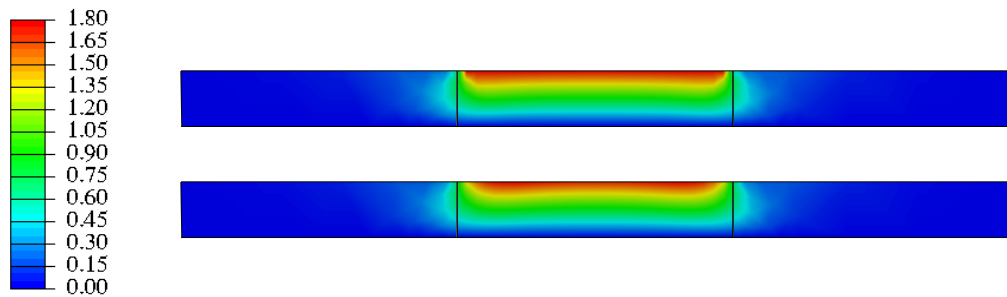


Figure 6.8: Displacement in a thin workpiece (μm) under (top) a uniform displacement and (bottom) a uniform pressure

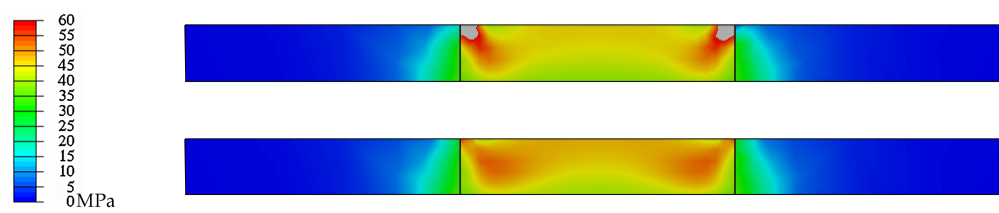


Figure 6.9: Mises stress fields in a thin workpiece under (top) a uniform displacement and (bottom) a uniform pressure

6.3 Sequential small-strain analysis

6.3.1 Aim

A major drawback with current FE approaches is the computational effort needed to capture the very large strains in friction stir (FS) processes. A typical fully coupled analysis requires a new mesh every time the geometry changes significantly; this means that a traditional fully coupled FE simulation involves remeshing many times per revolution, leading to large computational loads. It is possible to model seam FSW with an arbitrary Lagrangian–Eulerian approach, but this is very computationally intensive. In contrast, computational fluid dynamics approaches handle the large deformations much better than FE methods, but these methods lose the elastic-plastic nature of the metal, treating the alloys as viscous liquids. CFD can predict traverse forces during seam FSW, but not downforce, since the elastic stress field makes a significant contribution. The new approach presented here offers the advantage of being able to predict the downforce, while reducing the computational load and avoiding remeshing.

Work by Colegrove & Shercliff (2006) found that the predicted material condition during welding is very sensitive to the detail of the constitutive law chosen. Nonetheless, the deformation conditions are self-limited in FS processing to some extent. Firstly, the process is tightly constrained kinematically: the maximum strain-rate will be of an order given by the maximum surface velocity divided by the thickness of the deformation layer: $(\omega \times r)/h$. Secondly, FS processing is to a large extent self-limiting in temperature due to the negative feedback loop between power input and temperature, which are linked via the material’s constitutive law: as the material heats up it becomes softer, so less energy is dissipated when it deforms. This is particularly the case at temperatures near the solidus where the strength falls rapidly.

Sequential small-strain analysis (SSsA) is a novel calculation method developed specifically for FSSW and similar processes. It uses small-strain elastic-plastic FE analysis to capture enough of the flow behaviour to undertake computation of the coupled metal flow, heat generation and heat flow

in FS processing. The analysis relies on the fact that deformation occurs on much shorter timescales than heat flow, so any one point will undergo significant strain (much more than the maximum elastic strain) at nearly constant temperature.¹

Furthermore, provided the material is not undergoing work hardening the heat generation rate does not depend on the strain; this assumption is valid at the temperatures of interest during FSSW in Al. Consequently, it is possible to run a small-strain implicit analysis to produce a ‘snapshot’ of the heat generation rate and its spatial distribution for a fraction of one tool rotation, and to use this estimate of the power distribution in a thermal model running with much longer update intervals.

This approach allows the temperature and deformation fields to interact in a realistic manner, but is a computationally frugal approach when compared to fully coupled FE models. The method is presented here for friction stir spot weld models, but it could in principle be used for any process that shares the same characteristics of a constrained geometry, with rapid deformation processes, and heating processes characterised by longer timescales.

6.3.2 The model

The SSsA procedure is to calculate the instantaneous stresses and strain-rates using a stress-strain FE simulation, then run a purely thermal analysis with the calculated power for a longer timestep. In this way, the effects of compressing and deforming the workpiece can be captured, while avoiding a model with very large deformations. This is desirable because remeshing and other techniques usually used for large deformation models tend to reduce both model speed and/or accuracy.

During the deformation calculation, downforce and rotation are applied to the workpiece. During the first timesteps, deformation in the workpieces will

¹The choice of natural scales with which to compare heating and deformation rates is not obvious. However, choosing the time taken to double both temperature and strain seems reasonable. By this measure, deformation is occurring on the order of 50 to 100 times as fast as heating: the temperature doubles in 0.5 to 1 s, and the strain rate is of order 100 s⁻¹.

be predominantly elastic, and during later steps, there will be little change in the elastic strain and most of the additional movement will be due to plastic strain (once most of the deforming material has reached yield). Plotting the plastic strain rate for any point as a function of time should then show an asymptote. The asymptotic value matches the strain rate at that location at that time, as during the actual weld elastic strains will also be negligible by comparison with plastic strains.

The procedure for SSsA is as follows:

1. apply a loading condition including both rotation and downforce
2. calculate the output power based on the stress and strain-rate fields at the end of the analysis step
3. impose the power generation distribution (as a function of position) on a thermal model
4. run the thermal model
5. import the temperature field back into the deformation model for the next interval, and rerun.

As applied here to FSSW, the elastic-plastic analysis runs for a rotation of around 2° , taking about 0.2 ms at 200 rad/s (1910 rev/min). The deformation and heat generation thus calculated are assumed to remain constant for some longer time (typically 0.1 s). The calculated strain-rate and stress fields are used to calculate the power dissipation by plastic work for each element. After this, the deformation model is run again under the new temperature conditions, and new stress and strain-rate fields are calculated. The process continues, to estimate the strain-rate field and heat generation by plastic work for the whole duration of a weld. This enables predictions of the power generation and flow patterns without the need for a complete, computationally expensive, coupled thermal-stress FE simulation of the full weld.

The overall modelling procedure is summarised in Figure 6.10. The key innovation in this model is the decoupling of the thermal and deformation calculation steps, whilst maintaining an accurate temperature field at all

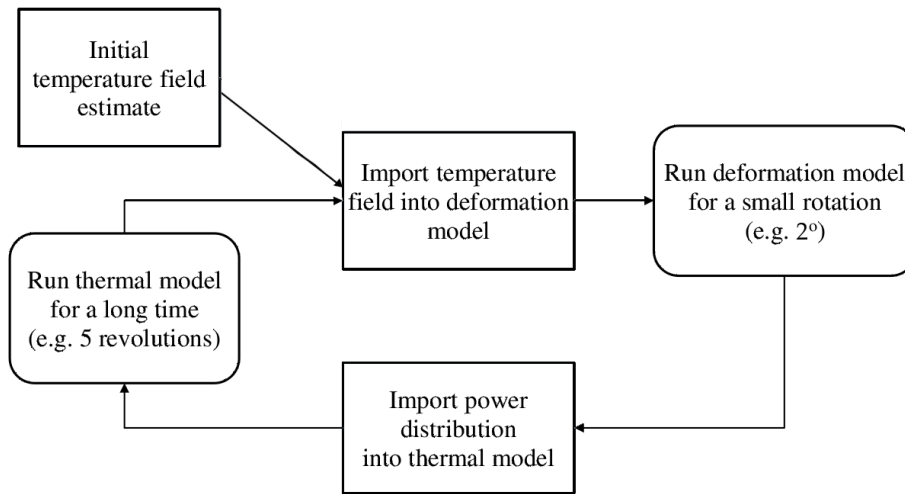


Figure 6.10: Calculation process for the snapshot model

times. This is important, since the workpiece properties depend strongly on temperature, both during the weld and for the final microstructure. Each step is explained in more detail below, where the process is illustrated for two theoretical welds, the first in a thick block of aluminium, the second in thin sheet material. The weld chosen for the initial model was a shallow plunge weld of 1 s duration at 760 rev/min (~ 80 rad/s); these conditions were chosen as representative of practical welding conditions.

Material model

The snapshot model can incorporate realistic material behaviour, including flow stress that depends on temperature and strain-rate. Strain dependence cannot be included (so Johnson-Cook models cannot be used), but any other constitutive law that can be implemented in Abaqus is theoretically possible, subject to stability constraints regarding temperature and strain-rate dependence (material models that weakened at increasing strain-rates, or hardened with increasing temperature, would be unstable). The lack of strain-hardening is not a problem for Al: constitutive data for Al at temperatures typically encountered in FSSW does not show any great degree of strain hardening, and the flow stress is strongly dependent on strain-rate and temperature.

For the present work, a sample material was needed. AA7449 was chosen as it is an important high strength aerospace alloy and is often considered to be difficult to weld due to its heat-treatable properties. It was modelled using Zener-Hollomon behaviour in the high temperature regime and single yield point non-strain-hardening plasticity for the low temperature regime. The use of this constitutive law for AA7449 in this regime follows work by Colegrove & Shercliff (2006). Zener-Hollomon behaviour is described by:

$$Z = \dot{\epsilon} e^{(Q/RT)} = A \sinh(\alpha\sigma)^n \quad (6.2)$$

The values used for each of the parameters in Equation 6.2 are given in Table 6.1; these values were derived at strain rates of 0.1 to 25 s⁻¹ and temperatures of 625 to 710 K (using results provided by Alcan). Zener-Hollomon strain-rate hardening is assumed for all strain rates above 10⁻³ s⁻¹. Below this strain-rate quasi-static behaviour with a yield stress that depends only on temperature is assumed. Zener-Hollomon behaviour has been shown to hold up to strain-rates of 100 s⁻¹ in 7000 series alloys and up to 1000 s⁻¹ in 1000 series (commercially pure Al). Above this rate Johnson-Cook models are usually used. These predict greater increases in flow stress with strain-rate, but these strain rates are above those found in FSSW.

A key issue in friction process modelling is the behaviour of the material near the solidus temperature, at which point melting commences and the viscosity will drop significantly. Classical Zener-Hollomon behaviour does not take account of phase changes, so another approach is required. Colegrove et al. (2007) used a model proposed by Seidel and Reynolds which predicts enhanced softening with temperature as compared to the standard Zener-

A	Q kJ	n	α	Softening temperature K	Solidus temperature K	Low T yield stress MPa
2.226×10^{12}	156	6.81	1.1×10^{-8}	768	773	590

Table 6.1: Zener-Hollomon parameters for AA7449 (data from Colegrove & Shercliff, 2006)

Hollomon model, with a linear reduction in flow stress as the temperature approaches the solidus (typically over an interval of up to 50 K). Above the solidus the material is assumed to have negligible shear strength. The flow stress for AA7449 using the parameters in Table 6.1 is illustrated in Figure 6.11.

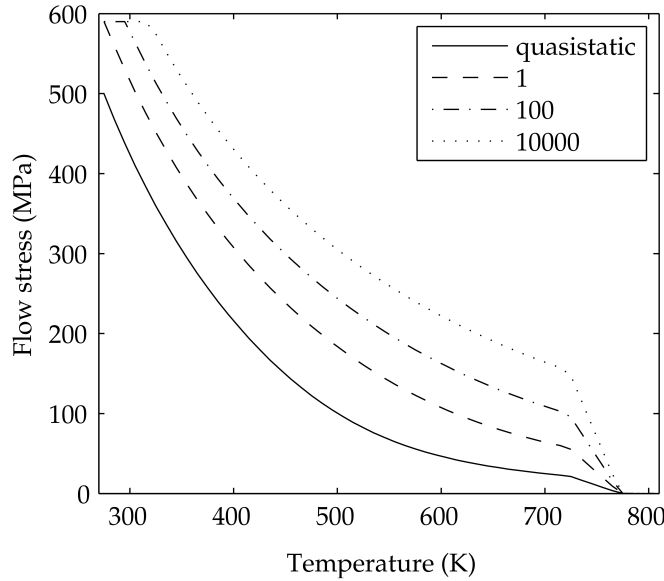


Figure 6.11: Flow stress against temperature at various strain-rates for AA7449

Thermal model and initial power estimate

The thermal model was built in Abaqus, as a 3D implicit finite element calculation using 8 node linear (hex) elements. The mesh is illustrated in Figure 6.12. As this model simulates a purely thermal problem, the runtime is comparatively fast, and it can include many of the features of real welds, such as backing plate, clamping arrangements and flash formation. The heat input is modelled in two parts, part as a surface power input and part as a volumetric power (split into 12 regions). The outer boundaries are all treated as insulating, with no heat losses across them.

For this study the ‘weld’ comprised a tool plunging with constant force into a homogeneous block of aluminium. In the first case, a semi-infinite

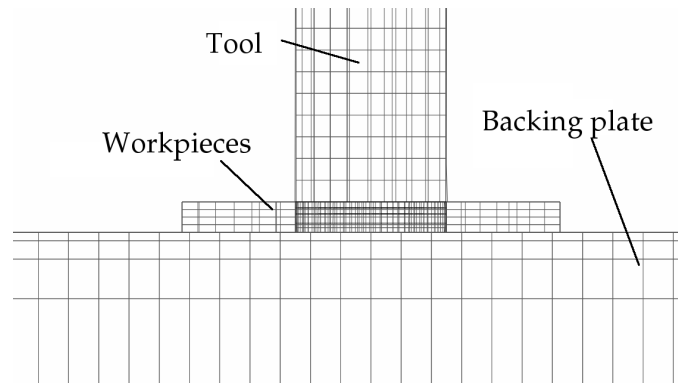


Figure 6.12: Mesh for the thermal model

block was modelled; semi-infinite in this context refers to a block of such a depth that the temperature rise at the far surface remained less than 1 K for the entire duration; in practice, this meant a model thickness of 20 mm for a 1 s weld, (twice the tool diameter).

In the first instance as a proof-of-concept, an initial estimate of the heat input was applied for 0.5 seconds, before switching to iterative heat generation and thermal models. While this may over- or under-estimate the weld temperature (and thus subsequent heat input), it provided a useful intermediate computation to test the effect of varying the duration of the deformation and thermal calculation steps. Subsequent refinement of the model enabled iterative calculations from cold; this work is presented in the case study modelling experimental welds in thin sheet.

This initial estimate was needed to bring the model into a stable regime. The value of this initial power was estimated from thermal modelling of AA6111 and 6082, and scaled by the relative strengths of the materials at room temperature. This power was initially applied as a surface heat flux to simulate frictional heating of the workpiece material from the cold state. The peak power applied was 1.5 kW; the shape and distribution of the power input was an exponential function as described in Chapter 4.

Deformation model

The deformation model was a stress calculation, again carried out in Abaqus implicit. The simulated time for each run of the deformation model was 200 μs , corresponding to a rotation of 0.016 rad (0.9°) at 760 rev/min (80 rad/s). This rotation is large enough to ensure that the strains in most of the deforming zone are well beyond the elastic limit, but small enough to ensure sufficient accuracy without needing to remesh the model domain during the calculation. At the end of each deformation calculation (i.e. after 200 μs) the power generation was estimated, and used in the next step of the thermal calculation. This was done for each timestep of the deformation model using the Abaqus variable ALLPD. ALLPD is the plastic work dissipation per element, but here the nugget is divided into 12 zones rather than into individual elements for simplicity.

Because the analysis starts from a zero-stress state, the plastic work increases throughout the calculation as the elastic strain component becomes negligible and a greater proportion of the deforming region starts to deform plastically. The plastic work rate increases towards an asymptote during the calculation, and it is this asymptotic value that is used as an input into the thermal model.

The loading applied to the top of the workpiece consists of downforce and horizontal velocity. The downforce is as found in Section 6.2. The surface velocity fields are the same as that used in the kinematic model, shown in Figure 5.5 (reproduced here as Figure 6.13). Each velocity distribution was applied in turn to test the sensitivity of the resulting heat generation to the slip condition.

Running this model calculates the strain throughout the model domain, including elastic and plastic components. The plastic strain components calculated under velocity distribution 3 are plotted in Figure 6.14 for 3 selected points. From this graph, the plastic strain-rate at the final increment can be calculated as the gradient of each line; the final strain-rate is the asymptotic value given by the straight line segment of each graph. The strain-rates caused by each surface velocity distribution are shown in Table 6.2.

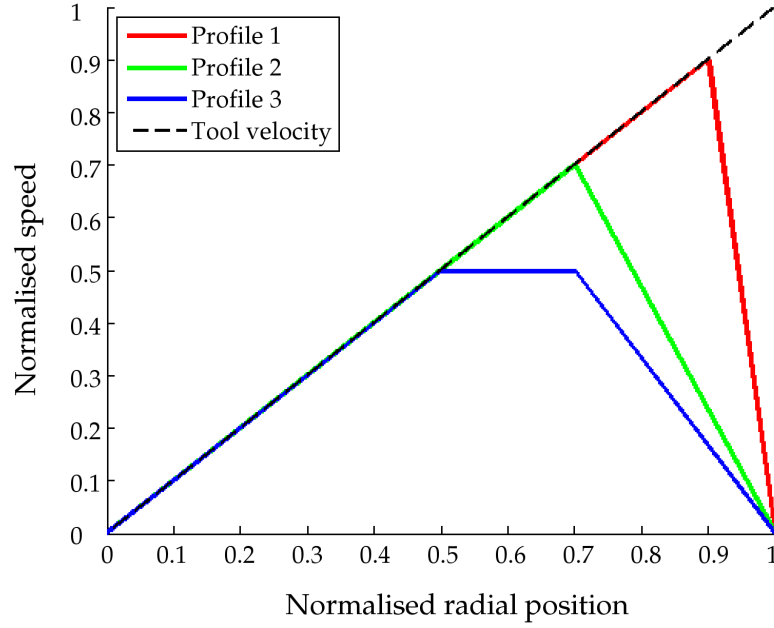


Figure 6.13: Velocity profiles applied to the tool contact patch

The velocity field chosen for further calculations was Profile 3, as this gave the most realistic results with the kinematic model in Chapter 5.

As well as calculating the strains, these models calculate the stress. Both downforce and rotation are crucial to the stress state in FSSW. The contribution of each can be assessed by looking at the Mises stress under the tool. Plots of the Mises stress are shown in Figure 6.15 for three situations: the case of 100 MPa downforce, but no rotation (top figure, identical to the output from the static plunge model presented in Section 6.2); the case of rotation, but only 10 MPa downforce (middle figure); and for rotation with 100 MPa downforce (bottom figure).

	r=2.5, z=0	r=5, z=0	r=5, z=0.5
Profile 1	102	50	25
Profile 2	152	20	9
Profile 3	138	13	6

Table 6.2: Plastic strain rates during the final increment, at selected locations (dimensions in mm)

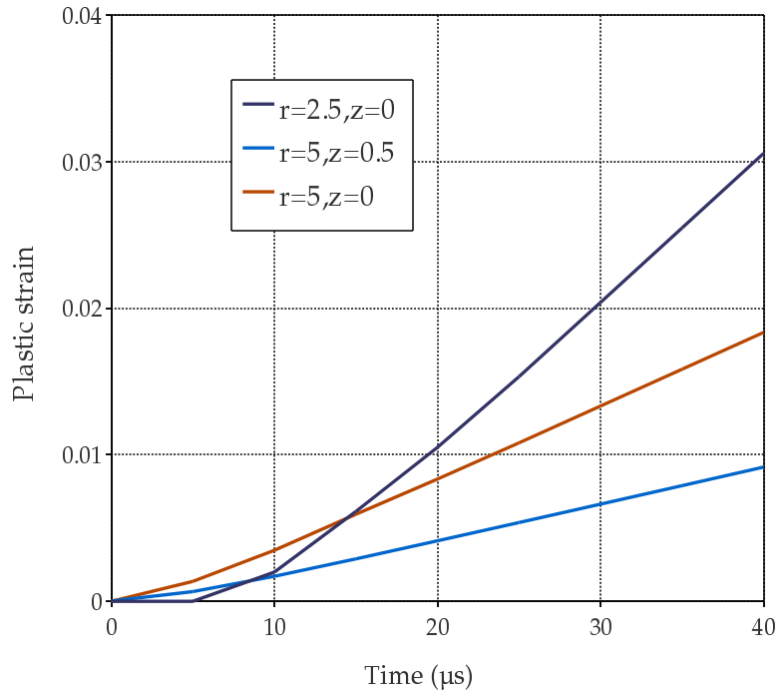


Figure 6.14: Plastic strain at locations indicated

This series of figures shows the importance of including downforce in models of FSSW. A 100 MPa pressure load alone only produces yield in a very small region using this material. Rotation alone causes yield in a slightly larger zone, but one that is constrained to lie near the surface. Both a large downforce and rotation together cause a large yielding zone, causing different behaviour to either rotation or downforce alone.

6.3.3 Proof-of-concept

The snapshot modelling approach was used first to model welding in a thick plate of AA7449. The thermal model was run initially for 0.5 s then with intervals of 0.1 s, and the deformation model was run for 0.2 ms each time. An example of the predicted power dissipation is shown in Figure 6.16. This figure was produced by the deformation model, running with the temperature field calculated as the output of the thermal model at 0.5 s. The top surface boundary condition was velocity distribution 3. This figure shows the power

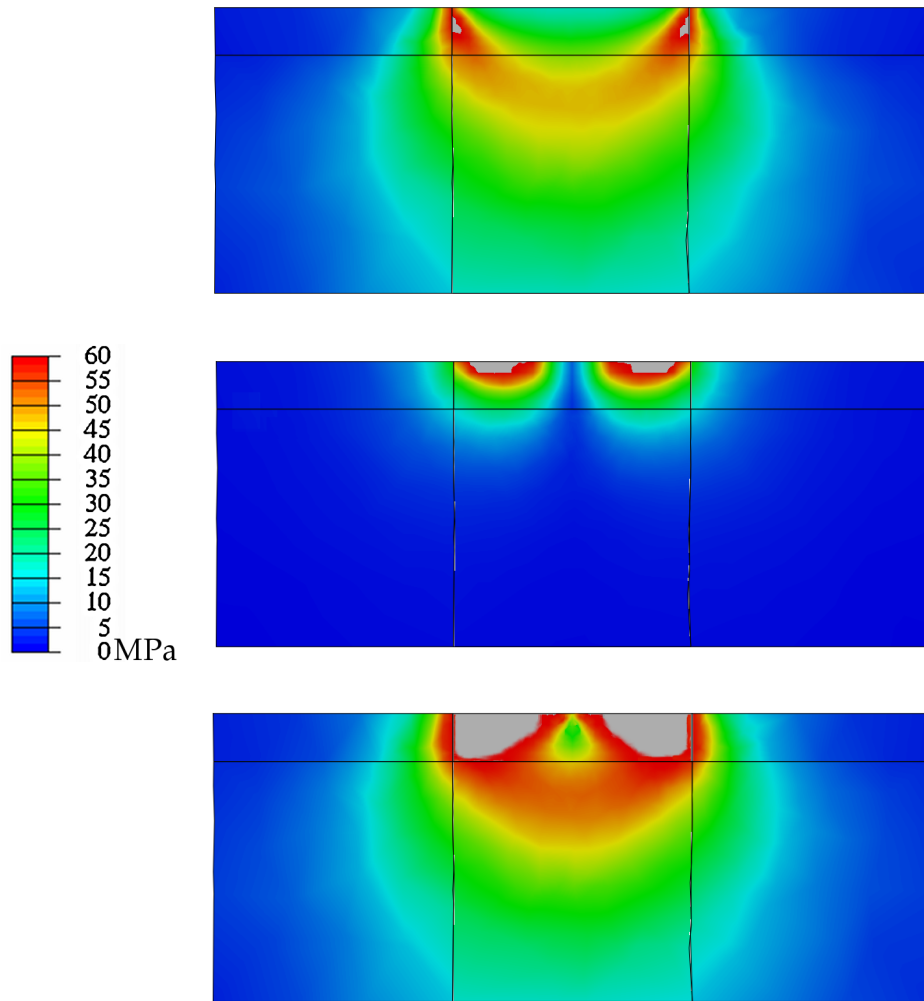


Figure 6.15: Mises stress fields
 Top: downforce, no rotation
 Middle: rotation, minimal downforce
 Bottom: downforce and rotation

dissipated within the workpiece due to plastic work at each step of the deformation model. By 0.2 ms, the power reached a steady-state, at an asymptotic value of 1500 W.

This model not only produced an estimate of the total power, but could calculate the power on an-element-by-element basis. Due to the manual steps required, rather than actually using the result for each element, the deforming region of the workpiece was divided into 12 regions, and the power calculated for each of these. The power density distribution predicted by the model is shown in Figure 6.17.

The total power input to the weld includes contributions from plastic work (shown in Figure 6.16) and frictional heating. The frictional heating contribution is calculated as:

$$P_f = 2\pi \int_0^{R_s} \tau_{z,\theta} \cdot \omega \times r \cdot |r| \cdot \delta \, dr \quad (6.3)$$

where P_f is the total frictional heating power, $\tau_{z,\theta}$ is the shear stress in the (z, θ) direction, ω is the rotation speed, r the radius and δ is the interface slip factor.

Like the plastic work, P_f can be calculated on an element-by-element basis. The total power contribution from both sources is shown in Figure 6.18 for each run of the deformation model, for 0.5 to 1 s.

This correctly predicts the drop-off in power that occurs as the workpiece heats up and softens. What is clear from this figure, and has not been established in the existing literature (either experimentally or from other modelling approaches), is the split between the friction and plastic work contributions. The top surface of the workpiece reaches a temperature very close to the solidus very early on in the weld, and then remains almost at a constant temperature as heat diffuses away from the hottest regions. Consequently, the power dissipated by friction also remains nearly constant after the very early part of the weld. Even if the assumed surface velocity profile is not exactly correct, the conclusion that most of the input power is dissipated as bulk heating stands.

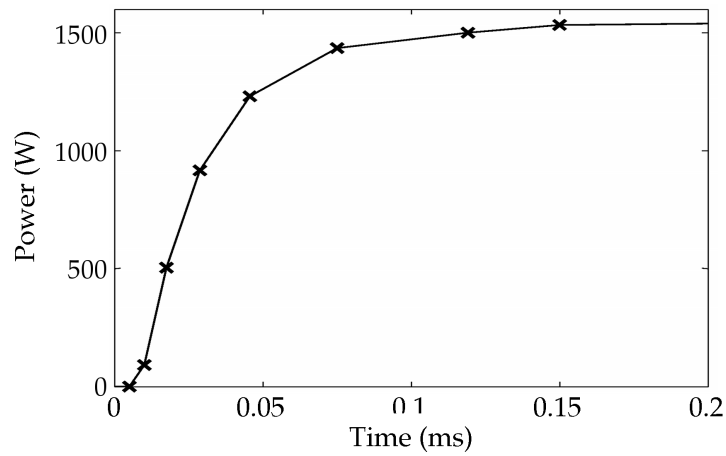


Figure 6.16: Power dissipated within the workpiece at 0.5 s

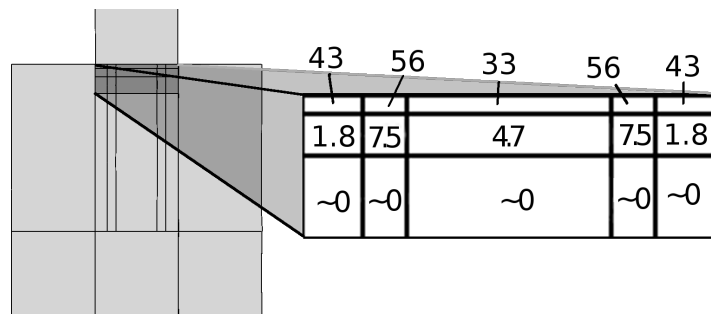


Figure 6.17: Power dissipation density within the workpiece at 0.5 s; the top three layers are deforming plastically, with the majority of the power dissipation occurring in the top layer. Power densities given in W mm⁻³.

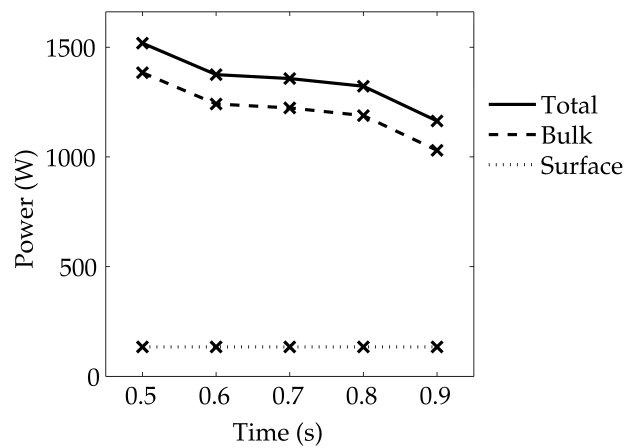


Figure 6.18: Total power dissipation, by plastic work & surface friction

6.3.4 Thin plate welding

As in the study of plunge effects with a static workpiece, modelling progressed from the case of a thick workpiece to more realistic geometries. To test the application of this method to other geometries, a model was developed for a 2 mm thick workpiece. All other properties were kept constant.

As in the case of the thick plate, the thermal model was run for 0.5 s using an initial estimate of the power input. The temperature field calculated from this model was used as an input into the deformation model, and the power dissipation in each of 12 sections was calculated. The power dissipation increased at each timestep of the deformation model, reaching an asymptote which was then used as the input to the next stage of the thermal model.

The total power dissipated in the weld is shown in Figure 6.19, and the corresponding temperature field is shown for three times in Figure 6.20. Under these conditions, the total power dissipation predicted by this model was lower than that predicted for the case of a thick plate, however, the power dissipated through frictional heating on the surface was slightly higher. This is due to the greater restraints to deformation that are present in the thin sheet case. Despite this, the majority (circa 85 %) of the power was still dissipated by plastic heating in the bulk of the nugget.

Although the surface slip profile must be assumed as an input, the exact form of this profile has relatively little bearing on the powers produced, and hence the temperatures reached. For the two most extreme power profiles considered as realistic (profiles 1 and 3 in Figure 6.13) the power difference for these conditions amounts to about 150 W, or roughly 10 % of the total power dissipation. As seen more clearly with the kinematic model presented in Chapter 5, the slip profile affects the flow pattern substantially, and where mechanical locking is significant it will affect the strength of the joint substantially. However, it is interesting that the precise details of the flow have comparatively little influence over the total power dissipation.

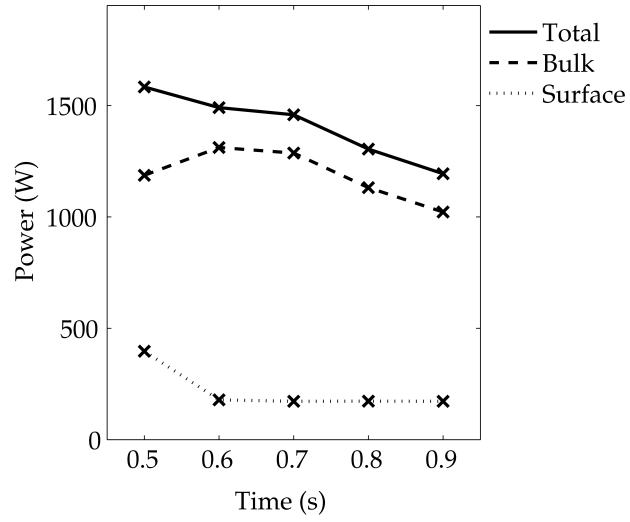


Figure 6.19: Total power dissipation, by plastic work and surface friction for thin sheet AA7449

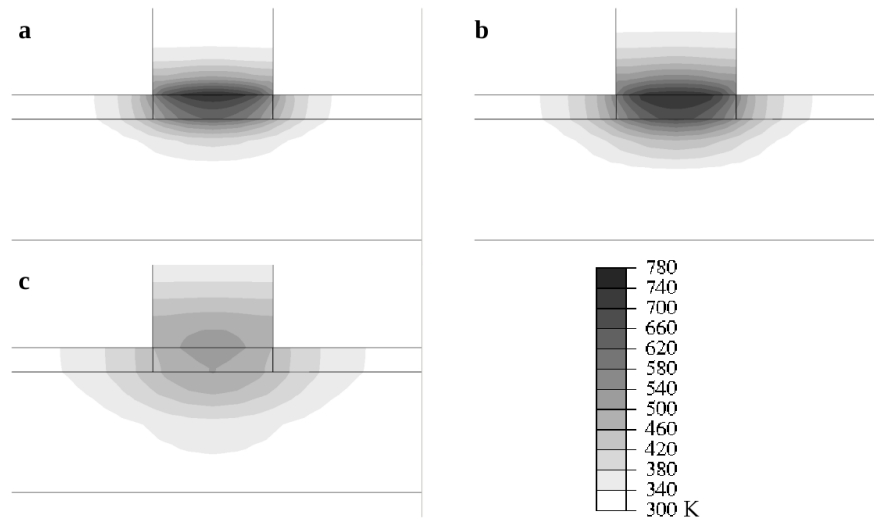


Figure 6.20: Temperature field for a weld in thin sheet AA7449
a: 0.5 s; b: 1 s; c: 1.5 s

6.3.5 Adaptive timesteps

In the previous section, the problem of ‘cold start’ conditions was identified. The problem arose because, during the early part of a weld, the contact conditions and power input evolve very rapidly. This led to numerical problems with resolving early stages of welds. The problem was resolved by reducing the time between each run of the deformation model; this ensured that the calculation was stable, and allowed successful calculation of solutions. However, the reduction in time interval required was substantial: at 760 rev/min (80 rad/s), successful cold start calculations required an update interval of 0.01 s.

Running the deformation model at such short intervals corresponds to running deformation calculations multiple times per revolution (every 48° at 800 rev/min). Although this still offers a significant reduction in calculation over fully-coupled models, it adds unnecessary calculations later in the weld when additional precision is not required. Furthermore, it is not feasible at present to run a model with so many stages as human intervention is required at each stage. The use of adaptive timesteps allows enhanced precision where necessary during the early stages and longer intervals between deformation calculations where this is possible in later steps. A number of schemes are possible to calculate the optimum timestep; the method proposed here, which is sufficient for present purposes, is to take the gradient of the power vs. time curve and extrapolate it to estimate the time interval required for a 10 % reduction in power.

A reduction in timestep is also necessary to maintain accuracy as the solidus is approached. The solution near the solidus is stable, but if the time increments between thermal updates are too long, ‘ringing’, or oscillation about the true steady-state power, can occur.

6.3.6 Case study and validation

Experiments were conducted at TWI covering a range of experimental conditions, as detailed in Chapter 3. A full simulation was performed of the standard case: two sheets of Al, at 760 rev/min (80 rad/s), for 1 s. Although

the experiments being modelled used both AA6111 and 6082, these are very similar alloys and the samples used were heat-treated to have the same room-temperature hardness.

Material data was taken from Sheppard & Jackson (1997). The material model used was, again, the Zener-Hollomon model, and a plot of flow stress against temperature for various strain-rates is given in Figure 6.21. Assuming the two alloys have the same strength at high temperature allows continued use of the previous axisymmetric model, and should involve no great loss of accuracy. A linear reduction in flow stress was imposed over the 50 K interval below the solidus, with the strength becoming negligible at the solidus itself.

With adaptive timesteps, the model was able to simulate an entire weld from start to finish. The total powers are shown in Figure 6.22, including the contributions from bulk deformation and surface heating. This enhanced model predicts that surface friction contributes a much larger fraction of the total power than previous uses of the model. However, the conclusion that most power is dissipated by plastic work still holds.

Experimental welds were made at TWI with identical conditions to those applied in this model. Temperature outputs from the model at locations 2, 6 and 10 mm from the weld centre, 0.1 mm from the base of the workpieces, are shown in Figure 6.23 alongside thermocouple measurements for the same locations in an experimental weld. This simulation ran entirely from cold: the only specified parameters concerning the power input were the tool speed, the slip profile as a function of radius, and the material properties. The model was able to predict the observed temperature rise reasonably closely.

Predicted temperatures during the cooling phase are less accurate. This is probably due to changes in contact conductance that occur as the tool is removed: contact across the joint is essentially perfect as the two parts have been welded, but away from the weld it is likely that the conductance falls as the downforce is removed. However, accurate predictions of the cooling rate are unimportant from a microstructural point of view, so this does not represent a serious flaw in the model.

Temperature predictions can be made for locations at the welding interface, where thermocouples cannot be placed as they would be destroyed

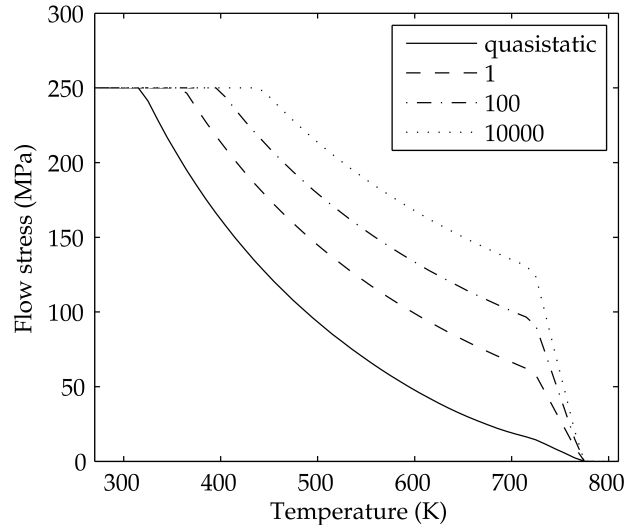


Figure 6.21: Flow stress against temperature at various strain-rates for AA6082

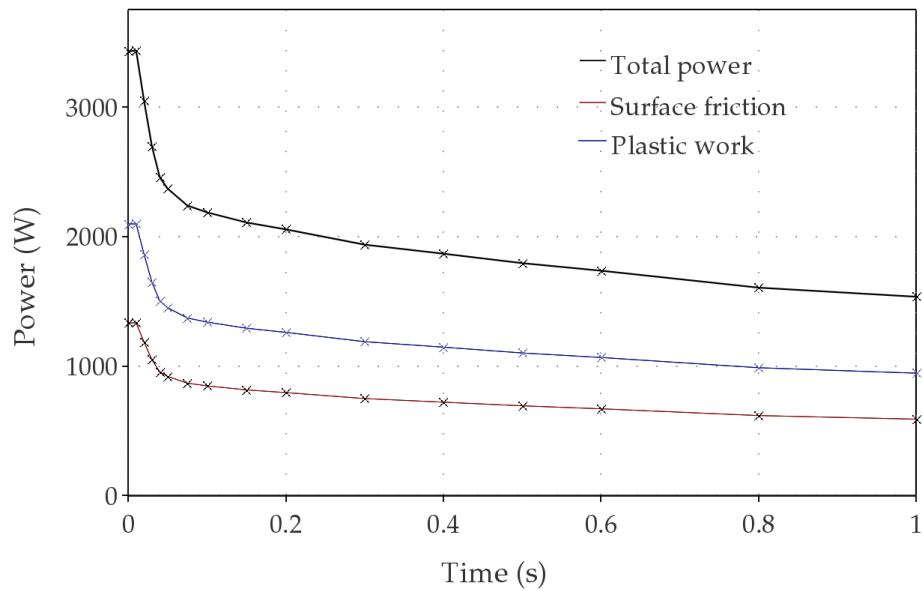


Figure 6.22: Predicted power dissipation by surface friction and plastic work for a weld in AA6082 at 760 rev/min (80 rad/s)

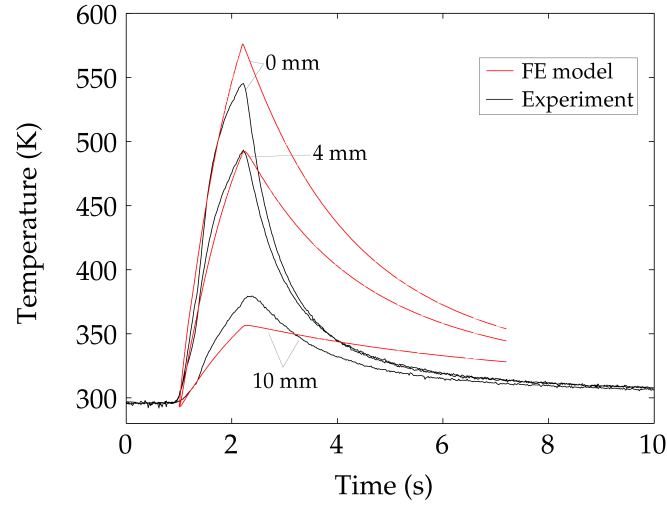


Figure 6.23: Temperature predictions (red) and experimental measurements (black) for a weld in AA6082

by the welding process. Peak temperatures at the centre and 5 mm from the centre are 660 K and 574 K, respectively — these fall just outside the regime identified as giving rise to optimum welds in Chapter 4, which matches well with weld strength tests. It is suggested that weld strengths could be improved slightly by increasing the power input.

6.3.7 Optimum welding with a copper backing plate

In Section 4.10.1, an optimum process window was found for welds using a copper backing plate. As that was a purely thermal model, the parameter space was described in terms of time and power input. However, in FSSW the power input is not an independently controllable parameter. Rather than assuming a power input distribution, the semi-coupled model presented in this chapter can analyse welds using a specified rotation speed. In Section 4.10.2, a copper anvil was suggested as a way to improve weld quality. This present section examines the powers, torques and temperature that arise when using a Cu anvil.

The thermal analysis indicates that higher powers are required with a

Cu backing plate. The variation of input power with rotation speed is not a fixed function, but varies depending on the backing plate material; a rotation speed of 160 rad/s (1528 rev/min) was selected for this analysis as a likely estimate.

As the steady-state heat flow was greater for the new case, the temperature field was more sensitive to the power input. Consequently, smaller timesteps were required. The calculated power at each step is shown in Figure 6.24.

There are two contributions to heat flow in the nugget: the conductive component (to the outer workpiece and backing plate), and the heat capacity term (representing heating of the nugget). With a Cu anvil, the former represents a greater proportion of the total. Consequently, the power dissipation drops off more slowly. As a result, the process window developed in Chapter 4 is no longer completely accurate: Figure 4.32 assumed that the shape of the power profile remained constant, increasing or decreasing by a uniform factor. The work in this chapter produces a more accurate power profile for high-speed welding with a copper anvil.

In Chapter 4, peak temperatures at the centre of the weld and 5 mm from the weld centre (both on the interface line) were used as a proxy for weld quality. A good-quality weld was defined as one with a high T_1 and a low T_2 . Peak temperatures at these locations for the two welds simulated here are given in Table 6.3.

The ratio η_T (see Equation 6.4 for a definition) is a useful measure of how effective the welding conditions are at raising the nugget temperature without causing overheating in the HAZ. For the steel backing plate weld, $\eta_T = 1.64$ and for the copper backing plate weld, $\eta_T = 1.67$. This suggests that the copper backing plate would cause a slight improvement in this ratio,

Backing plate	Nugget	HAZ
Steel	659	516
Copper	523	431

Table 6.3: Peak temperatures (K) in the nugget and HAZ, on the joint line

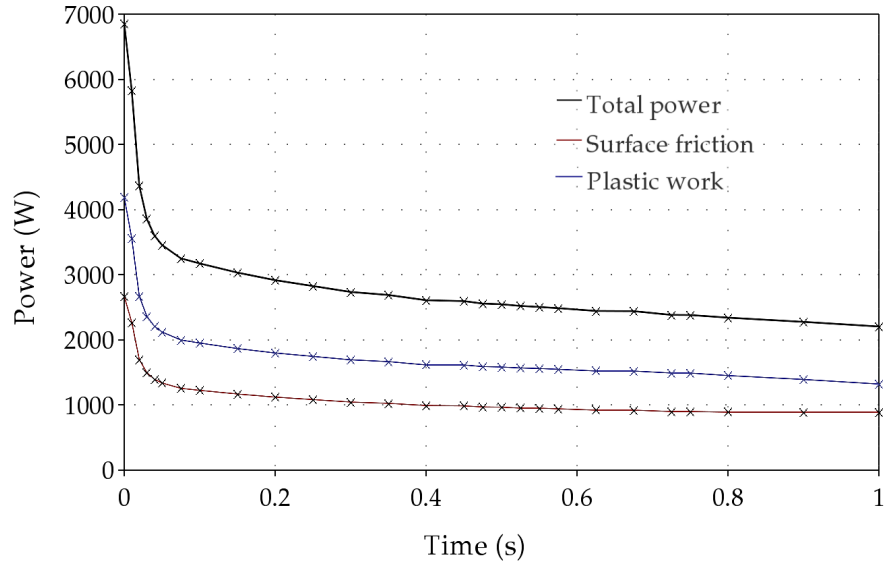


Figure 6.24: Predicted power for a weld with a copper backing plate, at 160 rad/s

however, the difference is minimal. This suggests that the benefit of switching to copper anvils may not be as large as first thought.

$$\eta_T = \frac{T_1 - T_0}{T_2 - T_0} \quad (6.4)$$

In Chapter 4, tentative values of T_1 and T_2 were suggested for high-strength welds based on experimental data. The suggested limits were $T_1 > 670$ K and $T_2 < 605$ K; for the present weld, $T_1 = 523$ K and $T_2 = 431$ K, so the nugget is colder than desired. With a copper backing plate, steady-state conditions are reached very quickly: by 0.5 s, the temperature field is already stable and the temperature at the tool to workpiece interface is very close to the solidus. Under these conditions, more heat cannot be added to the weld: an increase in tool speed reduces the flow stress, limiting the heat input, and increasing the duration of the weld simply maintains the extant temperature field for longer. Consequently, the results for T_1 and T_2 from this simulation suggest that welding under these conditions will not heat the interface sufficiently to produce a joint, and all deformation will be confined to the top sheet.

To circumvent this problem, other welding parameters may be varied: for example, the use of the wiper tool or deeper plunges (both of which extend the deformation zone deeper into the workpieces — see Chapters 3 and 5) may be needed. Of course, practical limitations may prevent the use of certain conditions, and one of the main constraints with FSSW is the torque capabilities of the machine. For example, the CS Powerstir machine used at Manchester has a maximum rated torque of 100 Nm (it is designed primarily for seam FSW, and is capable of welding thicker plate than used in these experiments — the power and downforce limits are far in excess of those required for thin sheet FSSW). The snapshot model can be used to calculate the required torque; the torque during the previous two simulations is shown in Figure 6.25. From these, it can be seen that the average torque required for welding with a copper backing plate is actually lower than with steel, despite the higher power. A lower average torque may well lead to lower tool wear and increase the life of the machine. However, it may be the *peak* torque that is more relevant, and this is very similar in both cases.

The reduced torque with a copper backing plate is beneficial, but the higher weld energies required represent a cost. In purely financial terms, this may be offset by lower tool wear; in environmental terms, it may be harder to justify. The analysis in Section 4.10.2 suggested that high-conductivity backing plates could bring about significant improvements in the strength of FSSW joints. The present chapter indicates that these improvements may lie outside the physically possible parameter space. Further analysis is needed to assess whether such welds are possible, and if so, whether the compromises entailed are justified.

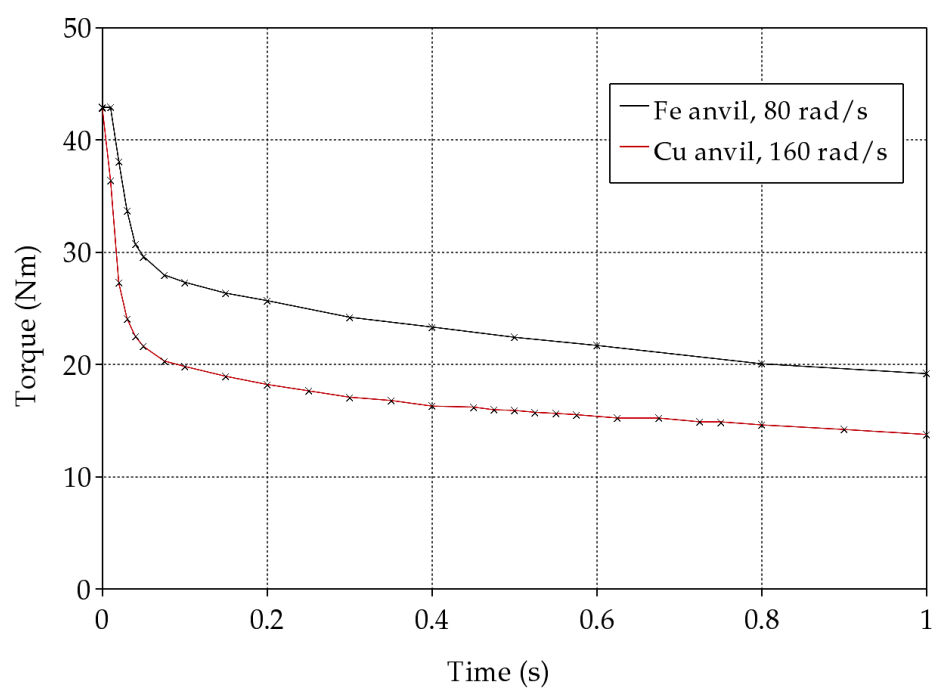


Figure 6.25: Predicted torque histories for a weld with a steel anvil at 80 rad/s (760 rev/min), and with a copper anvil at 160 rad/s (1528 rev/min)

6.4 Conclusions

The plunge analysis conducted in the first part of this chapter shows that an accurate representation of the tool is necessary. Even for a non-rotating case, surface friction affects the stress by constraining deformation of the workpiece — especially when, as in FSSW, the tool is much stiffer than the material to be welded. Neither a uniform pressure nor a uniform displacement, as sometimes used by previous modelling approaches, can be relied upon as accurate boundary conditions; only a finite-stiffness tool gives rise to realistic stresses in the workpiece.

The second part of this chapter introduced the sequential small-strain analysis method. This method appears to be an effective means of studying deformation and predicting power requirements during FSSW, provided that the slip condition at the interface and the material behaviour are both known. Even with an unknown slip condition — as is generally the case in practice — a degree of self-balancing occurs: if the model underestimates strain-rates in the bulk, there is correspondingly more slip (and heat generation) at the surface. A finer timestep and a finer grid would improve the accuracy but the method is practical in principle, and takes far less computation time than fully coupled models to solve similar problems. The only input data required concerns the weld geometry, an initial power estimate, a surface slip profile, and material constitutive data. Using the method to predict peak weld temperatures to within 30 K can be considered a substantial success. Although not as accurate as thermal models using measured or calibrated input powers, the snapshot model is also able to predict tool torques, and stresses and strains in the workpiece.

The novel sequentially coupled FE model therefore shows the potential to link the constitutive behaviour to the heat generation in a computationally efficient manner, and to shed light on the nature of the stick-slip behaviour under the tool. Further development of the approach depends on well-instrumented experiments to quantify the downforce and torque as functions of time, and independent measurement of the constitutive behaviour for the range of temperatures and strain-rates experienced in friction stir processing.

Following development of the model, the same method was used to analyse temperatures in the nugget and HAZ for novel welding conditions. The use of the snapshot model, combined with the process window developed earlier, shows that welding with high vertical heat flow conditions can lead to temperature fields that give rise to high-strength welds. A possible practical weld using AA6082 and a copper backing plate was simulated from a cold start, and the model was used to predict temperature, torque and power data. The use of a copper backing plate may be an effective method to increase the strength of joints in thin-sheet 6000 series aluminium alloys, although doing so requires higher weld energies.

The same techniques could be applied to the analysis of other geometries and alloy combinations to design effective experimental programmes for weld optimisation.

Chapter 7

Conclusions and further work

FSSW is a comparatively new and poorly-understood process. While much research has been carried out on continuous seam welding, including FSW, FSSW is a fast transient process where the heat flow and deformation are strongly linked. As a consequence, existing assumptions about input parameters result in poor models. In Chapter 4, the FE method was applied to simulate FSSW as a purely thermal process, and in doing so, a greater understanding of the boundary conditions present in FSSW was developed. This knowledge was applied to model a wide range of welds and develop a process window, which describes the relationship between power input and welding time that gives rise to optimum-strength welds. The analysis was extended to produce a second process window for welding with a copper backing plate, which illustrates the advantages of using high-diffusivity materials such as copper.

An analysis of heat flow in the weld could be successfully tackled with existing FE tools; however, material flow during welding is more complicated, and existing tools were poorly-suited to the task of modelling deformation. Two new approaches have been devised and developed: the kinematic method and sequential small-strain analysis.

The kinematic model involved a set of assumptions about the weld boundary conditions that, when applied together, led to a substantially simplified model of the welding process. The model could simulate flow in welding and

the resulting flow patterns were governed by a small number of dimensionless groups. The most important of these was $\bar{\omega}$, the ratio of the speed of rotation to the progression of the onset of deformation. The method was shown to produce weld images that agree with the patterns found in experimental welds, for top-down and section views, under a wide range of conditions. This shows that the underlying assumptions used to develop the model are likely to be correct, in particular, that metal flow during the process is primarily axisymmetric and highly constrained by surrounding cold material. The kinematic model was used to show a number of effects in more detail than can be seen in experimental welds, including the effects of a molten layer of zinc when welding galvanised steel and the flow patterns caused by deep plunge welding.

The second new approach developed was the sequential small-strain analysis method (SSsA), a form of sequentially-coupled FEA which can take account of elastic stresses and plastic flow caused by tool downforce and rotation. Welding simulations using this approach enabled predictions to be made of the spatial and temporal evolution of heat generation, directly from the constitutive behaviour of the alloy and the assumed velocity profile at the tool-workpiece interface. SSsA was used to model welds in thick and thin plate AA7449 as a proof-of-concept, and was then extended to simulate experimental welds in AA6082. The method produced temperature predictions that were compared to experimental thermocouple measurements, and that agreed well.

Early experimental work indicated that high-conductivity backing plates could give rise to high-strength welds. However, it was not possible to develop an understanding of the mechanisms involved from experimental work alone. The modelling work presented here explained the observed effects, and was used to model novel conditions and extend the process window to include simulated welds with copper backing plates. The SSsA model supported the conclusions of the thermal FE work, although it also showed that there could be practical difficulties involved in delivering sufficient power to the weld when using a copper anvil.

Overall, these three sets of analyses contribute to an enhanced understanding of the FSSW process. The models are fast, and well-suited for integration with microstructural models, such as models of HAZ softening or the formation of intermetallics at the interface in dissimilar welds. The techniques developed for sequential small strain FE analysis could also be investigated for use in other kinematically constrained solid-state friction joining processes.

References

- ABEDRABBO, N., POURBOGHRAAT, F. & CARSLEY, J. (2006)
Forming of aluminum alloys at elevated temperatures — part 1:
Material characterization, *International Journal of Plasticity* 22(2):314
- ADDISON, A. & ROBELOU, A. (2004), Friction stir spot welding: principal
parameters and their effects, in *Proc. 5th International Friction Stir
Welding Symposium*, TWI Ltd. (Metz, France)
- ALANKAR, A. & WELLS, M.A. (2010), Constitutive behavior of as-cast
aluminum alloys AA3104, AA5182 and AA6111 at below solidus tem-
peratures, *Materials Science and Engineering A: Structural Materials
Properties, Microstructure and Processing* 527(29–30):7812
- ALTENKIRCH, J., STEUWER, A., PEEL, M., RICHARDS, D.G. & WITHERS,
P.J. (2008), The effect of tensioning and sectioning on residual stresses in
aluminium AA7749 friction stir welds, *Mat. Sci. & Eng. A* 488(1-2):16
- The Aluminium Association (2000), Aluminum Standards and Data
- The Aluminium Association (2001), Alloy Designations and Chemical Com-
position Limits for Wrought Aluminum Alloys
- AMZA, G., CICIC, D.T., RONTESCU, C., APOSTOLESCU, Z. & PICA, D.
(2009), Theoretical and experimental research on the environmental impact
of certain welding processes, in L. Trilling et al. (eds.) *Proc. 4th int. conf.
on energy and environment*, IASME/WSEAS (Cambridge, England)
- ANDING, D.K. (2005), Constitutive equations in finite element codes: The
interatom model in Abaqus, *Structural Integrity & Durability* 1:95

- ARORA, A., NANDAN, R., REYNOLDS, A.P. & DEBROY, T. (2009)
Torque, power requirement and stir zone geometry in friction stir welding through modeling and experiments, *Scripta Materialia* 60(1):13
- ASHBY, M. & CEBON, D. (2009)
Cambridge Engineering Selector (software package), Granta Design
- ASKARI, A., SILLING, S., LONDON, B. & MAHONEY, M. (2001)
Modeling and analysis of friction stir welding processes, in *Friction Stir Welding & Processing* (ASM, Ohio, USA)
- AUKRUST, T. & LAZGHAB, S. (2000)
Thin shear boundary layers in flow of hot aluminium, *Int. Journal of Plasticity* 16(1):59
- AWANG, M., MUCINO, V., FENG, Z. & DAVID, S. (2005)
Thermo-mechanical modeling of friction stir spot welding (FSSW) process: Use of an explicit adaptive meshing scheme, *2nd SAE Congress*, SAE (Warrendale, USA)
- AWANG, M. & MUCINO, V.H. (2010)
Energy generation during friction stir spot welding (FSSW) of Al 6061-T6 plates, *Materials and Manufacturing Processes* 25(1):167
- BABU, S., SANKAR, V., JANAKI RAM, G., VENKITAKRISHNAN, P., MADHUSUDHAN REDDY, G. & PRASAD RAO, K. (2012)
Microstructures and mechanical properties of friction stir spot welded aluminum alloy AA2014, *Journal of Materials Eng. & Performance* 1–14
- BABU, S.S. (2009)
Thermodynamic & kinetic models for describing microstructure evolution during joining of metals & alloys, *Int. materials reviews* 54(6):333
- BACHMANN, M., AVILOV, V., GUMENYUK, A. & RETHMEIER, M. (2012)
Multi-physical FE simulation of an electromagnetic weld pool support in laser welding, in *10th int. sem.: numerical analysis for weldability*, T. U. Graz (Graz, Austria)

- BADARINARAYAN, H., HUNT, F. & OKAMOTO, K. (2007), FSSW
in *Friction stir welding and processing* (ASM International), 235–272
- BADARINARAYAN, H., YANG, Q. & ZHU, S. (2009)
Effect of tool geometry on static strength of friction stir spot-welded
aluminum alloy, *Int. Journal of Machine Tools & Manufacture* 49(2):142
- BAKAVOS, D., CHEN, Y., BABOUT, L. & PRANGNELL, P. (2011)
Material interactions in a novel pinless tool approach to friction stir spot
welding thin aluminum sheet, *Met. and Mat. Trans. A* 42:1266
- BAKAVOS, D., HADDADI, F. & PRANGNELL, P. (2009)
FSSW of aluminium automotive sheet (private communication)
- BAKAVOS, D. & PRANGNELL, P.B. (2009), Effect of reduced or zero pin
length and anvil insulation on friction stir spot welding thin gauge 6111
automotive sheet, *Science and Technology of Welding & Joining* 14:443
- BALAMUTH, L., KURIS, A. & KLEESATTEL, C. (1959)
Ultrasonic welding, USA Patent 3053124
- BALASUBRAMANIAN, K.R. (2012), Keyhole modelling of Nd:YAG laser
welding of stainless steel butt joint, in *10th international seminar: nu-
merical analysis for weldability*, T. U. Graz (Graz, Austria)
- BANERJEE, S., ROBI, P.S., SRINIVASAN, A. & KUMAR, L.P. (2010)
High temperature deformation behavior of Al-Cu-Mg alloys micro-alloyed
with Sn, *Materials Science and Engineering A*: 527(10-11):2498
- BARNES, T. & PASHBY, I. (2000)
Joining techniques for aluminium spaceframes used in automobiles, Part I:
solid and liquid phase welding, *Journal of Mat. Processing Tech.* 99(1):62
- BASTIER, A., MAITOURNAM, M.H., DANG VAN, K. & ROGER, F. (2006)
Steady state thermomechanical modelling of friction stir welding, *Science
and Technology of Welding & Joining* 11(3):278

- BASTIER, A., MAITOURNAM, M.H., ROGER, F. & VAN, K.D. (2008)
Modelling of the residual state of friction stir welded plates, *Journal of Materials Processing Technology* 200(1-3):25
- BHOJWANI, S. (2007), Smoothed particle hydrodynamics modeling of the friction stir welding process. Ph.D. thesis, University of Texas (USA)
- BILICI, M. & YÜKLER, A. (2012), Influence of tool geometry and process parameters on macrostructure and static strength in friction stir spot welded polyethylene sheets, *Materials & Design* 33:145
- BJORNEKLETT, B., GRONG, Ø., MYHR, O. & KLUKEN, A. (1999)
A process model for the heat-affected zone microstructure evolution in al-zn-mg weldments, *Metallurgical & Materials Trans. A: Physical Metallurgy and Materials Science* 30(10):2667
- BONTHA, S., KLINGBEIL, N.W., KOBRYN, P.A. & FRASER, H.L. (2006)
Thermal process maps for predicting solidification microstructure in laser fabrication of thin-wall structures, *Journal of Materials Processing Technology* 178(1-3):135
- BOZZI, S., HELBERT-ETTER, A., BAUDIN, T., CRIQUI, B. & KERBIGUET, J. (2010), Intermetallic compounds in Al 6016/IF-steel friction stir spot welds, *Materials Science and Engineering: A* 527(16–17):4505
- BROWN, J. (2008)
The effects of sealants and surface treatments on the faying surface of swept friction stir spot welds. Ph.D. thesis, Wichita State University (USA)
- BUFFA, G. & FRATINI, L. (2010)
Towards tool path numerical simulation in modified friction stir spot welding processes, *Advanced Materials Research* 83:1220
- BUFFA, G., FRATINI, L. & PIACENTINI, M. (2008)
On the influence of tool path in friction stir spot welding of aluminum alloys, *Journal of materials processing technology* 208(1):309

- BUFFA, G., FRATINI, L. & SHIVPURI, R. (2007)
CDRX modelling in friction stir welding of AA7075-T6 aluminum alloy:
Analytical approaches, *Journal of Materials Processing Tech.* 191(1-3):356
- CAO, X., JAHAZI, M., IMMARIGEON, J. & WALLACE, W. (2006)
A review of laser welding techniques for magnesium alloys, *Journal of Materials Processing Tech.* 171(2):188
- CARNEY, D. (2008), Advance metals gaining momentum, *Automotive Engineering International* 116(8):44
- CARPENTER (2012), Titanium datasheet
(Technical report, Dynamet Holdings Inc.)
- CARSLAW (1945), Introduction to the mathematical theory of the conduction of heat in solids, (Dover Publications, New York, USA)
- CERJAK, H. & BHADESHIA, H. (eds.) (2002), Mathematical Modelling of Weld Phenomena 6 (Maney Publishing, London, UK)
- CHARIT, I., MISHRA, R.S. & JATA, K.V. (2001), Superplastic behavior of friction stir processed aluminum-lithium alloy, in K.V. Jata (ed.) *Friction stir welding and processing*:225–234, TMS (Warrendale, USA)
- CHARIT, I., MISHRA, R.S. & MAHONEY, M.W. (2002)
Multi-sheet structures in 7475 aluminum by friction stir welding in concert with post-weld superplastic forming, *Scr. Mater.* 47:631
- CHEN & LIN (2010)
Optimal FSW process parameters for interface and welded zone toughness of dissimilar Al-steel joint, *Sci. & Tech. of Welding & Joining* 15(4):279
- CHEN, Y. (2010), Rapid FSSW for joining Al to steel automotive sheet (unpublished research)
- CHEN, Y. & NAKATA, K. (2009), Effect of tool geometry on microstructure and mechanical properties of friction stir lap welded magnesium alloy and steel, *Materials & Design* 30(9):3913

- CHOI, D.H., AHN, B.W., LEE, C.Y., YEON, Y.M., SONG, K. & JUNG, S.B. (2011), Formation of intermetallic compounds in Al and Mg alloy interface during friction stir spot welding, *Intermetallics* 19(2):125
- COLEGROVE, P., IKEAGU, C., THISTLETHWAITE, A., WILLIAMS, S., NAGY, T., SUDER, W., STEUWER, A. & PIRLING, T. (2009) Welding process impact on residual stress and distortion, *Science and Technology of Welding and Joining* 14(8):717
- COLEGROVE, P., PAINTER, M., GRAHAM, D. & MILLER, T. (2000) 3-dimensional flow and thermal modelling of the friction stir welding process, in *2nd Int. Symp. on Friction Stir Welding*:162–169, TWI Ltd. (Gothenburg, Sweden)
- COLEGROVE, P. & SHERCLIFF, H. (2004) Development of trivex friction stir welding tool part 2: three-dimensional flow modelling, *Science and Technology of Welding & Joining* 9(4):352
- COLEGROVE, P. & SHERCLIFF, H. (2006) CFD modelling of friction stir welding of thick plate 7449 aluminium alloy, *Science and Technology of Welding and Joining* 11(4):429
- COLEGROVE, P., SHERCLIFF, H. & HYOE, T. (2004) Development of the Trivex friction stir welding tool for making lap welds, in *Proc. 5th Int. Friction Stir Welding Symp.*, TWI Ltd. (Metz, France)
- COLEGROVE, P., SHERCLIFF, H. & THREADGILL, P. (2003) Modelling and development of the trivex friction stir welding tool, in *Proc. 4th Int. Symp. on Friction Stir Welding*, TWI Ltd. (Park City, USA)
- COLEGROVE, P.A. & SHERCLIFF, H.R. (2005) 3-dimensional CFD modelling of flow round a threaded friction stir welding tool profile, *Journal of Materials Processing Technology* 169(2):320
- COLEGROVE, P.A., SHERCLIFF, H.R. & ZETTLER, R. (2007), Model for predicting heat generation and temperature in friction stir welding from material properties, *Sci. & Tech. of Welding and Joining* 12(4):284

- CONNOLLY, C. (2007)
Friction spot joining in aluminium car bodies, *Industrial Robot* 34(1):17
- CONSTANTINESCU, A., CHARKALUK, E., LEDERER, G. & VERGER, L. (2004), A computational approach to thermomechanical fatigue, *International Journal of Fatigue* 26(8):805
- COOK, R., HANDBOY, T., FOX, S.L. & ARBEGAST, W. (2005)
Friction stir welding of dissimilar aluminum alloys, in *2005 TMS Annual Meeting*:35–42, TMS (San Francisco, USA)
- DAS, R. & CLEARY, P.W. (2007), Modelling plastic deformation and thermal response in welding using smoothed particle hydrodynamics, in P. Jacobs et al. (eds.) *16th Australasian Fluid Mechanics Conference*:253, University of Queensland (Brisbane, Australia)
- DEHELEAN, D. (2009), Environmental friendly welding - an evolution from 3d (dirty, dusty, dangerous) to 3c (cool, clever and clean), *Environmental Engineering and Management Journal* 8(4):957
- DESCHAMPS, A., GENEVOIS, C., NICOLAS, M., PERRARD, F. & BLEY, F. (2005), Study of precipitation kinetics: towards non-isothermal and coupled phenomena, *Philosophical Magazine* 85(26):3091
- DICKERSON (2002), FSW benchmark tests, Online at www-materials.eng.cam.ac.uk/FSW_Benchmark; accessed on 7/9/11
- DIPPE, W. (1970), Measurement of power required for the ultra-sonic welding of aluminium, *Schweiss Technik* 20(3):108
- DU, Y., CHANG, Y., HUANG, B., GONG, W., JIN, Z., XU, H., YUAN, Z., LIU, Y., HE, Y. & XIE, F.Y. (2003)
Diffusion coefficients of some solutes in FCC and liquid Al: critical evaluation and correlation, *Materials Science and Engineering: A* 363(1–2):140
- DUBOURG, L., GHOLIPOUR, J. & JAHAZI, M. (2009)
Friction stir welding of 2024-T3 aluminum tubes for hydroforming application, *Trends in Welding Research* 2008

- DUMONT, M., STEUWER, A., DESCHAMPS, A., PEEL, M. & WITHERS, P. (2006), Microstructure mapping in friction stir welds of AA7449 using SAXS, *Acta Materialia* 54(18):4793
- DUTTA, I. & ALLEN, S. (1991)
A calorimetric study of precipitation in commercial aluminium alloy 6061, *Journal of Materials Science Letters* 10:323
- ECHEVERRIA, A., ZABALETA, A., ALVAREZ, P., ALDANONDO, E., SOLIS, J. & DA SILVA, A. (2009), Influence of welding parameters and tool geometry on the mechanical performance of FSSW Al-Mg alloys, in *Proc. 8th int. conf. on trends in welding research* (Pine Mountain, USA)
- EISANDEH, H., HAMED, M. & HALVAEE, A. (2010)
New parametric study of nugget size in resistance spot welding process using finite element method, *Materials & Design* 31(1):149
- ESKIN, D., SUYITNO & KATGERMAN, L. (2004)
Mechanical properties in the semi-solid state and hot tearing of aluminium alloys, *Progress in Materials Science* 49(5):629
- ESKIN, G.I. (2001)
Broad prospects for commercial application of the ultrasonic (cavitation) melt treatment of light alloys, *Ultrasonics Sonochemistry* 8(3):319
- ESMAEILI, S., CHENG, L., DESCHAMPS, A., LLOYD, D. & POOLE, W. (2001), The deformation behaviour of AA6111 as a function of temperature and precipitation state, *Materials Science and Engineering A* 319-321:461
- FENG, Z., SANTELLA, M., DAVID, S., STEEL, R., PACKER, S., PAN, T., KUO, M. & BHATNAGAR, R. (2005)
Friction stir spot welding of advanced high-strength steels: a feasibility study, *SAE technical paper (2005-01)*:1248
- FERRASSE, S., SEGAL, V.M., HARTWIG, K.T. & GOFORTH, R.E. (1997)
Development of a submicrometer-grained microstructure in AA6061 using equal channel angular extrusion, *Journal of Materials Research* 12:1253

- FRATINI, L., BARCELLONA, A., BUFFA, G. & PALMERI, D. (2007)
Friction stir spot welding of AA6082-T6: Influence of the most relevant process parameters and comparison with classic mechanical fastening techniques, *Proc. Institution of Mechanical Engineers, Part B: Journal of Engineering Manufacture* 221(7):1111
- FRIGAARD, Ø., GRONG, Ø., BJORNEKLETT, B. & MIDLING, O. (1999)
Modelling of the thermal and microstructural fields during friction stir welding of aluminium alloys, in *Proc. 1st Int. Symp. on Friction Stir Welding*, TWI Ltd. (Thousand Oaks, USA)
- FRIGAARD, Ø., GRONG, Ø. & MIDLING, O. (2001)
A process model for friction stir welding of age hardening aluminum alloys, *Metallurgical and Materials Transactions A* 32:1189
- GATZEN, M. & CHONGBUNWATANA, K. (2012), Different strategies to simulate a deep penetration welding process, in *10th international seminar: numerical analysis for weldability*, T. U. Graz (Graz, Austria)
- GERLICH, A. & NORTH, T. (2011), Friction stir spot welding, *Innovations in Materials Manufacturing, Fabrication, and Environmental Safety*:193
- GERLICH, A., SU, P. & NORTH, T. (2005), Tool penetration during friction stir spot welding of Al and Mg alloys, *Journal of Materials Science* 40:6473
- GERLICH, A., SU, P. & NORTH, T. (December 2005), Peak temperatures and microstructures in aluminium and magnesium alloy friction stir spot welds, *Science and Technology of Welding & Joining* 10:647
- GRONG, Ø. (1997)
Metallurgical Modelling of Welding. (Maney Publishing, London, UK)
- GUERDOUX, S. & FOURMENT, L. (2007)
Error estimation and accurate mapping based ALE formulation for 3D simulation of FSW, in *Proc. 7th conf. numerical methods in industrial forming processes* 908:185, American Insitute of Physics (Porto, Portugal)

- GUERDOUX, S., FOURMENT, L., MILES, M. & SORENSSEN, C. (2004)
 Numerical simulation of the friction stir welding process using both lagrangian and ALE formulations, in *Proc. 8th conf. on numerical methods in industrial forming processes*:1259, Amer. Inst. Phys. (Columbus, USA)
- HADDADI, F. (2010), Effect of zinc coatings on ultrasonic welding of aluminium to steel (private communication)
- HADDADI, F. (2012)
 Joint Performance and Interface Reactions in Dissimilar Aluminium to Steel Ultrasonic Spot Welding, Ph.D. thesis, University of Manchester
- HAGHAYEGHI, R., ZOQUI, E.J. & BAHAI, H. (2009)
 An investigation on the effect of intensive shearing on the grain refinement of AA5754 aluminium, *Journal of Alloys and Compounds* 481(1-2):358
- HAMPEL, C.A. (1961)
 Rare metals handbook (Reinhold Publishing, New York, USA)
- HARGREAVES, B. (2009)
 Weld of difference, *Professional Engineering* 22(9):38
- HASHIMOTO, T., ALUMINIUM), S.J.S., NAKATA, K., KIN, Y.G. & UNIVERSITY), M.U.O. (1999), FSW joining of high strength Al alloy, in *Proc. 1st Int. Symp. on Friction Stir Welding*, TWI Ltd. (Thousand Oaks, USA)
- HE, X., PEARSON, I. & YOUNG, K. (2008)
 Self-pierce riveting for sheet materials: State of the art, *Journal of Materials Processing Technology* 199(1-3):27
- HECTOR, L., CHEN, Y., AGARWAL, S. & BRIANT, C. (2004)
 Texture characterization of autogenous Nd-YAG laser welds in AA5182-O and AA6111-T4, *Metallurgical and Materials Transactions A* 35(9):3032
- HECTOR, L., CHEN, Y.L., AGARWAL, S. & BRIANT, C. (2007)
 Friction stir processed AA5182-O and AA6111-T4 aluminum alloys: Part 2: Tensile properties and strain field evolution, *Journal of Materials Engineering and Performance* 16:404

- HERBELOT, C., HOANG, T., IMAD, A. & BENSEDDEQ, N. (2010)
Damage mechanisms under tension shear loading in friction stir spot welding, *Science and Technology of Welding & Joining* 15(8):688
- HERBELOT, C., HOANG, T., IMAD, A. & BENSEDDEQ, N. (2011)
Mechanical behaviour of a friction stir spot welding lap under static loading, in *Int. Conf. advances in materials & processing tech.* 1315:917
Amer. Inst. Phys (Paris, France)
- HINRICHS, J.F., SMITH, C.B., ORSINI, B.F., DEGEORGE, R.J., SMALE, B.J. & RUEHL, P.C. (2004)
Friction stir welding for the 21st century automotive industry, in *Proc. 5th int. symp. on friction stir welding*, TWI Ltd. (Metz, France)
- HYOE, T., SHERCLIFF, H. & COLEGROVE, P. (2003)
Thermal and microstructure modelling in thick plate AA7075 friction stir welds, in *Proc. TMS Spring Meeting, Friction Stir Welding II*:33
The Minerals, Metals and Materials Society (San Diego, USA)
- ION, J., SHERCLIFF, H. & ASHBY, M. (1992), Diagrams for laser materials processing, *Acta metallurgica et materialia* 40(7):1539
- IWASHITA, T. (2003)
Method and apparatus for joining, USA patent 6601751
- JAIN, M., ALLIN, J. & BULL, M.J. (1998), Deep drawing characteristics of automotive aluminum alloys, *Materials Science and Engineering A* 256:69
- JARIYABOON, M., DAVENPORT, A.J., AMBAT, R., CONNOLLY, B.J., WILLIAMS, S.W. & PRICE, D.A. (2010)
Effect of cryogenic cooling on corrosion of friction stir welded AA7010-T7651, *Anti-corrosion Methods and Materials* 57(2):83
- JATA, K., SANKARAN, K. & RUSCHAU, J. (2000)
Friction-stir welding effects on microstructure and fatigue of aluminum alloy 7050-T7451, *Metallurgical and Materials Transactions A* 31:2181

- JĘDRASIAK, P. (2012), Modelling of Friction Stir Spot Welding
M. Phil. thesis, University of Cambridge
- JĘDRASIAK, P., A. REILLY, H. R. SHERCLIFF, McSHANE, G.J., CHEN, Y.C. & PRANGNELL, P. (2012)
Thermal modelling of Al-Al & Al-steel friction stir spot welding, in *10th int. sem.: numerical analysis for weldability*, T. U. Graz (Graz, Austria)
- JOHNSON, R. et al. (2001), Forces in friction stir welding of aluminium alloys, in *Proc. 3rd int. symp. on Friction Stir Welding*:27 (Kobe, Japan)
- KAIBYSHEV, R., SITDIKOV, O., MAZURINA, I. & LESUER, D. (2002)
Deformation behavior of AA2219, *Mat. Sci. & Eng. A*: 334(1-2):104
- KALEMBA, I., DYMEK, S., HAMILTON, C. & Blicharski, M. (2009)
Microstructure evolution in friction stir welded aluminium alloys, *Archives of Metallurgy and Materials* 54(1):75
- KALYA, P., KRISHNAMURTHY, K., MISHRA, R.S. & BAUMANN, J.A. (2007), Specific energy and temperature mechanistic models for friction stir processing of Al-f357, in *Friction Stir Welding and Processing IV*:113, The minerals, metals & materials soc. (Orlando, USA)
- KAMP, N., SULLIVAN, A., TOMASI, R. & ROBSON, J. (2006a)
Modelling of heterogeneous precipitate distribution evolution during friction stir welding process, *Acta Materialia* 54(8):2003
- KAMP, N., SULLIVAN, A., TOMASI, R. & ROBSON, J.D. (2006b)
Modelling heterogeneous precipitation in 7xxx aluminium alloys during complex processing, *Materials Science Forum vol. 519*:1435-1440
- KAMPMANN, R. & WAGNER, R. (1991), Materials Science and Technology: A Comprehensive Treatment (Wiley-VCH, Weinheim, Germany)
- KATAYAMA, S. (1996), Laser welding phenomena and melting of aluminium alloys, *Journal of light metal welding and construction* 34(4):23

KHALID, A. (2002)

European-sponsored NDT research at TWI Ltd., *NDT.net vol. 7*:6

KHANDKAR, M., KHAN, J. & REYNOLDS, A. (2003), Prediction of temperature distribution and thermal history during friction stir welding: input torque based model, *Sci. & Tech. of Welding and Joining* 8(3):165

KHANNA, S., LONG, X., PORTER, W., WANG, H., LIU, C., RADOVIC, M. & LARA-CURZIO, E. (2005), Residual stresses in spot welded new generation Al alloys. Part a: thermophysical and thermomechanical properties of AA6111 and AA5754, *Sci. & Tech. of Welding and Joining* 10(1):82

KIHO RHEE, R.L. & THOMS, P.F. (2005)

The influence of severe plastic deformation on the mechanical properties of AA6111, *Journal of the Minerals, Metals and Materials Society* 57(5):62

KIM, J.H., KIM, D.G. & CHUNG, K.S. (2007)

Numerical simulation of fsw of AA6111-T4 sheets, *Key Engineering Materials: The Mechanical Behavior of Materials X*:1433

KOMANDURI, R. & HOU, Z.B. (2009), Unified approach and interactive program for thermal analysis of various manufacturing processes with application to machining, *Machining Science and Technology* 13(2):143

KWON, Y., SAITO, N. & SHIGEMATSU, I. (2002)

Friction stir process as a new manufacturing technique of ultrafine grained aluminum alloy, *Journal of Materials Science Letters* 21(19):1473

LAM, T.J., WIDENER, C.A., BROWN, J.M., TWEEDY, B.M. & BURFORD, D.A. (2009), Low Z-force friction stir spot welds - conventional tool & process development approach, in R. Mishra *et al.* (eds.) *Friction stir welding and processing V*, TMS (San Francisco, USA)

LAMBRAKOS, S.G., FONDA, R.W., MILEWSKI, J.O. & MITCHELL, J.E. (2003), Analysis of friction stir welds using thermocouple measurements, *Science and Technology of Welding & Joining* 8:385

- LATHABAI, S., PAINTER, M., CANTIN, G. & TYAGI, V. (2006), Friction spot joining of an extruded Al-Mg-Si alloy, *Scripta Materialia* 55(10):899
- LEE, C.Y., CHOI, D.H., YEON, Y.M. & JUNG, S.B. (2009)
Dissimilar friction stir spot welding of low carbon steel and Al-Mg alloy by formation of IMCs, *Science and Technology of Welding & Joining* 14:216
- LIENERT, T., STELLWAG, W., GRIMMETT, B. & WARKE, R. (2003)
Friction stir welding studies on mild steel, *Welding Journal* 82(1):1S
- LOMBARD, H., HATTINGH, D.G., STEUWER, A. & JAMES, M.N. (2009)
Effect of process parameters on the residual stresses in AA5083-T351 friction stir welds, *Mat. Sci. & Eng. A: 501*(1-2):119
- LONGHURST, W.R., STRAUSS¹, A.M., COOK¹, G.E. & FLEMING, P.A. (2010), Torque control of friction stir welding for manufacturing and automation, *Int. Journal of Advanced Manufacturing Tech.*
- LORRAIN, O., SERRI, J., FAVIER, V., ZAHROUNI, H. & EL HADROUZ, M. (2009), A contribution to a critical review of friction stir welding numerical simulation, *Journal of Mechanics of Materials and Structures* 4(2):351
- MA, Z.Y. (2008), Friction stir processing technology: A review, *Metallurgical and Materials Trans. A: Physical Metallurgy and Materials Sci.* 39A(3):642
- MACKWOOD, A. & CRAFER, R. (2005)
Thermal modelling of laser welding and related processes: a literature review, *Optics and Laser Technology* 37(2):99
- Magnesium Industry Council (1962), Magnesium in general engineering (Balding and Mansell, Wisbech, UK)
- MAHONEY, M., MISHRA, R.S., NELSON, T., FLINTOFF, J., ISLAMGALIEV, R. & HOVANSKY, Y. (2001)
High strain rate, thick section superplasticity created via friction stir processing, in *Friction stir welding & processing* (TMS, Warrendale, USA)

- MANDAL, S., RICE, J. & ELMUSTAFA, A. (2008)
Experimental and numerical investigation of the plunge stage in friction stir welding, *Journal of Materials Processing Technology* 203(1-3):411
- MANDAL, S. & WILLIAMSON, K. (2006)
A thermomechanical hot channel approach for friction stir welding, *Journal of Materials Processing Technology* 174(1-3):190
- MARDER, A. (2000), The metallurgy of zinc-coated steel, *Progress in Materials Science* 45(3):191
- MATHON, M.H., KLOSEK, V., DE CARLAN, Y. & FOREST, L. (2009)
Study of PM2000 microstructure evolution following FSW process, *Journal of Nuclear Materials* 386:475
- MEDINA, S.F. & HERNANDEZ, C.A. (1996), General expression of the Zener-Hollomon parameter as a function of the chemical composition of low alloy and microalloyed steels, *Acta Materialia* 44(1):137
- MIDLING, O. & GRONG, Ø. (1994), A process model for friction welding Al–Mg–Si alloys and Al–SiC metal matrix composites. 1: HAZ temperature and strain rate distribution, *Acta Metallurgica et Materialia* 42(5):1595
- MILLS, K. (2001), Recommended Values of Thermophysical Properties for Selected Commercial Alloys (ASM International, Russell, Ohio)
- MISHRA, R. & MA, Z. (2005), Friction stir welding and processing, *Materials Science & Engineering R - Reports* 50(1-2):1
- MISHRA, R. & MAHONEY, M. (eds.) (2007)
Friction stir welding and processing (ASM International, Russell, Ohio)
- MISHRA, R.S., MAHONEY, M.W., MCFADDEN, S.X., MARA, N.A. & MUKHERJEE, A.K. (2000), High strain rate superplasticity in a friction stir processed 7075 Al alloy, *Scr. Mater.* 42:163

- MITLIN, D., RADMILOVIC, V., PAN, T., CHEN, J., FENG, Z. & SANTELLA, M. (2006), Structure-properties relations in spot friction welded (also known as friction stir spot welded) 6111 aluminum, *Materials Science and Engineering: A* 441(1-2):79
- MORAITIS, G.A. & LABEAS, G.N. (2010), Investigation of friction stir welding process with emphasis on calculation of heat generated due to material stirring, *Science and Technology of Welding and Joining* 15(2):177
- MORTON, P. (1976), The Contribution of Physical Metallurgy to Engineering Practice (The Royal Society, London, UK)
- MUCI-KUCHLER, K.H., KALAGARA, S. & ARBEGAST, W.J. (2010) Simulation of a refill friction stir spot welding process using a fully coupled thermo-mechanical FEM model, *Journal of manufacturing science and engineering* 132(1):1087
- MURPHY, J. (1961), Interdiffusion in dilute aluminium-copper solid solutions, *Acta Metallurgica* 9(6):563
- MURR, L., FLORES, R., FLORES, O., MCCLURE, J., LIU, G. & BROWN, D. (1998a), Friction-stir welding: microstructural characterization, *Materials Research Innovations* 1:211
- MURR, L., LI, Y., FLORES, R., TRILLO, E. & MCCLURE, J. (1998b) Intercalation vortices and related microstructural features in the friction-stir welding of dissimilar metals, *Materials Research Innovations* 2:150
- MYHR, O. & GRONG, Ø. (1991a) Process modeling applied to 6082-T6 aluminum weldments. 1: Reaction-kinetics, *Acta metallurgica et materialia* 39(11):2693
- MYHR, O. & GRONG, Ø. (1991b) Process modeling applied to 6082-T6 aluminum weldments. 2: Applications of model, *Acta metallurgica et materialia* 39(11):2703

- MYHR, O., GRONG, Ø., KLOKKEHAUG, S., FJOER, H. & KLUKEN, A. (1997), Process model for welding of Al–Mg–Si extrusions, part 1: Precipitate stability, *Science and Technology of Welding & Joining* 2(6):245
- MYHR, O., KLOKKEHAUG, S., GRONG, O., FJAER, H. & KLUKEN, A. (1998), Modeling of microstructure evolution, residual stresses and distortions in 6082-t6 aluminum weldments, *Welding Journal* 77(7):286S
- NANDAN, R., DEBROY, T. & BHADOSHIA, H.K.D.H. (2008)
Recent advances in friction-stir welding - process, weldment structure and properties, *Progress in Materials Science* 53(6):980
- NEPPIRAS, E. (1965), Ultrasonic welding of metals, *Ultrasonics* 3(3):128
- NICOLAS, M. & DESCHAMPS, A. (2003)
Characterisation and modelling of precipitate evolution in an Al–Zn–Mg alloy during non-isothermal heat treatments, *Acta Materialia* 51(20):6077
- NISHIHARA, T. & NAGASAKA, Y. (2003)
Measurement of tool temperature during friction stir welding, in *Proc. 4th Int. Symp. on Friction stir welding*, TWI Ltd., (Park City, USA)
- OUYANG, J., JANDRIC, D., KOVACEVIC, R., SONG, M. & VALANT, M. (2003), Visualization of material flow during friction stir welding of the same and dissimilar aluminum alloys, in *Proc. 6th Int. Conf. on Trends in Welding Research*, ASM International (Phoenix, USA)
- PACKHAM, D.E. (2009), Adhesive technology and sustainability, *International journal of adhesion and adhesives* 29(3):248
- PALM, F., STEIGER, H. & HENNEBOHLE, U. (2003), Improved Verification of FSW-Process Modeling relating to the Origin of Material Plasticity, in *Proc. 4th int. symp. on friction stir welding*, TWI Ltd. (Park City, USA)
- PANTELI, A. (2012)
Friction joining of aluminium to magnesium for lightweight automotive applications. Ph.D. thesis, University of Manchester

- PARK, S.H.C., SATO, Y.S., KOKAWA, H., OKAMOTO, K., HIRANO, S. & INAGAKI, M. (2004), Corrosion resistance of friction stir welded 304 stainless steel, *Scripta Materialia* 51(2):101
- PARKER, B. (2011), Modelling of friction-based joining processes
M.Eng. thesis, University of Cambridge
- PARRINI, L. (2001a)
Design of advanced ultrasonic transducers for welding devices, *IEEE Trans. on Ultrasonics Ferroelectrics and Frequency Control* 48(6):1632
- PARRINI, L. (2001b), Ultrasonic technologies enable ultra-fine-pitch, low-temperature bonding, *Solid state technology* 44(2):97
- PARRINI, L. (2003)
New techniques for the design of advanced ultrasonic transducers for wire bonding, *IEEE Trans. on Electronics Packaging Manufacturing* 26(1):37
- PEEL, M., STEUWER, A., PREUSS, M. & WITHERS, P. (2003), Microstructure, mechanical properties and residual stresses as a function of welding speed in AA5083 friction stir welds, *Acta materialia* 51(16):4791
- PEEL, M., STEUWER, A., WITHERS, P., DICKERSON, T., SHI, Q. & SHERCLIFF, H. (2006), Dissimilar friction stir welds in AA5083-AA6082. Part 1: Process parameter effects on thermal history and weld properties, *Metallurgical and Materials Transactions* 37A:2183
- PENG, J., FUKUMOTO, S., BROWN, L. & ZHOU, N. (2004)
Image analysis of electrode degradation in resistance spot welding of aluminium, *Science and Technology of Welding & Joining* 9(4):331
- PHILLION, A., THOMPSON, S., COCKCROFT, S. & WELLS, M. (2008)
Tensile properties of as-cast AA3104, AA6111 & CA31218 at above solidus temperatures, *Materials Science and Engineering A*: 497(1-2):388
- POLMEAR (1995)
Light alloys: metalurgy of the light metals (Arnold, London, UK)

- PRANGNELL, P. & HEASON, C. (2005)
Grain structure formation during friction stir welding observed by the ‘stop action technique’, *Acta materialia* 53(11):3179
- PRANGNELL, P.B. & BAKAVOS, D. (2010)
Novel approaches to friction spot welding thin aluminium automotive sheet, *Materials Science Forum* 638:1237
- PRASAD, Y., GEGEL, H., DORAIVELU, S., MALAS, J., MORGAN, J., LARK, K. & BARKER, D. (1984)
Modeling of dynamic material behavior in hot deformation: Forging of Ti-6242, *Metallurgical and Materials Transactions A* 15:1883
- RAMAEKERS, J. & VEENSTRA, P. (1970)
The relation between effective deformation and micro-hardness in a state of large plastic deformation, *Annals of the CIRP* 18:541
- RICHARDS, D.G., PRANGNELL, P.B., WITHERS, P.J., WILLIAMS, S.W., NAGY, T. & MORGAN, S. (2010), Efficacy of active cooling for controlling residual stresses in FSW, *Sci. & Tech. of Welding & Joining* 15(2):156
- RIGAL, E., LE MAROIS, G., LECHLER, T., REIMANN, G., SCHLEISIEK, K., SCHAFFER, L. & WEIMAR, P. (2000)
Development of FM steels diffusion bonding technologies for blanket manufacturing applications, *Fusion engineering and design* 49:651
- ROBSON, J.D., KAMP, N. & SULLIVAN, A. (2007)
Microstructural modelling for friction stir welding of aluminium alloys, *Materials and Manufacturing Processes* 22(4):450
- ROHSENOW, W.M. & HARTNETT, J.P. (1998)
Handbook of Heat Transfer (McGraw-Hill, New York, USA: 1st edn. 1973)
- ROSAKIS, P., ROSAKIS, A.J., RAVICHANDRAN, G. & HODOWANY, J. (2000), A thermodynamic internal variable model for the partition of plastic work into heat and stored energy in metals, *Journal of the Mechanics and Physics of Solids* 48(3):581

- ROSENTHAL, D. (1946), Theory of moving sources of heat and its application to metal treatments, *ASME Transactions* 68:849
- ROSENTHAL, D. (1941), Mathematical theory of heat distribution during welding and cutting, *Welding Journal* 20(5):220
- RUSSELL, M. (2000), Development and modelling of friction stir welding Ph.D. thesis, University of Cambridge
- RUSSELL, M.J. & SHERCLIFF, H.R. (1999)
Analytical modelling of microstructure development in friction stir welding, in *Proc. 1st Int. Symp. on Friction Stir Welding* (Thousand Oaks, USA)
- RYKALIN, N. (1951), Calculation of heat flow in welding (Mashgiz, Moscow, Russia), *translated by Paley, Z. and Adams, C.*
- RYKALIN, N. & NIKOLAEV, A. (1971)
Welding arc heat flow, *Welding in the World* 9(3/4):112
- SATO, Y., URATA, M. & KOKAWA, H. (2002), Parameters controlling microstructure and hardness during friction-stir welding of precipitation-hardenable AA6063, *Metallurgical and Materials Trans. A* 33(3):625
- SATO, Y.S., PARK, S.H.C., MICHUUCHI, M. & KOKAWA, H. (2004)
Constitutional liquation during dissimilar friction stir welding of Al and Mg alloys, *Scripta Materialia* 50(9):1233
- SCHILING, C., STROMBECK, A.V., SANTOS, J.F.D. & HEESSEN, N.V. (2000), A preliminary investigation on the static properties of friction stir spot welding, in *2nd International Symposium on Friction Stir Welding* (Gothenburg, Sweden)
- SCHIPPER, L., STEINER, R., DUERR, P., AN, F. & STROM, S. (1992)
Energy use in passenger transport in OECD countries: changes since 1970, *Transportation* 19(1):25
- SCHMIDT (2012), Private communication

- SCHMIDT, H. & HATTEL, J. (2005)
A local model for the thermomechanical conditions in friction stir welding,
Modelling and Simulation in Materials Science and Engineering 13(1):77
- SCHMIDT, H. & HATTEL, J. (2008)
Thermal modelling of friction stir welding, *Scripta Materialia* 58(5):332
- SCHMIDT, H., HATTEL, J. & WERT, J. (2004)
An analytical model for the heat generation in friction stir welding,
Modelling and Simulation in Materials Science and Engineering 12(1):143
- SELLARS, C. & TEGART, W. (1972)
Hot workability, *International Metallurgical Reviews* 17:1
- SHEPPARD, T. & JACKSON, A. (1997)
Constitutive equations for use in prediction of flow stress during extrusion
of aluminium alloys, *Materials Science and Technology* 13:203
- SHEPPARD, T. & WRIGHT, D. (1979)
Determination of flow stress. 1: Constitutive equation for aluminum alloys
at elevated temperatures, *Met. Tech.* 6(pt 6):215
- SHERCLIFF, H. & ASHBY, M. (1990a)
A process model for age hardening of aluminum-alloys.
1: The model, *Acta Metallurgica et Materialia* 38(10):1789
- SHERCLIFF, H. & ASHBY, M. (1990b)
A process model for age hardening of aluminum-alloys.
2: Applications of the model, *Acta Metallurgica et Materialia* 38(10):1803
- SHERCLIFF, H. & ASHBY, M. (1991), Modelling thermal processing of
aluminium alloys, *Materials Science and Technology* 7(1):85
- SHERCLIFF, H. & COLEGROVE, P. (2002)
Modelling of Friction Stir Welding, in *Mathematical Modelling of Weld
Phenomena* 6:927 (Maney Publishing, London, UK)

- SHERCLIFF, H. & COLEGROVE, P. (2007), Process modeling, in *Friction stir welding and processing*:187 (ASM, Ohio, USA)
- SHIRDAZI, A. (2005), Diffusion bonding. Retrieved June 2013 from www.msm.cam.ac.uk/phase-trans/2005/Amir/bond.html.
- SHTRIKMAN, M. (2008a), Current state and development of friction stir welding (review). Part 2: improvement of tools and welding method, *Welding International* 22(10):712
- SMERD, R.O. (2005), Constitutive behaviour of aluminium alloy sheet at high strain rates. M.Phil. thesis, University of Waterloo (Ontario, Canada)
- SMITH, I., SHI, G., FREEMAN, R. & SMITH, F. (2004) Advanced joining techniques for the 21st century, in *Int. forum on welding tech. in aviation*, Chinese Mechanical Engineering Society (Beijing, China.)
- SNEDDON, I.N. (1965), The relation between load and penetration in the axisymmetric Boussinesq problem for a punch of arbitrary profile, *International Journal of Engineering Science* 3(1):47
- SOMASEKHARAN, A. & MURR, L. (2004), Microstructures in friction-stir welded dissimilar magnesium alloys and magnesium alloys to 6061-T6 aluminum alloy, *Materials Characterization* 52(1):49
- SONG, J.L., LIN, S.B., YANG, C.L., FAN, C.L. & MA, G.C. (2010) Analysis of intermetallic layer in dissimilar TIG welding-brazing butt joint of aluminium to steel, *Sci. & Tech. of Welding & Joining* 15(3):213
- SONG, M. & KOVACEVIC, R. (2002), A new heat transfer model for friction stir welding, in *Transactions of the North American manufacturing research institute: 30th North American Manufacturing Research Conference*:565–572, Soc. Manufacturing Engineers (Dearborn, USA)
- SONG, M. & KOVACEVIC, R. (2003a), Numerical and experimental study of the heat transfer process in friction stir welding, *Proceedings of the IMechE Part B: Journal of Engineering Manufacture* 217(1):73

- SONG, M. & KOVACEVIC, R. (2003*b*), Thermal modeling of friction stir welding in a moving coordinate system and its validation, *International Journal of Machine Tools and Manufacture* 43(6):605
- SONG, M., KOVACEVIC, R., OUYANG, J. & VALANT, M. (2003), A detailed 3D transient heat transfer model for friction stir welding, in *Proc. 6th Int. Conf. on Trends in Welding Research*, ASM international (Phoenix, USA)
- SOUNDARARAJAN, V., ZEKOVIC, S. & KOVACEVIC, R. (2005), Thermo-mechanical model with adaptive boundary conditions for friction stir welding of AA6061, *Int. Journal of Machine Tools & Manufacture* 45(14):1577
- SSAB Tunnplat, DC04 deep-drawing steel datasheet (Technical report)
- STEUWER, A., PEEL, M.J. & WITHERS, P.J. (2006)
Dissimilar friction stir welds in AA5083-AA6082: The effect of process parameters on residual stress, *Mat. Sci. & Eng. A*: 441(1-2):187
- STRATTON, D. & SORENSEN, C. (2005), Characterizing the frictional interface between PCBN and 1018 steel for friction stir welding numerical models, in *Proc. 2nd Int. Conf. on Computational Methods and Experiments in Material Characterisation*:311–320 (Ashurst, UK)
- SU, P., GERLICH, A., NORTH, T. & BENDZSAK, G. (2006*a*)
Energy utilisation and generation during friction stir spot welding
Sci. & Tech. of Welding & Joining 11:163
- SU, P., GERLICH, A., NORTH, T. & BENDZSAK, G. (2006*b*), Material flow during friction stir spot welding, *Sci. & Tech. of Welding & Joining* 11:61
- SULLIVAN, A. & ROBSON, J. (2008)
Microstructural properties of friction stir welded and post-weld heat-treated AA7449 thick plate, *Mat. Sci. & Eng. A*: 478(1-2):351
- SURYANARAYANA, C. (2001)
Mechanical alloying and milling, *Progress in materials science* 46(1-2):1

- TARTAKOVSKY, A., GRANT, G., SUN, X. & KHALEEL, M. (2006)
Modeling of friction stir welding process with smooth particle hydrodynamics, in *3rd SAE Congress*, SAE (Detroit, USA)
- THOMAS, W. (1999)
Friction stir welding of ferrous materials: a feasibility study, in *Proc. 1st Int. Symp. on Friction Stir Welding* (Thousand Oaks, USA)
- THOMAS, W., NICHOLAS, E. & SMITH, S. (2001)
Friction stir welding: tool developments, in *Proc. TMS annual meeting*:213 (Aluminum Assoc. & Minerals, Metals & Mat. Soc., (New Orleans, USA)
- THOMAS, W., STAINES, D., WATTS, E. & MORRIS, I. (2005)
The simultaneous use of two or more friction stir welding tools, *Int. Journal for the Joining of Materials* 17(1):1
- THOMAS, W., THREADGILL, P. & NICHOLAS, E. (1999)
Feasibility of friction stir welding steel, *Science and Technology of Welding and Joining* 4(6):365
- THOPPUL, S.D. & GIBSON, R.F. (2009)
Mechanical characterization of spot friction stir welded joints in aluminum alloys by combined experimental/numerical approaches. Part 1: Micromechanical studies, *Materials Characterization* 60(11):1342
- THREADGILL, P., LEONARD, A., SHERCLIFF, H. & WITHERS, P. (2009)
Friction stir welding of aluminium alloys, *Int. materials rev.* 54(2):49
- TOROS, S., OZTURK, F. & KACAR, I. (2008)
Review of warm forming of aluminum-magnesium alloys, *Journal of Materials Processing Technology* 207(1-3):1
- TOZAKI, Y., UEMATSU, Y. & TOKAJI, K. (2007a), Effect of processing parameters on static strength of dissimilar friction stir spot welds in aluminium, *Fatigue & Fracture of Eng. Mat. & Structures* 30(2):143

- TOZAKI, Y., UEMATSU, Y. & TOKAJI, K. (2007*b*), Effect of tool geometry on microstructure and static strength in friction stir spot welded aluminium alloys, *Int. Journal of Machine Tools and Manufacture* 47(15):2230
- TROEGER, L. & STARKE, E. (2000)
Microstructural and mechanical characterization of a superplastic 6xxx aluminum alloy, *Mat. Sci. & Eng. A*: 277(1-2):102
- TWI Ltd. (2012), Online resource (www.twi.co.uk), retrieved 06/06/12
- ULYSSE, P. (2002)
Three-dimensional modeling of the friction stir-welding process, *Int. Journal of Machine Tools and Manufacture* 42(14):1549
- UPADHYAY, P. & REYNOLDS, A. (2012)
Effects of forge axis force and backing plate thermal diffusivity on FSW of AA6056, *Materials Science and Engineering: A* 558(0):394
- VALANT, M., SOUNDARARAJAN, M. & KOVACEVIC, R. (2005)
A novel tool design for friction stir spot welding, in *Proc. 7th Int. Conf. on trends in welding research*, ASM International
- VOCE, E. (1955), A practical strain-hardening function, *Metallurgia* 51:219
- WANG, H., COLEGROVE, P.A. & DOS SANTOS, J. (2013)
Hybrid modelling of 7449-T7 aluminium alloy friction-stir welded joints, *Sci. Tech. Welding & Joining* 18(2):219
- WILDEN, J., JAHN, S. & BECK, W. (2008)
Some examples of current diffusion bonding applications, *Materialwissenschaft und Werkstofftechnik* 39(4-5):349
- WITTHAR, K., BROWN, J. & BURFORDL, D. (2011)
Swept FSSW in aluminum alloys through sealants and surface treatments, in *Friction Stir Welding and Processing VI*:417, TMS (San Diego, USA)
- WOO, W., CHOO, H., BROWN, D. & FENG, Z. (2007)
Influence of the tool pin and shoulder on microstructure and natural aging

- kinetics in friction-stir-processed AA6061–T6, *Metallurgical and Materials Trans. A* 38:69
- WOO, W., CHOO, H., WITHERS, P. & FENG, Z. (2009), Prediction of hardness minimum locations during natural aging in an aluminum alloy 6061-T6 friction stir weld, *Journal of Materials Science* 44:6302
- YAN, H.H. & ZHANG, K.F. (2010)
Processing of multi-sheet structures of an aluminum alloy by laser welding/superplastic forming, *Materials & design* 31(4):2220
- YENI, C., SAYER, S. & PAKDIL, M. (2009)
Comparison of mechanical and microstructural behaviour of TIG, MIG and friction stir welded AA7075, *Kovove materialy (metallic materials)* 47(5):341
- YEO, S. & NEO, K. (1998)
Inclusion of environmental performance for decision making of welding processes, *Journal of Materials Processing Technology* 82(1-3):78
- YU, L., NAKATA, K. & LIAO, J. (2009), Microstructural modification and mechanical property improvement in friction stir zone of thixo-molded AE42 Mg alloy, *Journal of Alloys and Compounds* 480(2):340
- ZENER, C. & HOLLOMON, J.H. (1944), Effect of strain rate upon plastic flow of steel, *Applied Physics* 15
- ZHANG, Z., YANG, X., ZHANG, J., ZHOU, G.
XU, X. & ZOU, B. (2011), Effect of welding parameters on microstructure and mechanical properties of friction stir spot welded 5052 aluminum alloy, *Materials & Design* 32(8):4461
- ZHAO, H., WHITE, D. & DEBROY, T. (1999)
Current issues and problems in laser welding of automotive aluminium alloys, *International Materials Reviews* 44(6):238
- ZHU, X.K. & CHAO, Y.J. (2002), Effects of temperature-dependent material properties on welding simulation, *Computers & Structures* 80(11):967